



CERTIFICATE

This is to certify that the research work presented in the thesis entitled “*Synthesis and Properties of Cu-Zn Spinel Ferrites: Bulk, Nanoparticles and Thin Films*” is an original work carried out by **MOHAMMED SULTAN ABDULRAB ESMAIL**. This work has been carried out under my supervision. The thesis is submitted by **MOHAMMED SULTAN ABDULRAB ESMAIL** for the degree of **DOCTOR OF PHILOSOPHY (PhD)** in Physics at the School of Physics, University of Hyderabad. This thesis work has not been submitted to any other university partially or fully for the award of any degree.

Prof. Rajender Singh
(Thesis Supervisor)

Dean,
School of Physics,
University of Hyderabad.

Place: Hyderabad

Date:



DECLARATION

I hereby declare that the thesis entitled “*Synthesis and Properties of Cu-Zn Spinel Ferrites: Bulk, Nanoparticles and Thin Films*” submitted to the University of Hyderabad for the award of the degree of Doctor of Philosophy in Physics is a record of original research work done by me under the supervision of Professor **RAJENDER SINGH**, School of Physics, University of Hyderabad, Hyderabad. This project has not been submitted partially or fully for any degree in any other university.

(Mohammed Sultan Abdulrab Esmail)

Place: Hyderabad

Date:

ACKNOWLEDGEMENTS

IN THE NAME OF ALLAH, MOST GRACIOUS, MOST MERCIFUL

First and foremost, I direct all my thanks and praise to **ALMIGHTY ALLAH**, The Cherisher and Sustainer of the World, Who created, Who has taught by the pen, has taught man what he did not know, for His guidance and assistance that facilitated every stage in my postgraduate studies and in my whole life. My success in everything can only come from ALLAH. In Him, I trust, and unto Him, I turn.

I would like to express my sincere appreciation and gratitude to my supervisor, Professor **RAJENDER SINGH**, for his invaluable guidance, thoughtful suggestions, steady encouragement and unlimited support over the years during my research at School of Physics, University of Hyderabad. Daily scientific interaction with him greatly enriched my research outlook. His patience and continuous support during difficult moments are greatly appreciated. His time spent with me in the lab especially during work with the sputtering system, where he taught me various skills, was really exiting to me. He deals with me generously, kindly and friendly throughout the period I worked with him. I will be forever in gratitude to him for giving me the opportunity to work under his direction.

I have my deep thanks to the dean of the School of Physics Prof. C. Bansal and the former deans, Prof. V. Srivastava and Prof. V.S.S. Sastry, for providing me the facilities for the successful completion of my work. I also thank all the faculty members who have helped me throughout my research. I am grateful to my dissertation committee at the school of physics HCU especially, Dr. **P. K. Suresh** for his patience and providing me constant advices throughout my research period.

I wish to express my deep appreciation to all members of the Central instruments Laboratory (CIL) staff at the University of Hyderabad for their unlimited help. I especially thank Dr. S.M. Ahmed, Mr. C. S. Murthy, Mr. Suresh, Dr. S. Manjunath, Mr. Nageshwar Rao, Mr. Sudhakar, Mr. Illayaa, Mr. Kishta Reddy and Mr. Rajkumar for the technical

support. They have provided me full access to CIL facilities (XRD, VSM, SEM, EDAX, ESR, Centrifuge etc.) giving me hands on experience. I also thank Mr. Sambasiva Rao, Mr. Mantoo Kumar and Giri Bahadur for the help they have provided me required for the low temperature experiments. I am grateful to the non teaching staff of the School of Physics especially Mr. Abraham and Mrs. Saramma for all the help they have provided regarding administrative matters.

I also thank the University Grant Commissions (UGC), New Delhi, India for providing me the JRF fellowship and financial support.

The best of my graduate time was with the great people in my laboratory. I was really very fortunate to work with this excellent group and enjoyed the time spent with them either in or outside the lab. We have shared bitterness and sweetness together in the lab. I would like to thank all of my former and present lab-mates, in particular, Dr. Joji Kurian, Sandhya, Rajesh Babu, Sai Priya, Vijayan and Venkaiah for the help they have given me and the long scientific discussions. I offer Especial thanks to Sai Priya and Venkaiah who proof read the thesis manuscript. I'm really lucky to do my research along with Dr. Joji Kurian. He was my lab-mate, my brother, my friend ... with him I did not feel I am alone. From him I learnt a lot. With him I shared thoughts, feelings and best moments. He is a good listener; to him I opened my heart and mind. Thanks a lot for great help and support I received during various stages of this work. In short, Dr. Joji Kurian is a unique person!

Now, I have to thank all former and present research scholars from school of physics for their help, support and discussions. I particularly thank Saravanan, Sudheendran and Brahma for helping me doing optical and dielectric properties. I also thank Abhilash and Ravi for helping me in measuring film thicknesses using profilometry. My special thanks to Sathish A. for helping me with the SEM and VSM acquisition. I also thank Prashant, Kiran, Uma, Lakshmi, Rizwan, Ashuthosh, Gnanavel, Thejal, Yugander, Shinto, Vasu, Ram Babu and all friends from the School of Physics and chemistry.

I have to thank all my friends who cross the seas, deserts and lands for seeking science and education from University of Hyderabad. First I would like to thank Dr. Abdul-Malik Mansour who guided me and who helped me getting admission to this University. I thank Mr. Amer Sallam for helping me in computer software repairs. I also thank all my friends,

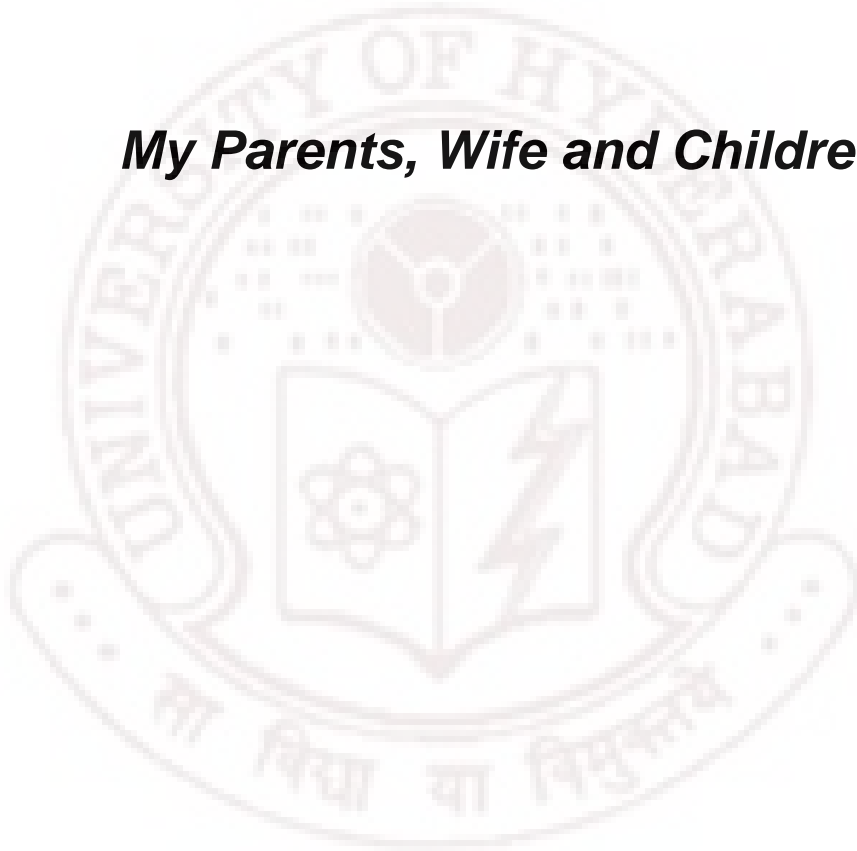
Mohammed Mansour, Mahmoud Mansour, Mohammed Al-Shormani, Anees Al-Nnajjar, Mohammed Al-Hosami, Hussain Al-Nakhee, Ahmed Ghaleb, Abdulrahman Al-Toaiti, Mansour Mohammed, Khaled Al-mozaije, Yaser, Ali Alnuzaili, Ali Shahrah, Tawfeeq, Muthanna, Ali Kasim, Mahmoud Al-Flasteni, Mohammed Hassan, Abdulkafe, Badea'a, Taha, Nesreen, Adnan, Abu Bakar, Fahem, Faisal, Mohammed Almasodi, Mujahed and all my friends.

Finally, I wish to express my heart felt gratitude to my proud parents (who I left them years away) for their continuous support and encouragement through all the years. To my beloved wife, Hamdah, thanks for all your loving care and for being behind me throughout all my endeavors. To my children I say: Yes, I have spent part of your enjoyment time for research. Yes, I have done that only for you. To Dr. Hameed, the first teacher, who sowed the first seed of research in me and made it grow, who taught me holding the pen, who taught me solving equations, I say to you that your tree has grown and has borne fruits. To my brothers Hamoud and Dammaj and my cousins Makki Saif, Mohammed and Abdul-Azeez and my uncle Abdul-Hameed thank you for financial support. The encouragement from my entire family was, and still is, the motivation for me to overcome all difficulties on the road of my life. I dedicate this work to them.

Mohammed Sultan

Dedicated to

My Parents, Wife and Children



CONTENTS

Chapter-1 Introduction (Spinel ferrites)	1
1.1 Historical development of ferrites	2
1.2 Ferrites vs. ferromagnetic materials	3
1.3 Crystal structure of ferrites	4
1.3.1 <i>Spinel ferrites</i>	5
1.4 Fundamentals of magnetism	8
1.4.1 <i>Classification of magnetic materials</i>	9
1.4.2 <i>The origin of exchange interactions</i>	12
1.4.3 <i>Magnetization curve</i>	13
1.4.4 <i>Magnetic anisotropy</i>	15
1.4.5 <i>Magnetism in Nanoparticles: Superparamagnetism</i>	18
1.4.6 <i>Ferromagnetic resonance (FMR)</i>	20
1.5 Dielectric properties of ferrites	31
1.5.1 <i>Dielectric constant and dielectric loss</i>	34
1.5.2 <i>Dielectric dispersion process</i>	35
1.6 Optical properties of ferrite thin films	38
1.6.1 <i>Optical parameters</i>	39
1.6.1.1 <i>Reflection–Transmission (RT) Method</i>	39
1.6.1.2 <i>Envelope method</i>	40
1.6.2 <i>Optical bandgap</i>	44
1.7 Review of work on copper ferrites.....	46
1.8 Review of work on zinc ferrites.....	48
1.9 Objectives of present work	54
1.10 Thesis organization.....	55
References	56

2.1 Materials Preparation methods**2.1.1 Ceramic processing of spinel ferrites (bulk form)**

<i>2.1.1.1 Reaction mechanism</i>	65
<i>2.1.1.2 Sintering process</i>	66
<i>2.1.1.3 Bulk Sample preparation</i>	69

2.1.2 Synthesis of Cu-Zn ferrite nanoparticles

<i>2.1.2.1 Ball Milling</i>	71
<i>2.1.2.2 Sonochemical Method</i>	72
<i>2.1.2.3 Sol-gel process</i>	72
<i>2.1.2.4 Microemulsion</i>	74
<i>2.1.2.5 The Hydrothermal Method</i>	74
<i>2.1.2.6 Combustion method</i>	75
<i>2.1.2.7 Coprecipitation method</i>	76
<i>2.1.2.7.1 Co-precipitation mechanism</i>	76
<i>2.1.2.8 Experimental procedure for synthesis of ferrite nanoparticles</i>	78

2.1.3 Thin films of Cu-Zn ferrites

<i>2.1.3.1 Thermal Evaporation</i>	81
<i>2.1.3.2 Pulsed laser deposition (PLD)</i>	81
<i>2.1.3.3 Sputtering</i>	83
<i>2.1.3.3.1 Sputtering process</i>	83
<i>2.1.3.3.2 Effect of magnetic field</i>	85
<i>2.1.3.3.3 Film growth</i>	86
<i>2.1.3.3.4 Film microstructure</i>	87
<i>2.1.3.3.5 Deposition Equipment (Sputtering system)</i>	88
<i>2.1.3.3.6 RF-magnetron Sputtering System</i>	91
<i>2.1.3.3.7 Experimental Procedure</i>	96

2.2 Characterization techniques

<i>2.2.1 X-Ray Diffraction (XRD)</i>	98
<i>2.2.2 Scanning electron microscopy (SEM)</i>	102
<i>2.2.3 Energy dispersive X-ray spectrometry (EDAX)</i>	104
<i>2.2.4 Profilometry</i>	105
<i>2.2.5 Atomic force microscopy (AFM)</i>	106

2.2.6 Vibrating Sample Magnetometer (VSM).....	108
2.2.7 Ferromagnetic resonance (FMR)	110
2.2.8 Optical transmittance	114
2.2.9 Dielectric measurements	116
References	118

Chapter-3 Properties of bulk Cu-Zn ferrites **122**

3.1 Crystal Structure	122
3.2 Microstructure analysis.....	125
3.3 Magnetization studies	127
3.4 Dielectric properties	132
3.4.1 AC electrical resistivity	132
3.4.2 Dielectric constant	133
3.4.3 Dielectric loss tangent	135
3.4.4 Composition dependence of dielectric properties	136
3.5 Effect of quenching on properties of CuFe_2O_4	138
References	143

Chapter-4 Studies on Cu-Zn ferrite nanoparticles **145**

4.1 Crystal structure.....	145
4.2 Microstructure analysis.....	146
4.3 Magnetic properties.....	148
4.4 FMR studies.....	150
4.5 Dielectric properties.....	157
4.6 Effect of heat treatment	
4.6.1 Copper ferrite nanoparticles.....	160
4.6.1.1 Crystal structure.....	160
4.6.1.2 Microstructural analysis.....	162
4.6.1.3 Magnetic properties	163
4.6.2 Zinc ferrite nanoparticles.....	166
4.6.2.1 Crystal structure (XRD analysis).....	166
4.6.2.2 Microstructural analysis	168
4.6.2.3 Magnetic properties	170

4.6.2.4 ESR study.....	173
References	176

Chapter-5 Studies on thin films of Cu-Zn ferrites 179

5.1 Copper ferrite (CuFe_2O_4) thin films

5.1.1 Effect of Ar- O_2 pressure	181
5.1.1.1 Structural analysis (XRD).....	181
5.1.1.2 Surface morphology (AFM).....	182
5.1.1.3 Magnetization studies (M-H plots)	185
5.1.1.3 Magnetization studies (ZFC-FC)	188
5.1.1.4 FMR studies	191
5.1.1.5 Optical properties	196

5.2 Zinc ferrite (ZnFe_2O_4) thin films

5.2.1 Effect of working gas pressure	198
5.2.1.1 Structural analysis (XRD).....	198
5.2.1.2 Film surface morphology (AFM)	200
5.2.1.3 Optical properties	202
5.2.1.3.1 Spectral transmittance	202
5.2.1.3.2 Refractive index	203
5.2.1.3.3 Absorption and extinction coefficients	206
5.2.1.3.4 Film thickness	207
5.2.1.3.5 Optical energy gap	208
5.2.1.4 Magnetic properties	209
5.2.1.4.2 FMR studies	212
5.2.2 Effect of Heat treatment	217
5.2.2.2 Structural analysis (XRD).....	217
5.2.2.2 Microstructural analysis	218
5.2.2.3 Film surface morphology (AFM studies)	219
5.2.2.4 M-H plots	220
5.2.2.4 Magnetization studies (ZFC-FC)	222
5.2.2.4 FMR studies	224

5.3 Copper-zinc ferrite ($\text{Cu}_{0.6}\text{Zn}_{0.4}\text{Fe}_2\text{O}_4$) thin films

5.3.1 Effect of Ar gas pressure	227
---------------------------------------	-----

5.3.1.1 Structural analysis (XRD)	227
5.3.1.2 Surface morphology (AFM)	229
5.3.1.3 Magnetization studies (M-H plots).....	231
5.3.1.4 FMR studies	233
5.3.2 Effect of O ₂ gas pressure	235
5.3.2.1 Surface morphology	235
5.3.2.2 Magnetization studies (M-H plots)	236
5.3.2.3 FMR Studies	237
5.3.3 Effect of (Ar+O ₂) gas mixture pressure	238
5.3.3.1 Structural analysis (XRD)	238
5.3.3.2 Surface morphology (AFM)	239
5.3.3.3 Magnetization studies (M-H plots)	240
5.3.3.4 Magnetization studies (ZFC-FC)	240
5.3.3.5 FMR studies	242
5.3.3.6 Optical properties	246
References	247
Summary and conclusions	253

CHAPTER 1

Introduction

Ferrites are an important class of technological materials that have been recognized to have significant potential in applications ranging from millimeter wave integrated circuitry to transformer cores and magnetic recording [1-6]. The technological importance of ferrites increased continuously as many discoveries required the use of magnetic materials [7]. The ferrofluid technology exploited the ability of the colloidal suspensions of micron-sized ferrite particles to combine the physical properties of the liquids with the magnetism of the crystalline bulk ferrite materials for various applications such as sealing, position sensing as well as the design of actuators [8, 9]. As such a tremendous technological progress in electronics was inevitably accompanied by the development of computing, transportation and non-volatile data storage technologies. Miniaturization of the electronic devices became critical, thereby leading to the reduction of the size of the magnetic materials to dimensions comparable to those of the atoms and molecules [10]. At this point, nanoscale ferrites have found enormous potential applications in medicine and life sciences [11]. The synthesis of ferrite nanoparticles with controllable dimensionality and tailorable magnetic properties along with the understanding of the structure-property correlations have become one of the topics of fundamental scientific importance [12, 13].

Ferrite thin films have the potential to replace bulky external magnets in current microwave devices. They can provide unique circuit functions that cannot be produced by other materials [14]. At microwave frequencies ferrite materials have low losses, high resistivity and strong magnetic coupling, making them irreplaceable constituents in microwave device technology such as isolators, circulators and phase shifters. Ferrite thin films have also attracted much attention in recent years as one of the candidates for high density magnetic recording and magneto-optical recording media because of their unique

physical properties such as high Curie temperature, large magnetic anisotropy, moderate magnetization, high corrosion resistance, excellent chemical and mechanical stability and large Kerr and Faraday rotations. Magnetic soft ferrite thin films with high resistivity and ac permeability were advanced for applications to multilayer chip inductors, micro-transformers, magnetic recording and high frequency switched mode power supply [15]. In addition to these applications, both copper and zinc ferrites have been proved to be good gas sensors and catalysts [16-19]. As fillers in composites, ferrites can improve the modulus of the polymer matrix and provide additional functionality such as electromagnetic interference (EMI) shielding [20, 21].



Figure 1.1: Some applications of ferrite materials (a) Circulator (b) Memory cores

1.1 Historical development of ferrites

Scientists believe that Greeks discover magnetism around 600BC in the mineral lodestone (magnetite Fe_3O_4), the first ferrite. Much later at about 1000AD the first application of ferrites was as lodestone used in compasses by marines to locate magnetic North. In 1600 William Gilbert published the first systematic experiments on magnetism and he described the earth as a big magnet in his book "De Magnete". The first systematic study on the relationship between chemical composition and magnetic properties of various ferrites was reported by Hilpert in 1909. About 20 years after Hilpert's work, Forestier, in France, started his chemical study on the preparation of various ferrites and measurements of their saturation magnetization as well as Curie temperature. During the 1930's research on soft ferrites continued, primarily by Kato and Takei and J. L. Snoek of the Phillips Research Laboratories in the Netherlands [22-a]. During this period Barth and Posniak discovered inverse ferrites (magnetic form) and normal ferrites (non-magnetic form). Landau and Lifschitz describe loss mechanisms in magnetic materials [22-b]. The appearance of first

commercial ferrite products for telecommunication was in 1945 as a result of the significant contributions of Snoek's group work (Philips) since 1930s. Kittel formulated theory of domain formation, coercive force and domain wall dynamics [22-c]. The work of Verwey and Heilmann [25] on the distribution of ions over the tetrahedral and octahedral sites in the spinel lattice has contributed to progress in the physics and chemistry of ferrites. In 1948, Neel [23-a] explained magnetism in ferrites on the basis of two anti-parallel magnetic sub-lattices (uncompensated anti-ferromagnetism). The invention of hexagonal ferrite magnets such as barium and strontium ferrite magnet was by Went *et al.* in 1952 [23-b]. In 1953 MIT built Whirlwind-I, the first computer with ferrite core memory. During 1950's Scientists from different countries developed square-loop ferrite cores as well as ferrite devices for microwave applications. In late 1950's Smit & Wijn [26] published a comprehensive book on ferrites. Since then developments have been made on the magnetic characteristics of ferrites that have improved microwave devices performances. At the end of the 20th century Sugimoto [7] published a paper which surveys the past, present and future of ferrites.

The first international conference on ferrites, ICF, was held in 1970 in Japan. Since then ten such conferences have been held. These conferences have contributed greatly to the advancement of the science and technology of ferrites. Significant advances in materials processing and device development has taken place during the last few years. The development of processing methods such as sol-gel, Sputtering, PLD and new analytic techniques like SPM extended X-ray absorbance fine structure analysis (EXAFS) over the recent years directed the research on ferrites towards nanoparticles and thin films. RF-Magnetron Sputtering and laser ablation deposition have been shown to allow the manipulation of cations within a unit cell providing opportunities to fabricate far from equilibrium structures and ultimately to tailor magnetic, electronic, and microwave properties for specific applications.

1.2 Ferrites vs. ferromagnetic materials

Ferrites, like ferromagnetic materials, consist of self saturated domains, exhibit spontaneous magnetization and show the characteristic hysteresis behavior and the

existence of magnetic ordering temperature. There are many parameters such as magnetization, coercivity, permittivity, permeability, resistivity etc. which play an important role in determining a particular application of magnetic material. These parameters are greatly influenced by porosity, grain size and microstructure of the sample. The resistivity of ferrites is at least six to twelve orders (depending on composition) higher than that of ferromagnetic materials such as permalloys and silicon iron. This has given ferrites a distinct advantage as magnetic materials of choice in high frequency applications [24]. Ferromagnetic materials are primarily metals and alloys but ferrites are ceramics. The saturation magnetization of ferrites is approximately one fifth to one eighth that of silicon irons. Ceramic processing techniques allow the economic fabrication of ferrite devices in various shapes and sizes (figure 1.2).



Figure 1.2: Ferrite devices in various shapes and sizes

1.3 Structure of ferrites

Ferrites are ceramic magnetic materials containing iron oxide as a major constituent. It refers to the entire family of iron oxides that includes spinels, garnets, hexaferrites, and orthoferrites [24].

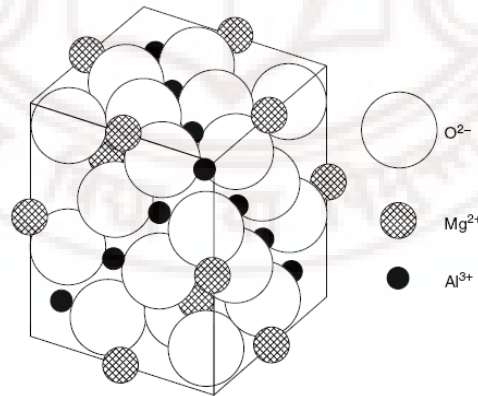
Table 1.1: Crystal types of ferrite materials

Type	Structure	General formula	Example
Spinel	Cubic	$1\text{MeO} \cdot 1\text{Fe}_2\text{O}_3$	Me = Ni, Mn, Co, Cu, Mg, Zn e.g., $\text{CuO} \cdot \text{Fe}_2\text{O}_3$
Garnet	Cubic	$3\text{Me}_2\text{O}_3 \cdot 5\text{Fe}_2\text{O}_3$	Me = Y, Sm, Eu, Gd, Dy, Ho, Er, Lu e.g., $3\text{Y}_2\text{O}_3 \cdot 5\text{Fe}_2\text{O}_3$
Magnetoplumbite	Hexagonal	$1\text{MeO} \cdot 6\text{Fe}_2\text{O}_3$	Me = Ba, Sr, Pb, Ca e.g., $\text{BaO} \cdot 6\text{Fe}_2\text{O}_3$
Ortho-ferrite	Perovskite	RFeO_3	R is rare earth

1.3.1 Spinel ferrites

Spinel ferrites are mixed oxides with general formula AB_2O_4 , where A is a metal ion with +2 valence and B is the Fe^{+3} ion. They have a spinel-type structure similar to that of the mineral “spinel”, MgAl_2O_4 (Figure 1.3). Substitution of A by divalent cation M (M: Mn, Co, Ni, Cu, Zn, Mg) and B by Fe forms ferrite MFe_2O_4 ($\text{MO} \cdot \text{Fe}_2\text{O}_3$). The unit cell of spinel ferrite contains eight molecules (8 formula units MFe_2O_4).

$$8 \text{MFe}_2\text{O}_4 = (8\text{M} + 16\text{Fe}) \text{ cations} + 32 \text{ Oxygen anions} = 56 \text{ ions}$$

**Figure 1.3:** The spinel crystal structure of MgAl_2O_4 [25].

In a typical spinel lattice (figure 1.3), The large 32 oxygen anions ($R_{\text{O}_2} = 1.4 \text{ \AA}$) arrange to form a nearly close packed fcc cubic lattice array forming two kinds of spaces between anions: tetrahedrally coordinated sites (A), surrounded by four nearest oxygen

ions, and octahedrally coordinated sites (B), surrounded by six nearest neighbor oxygen ions. The interstitial sites are schematically represented in Figures (1.4). There are 64 tetrahedral and 32 octahedral possible positions for cations in the unit cell. In order to achieve a charge balance of the ions, the interstitial voids will be only partially occupied by positive ions. Therefore, in stoichiometric spinels, only one-eighth ($8/64$) of the tetrahedral sites and one-half ($16/32$) of the octahedral sites are occupied by metal ions in such a manner as to minimize the total energy of the system. The distribution of cations that can be influenced by several factors such as the chemical composition (ionic radius, electronic configuration and electrostatic energy), method of preparation and preparation conditions [25-28].

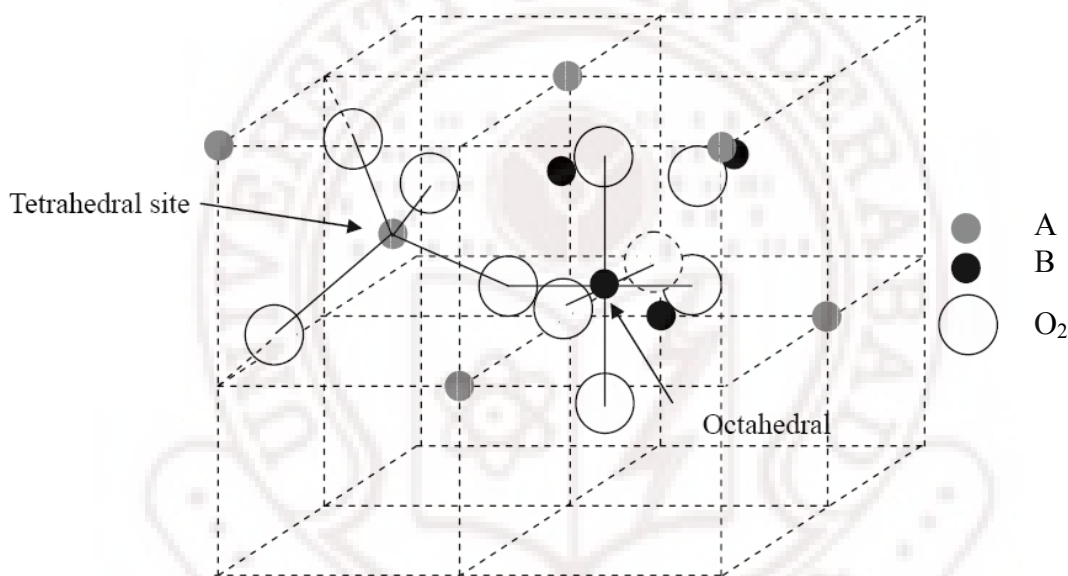


Figure 1.4: Schematic drawing of the spinel unit cell structure [29].

Depending on the cation distribution over the different crystallographic sites, the spinel compounds can be generally classified into two categories: normal and inverse spinels. Normal spinels have the general formula $(A)_t[B_2]_oO_4$ and contain all the trivalent metal ions $[B^{3+}]$ in the octahedral sites (o), whereas all the divalent metal ions (A^{2+}) reside in the tetrahedral sites (t). Transition metal ferrites, such as $ZnFe_2O_4$ and $CdFe_2O_4$, assume the normal spinel structure. In the inverse spinels, the divalent cations (A^{2+}) and half of the trivalent cations (B^{3+}) occupy the octahedral sites, whereas the other half of the B^{3+} metal ions lie in the tetrahedral sites. Most of the first series transition metal ferrites, such as $NiFe_2O_4$, $CoFe_2O_4$, Fe_3O_4 , and $CuFe_2O_4$, are inverse spinels; their site occupancy can be

described by the general formula $(B)_t[AB]_oO_4$. Some other spinel compounds possess the divalent and the trivalent metal ions randomly distributed over both the tetrahedral and the octahedral interstices. These compounds are named mixed spinels and their composition is best represented by the general formula $(A_{1-d}B_d)_t[A_dB_{2-d}]_oO_4$, where the inversion parameter, d , denotes the fraction of the trivalent cations (B^{3+}) residing in the tetrahedral sites. Mixed spinels occur in a wide range of compositions and are usually considered as intermediate compounds between the two extreme cases, i.e., normal and inverse spinels [27].

Representative ferrites adopting the mixed spinel structure include $MgFe_2O_4$ and $MnFe_2O_4$. Since magnesium ferrite contains 10% of the Mg^{2+} ions in the tetrahedral interstices and 90% in the octahedral interstices, according to the above mentioned formula, the cation distribution can be described as $(Mg_{0.1}Fe_{0.9})_t[Mg_{0.9}Fe_{1.1}]_oO_4$. Manganese ferrite, with 80% of the Mn^{2+} ions occupying the tetrahedral holes and 20% occupying the octahedral holes, can be written as $(Mn_{0.8}Fe_{0.2})_t[Mn_{0.2}Fe_{1.8}]_oO_4$. Therefore, the inversion parameter is 0.9 for $MgFe_2O_4$ and 0.2 for $MnFe_2O_4$. Usually, d varies between 0 (for normal spinel compounds) and 1 (for inverse spinels); the inversion parameter can also take intermediate values ($0 < d < 1$) and the corresponding ferrites adopt a mixed spinel structure characterized by a random occupancy of the tetrahedral and octahedral sites by the divalent (A^{2+}) and trivalent (B^{3+}) cations. Nanoparticles and thin films of inverse spinels such as $CuFe_2O_4$ and normal spinel such as Zn-ferrites also adopt a mixed spinel structure [28].

The exchange interaction between A and B sites is negative and the strongest among the cations so that the net magnetization comes from the difference in magnetic moment between A and B sites. The Fe cations are the sole source of magnetic moment and can be found on any of two crystallographically different sites: tetrahedral and octahedral sites [30].

Given the complexity of the crystal structures of cubic spinel ferrites, the structural disorder, ranging from cation disorder to grain boundaries, has a significant effect on the electronic and magnetic properties. Moreover, these ferrites have open crystal structures so that diffusion of metal cations readily occurs. Both $CuFe_2O_4$ and $ZnFe_2O_4$ and mixed $Cu_{1-x}Zn_xFe_2O_4$ ferrites are interesting materials for research and industrial applications and taken as ideal systems for spinel ferrites. The crystal structure of these materials is sensitive to the preparation conditions and consequently influences their typical electrical and magnetic properties.

1.4 Fundamentals of magnetism

A magnetic field is produced whenever there is an electrical charge in motion. In atoms, the magnetic moment originates from the motion of the electron spin and the orbital angular momentum around the nucleus as shown in figure 1.5. The net magnetic moment of an atom is just the sum of the magnetic moments of each of the constituent electrons, including both orbital and spin contributions. Moment cancellations due to opposite direction of electrons moment paired are also needed to be taken into account [28, 31].

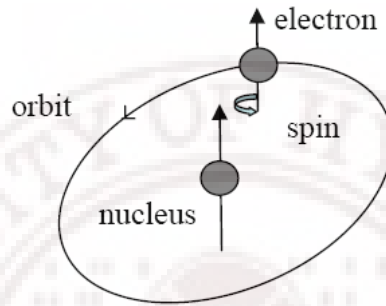


Figure 1.5: The orbit of a spinning electron about the nucleus of an atom

When a material is placed in a magnetic field, the flux density (or magnetic induction B) is given by

$$\mathbf{B} = \mathbf{H} + 4\pi\mathbf{M} \quad [\text{CGS}] \quad (1.1)$$

where \mathbf{H} is the magnetic field and \mathbf{M} is the magnetization. The nature of \mathbf{H} , \mathbf{M} and \mathbf{B} is fundamentally all the same, as implied by equation (1).

The units of these three parameters are also similar, and depend on the system of units being used. There are currently three systems of units that are widely used, including CGS or Gaussian system and SI system (Appendix A).

The susceptibility of a material χ is the ratio between the magnetization and the field given by

$$\chi = \mathbf{M} / \mathbf{H} \quad (\text{emu/Oe.cm}^3) \quad (1.2)$$

The permeability of a material relates the magnetic induction to the field by

$$\mathbf{B} = \mu\mathbf{H} \quad (\text{dimensionless}) \quad (1.3)$$

Since $\mathbf{B} = \mathbf{H} + 4\pi\mathbf{M}$, we have $\mathbf{B} / \mathbf{H} = 1 + 4\pi\mathbf{M} / \mathbf{H}$

$$\mu = 1 + 4\pi\chi \quad (1.4)$$

When characterizing magnetic properties, the susceptibility is the main parameter that is usually considered as it provides a measure of the response of the sample to an applied

magnetic field. The differences in magnetic behavior of materials are most often described in terms of the temperature and field dependence of the susceptibility [28].

1.4.1 Classification of magnetic materials

In metals such as iron, cobalt and nickel (transition metals) having unfilled sub-valence shells, the magnetic moments of the inner shell (the d-shell) electrons remain uncompensated. This results in each atom acting as a small magnet. In addition, within each crystal the atoms are sufficiently close and the magnetic moments of the individual atom are sufficiently strong. This leads to a strong positive quantum-mechanical exchange interaction and long range ordering of magnetic moments which manifests itself as *ferromagnetism*. There are three conditions that must be met simultaneously before a substance shows ferromagnetic behavior [24]. They are as follows

- There must be an unfilled electron shell within the atom
- There must be uncompensated electronic spins in this unfilled inner shell
- The ions of the atoms must form a crystal lattice having a lattice constant at least three times the radius of the unfilled electron shell.

If the adjacent moments are aligned antiparallel as a result of a strong negative interaction and only one type of magnetic moment is present, the neighboring atomic moments cancel each other resulting in zero net magnetization. The material is then said to exhibit *anti-ferromagnetism*. The situation can be interpreted as the result of simultaneous existence of the two sub-lattices. A sublattice is a collection of all the magnetic sites in a crystal with identical behavior, with all moments parallel to one another and pointing in the same direction, which are spontaneously magnetized and have the same intensity. Typical examples of anti-ferromagnetic materials are the metals Cr and α -Mn.

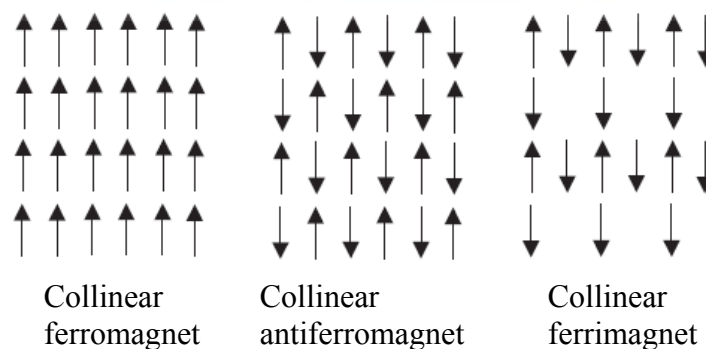


Figure 1.6: Schematic representation of magnetic structures for ferromagnetic, antiferromagnetic and ferrimagnetic materials.

Sublattices (two or more) can also have spontaneous magnetization in opposite direction but with different intensities. For instant, when a material contains magnetic ions of different species and magnetic moments, or the same species occupying crystallographically inequivalent sites, the resulting moments of the sublattices i.e. parallel or antiparallel to one another and the dominant exchange interaction is mediated by the neighboring nonmagnetic ions. Such materials have a spontaneous magnetization, which is weaker than materials whose magnetic moments are oriented in the same direction and yet strong enough to be of technical significance. These materials are said to exhibit *ferrimagnetism*, a term coined by Neel (1948). Lodestone or magnetite, $\text{FeO} \cdot \text{Fe}_2\text{O}_3$, is an example of naturally occurring ferrimagnetic substance. The origin of magnetism in ferrites is due to [29]:

- Unpaired 3d electrons
- Superexchange between adjacent metal ions
- Nonequivalence in number of A and B- sites.

In the free state, the total magnetic moment of an atom containing 3d electrons equal to the sum of the electron spin and orbital moments. In ferrites (magnetic oxides), the orbital magnetic moment is mostly “quenched” by the electron field, caused by the surrounding oxygen about the metal ion (crystal field). The atomic magnetic moment (m) becomes the moment of the electron spin and is equivalent to ($m = \mu_B n$) where μ_B is the Bohr magneton and n the no. of unpaired electrons. Indirect exchange interaction (superexchange) takes place between adjacent metal ions separated by oxygen ions (A-O-B, B-O-B and A-O-A). Where all A-B, B-B and A-A coupling are negative. The strength of these interactions depends on the degree of orbital overlap of oxygen orbits and the transition metal orbits. The interaction will decrease as the distance between the metal ions increases and the angle of Me-O-Me bonds decreases from 180° to 90° . The only important interaction in spinel ferrites is the AB interaction since the angle is about 125° while BB is negligible because the angle is 90° . $|AB \text{ coupling}| > |BB \text{ coupling}| > |AA \text{ coupling}|$. The interaction is such that antiparallel alignment occurs when both ions have 5 or more 3d electrons or 4 or fewer 3d electrons. Parallel alignment occurs when one ion has ≤ 4 electrons and the second ion has ≥ 5 electrons. Since the common ferrite ions (Mn^{2+} , Fe^{2+} , Ni^{2+} , Co^{2+} , Cu^{2+}) have more than 5d electrons, the magnetic moments are aligned antiparallel between A and B sites. Since there are twice as many B-site occupied as A-sites, the B-site will

dominate over the A site resulting in ferrimagnetism (Neel 1948). The net saturation magnetization is equal to the vector sum of the net moments of each sublattice [24].

$$M_S = |M_B - M_A| \quad (1.5)$$

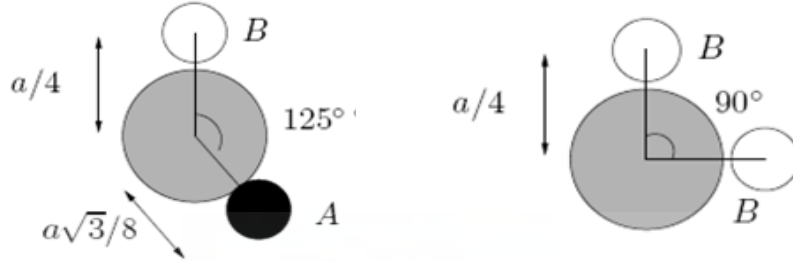


Figure 1.7: Some of the configurations of ion pairs which probably make the greatest contributions to the exchange energy in the spinel lattices [26].

The existence of exchange field changes the state of the material from paramagnetic to ferrimagnetic. The effect of exchange field is opposed by thermal agitations and above a certain temperature called the Curie temperature, the ferrimagnetism is destroyed. In the mean field theory, to characterize A–A, B–B, and A–B exchange interactions molecular-field coefficients $\lambda_{E,aa}$, $\lambda_{E,bb}$, and $\lambda_{E,ab} = \lambda_{E,ba}$ are introduced, and these coefficients may have negative or positive signs. Keeping in mind that for $T > T_C$ (the Curie temperature) the system is a disordered paramagnet, and for $T < T_C$ the system is a ferrimagnet. To reiterate, in a ferrimagnetic material, magnetic moment of sublattice A and that of sublattice B are in opposite direction but with unequal amplitudes, which gives rise to non zero net magnetization. The total magnetic field in the absence of external magnetic field acting on a magnetic dipole in each sublattice is (in cgs units) [33]

$$H_a = \lambda_{E,aa}M_a + \lambda_{E,ab}M_b \quad (1.6a)$$

$$H_b = \lambda_{E,aa}M_a + \lambda_{E,bb}M_b \quad (1.6b)$$

The magnetization of each sub-lattice can be described by the Curie relations where they have their own Curie constants C_a and C_b , which are not identical since each sublattice contains different kinds of ions on different crystallographic sites, as

$$M_a = \frac{C_a}{T}(H_0 + H_a) \quad (1.7a)$$

$$M_b = \frac{C_b}{T}(H_0 + H_b) \quad (1.7b)$$

Solving Eqs. (1.6) and (1.7), the inverse susceptibility of a ferrimagnet in the paramagnetic regime can be expressed as follows [33, 34]

$$\frac{1}{\chi} = \frac{H_0}{M_a + M_b} = \frac{T}{C} + \frac{1}{\chi_0} - \frac{K}{T - \Theta'} \text{ in [cgs units]} \quad (1.8)$$

where $1/\chi_0$, K , C and Θ' are constants depending on C_a , C_b , $\lambda_{E,aa}$, $\lambda_{E,bb}$, and $\lambda_{E,ab}$

1.4.2 The origin of exchange interactions

The origin of various exchange interactions in the magnetic materials have been described in the literature [32, 34, 35]. A brief description of these interactions is given below.

(a) Direct Exchange Interaction

When paramagnetic ion/atom cores are next to each other on the lattice sites and if they are not sufficiently tightly bound so that their electron clouds do overlap then they can have direct exchange. All localized dipole moment would tend to align parallel (had the temperature been absolute zero).

(b) Superexchange Interaction

Superexchange interaction is defined as an indirect exchange interaction between magnetic ions which is mediated by a non-magnetic ion placed in between. Sometimes one component of an alloy might be having intrinsic magnetic dipole moment whereas other component might be non magnetic. Even when the wave functions of two magnetic ions do not overlap, such crystal can have appreciable spontaneous magnetization. Two magnetic ions interact with the mediation of non magnetic ion. In such cases when paramagnetic ion/atom electron clouds don't overlap and there is another non paramagnetic atom/ion sitting in between we call such interactions as superexchange interaction.

(c) Double exchange interaction

Zener (1951) proposed this exchange mechanism to account for the interaction between adjacent ions of parallel spins via a neighboring oxygen ion. The argument requires the presence of ions of the same metal in different valence states. In magnetite, for example, Zener's argument would envisage the transfer of one electron from the Fe^{2+} ion, with six

electrons in its 3-d shell, to the nearby oxygen ion and the simultaneous transfer of an electron with parallel spin to the Fe^{3+} ion nearby.

(d) Indirect Exchange Interaction

In metallic and semiconducting surroundings another kind of exchange interaction can dominate. In the sea of conduction electrons two paramagnetic ions/atoms can interact with each other by the mediation of free electrons. This type of exchange interaction is called indirect exchange interaction. One of the main mechanisms for indirect exchange interactions in dilute magnetic semiconductors (DMS) is RKKY mechanism.

(e) Itinerant Exchange

For those electrons that are not well localized and are shared by the entire crystal, such electrons can have exchange interaction among themselves. Such electron-electron interactions are called itinerant exchange interaction.

1.4.3 Magnetization curve

The magnetization curve describes the change in magnetization or magnetic flux of the material with the applied field [40]. When a field is applied to a material with randomly oriented magnetic moments, it will be progressively magnetized due to movement of domain boundaries. Initially, when no field is applied, the magnetic dipoles are randomly oriented in domains, thus the net magnetization is zero. When a field is applied, the domains begin to rotate, increasing their size in the case of the domains with direction favorable with respect to the field, and decreasing for the domains with unfavorable direction. As the field increases, the domains continue to grow until the material becomes a single domain, which is oriented in the field direction. At this point, the material has reached *saturation* (Figure 1.8). As the magnetic field is increased or decreased continuously, the magnetization of the material increases or decreases but in a discontinuous fashion. This phenomenon is called the *Barkhausen effect* and is attributed to discontinuous domain boundary motion and the discontinuous rotation of the magnetization direction within a domain [41].

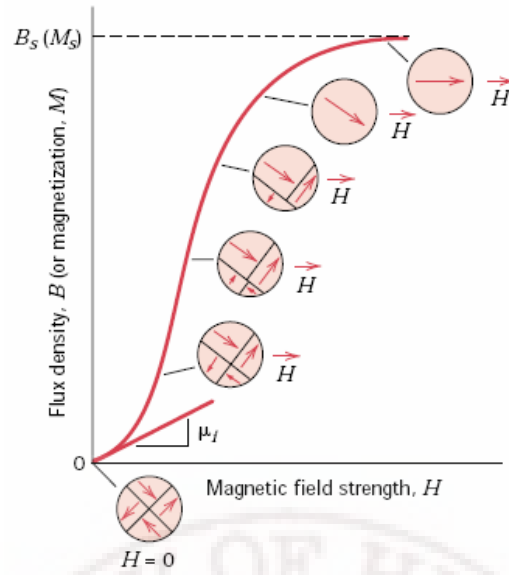


Figure 1.8: Magnetization curve with domain configurations at different stages of magnetization [40].

The typical magnetization curve can be divided into three regions [32]:

- a. Reversible region:* The material can be reversibly magnetized or demagnetized. Changes in magnetization occur due to rotation of the domains with the field.
- b. Irreversible region:* Domain wall motion is irreversible and the slope increases greatly.
- c. Saturation region:* Irreversible domain rotation. It is characterized by a required large amount of energy to rotate the domains in the direction of the field.

If the field is reduced from saturation, with eventual reversal of field direction, the magnetization curve does not retrace its original path, resulting in what is called a *hysteresis loop*. This effect is due to a decrease of the magnetization at a lower rate. The area inside the hysteresis loop is indicative of the magnetic energy losses during the magnetization process. When the field reaches zero, the material may remain magnetized (i.e., some domains are oriented in the former direction). This residual magnetization is commonly called *remanence* M_r . To reduce this remanent magnetization to zero; a field with opposite direction must be applied. The magnitude of field required to lower the sample magnetization to zero is called the *coercivity* H_c (Figure 1.9).

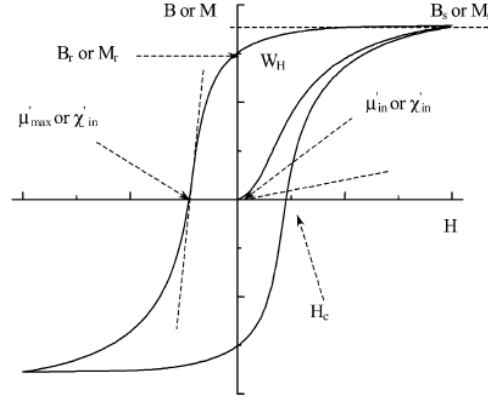


Figure 1.9: Magnetic properties of materials as defined on the B-H plane or flux density B versus magnetic field H, (or the M-H plane of magnetization M versus magnetic field H). These include coercivity H_C , remanence B_R (M_R), hysteresis loss W_H , initial permeability μ_{in} (initial susceptibility χ_{in}), maximum differential permeability μ_{max} (maximum differential susceptibility χ_{max}) and saturation flux density B_S (saturation magnetization M_S) [42].

1.4.4 Magnetic anisotropy

Magnetic anisotropy energy is the energy difference between two directions of the magnetization with respect to a crystallographic axis. The total magnetization of a system prefers to lie along a certain direction called the easy axis. The energy difference between the easy and hard axis results from different kinds of magnetic anisotropies, which can be distinguished to their origin as magnetocrystalline anisotropy, shape anisotropy, growth-induced anisotropy and stress-induced anisotropy.

(a) Magnetocrystalline anisotropy

The Magnetocrystalline anisotropy is an intrinsic property, related to the crystal symmetry of the material and based on the interaction of spin and orbital motion of the electrons. The strength of the spin-orbit coupling controls the magnitude of the anisotropy effects. When the spin-orbit interaction is considered as a perturbation, it is called anisotropic exchange interaction.

For crystals with cubic symmetry, the anisotropy energy can be written in terms of the direction cosines ($\alpha_1, \alpha_2, \alpha_3$) of the internal magnetization with respect to the three cube edges [29]

$$E_a = K_1(\alpha_1^2\alpha_2^2 + \alpha_2^2\alpha_3^2 + \alpha_3^2\alpha_1^2) + K_2\alpha_1^2\alpha_2^2\alpha_3^2 + \dots \quad (1.9)$$

where K_1 and K_2 are the first- and second-order temperature dependent magnetocrystalline anisotropy constants respectively and $\alpha_1 = \cos\alpha$, $\alpha_2 = \cos\beta$, $\alpha_3 = \cos\gamma$, α , β , γ being the angles between the magnetization and the three crystal axes.

In the case of hexagonal symmetry the anisotropy energy can be expressed as [29]

$$E_a = K_1 \sin^2 \theta + K_2 \sin^4 \theta + \dots = \sum K_n \sin^{2n} \theta \quad (1.10)$$

where θ is the angle between the magnetization and the c-axis. This kind of anisotropy is usually referred to as *uniaxial* anisotropy.

(b) Shape anisotropy

In the case of a nonspherical sample it is easier to magnetize along a long axis than along a short direction. This is due to the demagnetizing field, which is smaller in the long direction, because the induced poles at the surface of the sample are further apart [43]. For a spherical sample there is no shape anisotropy. The magnetostatic energy density can be written as [28]

$$E = \frac{1}{2} \mu_0 N_d M_s^2 \quad (1.11)$$

where N_d is a tensor and represents the demagnetized factor (which is calculated from the ratios of the axis). M is the saturation magnetization of the sample. The shape anisotropy energy of a uniform magnetized ellipsoid is given by:

$$E = \frac{1}{2} \mu_0 (N_x M_x^2 + N_y M_y^2 + N_z M_z^2) \quad (1.12)$$

where the tensors satisfied the relation $N_x + N_y + N_z = 1$

(c) Surface anisotropy

In small magnetic nanoparticles a major source of anisotropy results from surface effects. The surface anisotropy is caused by the breaking of the symmetry and a reduction of the nearest neighbor coordination. The effective magnetic anisotropy for a thin film can be described as the sum of volume and surface terms [Johnson 1996]:

$$K_{eff} = K_v + \frac{2}{t} K_s \quad (1.13)$$

where t is the thickness of the film, K_s is the surface contribution, and K_v is the volume contribution consisting of magnetocrystalline, magnetostriction and shape anisotropy. In

the case of small spherical particles with diameter d the effective magnetic anisotropy can be expressed as

$$K_{eff} = K_v + \frac{S}{V} K_s = K_v + \frac{6}{d} K_s \quad (1.14)$$

where $S = \pi d^2$ and $V = \frac{1}{6} \pi d^3$

are the surface, and the the volume of the particle respectively.

(d) Growth-induced anisotropy

The growth-induced anisotropy arises from the special conditions during the growth process. In this case, a certain ordering of the respective ions takes place along the growth directions, which leads to a uniaxial growth-induced anisotropy [29]. For polycrystalline specimens, the induced anisotropy energy is

$$E = K_u \sin^2(\theta - \theta_u) \quad (1.15)$$

where K_u is the induced anisotropy constant and $(\theta - \theta_u)$ is the angle of the measuring field (θ) relative to the induced field (θ_u).

(e) Stress-induced anisotropy

The influence of the stress or strain also affects the preferred directions of magnetization due to the magneto-elastic interactions. Strain in a ferromagnet changes the magnetocrystalline anisotropy and may thereby alter the direction of the magnetization. This effect is the 'inverse' of magnetostriction, the phenomenon that the sample dimensions change if the direction of the magnetization is altered. The energy per unit volume associated with this effect can, for an elastically isotropic medium with isotropic magnetostriction, be written as [45]

$$E = -K \cos^2 \theta \quad (1.16)$$

with

$$K = -\frac{3}{2} \lambda \sigma = -\frac{3}{2} \lambda E \varepsilon \quad (1.17)$$

Here σ is the stress which is related to the strain, ε , via the elastic modulus E by $\sigma = \varepsilon E$. The magnetostriction constant λ depends on the orientation and can be positive or negative. The angle θ measures the direction of the magnetization relative to the direction of uniform stress. If the strain in the film is non-zero, the magneto-elastic coupling

contributes in principle to the effective anisotropy [46]. When the parameters are constant (not depending on the magnetic film thickness (t)) this contribution can be identified with a volume contribution K_v . Strain in films can be induced by various sources. Among them are thermal strain associated with differences in thermal expansion coefficients, intrinsic strain brought about by the nature of the deposition process and strain due to non-matching lattice parameters of adjacent layers [47].

1.4.5 Magnetism in Nanoparticles: Superparamagnetism

When the diameter of magnetic nanoparticles is small enough, each particle behaves as a single magnetic domain. Consequently, the alignment of spins under applied field is no longer impeded by domain walls. Further reduction in particle size allows for thermal vibrations to randomly fluctuate the net spins and the domains are considered unstable. Since the particles' net spins are randomly oriented, they cancel each other and the net moment of the collective particles is zero. If a magnetic field is applied, the particles will align producing a net moment. This behavior is characteristic of paramagnetic materials, but the difference is that each molecule has a large net moment, e.g. $4 \mu_B$ per molecule of Fe_3O_4 . Thus, Bean coined the term *superparamagnetism* in 1959 [28].

There are two characteristic behaviors of superparamagnetism: 1) magnetization curves, i.e. magnetization vs. applied field, do not change with temperature and 2) no hysteresis is observed, i.e. coercivity, $H_c = 0$. For nanoparticles to exhibit superparamagnetism, they must be small enough that each particle is a single domain and the energy barrier for spin reversal is easily overcome by thermal vibrations. Magnetic particles generally become single domain when they are less than 100 nm, and this limit is a function of the material properties [36]. Morrish and Yu determined that Fe_3O_4 particles are single domains when the diameter is 50 nm or less [37]. As the particle size decreases, the coercivity decreases until it reaches $H_c = 0$. At this critical particle size, the particles are superparamagnetic. The change in coercivity with particle diameter is shown in Figure 1.10.

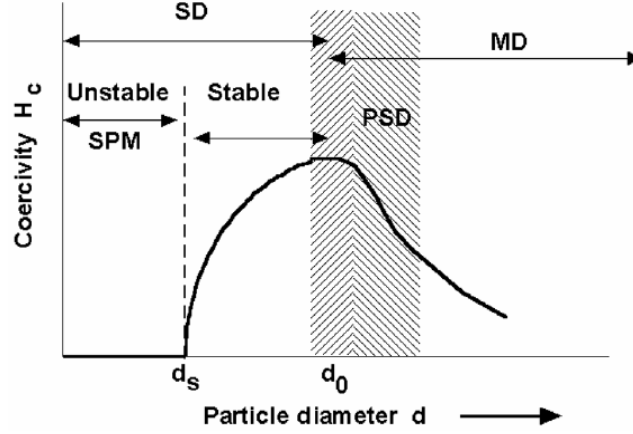


Figure 1.10. Schematic of changes in H_c with particle diameter, from Cullity [28]. SD: Single Domain, MD: Multi Domain, SPM: superparamagnetic, PSD: Pseudo Single Domain

Superparamagnetism behavior is observed in particle sizes that meet the following criteria [28]:

$$V_p \leq \frac{25kT}{K} \quad (1.18)$$

where V_p is the volume of the particle, k is Boltzman's constant, T is temperature, and K is the anisotropy constant. In other words, if the energy barrier, $\Delta E = KV_p$, is greater than $25kT$, the net spin within each particle cannot fluctuate randomly from thermal vibrations and they are considered stable. Particles that are superparamagnetic at room temperature can become stable when the temperature is lowered according to Equation (1). This temperature is called the blocking temperature, T_B .

Prediction of the critical particle size for onset of superparamagnetism is highly dependent on the accuracy of anisotropy constant, K . The anisotropy constant of nanoparticles is a contribution of different types: crystal, shape, interaction, and surface anisotropies. Crystal anisotropy is intrinsic to the material, while the others are induced or extrinsic. In a crystal, there is a preferred magnetization direction called the easy axis. If the applied field does not align with direction of the easy axis, the crystal anisotropy resists the domains from rotating and aligning with the field. As a result, higher fields must be applied to make all of the domains align. Shape anisotropy applies when the particles are not spherical, with the preferred alignment along the long axis of the particle. Exchange anisotropy is observed in small particles when they are in close contact, such as in clusters [38]. Its existence should be noted since it can change the anisotropy contribution of each particle. Surface anisotropy can contribute significantly to the overall

anisotropy of nanoparticles [38, 39]. Its effect is caused by the existence of a magnetically dead layer, spin canting, and presence of disorder and defects on the surface layer [38]. The overall anisotropy energy, E_A , of a spherical nanoparticle is given by the following equation

$$E_A = K_C V_P \sin^2 \theta + E_{intrxn} + E_{surface} \quad (1.19)$$

where K_C is the crystal anisotropy constant, E_{intrxn} is the contribution of interaction between particles, and D is the particle diameter.

Goya and coworkers estimated the effective anisotropy constant, K , of magnetite nanoparticles [39] and have accounted for bulk and surface contributions. Due to the surface effects, the anisotropy constant was increased from 1.1×10^4 erg/cm³ to 3.9×10^4 erg/cm³. Applying Equation (1) the critical diameter for superparamagnetism is 18.5 nm for Fe₃O₄.

1.4.6 Ferromagnetic resonance (FMR)

In a magnetic resonance experiment, a spin, whether electronic or nuclear, will precess about the direction of an applied magnetic field when the resonance condition is satisfied by the application of the appropriate strength magnetic (static and rf) field. In the case of nuclear spins this is termed *nuclear magnetic resonance* (NMR), while in the case of electronic spins the phenomenon is labeled in function of the type of material in question. For example, in paramagnetic materials it is referred to as *electron paramagnetic resonance* (EPR), also known as *electron spin resonance* (ESR) and in ferromagnetic materials as *ferromagnetic resonance* (FMR). There are further classifications, such as *antiferromagnetic resonance* (AFMR) and *spin wave resonance* (SWR), which apply to antiferromagnetic and ferromagnetic systems (where confinement effects via magnetic boundaries can permit the excitation of standing *spin wave* modes of oscillation), respectively [48].

In the simplest case, i.e. EPR, the electronic system possesses an intrinsic magnetic moment due to its spin. The magnetic moment has two possible orientations with two distinct energies, lower or higher energy, in the presence of an applied field (Zeeman Effect). The transition states refer to the electrons spin states, clockwise ($m_s = +\frac{1}{2}$) or anti-clockwise ($m_s = -\frac{1}{2}$) (Figure 1.11). When an oscillating electron magnetic radiation of the appropriate frequency ν is applied perpendicular to the external magnetic field H ,

transition can occur between the two spin states and the intrinsic spin is ‘flipped’. The difference between the two energy levels [49],

$$\Delta E = E_+ - E_- = g\mu_B H \quad (1.20)$$

corresponds to the energy of the absorbed photon ($\Delta E = h\nu$) that is required to cause a transition.

Thus the resonance condition is:

$$h\nu = g\mu_B H \quad (1.21)$$

In equations (1.20) and (1.21), g represents the g-value ($g_e = 2.00232$ for a free electron), which is characteristic for each radical. H is the magnetic field, μ_B is the Bohr magneton $\mu_B = e\hbar/2m_e$ ($9.274 \times 10^{-24} \text{ JT}^{-1}$), h ($6.6262 \times 10^{-34} \text{ J.s}$) is Planck’s constant and ν corresponds to the frequency of the absorbed photon in Hz.

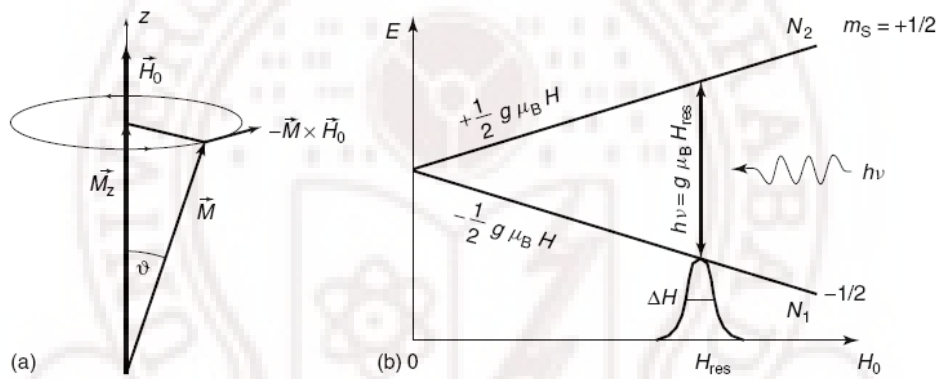


Figure 1.11: (a) Sketch of the uniform precession of vector \vec{M} about the external field \vec{H}_0 . (b) Energy level diagram for a spin $m_s = \pm 1/2$ system and the dipole transition for \vec{h}_{mw} being perpendicular to \vec{H}_0 [49].

In the case of ferromagnetic systems, where there is a strong exchange interaction between neighboring spins, corrections must be introduced due to the internal field created by, for example, exchange field, demagnetizing effects and the various magnetic anisotropies which can be present.

(a) Equation of motion for magnetization vector

In order to describe the dynamics of ferromagnetic magnetization it is usually not necessary to consider the microscopic picture of ferromagnet (FM). It is more convenient to describe the magnetic state of the FM by introducing the so-called macro-spin M , which

is defined as the total magnetic moment per unit volume. Below the Curie temperature the magnitude of M is equal to the saturation magnetization M_s , which for bulk Cu-ferrite (CuFe_2O_4) is $4\pi M_s = 1700$ G. An applied magnetic field H exerts a torque on M , resulting in precessional motion of the magnetization [50]. The magnetic field puts a torque on the magnetization which causes the magnetic moment to precess (Figure 1.12 (a)). In the absence of radio-frequency (RF) magnetic pumping field to sustain this precession, the rotation will not keep precessing and eventually spiral into alignment with the direction of the static magnetic axis as shown in Figure 1.12 (b). With applying an RF magnetic field in the plane normal to the static applied field, a pumping action can occur to maintain the precession of the magnetic dipoles as shown in Figure 1.12 (c). This RF applied field will have the strongest interaction with the magnetic dipoles when its frequency is at resonant frequency (ω_0).

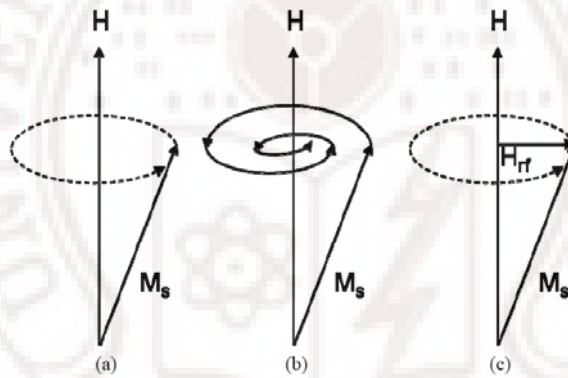


Figure 1.12: (a) The precession of a magnetic dipole caused by the external magnetic field without any loss. (b) Friction loss causes magnetic dipole to align with the external magnetic field. (c) An RF magnetic field causes the magnetic dipole precess along the axis of external magnetic field [50].

There are two approaches that can be applied to analyze FMR data in thin films [51]:

- (i) the energy method introduced by Smit and Beljers and
- (ii) the vectorial formalism given by the Landau-Lifshitz (LL) equation of motion

Here we will start the analysis of FMR using the second approach as described in reference 33 and 52. When a magnetic dipole (\mathbf{m}) is immersed in a static magnetic field (\mathbf{H}), it precesses about the field axis with an angular frequency ω_0 . The torque acting on \mathbf{m} is expressed by

$$\mathbf{T} = \mu_0 \mathbf{m} \times \mathbf{H} \quad (1.22)$$

where μ_0 is the permeability of vacuum.

The spin angular momentum J is oppositely directed to \mathbf{m} through the relation

$$\mathbf{m} = -\gamma \mathbf{J} \quad (1.23)$$

where the gyromagnetic ratio $\gamma = ge/2mc = 1.76 \times 10^{10} \text{ rad/sG} = 2.8 \text{ MHz/G}$

The torque acting on a body, see Figure 1.13 for a pictorial view, is equal to the rate of change of angular momentum of the body:

$$\mathbf{T} = \frac{d\mathbf{J}}{dt} \quad (1.24)$$

Combining equations (1.22), (1.23) and (1.24)

$$\mathbf{T} = \frac{d\mathbf{J}}{dt} = \frac{-1}{\gamma} \frac{d\mathbf{m}}{dt} = -\mu_0 \mathbf{m} \times \mathbf{H} \quad (1.25)$$

Under a strong enough static magnetic field, the magnetization of the material is assumed to be saturated and the total magnetization vector is given by $\mathbf{M} = N\mathbf{m}$, where N is the effective number of dipoles per unit volume. We can then obtain the macroscopic equation of motion of the magnetization vector from Eq. 1.25 as

$$\frac{1}{\gamma} \frac{d\mathbf{M}}{dt} = -\mu_0 \mathbf{M} \times \mathbf{H} \quad (1.26)$$

The minus sign is due to the negative charge of the electron that is carried out from γ . In many cases the absolute value of the electronic charge is used for practical purposes and the minus sign is removed (That's why the torque in Figure 1.13 is shown in the direction of $-\mathbf{m} \times \mathbf{H}$).

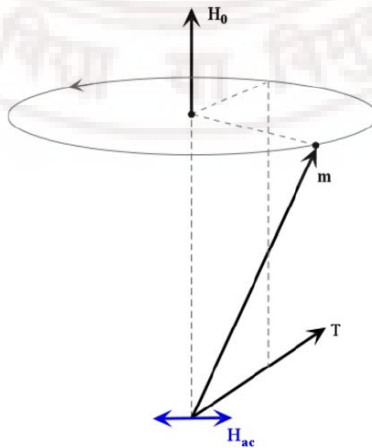


Figure 1.13: A schematic of dipole moment \mathbf{m} precessing about a static magnetic field \mathbf{H}_0 . When the frequency of the alternating magnetic field \mathbf{H}_{ac} (where $\mathbf{H}_{ac} \perp \mathbf{H}_0$) is near the natural precession frequency the precession of the magnetic moment grows [33].

If the dipole is subjected to a small transverse RF-magnetic field H_{ac} at an angular frequency ω , the precession will be forced at this frequency and an additional transverse component will occur. Then \mathbf{H} is the vector sum of all fields, external and internal, acting upon the magnetization and includes the DC field \mathbf{H}_i and the RF field \mathbf{H}_{ac} . Because H_{ac} is much smaller than \mathbf{H}_i there is a linear relationship between \mathbf{H} and \mathbf{M} . The actual relationship between the magnetic intensity \mathbf{H} , which is averaged over the space for many molecules within the magnetic material, and the external applied field depends upon the shape of the ferrite body. \mathbf{H}_i is the vector sum of all DC fields within the material including that due to the externally applied DC field \mathbf{H}_0 and any time-independent internal fields. For simplicity, we will assume that the medium is infinite, i.e. there is no demagnetization correction that depends on the shape of the material, the crystal anisotropy or magnetostriction is zero, and only the externally applied DC field H_0 contributes to the total internal field \mathbf{H}_i , and it is large enough to saturate the magnetization. The total magnetic field can be expressed as

$$\mathbf{H} = \mathbf{H}_0 + \mathbf{H}_{ac} \quad (1.27)$$

The resulting magnetization will then have the form

$$\mathbf{M} = \mathbf{M}_s + \mathbf{M}_{ac} \quad (1.28)$$

where \mathbf{M}_s is the DC saturation magnetization and \mathbf{M}_{ac} is the AC magnetization. In Eq. 1.28, we have assumed that the \mathbf{H} field is strong enough to drive the magnetization into saturation, which is true for practical applications. The DC equation can be obtained from Eq. 1.26 by neglecting all the AC terms:

$$\mu_0 \gamma \mathbf{M}_s \times \mathbf{H}_0 = 0 \quad (1.29)$$

which indicates that, to the first order, the internal DC field (\mathbf{H}_i if contributions other than \mathbf{H}_0 are included) and the magnetization are in the same direction. Substituting Eqs. 1.27, 1.28 into Eq. 1.26 (removing the minus sign) and taking into account $d\mathbf{M}_s/dt = 0$ we obtain

$$\frac{d\mathbf{M}_{ac}}{dt} = \mu_0 \gamma (\mathbf{M}_s \times \mathbf{H}_{ac} + \mathbf{M}_{ac} \times \mathbf{H}_0) \quad (1.30)$$

The products of the AC terms (second order terms) are neglected in Eq. 1.30 since the magnitudes of the AC components are much smaller than those of the DC components. Further assuming that the AC field, and therefore the AC magnetization, have a harmonic time dependence, $e^{j\omega t}$, and by arbitrarily choosing the applied DC field direction along the

z-axis (therefore, the RF field is in the x-y plane) the components of Eq. 1.30 in the Cartesian coordinate system can be written as

$$j\omega M_x = \omega_0 M_y - \omega_m H_y \quad (1.31)$$

$$j\omega M_y = -\omega_0 M_x + \omega_m H_x \quad (1.32)$$

$$j\omega M_z = 0 \quad (1.33)$$

where $\omega_0 = \mu_0 \gamma H_0$, $\omega_m = \mu_0 \gamma M_s$

ω_0 is called the Larmor frequency, which defines the natural precession frequency under a static magnetic field (see Figure 1.13 for the precession motion). Solving Eqs. 1.31, 1.32 for M_x and M_y gives ($M_z = 0$ from Eq. 1.33):

$$M_x = \frac{\omega_0 \omega_m}{(\omega_0^2 - \omega^2)} H_x - \frac{j\omega \omega_m}{(\omega_0^2 - \omega^2)} H_y \quad (1.34)$$

$$M_y = \frac{j\omega \omega_m}{(\omega_0^2 - \omega^2)} H_x + \frac{\omega_0 \omega_m}{(\omega_0^2 - \omega^2)} H_y \quad (1.35)$$

These solutions can be written in tensor form:

$$\mathbf{M}_{ac} = [\chi_{ac}] \mathbf{H}_{ac} = \begin{bmatrix} \chi_{xx} & \chi_{xy} & 0 \\ \chi_{yx} & \chi_{yy} & 0 \\ 0 & 0 & 0 \end{bmatrix} \begin{bmatrix} H_x \\ H_y \\ H_z \end{bmatrix} \quad (1.36)$$

where $[\chi]$ is the dynamic susceptibility tensor. Notice that for the given configuration (applied field in the z-direction) the total magnetization can be written as

$$\begin{aligned} \mathbf{M} = \mathbf{M}_s + \mathbf{M}_{ac} &= \begin{bmatrix} M_x \\ M_y \\ M_s \end{bmatrix} = \begin{bmatrix} \chi_{xx} & \chi_{xy} & 0 \\ \chi_{yx} & \chi_{yy} & 0 \\ 0 & 0 & \chi_0 \end{bmatrix} \begin{bmatrix} H_x \\ H_y \\ H_0 \end{bmatrix} \\ &= [\chi](\mathbf{H}_0 + \mathbf{H}_{ac}) \end{aligned} \quad (1.37)$$

where $\chi_0 = M_s / H_0$. Comparing Eq. 1.36 with Eqs. 1.34, 1.35, the elements of $[\chi]$ are obtained as

$$\chi_{xx} = \chi_{yy} = \frac{\omega_0 \omega_m}{\omega_0^2 - \omega^2} \quad (1.38)$$

$$\chi_{xy} = -\chi_{yx} = -\frac{j\omega \omega_m}{\omega_0^2 - \omega^2} \quad (1.39)$$

One can now derive the permeability tensor $[\mu]$ using

$$\mathbf{B} = \mu_0(\mathbf{M} + \mathbf{H}) = \mu_0(1 + [\mu])\mathbf{H} = [\mu]\mathbf{H} \quad (1.40)$$

The conventional notation (referred to as the Polder tensor) for the permeability tensor for a magnetic field bias along the z-direction is

$$[\mu] = \begin{bmatrix} \mu & -jK & 0 \\ jK & \mu & 0 \\ 0 & 0 & \mu_0 \end{bmatrix} \quad (1.41)$$

where

$$\mu = \mu_0(1 + \chi_{xx}) = \mu_0(1 + \chi_{yy}) = \mu_0 \left(1 + \frac{\omega_0 \omega_m}{\omega_0^2 - \omega^2} \right) \quad (1.42)$$

$$jK = -\mu_0 \chi_{xy} = \mu_0 \chi_{yx} = j\mu_0 \frac{\omega \omega_m}{\omega_0^2 - \omega^2} \quad (1.43)$$

As shown in Eq. 1.41 the permeability tensor is anti-symmetric owing to xy and yx terms having opposite signs, unlike the conductivity and permittivity tensors. Such anti-symmetrical condition of ferrites is necessary for nonreciprocal devices. Obviously, the permeability tensor has a singularity at $\omega = \omega_0$, which is known as the ferromagnetic (or gyromagnetic) resonance. When the driving frequency ω is equal to the natural precession frequency ω_0 the energy from the microwave field is transferred most efficiently to the system of spins. At $\omega \neq \omega_0$ there is an oscillating component of the magnetization superimposed on the steady-state precession and the nearer the frequency of the microwave field to the natural precession frequency, the greater the energy absorbed by the spins will be. To observe this resonance, either the frequency or the applied DC field H_0 can be swept until the precession frequency equals the microwave frequency.

(b) Demagnetization effect

In the discussions of the microwave susceptibility so far, the medium has been assumed to be infinite. However, one needs to evaluate the magnetic fields in samples of finite size, and demagnetization effects arise for finite samples. The analysis of these effects is simplified for uniformly shaped samples (sphere, cylinder, thin slab, etc.), for which the demagnetization factors can be easily obtained [52-54]. With the precession of \mathbf{M} , the demagnetization fields $\mathbf{H}_d = -N_d \mathbf{M}$ along different directions have to be taken into account, and since the demagnetization factors depend on the shape, the form of the

sample is important. In the case of an ellipsoidal sample, with principal axis coinciding with the coordinate axis, N_d is a diagonal tensor given by

$$N_d = \begin{pmatrix} N_x & 0 & 0 \\ 0 & N_y & 0 \\ 0 & 0 & N_z \end{pmatrix} \quad (1.44)$$

and

$$\begin{aligned} \mathbf{H}_d = -N_d \mathbf{M} &= - \begin{pmatrix} N_x & 0 & 0 \\ 0 & N_y & 0 \\ 0 & 0 & N_z \end{pmatrix} \begin{pmatrix} M_x \\ M_y \\ M_z \end{pmatrix} \\ &= -(N_x M_x \mathbf{i} + N_y M_y \mathbf{j} + N_z M_z \mathbf{k}) \end{aligned} \quad (1.45)$$

Now, the total field \mathbf{H} acting on \mathbf{M} is

$$\mathbf{H} = \mathbf{H}_0 + \mathbf{H}_{ac} + \mathbf{H}_d \quad (1.46)$$

With $\mathbf{H}_{ac} = \mathbf{H}_1 e^{j\omega t}$

Neglecting relaxation effects, the motion of \mathbf{M} is given as

$$\frac{d\mathbf{M}}{dt} = -\mu_0 \gamma \mathbf{M} \times (\mathbf{H}_0 + \mathbf{H}_{ac} + \mathbf{H}_d) \quad (1.47)$$

One can assume that the magnetization does not deviate much from the equilibrium value (the saturation magnetization), that is, $\mathbf{M}_z \approx \mathbf{M}_s$. In the stationary regime, $\mathbf{M}_x = \mathbf{M}_x(0)e^{j\omega t}$ and $\mathbf{M}_y = \mathbf{M}_y(0)e^{j\omega t}$. Inserting these expressions into eq. (1.47), we obtain:

$$j\omega M_x = -\gamma\mu_0 [M_y M_z (N_z - N_y) + M_y H_0 + M_z H_1] \quad (1.48a)$$

$$j\omega M_y = -\gamma\mu_0 [M_x M_z (N_x - N_z) + M_x H_0 + M_z H_1] \quad (1.48b)$$

$$j\omega M_z \cong 0 \quad (1.48c)$$

The condition for the existence of solutions for this system of equations is that the determinant of the coefficients be equal to zero; for $H_{ac} = H_1 = 0$,

$$\begin{vmatrix} j\omega & -\gamma[H_0 + (N_y - N_z)M_s] \\ \gamma[H_0 + (N_y - N_z)M_s] & j\omega \end{vmatrix} = 0 \quad (1.49)$$

The root of the resulting equation is the frequency

$$\omega_0 = \gamma \{ [H_0 + (N_y - N_z)M_s] [H_0 + (N_x - N_z)M_s] \}^{1/2} \quad (1.50)$$

Where $M_z \approx M_s$

This is the frequency of precession of the magnetization; the individual magnetic moments precess in phase, and therefore ω_0 is called the uniform mode precession frequency. This

formula was first obtained by C. Kittel 1948 [53]. Maximum electromagnetic energy is absorbed around this frequency by a small ellipsoid sample (ferromagnetic resonance, FMR).

The resonance frequency given by eq. (1.50) depends on the shape of the sample. For a spherical sample, the demagnetizing factors are $N_x = N_y = N_z = 1/3$ and the resonance frequency simplifies to

$$\omega_0 = \gamma H_0 \quad (1.51)$$

For a sample in the form of a thin film:

With $H_0 \perp$ film plane (plane xy), $N_x = N_y = 0$ and $N_z = 4\pi$ we have

$$\omega_0 = \gamma(H_0 - 4\pi M_s) \quad (1.52)$$

With $H_0 \parallel$ to the film plane (xz plane) $N_x = N_z = 0$ and $N_y = 4\pi$ giving

$$\omega_0 = \gamma[H_0(H_0 + 4\pi M_s)]^{1/2} \quad (1.53)$$

which are the well known Kittel's equations.

Table 1.2: Demagnetizing factors and ferromagnetic resonance conditions for selected geometries. [53]

Geometry	N_x	N_y	N_z	FMR condition
Sphere	1/3	1/3	1/3	$\omega_0 = \gamma H_0$
Infinite circular cylinder	2π	2π	0	$\omega_0 = \gamma (H_0 + 2\pi M_s)$
Perpendicularly magnetized film	0	0	4π	$\omega_0 = \gamma (H_0 - 4\pi M_s)$
In-plane magnetized film	0	4π	0	$\omega_0 = \gamma [H_0(H_0 + 4\pi M_s)]^{1/2}$

(c) Anisotropy effect

Taking into account possible anisotropies of a film, Smit and Beljers (second approach) have shown that the equation of motion may be expressed in terms of the total free energy density E instead of effective fields. The contribution to the free energy density, in an external magnetic field, is coming from [51]:

$$E = E_0 + E_d + E_a + E_{ex} \quad (1.54)$$

where E_0 describes the energy contribution of the external magnetic field, E_d is the energy of the demagnetizing field of the sample, E_a depends on the crystalline structure of the investigated sample (and it is caused by the spin-orbit coupling) and E_{ex} represents the energy of exchange interaction.

According to Smit and Beljers model [54], the resonance frequency is given by

$$\left(\frac{\omega}{\gamma}\right)^2 = H_{eff}^2 = \frac{1}{M_0^2 \sin^2 \theta} \left\{ \frac{\partial^2 E}{\partial \phi^2} \frac{\partial^2 E}{\partial \theta^2} - \left(\frac{\partial^2 E}{\partial \phi \partial \theta} \right)^2 \right\} \quad (1.55)$$

In this equation E is the total free energy density of the system, and θ and ϕ are the polar and azimuthal angles of the magnetization. The easy direction of the magnetization can be determined by calculating the equilibrium positions θ_0 , ϕ_0 of the magnetization for a given external field value. For this the total free energy density E has to be a minimum, i.e. the equilibrium values can be obtained from the conditions $(\partial E / \partial \theta)_{\theta=\theta_0} = 0$ and $(\partial E / \partial \phi)_{\phi=\phi_0} = 0$.

For a system with tetragonal symmetry which occurs frequently in thin films, the free energy per unit volume is written in the form [55, 56]

$$E = -MH_0 \cos(\theta - \theta_H) + (2\pi M^2 - K_{2\perp}) \cos^2 \theta - 1/2 K_{4\perp} \cos^4 \theta - 1/8 K_{4\parallel} (3 + \cos 4\phi) \sin^4 \theta - K_{2\parallel} \cos^2(\phi - \phi_H) \sin^2 \theta \quad (1.56)$$

where θ and θ_H are the polar angles of the magnetization and the external magnetic field is measured from the film to normal and ϕ and ϕ_H are the azimuthal angles measured with respect to the in-plane direction. A negative value indicates an easy direction in the film plane, whereas a positive value shows a preferential direction normal to the film plane. $K_{2\perp}$ is the out-of-plane anisotropy constant and $K_{2\parallel}$ is the in-plane anisotropy constant which is usually very small and may result from a slight mis-cut of the substrate which leads to a preferential direction in the film plane. $K_{4\parallel}$ and $K_{4\perp}$ are the fourfold in-plane and out-of-plane anisotropy constants respectively, M is the magnetization of the sample and H_0 is the resonance field.

The resonance conditions derived from Eq. 1.56 is written for polar geometry in the form:

$$\left(\frac{\omega}{\gamma}\right)^2 = \left\{ H_0 \cos(\theta - \theta_H) + \left(M_{eff} + \frac{K_{4\perp}}{M} - \frac{K_{4\parallel}}{2M} \right) \cos 2\theta + \left(\frac{K_{4\perp}}{M} + \frac{K_{4\parallel}}{2M} \right) \cos 4\theta \right\} \\ \times \left\{ H_0 \cos(\theta - \theta_H) + \left(M_{eff} + \frac{K_{4\perp}}{M} - \frac{K_{4\parallel}}{2M} \right) \cos^2 \theta + \left(\frac{2K_{4\perp}}{M} + \frac{K_{4\parallel}}{M} \right) \cos^4 \theta - \frac{2K_{4\parallel}}{M} \right\} \quad (1.57)$$

where

$$M_{eff} = -4\pi M + \frac{2K_2}{M} \quad (1.58)$$

For $\theta = \theta_H = 0^\circ$ (M and H perpendicular to the film plane)

$$\frac{\omega}{\gamma} = H_0 - 4\pi M + \frac{2(K_2 + K_{4\perp})}{M} \quad (1.59)$$

For $\theta = \theta_H = 90^\circ$ (M and H parallel to the film plane)

$$\left(\frac{\omega}{\gamma}\right)^2 = \left(H_{0\parallel} + \frac{2K_{4\parallel}}{M} \right) \left(H_{0\parallel} + 4\pi M - \frac{2(K_2 - K_{4\parallel})}{M} \right) \quad (1.60)$$

For azimuthal geometry $\theta = \theta_H = 90^\circ$ (M and H parallel to the film plane) one finds the follow resonance condition

$$\left(\frac{\omega}{\gamma}\right)^2 = \left(H_{0\parallel} \cos(\varphi - \varphi_H) + \frac{2K_{4\parallel}}{M} \cos 4\varphi \right) \times \left(H_{0\parallel} - M_{eff} + \frac{K_{4\parallel}}{2M} (3 + \cos 4\varphi) \right) \quad (1.61)$$

By analysis of the width and shape of the resonance, information about the magnetic anisotropy, the relaxation of the magnetization, the g-factor, Curie temperature, and anisotropy coefficients can be extracted. The resonance field H_0 defines as the zero crossing of the absorption derivative and ΔH_{pp} the peak-to-peak linewidth defines as the field between the minimum and the maximum of the absorption derivative. The magnitude of H_0 and its dependence on the orientation of the field, the sample thickness and the temperature provides information about the magnetic anisotropy of the sample. The peak-to-peak resonance linewidth, ΔH_{pp} , yields information about the relaxation rate of the magnetization. Two mechanisms are responsible for this relaxation, namely the intrinsic damping of the magnetization and the magnetic inhomogeneities of the sample [57]. The inhomogeneous contribution is caused by the inhomogeneous local field distribution. This produce a range of resonance conditions which will give rise to a superposition of

resonance, resulting in an overall linewidth broadening. The frequency dependent resonance linewidth can be expressed as

$$\Delta H_{pp}(\omega) = \Delta H_{inhom} + \Delta H_{hom} = \Delta H_{inhom} + \frac{2}{\sqrt{3}} \frac{G}{\gamma^2 M} \omega \quad (1.62)$$

where the term ΔH_{inhom} is due to the magnetic inhomogeneities in the magnetic sample due to a spread in the crystalline axes, variations in grain size, effect of surface spins etc. The second term describes the intrinsic damping of the precession of the magnetization M , and γ is the gyromagnetic ratio. The Gilbert parameter (G) has values of the order of 10^{-8} s^{-1} . By making multi-frequency measurements it is possible to determine the Gilbert damping parameter (it is obtained from the slope of the frequency variation of the peak-to-peak line width of the FMR signal). The intensity of the absorption signal can be used to estimate the magnetization of the sample. For signal derivatives with a Lorentzian lineshape the intensity is proportional to the product: $A \times (\Delta H_{pp})^2$ [47]. In order to get a correct value of the magnetization, one needs a perfect calibration of the FMR spectrometer because the amplitude of the signal is very sensitive to the location of the sample within the cavity.

1.5 Dielectric properties of ferrites

The dielectric is referred to as a material that permits the passage of an electric field or electric flux, and has the ability to store electrical charges but does not normally conduct electric current. However, a dielectric is generally considered as a nonconducting or an insulating material [58-60]. The electrons are bound to microscopic regions within the material, i.e. the atoms, molecules, in contrast to being freely movable in and out of macroscopic system under consideration. Most of the dielectric materials are solids such as ceramic, mica, glass, plastics, and the oxides of various metals. The degree to which a medium resists the flow of electric charge, defined as the ratio of the electric displacement to the electric field strength. It is more common to use the *relative dielectric permittivity* ϵ_r .

The behavior of dielectrics in electric fields continues to be an area of study that has fascinated physicists, chemists, material scientists, electrical engineers, and, more recently biologists [59]. They exhibit an electric dipole structure, in which positive and negative electrically charged entities are separated on a molecular or atomic level by an applied electric field. This is called *polarization P*.

According to Poisson's equation, each free charge acts as a source for the dielectric displacement D

$$\text{Div}D = \rho_{\text{free}} \quad (1.63)$$

Here ρ_{free} defines the density of free carriers. Under the electric field (E), D is described by

$$D = \epsilon_0 E + P \quad (1.64)$$

The term $\epsilon_0 E$ describes the vacuum contribution to the displacement D caused by an electric field E and P represents the electrical polarization of the matter in the system. The surface charge of density σ_s consisting of two portions: the bound charge σ_b and the free charge $\sigma_s - \sigma_b$. The free charge portion produces the electric Field E and the electric flux density of $\epsilon_0 E$, while the bound charge portion produces polarization P . For many dielectric materials, P is proportional to the electric field strength E through the relationship:

$$P = \epsilon_0 \chi_e E \quad (1.64)$$

This leads to

$$D = \epsilon_0 (1 + \chi_e) E = \epsilon_0 \epsilon_r E \quad (1.65)$$

Here χ_e is the electrical susceptibility and ϵ_r the relative permittivity (or dielectric constant).

When a voltage is applied across the dielectric, energy is stored by one or more of the following mechanisms [58, 61]. They are

- 1) Electronic polarization P_e
- 2) Ionic polarization P_i
- 3) Orientation polarization P_o
- 4) Interfacial or Space Charge polarization P_s

The polarization of dielectric material results from the four contributions can be written as follows (Figure 1.14)

$$P = P_e + P_i + P_o + P_s \quad (1.66)$$

The first term is the electronic polarization, P_e , which arises from a displacement of the centre of the negatively charged electron cloud relative to the positive nucleus of an atom by the electric field. The resonance of the electronic polarization is around 10^{15} Hz; it can be investigated through optical methods.

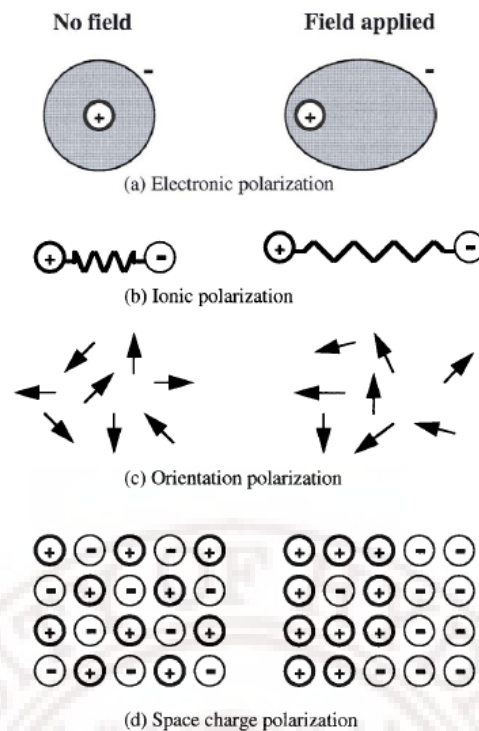


Figure 1.14: Schematic representation of different polarization mechanisms operational in a ceramic [61].

The second term is the ionic polarization, P_i , which originates from the relative displacement or separation of cations and anions from each other in an ionic solid, and their resonance is in the infrared region of 10^{12} - 10^{13} Hz. The third contribution is the orientation polarization, P_o , which is found only in materials with permanent dipole moments. This polarization is generated by a rotation of the permanent moment in the direction of the applied electric field. The polarization due to the orientation of electric dipoles takes place in the frequency range from mHz, in the case of reorientation of polar ligands of polymers up to a few GHz in liquids such as water. The last one, P_s , is the space charge polarization. This type of polarization results from the build-up of charges at interfaces of heterogeneous systems. Depending on the local conductivity, the space charge polarization might be occurring over a wide frequency range from mHz up to MHz. As shown in Figure 1.15 the different polarization mechanisms not only take place on different time scales but also exhibit different frequency dependence.

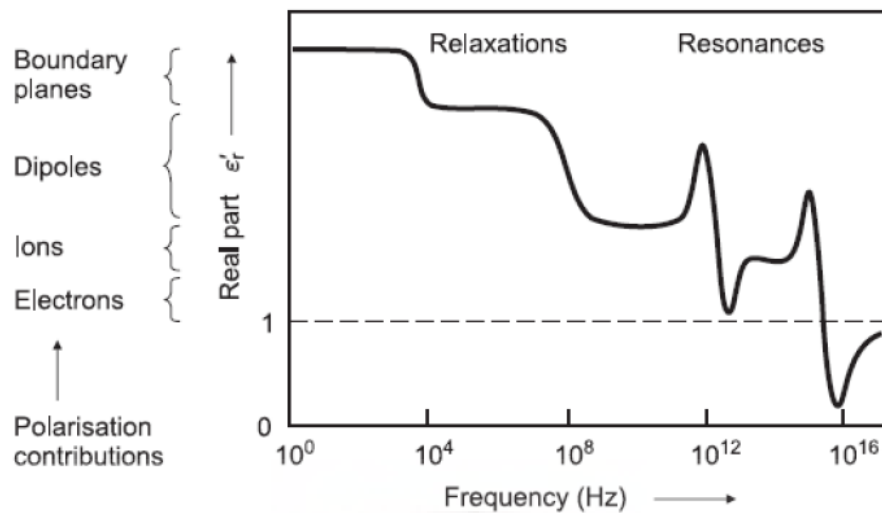


Figure 1.15: Frequency dependent relative dielectric constant [62].

1.5.1 Dielectric constant and dielectric loss

The dielectric constant is a material property which is technically important and is also helpful in understanding basic crystal physics. Combined with other information like the refractive index and the absorption frequency it throws light on the bonding in crystals. In theoretical studies of lattice dynamics, the dielectric constant forms one of the input parameters. Measurement of dielectric constant and loss as a function of frequency and temperature helps in understanding the polarization mechanism, process of conduction, influence of impurities and phase transition. AC conductivity obtained from the dielectric properties combined with the data on DC conductivity yields useful information on defect formation and nature of conduction [60].

Dielectric materials are characterized by a high dielectric constant, which is always greater than unity and represents the increase in charge storing capacity by insertion of a dielectric medium between two plates of the capacitor (Figure 1.16) [64].

The capacitance C of the capacitor is a measure of this charge and is defined by

$$C = \frac{\epsilon_0 A}{d} \quad (1.67)$$

where A is the area of the parallel plates and d is the distance of separation between them and ϵ_0 (8.854×10^{-14} F/cm) is the permittivity of the free space.

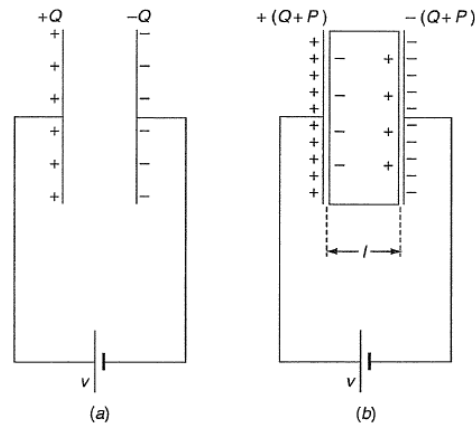


Figure1.16: Parallel plate capacitor (a) with a vacuum (b) filled with dielectric under short circuit condition ($E = \text{constant}$) [64].

If a dielectric material is inserted between the plates, the charge on the plates increase due to polarization in the material. The capacitance is now given by

$$C = \frac{\epsilon_r \epsilon_0 A}{d} \quad (1.68)$$

ϵ_r is a relative permittivity of the dielectric material.

The relative dielectric permittivity is written as a complex function:

$$\epsilon_r^* = \epsilon_r' - i\epsilon_r'' \quad (1.69)$$

The real part ϵ_r' characterizes the displacement of the charges, and the imaginary part ϵ_r'' the dielectric losses. The loss tangent is defined as

$$\tan \delta = \frac{\epsilon_r'}{\epsilon_r''} \quad (1.70)$$

For microwave ceramics frequently a quality factor Q is quoted:

$$Q = \frac{1}{\tan \delta} \quad (1.71)$$

Dielectric ceramics and polymers are used as insulators. Dielectric materials for capacitors must have a high dielectric constant, low dielectric loss, high electrical breakdown strength, low leakage currents, etc.

1.5.2 Dielectric dispersion process

In dielectrics, a dielectric relaxation phenomenon reflects the delay (time dependence) in the frequency response of a group of dipoles submitted to an external applied electric field

[58-60]. Not all the polarization vectors can always follow the variation of the alternating field. The frequency response is expressed in terms of the complex dielectric permittivity (Eq 8) $\epsilon_r^*(\omega) = \epsilon_r'(\omega) - i\epsilon_r''(\omega)$ where $\omega = 2\pi f$ is the angular frequency, f is the circular frequency (in hertz) of the oscillating field and i a complex number ($i^2 = -1$).

The variation of the dielectric constant with frequency of an ionic crystal is similar to the variation of polarizability and polarization. At low frequencies of the order of a few Hz, the dielectric constant is made up of contributions from electronic, atomic and space charge polarization. When measurements are carried out as a function of frequency, the space charge polarization ceases after a certain frequency and the dielectric constant becomes frequency independent. The frequency beyond which the variation ceases may fall in the range of a few kHz to MHz. The frequency-independent value is taken as the true static dielectric constant. Hence, generally, the dielectric constant is measured as a function of frequency to obtain the true static dielectric constant. The dielectric constant measured in the frequency independent region is taken as static or low frequency dielectric constant ϵ_s (sometimes referred to as infrared dielectric constant ϵ_{ir}). As the frequency is increased further, the value remains unaffected till the strong resonance absorption frequency is approached in the infrared region. Beyond the resonant frequency, since the ions cannot follow the field, the polarization due to electronic contribution alone persists. Hence the dielectric constant in this region is termed 'optical' (ϵ_{opt}) or high frequency dielectric constant (ϵ_∞) [60].

Under the influence of static field, the dielectric constant is treated as a real number. The system is assumed to get polarized instantaneously on the application of the field. When the dielectric is subjected to alternating field, the displacement cannot follow the field due to inertial effects and spatially oriented defects [63-67]. The dielectric constant is then treated as a complex quantity $\epsilon_r^*(\omega)$.

$$\epsilon_r^*(\omega) = \epsilon_f + \frac{\epsilon_s - \epsilon_f}{1 - i\omega\tau} \quad (1.72)$$

So, the variation of real and imaginary parts of the complex dielectric constant with frequency ω is given by the Debye equations

The real part of ϵ_r^* is

$$\epsilon_r'(\omega) = \epsilon_f + \frac{\epsilon_s - \epsilon_f}{1 + \omega^2\tau^2} \quad (1.73)$$

And the imaginary part of ϵ_r^* is

$$\varepsilon_r''(\omega) = \frac{(\varepsilon_s - \varepsilon_f)\omega\tau}{1 + \omega^2\tau^2} \quad (1.74)$$

where τ is the relaxation time, ε' is identified with the measured dielectric constant ε and ε'' is a measure of the average power loss in the system. The loss is expressed in terms of the phase angle δ as $\tan \delta = \varepsilon''/\varepsilon'$.

The loss ($\tan \delta$) in general consists of two contributions; one, due to conduction and the other due to relaxation effects. The loss due to conduction of free carriers is expressed in terms of conductivity (σ) [60]

$$\tan \delta = \frac{4\pi\sigma}{\omega\varepsilon_r'} \quad (1.75)$$

A plot of $\log (\tan \delta)$ against $\log \omega$ will give a straight line. If ε_r'' (i.e. $\varepsilon_r' \tan \delta$) is proportional to inverse frequency, the conduction is frequency independent and is equivalent to DC energy loss.

The dipolar impurities or dipoles created by defects show relaxation effects. The loss due to relaxation effects is obtained by combining Debye eq. (12) and (13) as

$$\tan \delta = \frac{\varepsilon_r''(\omega)}{\varepsilon_r'(\omega)} = \frac{(\varepsilon_s - \varepsilon_f)\omega\tau}{\varepsilon_s + \varepsilon_f\omega^2\tau^2} \quad (1.76)$$

The frequency dependence of the loss due to relaxation effects differs from that of conduction loss. Unlike the conduction loss, which shows a linear $\log (\tan \delta)$ versus frequency plot, the loss due to relaxation effects shows a maximum at a certain frequency. The net effect on the appearance of the curve when both the effects are present will be a peak superimposed on a straight line. The departure from a straight line depends on the features of the peak like breadth, sharpness, etc.

The total contribution to dielectric loss ($\tan \delta$) is the sum of the conduction loss given by (14) due to free vacancies and the dipolar Debye loss (15). Thus

$$\tan \delta = \frac{4\pi\sigma}{\omega\varepsilon_r'} + \frac{(\varepsilon_s - \varepsilon_f)\omega\tau}{\varepsilon_s + \varepsilon_f\omega^2\tau^2} \quad (1.77)$$

At normal temperatures and low frequencies up to a few kHz the second term is negligible. The first term becomes predominant and conductivity may be obtained from the dielectric loss from the equation (14) [60]

$$\sigma = \varepsilon_0\varepsilon_r'\omega \tan \delta \quad (1.78)$$

where ϵ_0 is the vacuum dielectric constant. Unlike the conduction loss, the Debye loss is not explicitly defined. The loss may be due to rotating polar entities, defects such as impurity-vacancy, impurity-interstitial pairs and electrode polarization or even due to the presence of air gaps. It may be seen from that the conductivity can be estimated using data on dielectric constant and loss.

1.6 Optical properties of ferrite thin films

The optical properties of thin films are of significant importance, both in basic and applied research. The wide use of thin films in optical devices requires a good knowledge of such properties. The optical behavior of a thin film is a function of its interactions with electromagnetic radiation. Possible interactive phenomena are reflection, transmission, and absorption of the incident light onto the surface of the thin film. When light proceeds from one medium into another (e.g. from air into a thin film), some of the light radiation will be reflected at the interface between the two media, some may be transmitted through the medium, and some will be absorbed within it if the material of a thin film is absorbing (metal and semimetal) [68]. The principle of conservation of energy determines that for any light radiation-matter interaction, the intensity I_0 of the incident beam on the surface of the thin film at a particular wavelength must equal the sum of the intensities of the reflected, transmitted, and absorbed beams, denoted as I_R , I_T , and I_A , respectively, i.e.,

$$I_0 = I_R + I_T + I_A \quad (1.79)$$

An alternate form is

$$R + T + A = 1 \quad (1.80)$$

where R , T , and A represent the reflectance (I_R/I_0), transmittance (I_T/I_0), and absorbance (I_A/I_0), respectively. The sum of these macroscopic quantities which are usually known as the optical properties of the thin film must equal unity since the incident radiant flux at one wavelength is distributed totally between reflected, transmitted, and absorbed intensity.

For a complete understanding of the optical behavior of a thin film, a good knowledge of the structure of the film is also necessary. The optical properties of ferrite thin films depend on the deposition methods, microstructure, the impurity concentration, the annealing temperature and on surface morphology of the films. The propagation of light

through a medium is quantified by the complex refractive index (n^*) where $n^* = n - ik$. The real part n which determines the velocity of light in the medium is called the refractive index and the imaginary part, k , the extinction coefficient is related to the absorption coefficient by the equation: $k = \alpha \lambda / 4\pi$.

1.6.1 Optical parameters

The optical constants of thin films could be measured experimentally by several methods including reflection or/and transmittance, spectrophotometry, interferometry, transmittance data (envelope), and Ellipsometry. There are a number of methods that can be used for the routine determination of the wavelength dependent complex refractive index of thin films, using simple spectrophotometric equipment [70].

1.6.1.1 Reflection – Transmission (RT) Method

In the reflection - transmission (RT) method, the film is illuminated by unpolarized radiation, and the intensities of reflected and transmitted beams are measured as a function of wavelength. The photometric measurements of reflectance R and transmittance T at normal incidence are recognized as the most suited for determining the optical constants n and κ of a thin film material over a wide wavelength range. The result from this method is sensitive to the film surface properties. For normal incidence, the reflection coefficient, r , is obtained as [69]

$$r = \frac{1 - n^*}{1 + n^*} = \frac{1 - n + ik}{1 + n - ik} \quad (1.81)$$

The reflectance R is then defined by

$$R = |r|^2 = \left| \frac{1 - n + ik}{1 + n - ik} \right|^2 = \frac{(1 - n)^2 + k^2}{(1 + n)^2 + k^2} \quad (1.82)$$

The reflectance and transmittance are related by

$$T = (1 - R)^2 \exp(-\alpha d) \quad (1.83)$$

These two relations offer a convenient method for determining the optical constants from the R and T data on the same film.

1.6.1.2 Envelope method

The envelope method was proposed by Manifacier et al [71] and developed by Swanepoel [72] for transmission measurements to evaluate film thickness and the optical constants such as the refractive index n , extinction coefficient k , and absorption coefficient α from the transmission spectra. This method is based on the use of the extremes of the interference fringes of transmission spectrum for calculation the refractive index and film thickness in both weak absorption region and transparent region.

The envelopes are constructed by curve fitting to connect the maxima (T_M) and minima (T_m). Consider the optical system consists of ferrite thin films deposited onto thick, finite, transparent (glass) substrates. The homogeneous film has thickness d and complex refractive index $n = n - ik$, where, n is the refractive index and k the extinction coefficient, which can be expressed in terms of the absorption coefficient α by the equation: $k = \alpha \lambda / 4\pi$. The thickness of the substrate is several orders of magnitude larger than d and its index of refraction is n_s . The system is surrounded by air with refractive index $n_0 = 1$. Taking all the multiple reflections at the three interfaces into account (air (n_0)/film (n_f)/thick transparent substrate (n_s)/air (n_0)), it can be shown that in the case $k^2 \ll n^2$ the expression for the transmittance T for normal incidence is given by [72]

$$T = \frac{Ax}{B - Cx \cos \varphi + Dx^2} \quad (1.84)$$

where

$$A = 16n^2n_s, \quad B = (n+1)^3(n+n_s^2), \quad C = 2(n^2-1)(n^2-n_s^2), \\ D = (n-1)^3(n-n_s^2), \quad \varphi = 4\pi nd / \lambda \quad \text{and} \quad x = \exp(-\alpha d)$$

The extremes of the interference fringes can be obtained from equation (1) by setting the interference condition $\cos \varphi = +1$ for maxima T_M and $\cos \varphi = -1$ for minima T_m and can be written as

$$T_M = \frac{Ax}{B - Cx + Dx^2} \\ T_m = \frac{Ax}{B + Cx + Dx^2} \quad (1.85)$$

The interference maxima T_M and minima T_m can be considered to be a continuous function of λ and experimentally determined by the envelopes as shown in figure 1.17. From the two new formulae (1.85) the optical constants can be derived. (Next section)

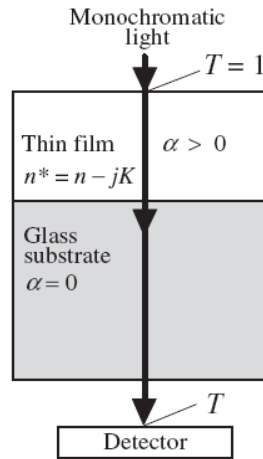


Figure 1.17: Schematic sketch of the typical behavior of light passing through a thin film on a substrate with normal incident [69].

(a) Refractive index

According to Swanepoel's method [72], the refractive index, n , values were calculated from the transmission spectra of the films. A typical transmission spectrum at normal incidence has two spectral regions: the region of weak and medium absorption and the strong absorption region. In the weak and medium absorption region, a first approximation of the real part of the refractive index n of the film can be calculated by the following expression:

$$n = \left[N + \sqrt{N^2 - n_s^2} \right]^{\frac{1}{2}} \quad (1.86)$$

where

$$N = 2n_s \left[\frac{T_M - T_m}{T_M T_m} \right] + \frac{n_s^2 + 1}{2}$$

where T_M and T_m are the transmission maximum and the corresponding minimum at a certain wavelength, λ , and n_s is the refractive index of the substrate used (for glass $n_s=1.52$)

(b) Cauchy dispersion relation

In the Cauchy relationship, the dispersion relationship between the refractive index (n) and wavelength of light (λ) is commonly stated in the following form [69]:

$$n(\lambda) = A + \frac{B}{\lambda^2} + \frac{C}{\lambda^4} \quad (1.87)$$

where A , B , and C are material-dependent specific constants that fits the Cauchy model. Equation (1) is known as Cauchy's formula and it is typically used fit for the refractive index as a function of the wavelength in the visible spectrum region for various optical glasses and is applies to *normal dispersion*, when n decreases with increasing λ . The third term is sometimes dropped for a simpler representation of n versus λ behavior.

(c) Single-Oscillator Model

An intuitive guide to explaining dispersion in insulators is based on a single-oscillator model in which the electric field in the light induces forced dipole oscillations in the material (displaces the electron shells to oscillate about the positive nucleus) with a single resonant frequency ω_0 . According to a single-oscillator model of Wemple-DiDomenico (WD-model), the relation between the refractive index (n) and photon energy, $h\nu$, at photon energies below the interband absorption edge can be written as follows [73]

$$n^2(h\nu) - 1 = \frac{E_o E_d}{E_o^2 - (h\nu)^2} \quad (1.88)$$

where $h\nu$ is the photon energy, E_d is the dispersion energy or the oscillator strength and E_o is the oscillator energy. The first parameter measures the average strength of the interband optical transitions, associated with the changes in the structure of the material. The second one, can be correlated with the optical band gap by the empirical formula $E_o = 2E_g$.

By plotting of refractive-index factor $(n^2 - 1)^{-1}$ against $(h\nu)^2$ and fitting a straight line, E_o and E_d can be determined directly from slope, $(E_o E_d)^{-1}$, and the intercept E_o/E_d on the vertical axis.

An important achievement of the WD-model is that it relates the dispersion energy E_d to other physical parameters of the material, through an empirical formula [73, 74] $E_d = \beta N_c Z_a N_e$ (eV) where N_c , the coordination number of the cation nearest neighbor to the anion, Z_a , the formal chemical valency of the anion, and, N_e , the total number of valence electrons per anion and β is a two-valued constant ($\beta_i = 0.26 \pm 0.03$ eV and $\beta_c = 0.37 \pm 0.04$ eV, for ionic and covalent compounds respectively).

(d) Film thickness

The thickness (d) of the films can be determined from the interference fringes of transmission data by calculating the refractive index of the thin film corresponding to two adjacent maxima (or minima) given as $n(\lambda_1)$ at λ_1 and $n(\lambda_2)$ at λ_2 [75, 76]

$$d = \frac{\lambda_1 \lambda_2}{2(n(\lambda_1)\lambda_2 - n(\lambda_2)\lambda_1)} \quad (1.89)$$

where $n(\lambda_1)$ and $n(\lambda_2)$ are the refractive indexes in two consecutive maxima (or minima) and λ_1 and λ_2 the corresponding wave lengths. Thickness measurements made by a surface stylus profilometer can be carried out to cross check the results obtained by the method employing only transmission spectra $T(\lambda)$.

(e) Absorption and extinction coefficients

The absorption coefficient (α) can be evaluated from transmission data using the relation [72] as follows

$$x = \exp(-\alpha d), \quad \alpha = -\frac{1}{d} \ln[x] \quad (1.90)$$

where d is the film thickness and x is absorbance

In the region of weak and medium absorption, parameter x is given by:

$$x = \frac{E_M - [E_M^2 - (n^2 - 1)^3 (n^2 - n_s^4)]^{1/2}}{(n - 1)^3 (n - n_s^2)} \quad (1.91)$$

where

$$E_M = \frac{8n^2 n_s}{T_M} + (n^2 - 1)(n^2 - n_s^2)$$

In the region of strong absorption the interference fringes disappear and the absorption coefficient (α) can be calculated from the relation:

$$\alpha = -\frac{1}{d} \ln \left(\frac{(n + 1)^3 (n + n_s^2)}{16n^2 n_s} T \right) \quad (1.92)$$

where T is the transmittance of the films in the strong absorption region.

The extinction coefficient, k , is calculated from relation

$$k = \frac{\alpha \lambda}{4\pi} \quad (1.93)$$

The low value of the extinction coefficient (in the order of 10^{-2}) is a qualitative indication of good surface smoothness of the films.

(f) Dielectric constant

The optical properties of any material are characterized by two parameters n and k . The complex dielectric constant is an intrinsic material property. The real part of it is associated with the way in which the speed of light varies in a material other than air. The imaginary part is related to the absorb energy from electric field due to dipole motion. The real ϵ_1 and imaginary ϵ_2 parts of dielectric constant of the films could be determined using the following relations [69]

$$\epsilon = n^2 = \epsilon_1 + i\epsilon_2, \quad n^2 = (n + ik)^2$$

$$\epsilon_1 = n^2 - k^2 \text{ and } \epsilon_2 = 2nk \quad (1.94)$$

where $k = \alpha\lambda/4\pi$

In explicit terms, n and k can be related to the dielectric constants as follows

$$n = \left(\frac{1}{2} \left(\left(\epsilon_1^2 + \epsilon_2^2 \right)^{1/2} + \epsilon_1 \right) \right)^{1/2}$$

$$k = \left(\frac{1}{2} \left(\left(\epsilon_1^2 + \epsilon_2^2 \right)^{1/2} - \epsilon_1 \right) \right)^{1/2} \quad (1.95)$$

1.6.2 Optical bandgap

When an incoming photon with energy, $E = h\nu$ is absorbed, it can interact with one of four types of carriers: inner shell electrons, valence electrons, free carriers, or electrons trapped by localized impurities and other defects [69]. The fundamental absorption process occurs when a valence electron is promoted to a higher energy state (e.g. conduction band). The optical band gap E_g for the films can be estimated from absorption coefficient α using the Tauc relation [77] which is given by

$$\alpha h\nu = A(h\nu - E_g)^q \quad (1.96)$$

where A is a constant depends on the transition probability, $(h\nu)$ is energy of incident photon and (q) is an index that characterizes the optical absorption process and is theoretically equal to 2, 1/2, 3 or 3/2 for allowed indirect, allowed direct, forbidden indirect and forbidden direct electronic transitions, respectively depending on the nature of the electronic transition responsible for the reflection [78].

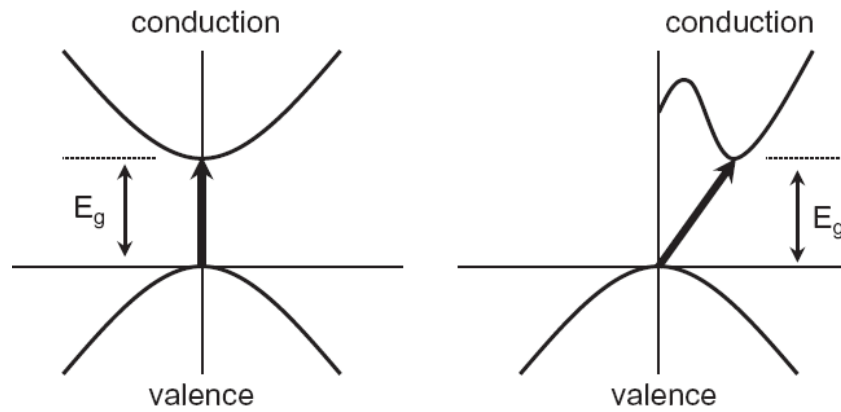


Figure 1.18: Direct (left) and indirect (right) band gap transition [79]

A direct transition occurs when the valence band maximum and the conduction band minimum are at the zone center where $k = 0$ in the Brillouin zone, and an indirect one occurs when the conduction band minimum does not occur at $k = 0$, but rather at some other value of k which is usually at the zone edge or close to it (figure 1.18) [79]. For a direct transition, a photon with energy $h\nu$ can be absorbed promoting a valence band electron to the conduction band, creating an electron–hole pair. This process involves a two body collision (electron and photon) accompanied by strong light absorption, whereas for an indirect transition between two bands with different wave vectors, both the kinetic energy and the potential energy of an electron must be changed, which requires the assistance of phonon. Hence, this process involves a three-body collision (electron, photon and phonon) and relatively weak light absorption [79, 80].

The band gap energy, E_g of the film can be obtained by extrapolating the linear portion of the plot of $(\alpha h\nu)^2$ and $(\alpha h\nu)^{1/2}$ against $h\nu$ to $(\alpha h\nu)^2 = 0$ and $(\alpha h\nu)^{1/2} = 0$ for direct and indirect bandgap respectively [81].

1.7 Review of work on copper ferrites

The attention has been focused on copper ferrites and copper containing ferrites because of their interesting electrical and magnetic properties and crystal structure changes due to heat treatment. Copper ferrite (CuFe_2O_4) is a ferrimagnetic semiconductor with the spinel structure. It can be prepared by solid state reaction of an equimolar mixture of copper and iron oxides. According to the $\text{CuO-Fe}_2\text{O}_3$ phase diagram, CuFe_2O_4 is formed between 1000 and 1100 °C [82]. In fact, copper ferrite is distinguished among other spinel ferrites by the fact that it undergoes a structural phase transition accompanied by a reduction in the crystal symmetry to tetragonal at a temperature of 390 °C due to disorientation of Jahn–Teller distortion as a result of thermal motion of lattice at high temperatures [83–85]. This transition is strongly affected by the distribution of Cu ions on the two sublattices and the oxygen stoichiometry. For bulk CuFe_2O_4 , these parameters can be altered by adjusting preparation conditions such as sintering temperature, cooling rate, gaseous environment etc. Under slow cooling Cu-ferrite crystallizes in a tetragonal structure with lattice parameter ratio c/a of about 1.06. Tetragonal phase of Cu-ferrite has inverse spinel structure with almost all Cu^{2+} ions occupying octahedral sublattice, whereas Fe^{3+} ions divide equally between the tetrahedral and octahedral sublattices. With increasing the number of Cu^{2+} ions on tetrahedral sublattice the distortion decreases stabilizing the cubic symmetry with large magnetic moment at room temperature [86].

Copper ferrite (CuFe_2O_4) nanoparticle has gained significant attention in recent years. The preparation of CuFe_2O_4 nanowalls, nanorods and nanodisks using electrochemical method, reverse micelle and hydrothermal methods has been reported by [87, 88]. In addition, CuFe_2O_4 nanoparticles have been prepared by co-precipitation method [89, 90], precipitation in polymer matrix [91], mechanical milling [92–95], sol-gel method [96], combustion [97], auto-combustion [98, 99], Electrochemical [100], etc. The preparation of CuFe_2O_4 nanoparticles by these processes reduces the average grain size of CuFe_2O_4 and induces cation redistribution between tetrahedral and octahedral sites.

Copper ferrites have been characterized and studied by several techniques to explore the cation distribution between A- and B-sites. These include Rietveld structure refinement of the cation distribution in ferrite fine particles by X-ray powder diffraction [101], X-ray magnetic circular dichroism [102], EXAFS and XANES investigations [103], Mossbauer spectroscopy [104–110], Near Infrared Faraday rotation and Magneto-optic Kerr effect (MOKE) [111–115] etc. The effect of SnO_2 coating on the zero field cooled

(ZFC) and field cooled (FC) magnetization magnetic properties of nanocrystalline CuFe_2O_4 has been reported by R. K Selvan et al. [116].

The transport properties such as dc-conductivity, thermoelectric power and dielectric constant have also been carried out on CuFe_2O_4 compound [82, 117]. The phase transition studies of this compound have been done by Murthy et al. [118]. Mazen et al [119] studied the thermal and electrical properties of this material. The magnetostriction of a number of copper-containing ferrite spinels was measured by Antoshina and Goryaga [120]. It was found that the magnetostriction decreases with temperature that is conjectured to the increase in the degree of covalency among the $\text{Cu}^{2+}\text{--O}^{2-}$ ions, which, in turn, reduces their spin-orbit coupling.

These materials have a wide range of applications, including gas sensors [121-123], Catalyst [124-126] CO_2 decomposition [127], negative electrodes for Li-ion batteries [128], hydrogen production [129], magnetic adsorbents [130], etc.

Thin films of copper ferrites are also of great interest. There have been a number of studies on Cu-ferrite thin films with the objective of enhancing magnetization for applications deposited either by RF-sputtering [131-139] or Pulsed laser deposition [140, 141]. In these studies higher magnetization values were achieved either by substrate heating or annealing the films at high temperatures or by applying high power and high working gas pressure. Zuo et al. [142] predicted that a high magnetization may be achieved by increasing the number of Cu^{2+} ions on A-sublattice.

The studies on bulk $\text{Cu}_{0.5}\text{Fe}_{2.5}\text{O}_4$ ferrite shows the ordering of the Cu^{+} ions to the tetrahedral A-site when material is quenched from high temperature in a highly reducing atmosphere [143].

1.8 Review of work on zinc ferrites

Stoichiometric bulk Zinc ferrite (ZnFe_2O_4) prepared by the classical ceramic route exhibits a normal spinel structure where Zn^{2+} and Fe^{3+} ions occupy the tetrahedral (A) and the octahedral (B) spinel sites, respectively [144]. It displays a long-range antiferromagnetic ordering below 10 K with zero magnetization at room temperature. The magnetic ordering in ferrites is driven by the A–A, B–B and A–B interactions. The intra-site interaction of the magnetic moment of the cations on the A or B sites is much weaker than the A–B inter-site one. If the tetrahedral sites are exclusively occupied by non-magnetic ions i.e. Zn^{2+} , magnetic interaction occurs only between Fe^{3+} ions in the octahedral sites, and the weak negative B–B interaction leads to an antiferromagnetic long-range order [145].

The formation of bulk zinc ferrite from a dry mixture of ZnO and Fe_2O_3 by the solid state reaction method was extensively studied [144-148]. Experimental results indicated that the reaction rate could be increased by an increase in density of solid sample or reaction temperature. The reaction rate was also found to be increased by reducing the grain size of zinc oxide or iron oxide and the molar ratio of $\text{Fe}_2\text{O}_3/\text{ZnO}$ [144].

The influence of simultaneous thermal and ultrasonic treatments on the kinetics and mechanism of the reaction between ZnO and $\alpha\text{-Fe}_2\text{O}_3$ was studied in a temperature range of 600–800 °C [145]. It was shown that ultrasound action leads to a considerable increase in conversion at the initial stage of interaction and changes the mechanism of the solid-phase reaction at the main stage over the entire temperature range.

The kinetics of zinc ferrite formation in the rate deceleration period was studied by Xia and Pickles [146]. They found that the initial surface chemical reaction involved in zinc ferrite formation is very rapid at any given temperature, and the reactants quickly covered with zinc ferrite. Then, the reaction rate becomes decelerated. The kinetics of zinc ferrite formation during this rate deceleration period was studied in the temperature range of 873 to 1073 K. The activation energy was found to be about 168 kJ mol⁻¹. This activation energy indicates that diffusion is rate controlling.

The progress of the formation of zinc ferrite annealed at 1200 °C was monitored by XRD and XPS analyses at different time intervals [147]. The presence of octahedral zinc cation was observed along with the regular tetrahedral Zn in the sample that had undergone 30 minute heat treatment. After three hours of heating, pure normal zinc ferrite was formed.

The magnetic properties of the normal spinel ZnFe_2O_4 were investigated using neutron diffraction (ND), muon-spin rotation/relaxation (μSR) and ^{57}Fe and ^{67}Zn Mossbauer spectroscopy (MS) [148]. The results show that the inversion is below limits of detection in samples which were slowly cooled from 1200 °C to room temperature. It also conform that below $T_N = 10.5$ K the spinel exhibits long-range antiferromagnetic order (LRO).

The synthesis of ferrite nanoparticles is of great interest for tailoring of specific magnetic properties. When the size of magnetic particles reduces into nanometer-sized scale, the surface area/volume increases greatly, resulting in novel phenomena. Superparamagnetism, magnetic quantum tunneling and spin-glass-like behavior are some examples in the field of nanomagnetism [149, 150]. These magnetic properties make magnetic nanoparticles to have many technological applications including magnetic data storage, ferrofluid, medical imaging, drug targeting, and catalysis [151-153]. The zinc ferrite, ZnFe_2O_4 , one of the iron based cubic spinel series, shows significant changes in its magnetic properties by reducing the grains to the nanometer-sized range [154, 155].

Zinc ferrite nanoparticles have been synthesized by several methods. Pavljukhin et al. [156] reported that the zinc ferrite (ZnFe_2O_4) fine particles obtained by mechanical activation of bulk ZnFe_2O_4 crystal yield high magnetization even at room temperature. Sato et al. [157] also prepared ultrafine ZnFe_2O_4 particles of several nanometers in size by the coprecipitation method. They found the formation of short-range and long-range magnetic order in small ZnFe_2O_4 particles below and above approximately 30 K. Below 30 K, the appearance of spontaneous magnetization and its hysteretic property is confirmed for small ZnFe_2O_4 particles and explained in terms of the presence of non-collinear spontaneous magnetization due to the formation of a long-range magnetic order in small particles.

Since then, a wide variety of methods have been applied to synthesize ZnFe_2O_4 in the form of nanoparticles. These include the *co-precipitation method* [158-161], *microemulsion method* [149, 159, 162], the critical *sol-gel* processing or *aerogel* method [163-169], *hydrothermal process* [160, 170, 195], *rapid quenching method* [152-155], *mechanical ball-milling* [156, 163, 166, 171-183], *hydrolysis in a polyol medium* [184], *spray pyrolysis* [185], *citrate precursor* [186, 187], *combustion* [187, 188], *tartrate precursor* [189], *RF-thermal plasma reactor* [190], *thermal decomposition* [191],

electrodeposition [192], *solvothral method* [193-195], *pulsed wire discharge* (PWD) [196], *Sonochemical emulsification and evaporation* [197] etc.

In a recent study, nanocrystalline ZnFe_2O_4 powders have been synthesized successfully by pulsed wire discharge (PWD) method using metallic Fe and Zn wires in oxygen gas [194]. Since high temperature and energy densities can be easily achieved in this method. PWD offers unique advantages for the synthesis of ultrafine ZnFe_2O_4 powder with novel properties without extra heat treatment.

The average particle size of the nanoparticles has usually been determined by x-ray diffraction (XRD) methods i.e. calculated from Scherrer's formula, and confirmed by transmission electron microscopy (TEM) or scanning electron microscopy (SEM). Ultrafine zinc ferrite particles prepared by the above synthesis methods have similar average particle sizes, the smallest particles are near 2-6 nm, the largest near 35 nm. When ultrafine particles are annealed typically between 500 and 800°C, the particle size increases. For nanoparticles, several properties such as the chemical reactivity, Neel temperature and melting point differ in comparison with corresponding bulk according to their degree of cationic inversion.

The common feature to the above studies, and one of the main stimuli to the continuing interest, is the enhancement in magnetic properties observed in nanostructured or nanocrystalline particles compared with the magnetic behavior exhibited by equilibrium ZnFe_2O_4 . While many factors contribute to this enhanced magnetization, the prime factor appears to be linked with the nonequilibrium distribution of the magnetic irons and diamagnetic zinc cations. For ZnFe_2O_4 nanoparticles the key feature is the redistribution of Fe^{3+} into tetrahedral interstices and Zn^{2+} into octahedral interstices. This cationic rearrangement leads to the formation of two (A) and [B] magnetic sublattices which are then responsible for the enhanced magnetization displayed when compared with normal ZnFe_2O_4 in its equilibrium state [e.g. 224]. As explained by several authors, the overall magnetic behavior can be well accounted for in terms of a *superexchange interaction* of the type $\text{Fe}^{3+}(\text{A})\text{O}^{2-}\text{Fe}^{3+}[\text{B}]$ occurring as a result of this cationic re-distribution in nanoscale ZnFe_2O_4 .

Details of the structural features and enhanced magnetization exhibited by nanoscale ZnFe_2O_4 have been extensively investigated by several groups using a variety of techniques including: *magnetization* [161, 172, 174, 198-201], *permeability* and

permittivity [194, 198], *Infrared* [197, 199], *Mossbauer spectroscopy* [148, 157, 161, 172, 174, 196, 202, 204-208], *X-ray photoelectron spectroscopy* [209], *neutron scattering* [175, 177, 179, 197, 210], *muon spin rotation/relaxation* [148, 175, 197], *Extended X-ray absorption fine structure (EXAFS)* [211, 212], *specific heat* [206], the *Faraday effect* [203], *nuclear magnetic resonance (NMR)* [182], *electron paramagnetic resonance (EPR)* [213, 214] as well as a range of standard laboratory characterization techniques.

The main results one can conclude from the mentioned investigations are summarized as follows:

- (i) Presence of competing ferro- and antiferromagnetic exchange interactions arising from Fe clustering,
- (ii) Breaking of superexchange bonds due to oxygen vacancies produced during preparation.
- (iii) The analysis of x-ray diffraction, neutron powder diffraction, and calorimetric data has also been interpreted as indicating the presence of octahedral zinc.
- (iv) EXAFS data indicates that the structure around the Zn atom differs between bulk and nanocrystalline zinc ferrite. It revealed that Zn^{2+} ions occupy B-sites in addition to the normal A-sites. It is thought that the occupation of B-sites by Zn^{2+} brings about Fe^{3+} ions in both A- and B-sites, and the strong *superexchange interaction* between Fe^{3+} ions in A- and B-sites, J_{AB} , causes high magnetization at room temperature.
- (v) Magnetic studies, including zero-field cooling (ZFC), field cooling (FC) magnetic susceptibility and hysteresis curves show that for the as-prepared ZnFe_2O_4 , $M_{FC}(T)$ monotonically increases with decreasing temperature, whereas $M_{ZFC}(T)$ shows a maximum, corresponding to spin freezing temperature T_f . Such a behavior is caused by the disordered cation distribution of Zn^{2+} and Fe^{3+} ions in the spinel structure.
- (vi) An enhanced magnetization of many times that of bulk zinc ferrite was observed for the nanoparticles regardless of synthesis method. The magnetization has reached value of about 78 emu/g at 5K [184]. For comparison, table 1.3 shows the saturation magnetization of ZnFe_2O_4 nanoparticles obtained by different synthesis methods.

Table 1.3: Comparison of the degree of structure inversion, the blocking temperature, T_B , and the saturation magnetization of ZnFe_2O_4 nanoparticles obtained by different synthesis methods.

Reference	Synthesis method	Part. Size (nm)	δ %	Method of determination of the local structure	M_s (emu/g)
This work	Coprecipitation RF magnetron Sputtering			FMR, FC-ZFC FMR, FC-ZFC	12 (RT) 42 (RT)
Ammar 2006 [184] Ammar 2004 [215]	Polyol method	6.6 14.8	25 18	6 T field-Mossbauer	78 (5K) 54 (5K)
H. H. Hamdeh 1997 [163]	Supercritical sol-gel + drying at 513 K	8.1	22	Rietveld refinement on XRD	22(5K)
	Supercritical sol-gel + drying at 513K + ball milling for 10 h	10.3	10	Rietveld refinement on XRD	73 (10K)
C. R. Bluncson 1994 [216]	Hydrothermal in supercritical methanol	5-20	0	Mossbauer at RT	38 (4.2K)
S.-H. Yu 2003 [200]	Hydrothermal in ammonia solution	300	$\neq 0$	Cation inversion suspected	61 (80 K)
G. F. Goya 2000 [173]	Ball milling	36	7	Rietveld refinement on neutron diffraction	20.7 (4.2K)
	Ball milling + calcinations at 773 K	50	16	Rietveld refinement on neutron diffraction	40 (4.2 K)
C. N. Chinnasamy 2000 [174]	Ball milling	11 14	36 24	6 T field-Mossbauer at 10 K 6 T field-Mossbauer at 10 K	10 (RT) 7.5 (RT)
F. J. Burghart 2000 [174]	Ball milling	9	43	Rietveld refinement on neutron diffraction	58 (5K)
T. Sato 1990 [157] B. Jeyadevan 1994 [211]	Coprecipitation at 373 K	5.5	$\neq 0$	EXAFS analysis at Zn Kedge	35 (4.2 k)
	Coprecipitation at 373 K + calcinations at 973 K	96	11	6 T field-Mossbauer at 10 K	Not given
T. Kamiyama 1992 [217]	Coprecipitation at 373 K	5.5	$\neq 0$	Cation inversion suspected	46.9 (5K)
	Coprecipitation at 373 K + calcinations at 773 K	29	7	Rietveld refinement on neutron diffraction	26.4 (5 K)
K. Tanaka 1998 [155]	Quenching	—			23.8 (RT) 15 (RT)
P. Y. Lee 2007 [196]	Pulsed wire discharge (PWD)	45			25 (RT)
A. Kundu 2003 [161]	Coprecipitation using Urea	15		Mossbauer	21 (RT) 50 (10K)
K. Tanaka 2003 [203]	RF-Sputtering	10		Faraday Effect	32 (RT)
N. Wakiya et al. 07 [218]	PLD at 500 °C, $H_A = 0$ In $H_A = 2\text{kOe}$			M-H	7.43 (RT) 56.6 (RT)
W. Jiang 2009 [195]	one-pot solvothermal method			Mossbauer	83.4 (RT)

Nanometer-sized zinc ferrite particles capped with a layer of surfactant were synthesized by coprecipitation and microemulsion [219]. The surfactant capping effectively inhibited grain growth, and it was observed that the zinc ferrite nanoparticles with a capping layer could readily be dispersed in some organic media due to their surface modification.

Zinc ferrite is a promising gas sensor material. The gas-sensing properties of ZnFe_2O_4 thin films deposited on alumina substrates by an ultrasonic nebulization and pyrolysis method exhibit moderate sensitivity and good selectivity to CO , demonstrating that nanocrystalline ZnFe_2O_4 thin films deposited by this technique are promising CO -sensing materials [185]. Gas sensing properties of ultrafine ZnFe_2O_4 prepared by water-in-oil (W/O) microemulsion method have been carried out by X. Niu et al. [220]. Their main results of gas sensing measurement show that the ZnFe_2O_4 sensors have a high sensitivity, excellent selectivity and quick response behavior to Cl_2 gas. The response of ZnFe_2O_4 to Cl_2 gas shows the resistance increase that indicates an n-type semiconductor behavior. Non-stoichiometric zinc ferrites were used as catalysts for the oxidative dehydrogenation of 1-butene [162]. The parallelism between the macroscopic magnetization of the ferrites and their capacity of transforming 1-butene into butadiene, CO_2 and 2-butene, by an oxidative dehydrogenation reaction, suggests that the “freezing” of the magnetic moments in the octahedral sites could cause this catalytic behavior.

The performance of zinc ferrites as desulfurization sorbents at high temperature was evaluated [221]. Performance of the zinc ferrite for H_2S absorption was also evaluated using a fixed bed flow type reactor [222]. The effect of the modifier ion on the properties of ZnFe_2O_4 pigment has been done [223]. It was found that the ZnFe_2O_4 crystallizes at 600°C , with a reflectance peak between 650–700 nm, corresponding to the red-brick color.

In contrast to the large number of studies on bulk and nanoparticles of ZnFe_2O_4 , there are few reports on thin films of ZnFe_2O_4 prepared either by RF-sputtering [203, 224–228] or pulsed laser deposition (PLD) [218, 229–233]. RF-magnetron sputtering and PLD are promising techniques to prepare nanocrystalline ZnFe_2O_4 thin films. It is considered that the preparation of the ZnFe_2O_4 thin film by the sputtering method, which involves very *rapid cooling* of vapor to form the solid state phase, causes the random distribution of

Zn^{2+} and Fe^{3+} ions in the spinel structure. In such a situation, Fe^{3+} ions occupy both octahedral and tetrahedral sites, and the strong superexchange interaction among them gives rise to ferrimagnetic properties accompanied with high magnetization [224]. Epitaxial thin films of spinel ZnFe_2O_4 were grown along the (111) direction using laser-molecular beam epitaxy (laser-MBE) on an Al_2O_3 (0001) single crystal substrate [234].

Recently [228], it has been reported that a spatially selective change of magnetism from paramagnetic to ferrimagnetic-like behaviors in normal spinel ZnFe_2O_4 thin film under irradiation with 780 nm femtosecond laser pulses. The distribution of Zn^{2+} and Fe^{3+} ions in the irradiated region on the film surface becomes disordered because of local heating to high temperatures, and the metastable phase of ZnFe_2O_4 is frozen by the rapid quenching after irradiation, resulting in the formation of the ferrimagnetic phase. The ferrimagnetic phase reverts to the paramagnetic state by annealing at 800 °C.

1.9 Objectives of present work

The general objectives of the present work are to investigate the composition, crystal structure and grain size dependence of the electronic, magnetic and optical properties of Cu-Zn ferrites ($\text{Cu}_{1-x}\text{Zn}_x\text{Fe}_2\text{O}_4$, $0 \leq x \leq 1$).

The Specific Objectives

- ❖ To synthesize bulk, nanoparticles and thin films of CuFe_2O_4 , ZnFe_2O_4 and $\text{Cu}_{0.6}\text{Zn}_{0.4}\text{Fe}_2\text{O}_4$ ferrites.
- ❖ To characterize bulk, nanoparticles and thin films of ferrites from their structure, compositional and morphological point of view.
- ❖ To study the magnetic (magnetization and FMR) and dielectric properties of the bulk and nanoparticles of the synthesized ferrites.
- ❖ To study the magnetic (Magnetization and FMR) and optical properties of the synthesized ferrite films.

Scope of study

To attain the above mentioned objectives, the following tasks were carried out

- (1) Synthesis of magnetic ferrites MFe_2O_4 (where M: Cu, Zn and their mixture) using different physical and chemical methods as follows:
 - (a) Ceramic method (Solid state reaction) for bulk samples

- (b) Chemical methods (coprecipitation) for nanoparticle samples, and
 - (c) Deposition methods (RF-magnetron sputtering) for nanocrystalline thin film samples
- (2) Study the crystal structure of the synthesized samples using (XRD) to ascertain the phase formation and for determining the particle size using peak broadening analysis.
 - (3) Observe the morphology, particle size, chemical composition, and the crystallinity of the prepared samples using different microscopic probes like Atomic Force Microscopy (AFM), Scanning Electron Microscopy (SEM) and Energy Dispersive X-Ray Analysis (EDAX).
 - (4) Study the static and dynamic magnetic properties of the samples using Vibrating Sample Magnetometer (VSM) and Electron Spin Resonance (ESR).
 - (5) Study the dielectric properties of the synthesized samples using Impedance Analyzer.
 - (6) Study the optical properties of CuFe_2O_4 , ZnFe_2O_4 and $\text{Cu}_{0.6}\text{Zn}_{0.4}\text{Fe}_2\text{O}_4$ thin films and determine the optical constants of the film films such as refractive index (n), extinction coefficient (k) and energy band gap using transmission spectra recorded on UV-VIS-IR spectrophotometer.

1.10 Thesis organization

The thesis has been organized in five chapters as follows

Chapter 1 includes the literature survey and the theoretical background with a focus on the fundamentals of magnetism, general information on the ferrite materials, description of the spinel structure, magnetic anisotropy, ferromagnetic resonance (FMR) theory and dielectric properties of ferrite materials. The objectives of the present work are also listed in this chapter.

Chapter 2 contains the details of the experimental techniques used in the present study are described in this chapter. These include the preparation methods of the ferrite materials and their characterization. The sample synthesis has been carried out using different physical and chemical methods, which include solid state reaction for bulk samples,

coprecipitation for nanoparticle samples, and RF-magnetron sputtering for nanocrystalline thin film samples.

Chapter 3 presents results obtained on $\text{Cu}_{1-x}\text{Zn}_x\text{Fe}_2\text{O}_4$ ($0 \leq x \leq 1$) ferrite bulk samples prepared by standard ceramic method.

Chapter 4 deals with the results on Cu-Zn ferrite nanoparticles synthesized by modified coprecipitation.

Chapter 5 contains a detailed study of the structural, magnetic and optical properties of ferrosinell $\text{Cu}_{1-x}\text{Zn}_x\text{Fe}_2\text{O}_4$ ($x = 0, 0.4$ and 1) thin films deposited by rf-magnetron sputtering.

At the end of the thesis the main results and conclusions are summarized.

References

- [1] M. Pardavi-Horvath, *J. Magn. Magn. Mater.* **215-216** (2000) 171-183.
- [2] E. Schloemann, *J. Magn. Magn. Mater.* **209** (2000) 15–20.
- [3] J. D. Adam, L. E. Davis, G. F. Dionne, E. F. Schloemann and S. N. Stitzer, *IEEE Trans. Microwave Theory Tech.* **50** (2002) 721–737.
- [4] C. Miclea, C. Tanasoiu, C. F. Miclea, A. Gheorghiu and V. Tanasoiu, *J. Magn. Magn. Mater.* **290–291** (2005) 1506–1509.
- [5] V. G. Harris, A. Geiler, Y. Chen, S. D. Yoon, M. Wu, A. Yang, Z. Chen, P. He, P. V. Parimi, X. Zuo, C. E. Patton, M. Abe, O. Acher and C. Vittoria, *J. Magn. Magn. Mater.* **321** (2009) 2035–2047.
- [6] D. Stoppels, *J. Magn. Magn. Mater.* **160** (1996) 323–328.
- [7] M. Sugimoto, *J. Am. Ceram. Soc.* **82** (1999) 269–280.
- [8] J. A. Gomes, M. H. Sousa, G. J. da Silva, F. A. Tourinho, J. M. Filho, R. Itri, G. de M. Azevedo and J. Depeyrot, *J. Magn. Magn. Mater.* **300** (2006) e213– e216.
- [9] M. H. Sousa, F. A. Tourinho, J. Depeyrot, G. J. da Silva and M. C. F. L. Lara, *J. Phys. Chem. B* **105** (2001) 1168–1175.
- [10] J. T. Lue, *Physical Properties of Nanomaterials*, In Encyclopedia of Nanoscience and Nanotechnology Edited by H. S. Nalwa, American Scientific Vol. **X** (2007) 1–46.
- [11-a] Q. A. Pankhurst, J. Connolly, S. K. Jones, and J. Dobson, *J. Phys. D: Appl. Phys.* **36** (2003) R167-R181.
- [11-b] P. Tartaj, M. del Puerto Morales, S. Veintemillas-Verdaguer, T. Gonzalez-Carreño, and C. J. Serna, *J. Phys. D: Appl. Phys.* **36** (2003) R182-R197.

- [11-c] C. C. Berry and A. S. G. Curtis, *J. Phys. D: Appl. Phys.* **36** (2003) R198-R206.
- [12] J. Richardi, *Assemblies of Magnetic Nanoparticles*, In: Nanomaterials and Nanochemistry, Edited by C. Brechignac, P. Houdy and M. Lahmani, Springer-Verlag Berlin Heidelberg (2007).
- [13] M. A. Willard, L. K. Kurihara, E. E. Carpenter, S. Calvin and V. G. Harris, *International Materials Reviews* **49** (2004) 125–170.
- [14] Y. Suzuki, *Annu. Rev. Mater. Res.* **31** (2001) 265–89.
- [15-a] C. V. G. Reddy, S. V. Manorama and V. J. Rao, *J. Mater. Sci. Lett.* **19** (2000) 775–78.
- [15-b] I. Zaquine, H. Benazizi and J. C. Mage, *J. Appl. Phys.* **64** (1988) 5822–5824.
- [16] Z. Jiao, M. Wu, J. Gu and Z. Qin, *IEEE Sensors J.* **3** (2003) 435–438.
- [17] Z. Sun, L. Liu, D. Jia and W. Pan, *Sensors and Actuators B* **125** (2007) 144–148.
- [18] H. Lee, J. C. Jung, H. Kim, Y-M. Chung, T. J. Kim, S. J. Lee, S-H. Oh, Y. S. Kim and I. K. Song, *Catal. Lett.* DOI 10.1007/s10562-008-9476-7
- [19] S. Kameoka, T. Tanabe and A. P. Tsai, *Catalysis Letters* **100** (2005) 89-93
- [20] S. Celozzi, R. Araneo and G. Lovat, *Electromagnetic Shielding*, Wiley, New Jersey (2008).
- [21] C. Tong, *Advanced materials and design for electromagnetic interference shielding*, Taylor & Francis, CRC, FL, (2009).
- [22-a] J. L. Snoek, *New Developments in Ferromagnetic Material*, Elsevier, Amsterdam (1949).
- [22-b] A. P. Greifer, *IEEE Trans. Magn.* **5** (1969) 774–811.
- [22-c] E. P. Wohlfarth, *Handbook of Magnetic Materials*, Vol **3**, North-Holland (1982).
- [23-a] L. Neel, *Ann. Phys. (Paris)* **3** (1948) 137.
- [23-b] J. L. Went, G. W. Ratenau, E. W. Gorter, and G. W. van Oosterhout, *Philips Tech. Rev.*, **13** (1951) 194–208.
- [24] B. B. Ghate and A. Goldman, *Ferrimagnetic ceramics*, In: Materials science and technology, Vol 11 “structure and properties of ceramics Ed by M.V. Swain” Ed R.W. Cahn, P Haasen and E.J. Kramer (1994).
- [25] E. J. W. Verwey and E. L. Heilmann, *J. Chem. Phys.* **15** (1947) 174–180.
- [26] J. Smit and H. P. J. Wijn, *Ferrites*, Philips’ Tech Lab, Netherlands (1959).
- [27] K. E. Sickafus, J. M. Wills and N. W. Grimes, *J. Am. Ceram. Soc.* **82** (1999) 3279–3292.
- [28] B. D. Cullity and C. D. Graham, *Introduction to magnetic materials*, 2nd Ed. IEEE Press. USA (2009).
- [29] P. I. Slick, *Ferrites for non-microwave applications*, In: Handbook of Magnetic Materials, Vol. **2**, Ed. by E.P Wohlfarth, North-Holland (1982).
- [30] M. A. Willard, Y. Nakamura, D. E. Laughlin and M. E. McHenry, *J. Am. Ceram. Soc.* **82** (1999) 3342–3346.
- [31] N. Spaldin, *Magnetic materials: Fundamentals and device applications*, Cambridge University press, Cambridge (2003).
- [32] A. Goldman, *Modem Ferrite Technology*, 2nd Ed. Springer, New York (2006).
- [33] U. Ozgur. Y. Alivov and H. Morkoc, *J Mater Sci: Mater. Electron.* **20** (2009) 789–834.
- [34] K. J. Standley, *Oxide magnetic materials*, Oxford University Press, London (1962).
- [35] S. Blundell, *Magnetism in condensed matter*, Oxford University Press, London (2001).
- [36] R. M. Cornell and U. Schwertmann, *The Iron Oxides*, 2nd ed. Weinheim: Wiley-VCH Verlag GmbH & Co. (2003).

- [37] A. H. Morrish and S. P. Yu, *Phys. Rev.* **102** (1956) 670-673.
- [38] X. Batlle and A. Labarta, *J. Phys. D: Appl. Phys.* **35** (2002) R15-R42.
- [39] G. F. Goya, T. S. Berquo, F. C. Fonseca, and M. P. Morales, *J. Appl. Phys.* **94**(2003) 3520–3528.
- [40] W. Callister, *Materials science and engineering an introduction*, 6th ed. Wiley, New York (2003).
- [41] S. Chikazumi, *Physics of Magnetism* John Wiley and Sons, (1964).
- [42] D. C. Jiles, *Acta Materialia* **51** (2003) 5907–5939.
- [43] C. M. Sorensen, *Magnetism*, In: *Nanoscale materials in chemistry* Edited by K. J. Klabunde, Wiley, New York (2001).
- [44] M. T. Johnson, P. J. H. Bloemen, F. J. A. den Broeder and J. J. de Vries, *Rep. Prog. Phys.* **59** (1996) 1409–1458.
- [45] M. Farle, *Rep. Prog. Phys.* **61** (1998) 755-826.
- [46] H-R Wenk and P Van Houtte, *Rep. Prog. Phys.* **67** (2004) 1367–1428
- [47] E.-L. Salabas, *Structural and Magnetic Investigations of Magnetic Nanoparticles and Core-Shell Colloids*, PhD thesis, Universität Duisburg, Germany (2004).
- [48] D. S. Schmool, R. Rocha, J. B. Sousa, J. A. M. Santos, G. N. Kakazei, J. S. Garitaonandia, D. Martin Rodriguez, L. Lezama and J. M. Barandiaran, *J. Optoelectronics Adv. Mater.* **6** (2004) 541.
- [49] K. Baberschke, *Investigation of Ultrathin Ferromagnetic Films by Magnetic Resonance* In: *Handbook of Magnetism and Advanced Magnetic Materials*. Ed. by H. Kronmuller and S. Parkin. Vol **3**: *Novel Techniques for Characterizing and Preparing Samples*, John Wiley & Sons (2007).
- [50] Yu-Wei Su, *Fabrication and Characterization of Ferrimagnetic Film for RF/Microwave Crosstalk Suppression*, MSc in chem. Engineering, Oregon State University (2007).
- [51] J. Lindner and K. Baberschke, *J. Phys.: Condens. Matter.* **15** (2003) R193–R232.
- [52] S.V. Vonsovskii, *Ferromagnetic Resonance*, Pergamon Press, Oxford, UK, (1966).
- [53] C. Kittel, *Phys. Rev.* **73** (1948) 155.
- [54] A. P. Guimaraes and I. S. Oliveira, *Magnetism and magnetic resonance in solids*, Wiley, New York (1998).
- [55] J. Smit and H. G. Beljers *Phillips Res. Rep.* **10** (1955) 113–130.
- [56] J. Lindner and K. Baberschke, *J. Phys.: Condens. Matter.* **15** (2003) S465-S478.
- [57] M. J. Hurben and C. E. Patton, *J. Appl. Phys.* **83** (1998) 4344-4365.
- [58] K. C. Kao, *Dielectric phenomena in solids*, Elsevier, USA (2004).
- [59] G. G. Raju, *Dielectrics in Electric Fields*, Marcel Dekker, New York (2003).
- [60] D. B. Sirdeshmukh, L. Sirdeshmukh and K. G. Subhadra, *Micro- and Macro-Properties of Solids: Thermal, Mechanical and Dielectric Properties*, Springer, New York (2006).
- [61] W. D. Kingery, H. K. Bowen, and D. R. Uhlmann, *Introduction to Ceramics*, Wiley, New York (1976).
- [62] R. Waser *Nanoelectronics and Information technology*, WILEY-VCH, Weinheim (2003).
- [63] Prashant N. Kumta, Jin Yong Kim, In: *Handbook of low and high dielectric constant materials and their applications*, Vol. 1 Ed. by H. S. Nalwa, Academic press (1999) p. 83.
- [64] T. Blythe and D. Bloor, *Electrical properties of polymer*, 2nd Ed Cambridge Univ. Press, UK (2005).
- [65] L. F. Chen, C. K. Ong and C. P. Neo V. V. Varadan and V. K. Varadan, *Microwave Electronics*, Wiley, England (2004).

- [66] E. Barsoukov and J. R. Macdonald *Impedance Spectroscopy: Theory, Experiment, and Applications* 2nd Ed. Wiley, New Jersey 2005.
- [67] E. Riande and R. Diaz-Calleja, *Electrical Properties of Polymers*, Marcel Dekker, New York (2004).
- [68] M. Fox, *Optical properties of solids*, Oxford University press, Great Britain (2001).
- [69] J. Singh, *Optical properties of condensed matter and applications*, Wiley, England (2006).
- [70] D. Poelman and P. F. Smet, *J. Phys. D: Appl. Phys.* **36** (2003) 1850
- [71] J. C. Manifacier, J. Gasiot and J. P. Fillard, *J. Phys. E: Sci. Instrum.* **9** (1976) 1002
- [72] R. Swanepoel, *J. Phys. E: Sci. Instrum.* **16** (1983) 1214.
- [73] S.H. Wemple and M. Di Domenico, *Phys. Rev.* **23** (1969) 1156.
- [74] S.H. Wemple and M. Di Domenico, *Phys. Rev B.* **3** (1971) 1338.
- [75] E. Marquez, J. R. Malo, P. Villares, R. J. Garay, P. J S Ewen, A. E. Owen, *J. Phys. D: Appl. Phys.* **25** (1992) 535
- [76] K. L. Chopra, *Thin film phenomena*, McGraw-Hill, New York (1969).
- [77] J. Tauc, *Amorphous and Liquid Semiconductors*, Plenum Press, New York (1974).
- [78] A. F. Qasrawi, *Cryst. Res. Technol.* **40** (2005) 610.
- [79] F. Wooten, *Optical properties of solids*, Academic press, New York (1972).
- [80] N. Tigau, V. Ciupina and G. Prodan, *J. Crystal Growth* **277** (2005) 529.
- [81] L. Liang, Y. Sheng, Y. Xu, D. Wu and Y. Sun, *Thin Solid Films* **515** (2007) 7765–7771.
- [82] V. V. Parfenov and R. A. Nazipov, *Inorganic Materials* **38** (2002) 78–82.
- [83] Y. Yamada and T. Mitui, *J. Phys. Soc. Jpn.* **17** (1962) 1897.
- [84] H. Ohnishi and T. Teranishi, *J. Phys. Soc. Jpn.* **16** (1961) 35.
- [85] R. G. Kulkarni and V. Patil *J. Mater. Sci.* **14** (1979) 2221–2223
- [86] Ph. Tailhades, C. Villette, A. Rousset, G. U. Kulkarni, K. R. Kannan, C. N. R. Rao and M. Lenglet, *J. Solid State Chem.* **141**, (1998) 56–63.
- [87] J. Q. Qi, W. P. Chen, M. Lu, Y. Wang, H. Y. Tian, L. T. Li and H. L. W. Chan, *Nanotechnology* **16** (2005) 3097–3100.
- [88] J. Du, Z. Liu, W. Wu, Z. Li, B. Han and Y. Huang, *Mater. Res. Bull.* **40** (2005) 928–935.
- [89] S. Roy and J. Ghose, *J. Appl. Phys.* **87** (2000) 6626–6628.
- [90] D. Pajic, K. Zadro, R. E. Vanderberghe and I. Nedkov, *J. Magn Magn. Mater.* **281** (2004) 353–363.
- [91] S. Roy and J. Ghose, *J. Magn Magn. Mater.* **307** (2006) 32–37.
- [92] G. F. Goya, *J. Mater. Sci. Lett.* **16** (1997) 563–565.
- [93] G. F. Goya, H. R. Rechenberg and J. Z. Jiang, *J. Appl. Phys.* **84** (1998) 1101–1108.
- [94] J. Z. Jiang, G. F. Goya and H. R. Rechenberg, *J. Phys.: Condens. Matter* **11** (1999) 4063–4078.
- [95] S.J. Stewart, M.J. Tueros, G. Cernicchiaro and R.B. Scorzelli, *Solid State Comm.* **129** (2004) 347–351.
- [96] M. Bomio, P. Lavela and J. L. Tirado, *J. Solid State Electrochem.* **12** (2008) 729–737.
- [97] R. K. Selvan, C. O. Augustin, L. J. Berchmans and R. Saraswathi, *Mater. Res. Bull.* **38** (2003) 41–54.
- [98] D. Gingasu, I. Mindru, L. Patron, O. Carp, D. Matei, C. Neagoe and I. Balint, *J. Alloys Comp.* **425** (2006) 357–361.
- [99] T. Liu, L. Wang, P. Yang and B. Hu, *Materials Letters* **62** (2008) 4056–4058.
- [100] S.D. Sartale and C.D. Lokhande, *Mater. Chem. Phys.* **70** (2001) 274–284.

- [101] J. A. Gomes, M. H. Sousa, F. A. Tourinho, J. Mestnik-Filho, R. Itri and J. Depeyrot, *J. Magn Magn. Mater.* **289** (2005) 184–187.
- [102] S. J. Stewart, S. J. A. Figueroa, M. B. Sturla, R.B. Scorzelli, F. Garcia, and F. G. Requejo, *Physica B* **389** (2007) 155–158.
- [103] V. Krishnan, R. K. Selvan, C. O. Augustin, A. Gedanken and H. Bertagnolli, *J. Phys. Chem. C* **111** (2007) 16724–16733.
- [104] V. V. Parfenov and R. A. Nazipov, *Inorganic Materials* **38** (2002) 78–82.
- [105] R. A. Borzi, S. J. Stewart, G. Punte, R. C. Mercader, G. Cernichiaro and F. Garcia, *Hyperfine Interactions* **148/149** (2003) 109–116.
- [106] S. J. Stewart, R. C. Mercader, G. Punte, J. Desimoni, G. Cernichiaro and R. B. Scorzelli, *Hyperfine Interactions* **156/157** (2004) 89–95.
- [107] A. D. Al-Rawas, A. Rais, A. A. Yousif, A. M. Gismelseed, M. E. Elzain, S. Mazen and A. Al-Falaky, *J. Magn Magn. Mater.* **269** (2004) 168–175.
- [108] S.J. Stewart, M.J. Tueros, G. Cernicchiaro and R.B. Scorzelli, *Solid State Comm.* **129** (2004) 347–351.
- [109] R. K. Selvan, C. O. Augustin, M. I. Oshtrakh, O. B. Milder and V. A. Semionkin, *Hyperfine Interact* **165** (2005) 231–237.
- [110] S. Roy and J. Ghose, *J. Magn Magn. Mater.* **307** (2006) 32–37.
- [111] K. Shinagawa and Z. Simsa, *IEEE Trans. Mag.* **37** (2001) 2398.
- [112] K. J. Kim, J. H. Lee and S. H. Lee, *J. Magn Magn. Mater.* **279** (2004) 173–177.
- [113] M. Veis, V. Kolinsky, S. Visnovsky, P. D. Kulkarni, M. Desai, N. Venkataramani, S. Prasad and R. Krishnan, *J. Magn Magn. Mater.* **272–276** (2004) e885–e886.
- [114] S. Visnovsky, M. Veis, E. Liskova, V. Kolinsky, P. D. Kulkarni, N. Venkataramani, S. Prasad and R. Krishnan, *J. Magn Magn. Mater.* **290–291** (2005) 195–197.
- [115] M. Kucera, V. Kolinsky, S. Visnovsky, D. Chvostova, N. Venkataramani, S. Prasad, P. D. Kulkarni and R. Krishnan, *J. Magn Magn. Mater.* **316** (2007) e688–e691.
- [116] R. K Selvan, C.O. Augustin, C. Sanjeeviraja and D. Prabhakaran, *Solid State Comm.* **137** (2006) 512–516.
- [117] A. N. Patil, R. P. Mahajan and S. A. Patil, *Ind. J. Pure Appl. Phys.* **38** (2000) 651.
- [118] S. R. C. Murthy, S. Muhanty and J. Ghose, *Mater. Res. Bull.* **22** (1987) 1665.
- [119] S. A. Mazen, M.A. Ahmad and B. A. Sabrah, *Phys. Stat. Sol. A* **70** (1982) K71.
- [120] L. G. Antoshina and A. N. Goryaga, *Phys. Solid State* **43** (2001) 898–901.
- [121] C. V. G. Reddy, S. V. Manorama and V. J. Rao, *J. Mater. Sci. Lett.* **19** (2000) 775–778.
- [122] S. Tao, F. Gao, X. Liu and O. T. Sorensen, *Mater. Sci. Eng. B* **77** (2000) 172–176.
- [123] Z. Sun, L. Liu, D. Jia and W. Pan, *Sensors and Actuators B* **125** (2007) 144–148.
- [124] S. Kameoka, T. Tanabe and A. P. Tsai, *Catalysis Letters* **100** (2005) 89–93.
- [125] M. H. Khedr, A. A. Farghali, *Applied Catalysis B: Environmental* **61** (2005) 219–226.
- [126] T. Liu, L. Wang, P. Yang and B. Hu, *Materials Letters* **62** (2008) 4056–4058.
- [127] H. C. Shin, S. C. Choi, K. D. Jun and S. H. Han, *Chem. Mater.* **13** (2001) 1238–1242.
- [128] Y. N. NuLi, Q. Z. Qin, *J. Power Sources* **142** (2005) 292.

- [129] K. Faungnawakij, Y. Tanaka, N. Shimoida, T. Fukunaga, R. Kikuchi, and K. Eguchi, *Appl. Catal., B* **74** (2007) 144.
- [130] G. Zhang, J. Qu, H. Liu, A. T. Cooper and R Wu, *Chemosphere* **68** (2007) 1058.
- [131] G. Srinivasan, B. U. M. Rao, J. Zhao and M. S. Seehra, *Appl. Phys. Lett.* **59** (1991) 372-374.
- [132] M. M. Ibrahim, M. S. Seehra and G. Srinivasan, *J. Appl. Phys.* **75** (1994) 6822.
- [133] C. Baubet, Ph. Tailhades, C. Bonningue, A. Rousset and Z. Simsa, *J. Phys. Chem. Solids* **61** (2000) 863–867.
- [134] M. Desai, S. Prasad, N. Venkataramani, I. Samajdar, A. K. Nigam and R. Krishnan, *J. Magn. Magn. Mater.* **246** (2002) 266–269.
- [135] M. Desai, S. Prasad, N. Venkataramani, I. Samajdar, A. K. Nigam, and R. Krishnan, *IEEE Trans Mag.* **38** (2002) 3012.
- [136] M. Desai, S. Prasad, N. Venkataramani, I. Samajdar, A. K. Nigam and R. Krishnan, *J. Appl. Phys.* **91**(2002) 2220- 2227.
- [137] P. D. Kulkarni, M. Desai, N. Venkataramani, S. Prasad and R. Krishan, *J. Magn. Magn. Mater.* **272–276** (2004) e793–e794.
- [138] E. Mugnier, I. Pasquet, A. Barnabe', L. Presmanes, C. Bonningue and P. Tailhades, *Thin Solid Films* **493** (2005) 49–53.
- [139] M. Ahmad, M. Desai and R. Khatirkar, *J. Appl. Phys.* **103** (2008) 013903.
- [140] A. Yanga, Z. Chen, X. Zuo, D. Arena, J. Kirkland, C. Vittoria and V. G. Harris, *Appl. Phys. Lett.* **86** (2005) 252510.
- [141] A. Yang, X. Zuo, L. Chen, Z. Chen, C. Vittoria, and V. G. Harris, *J. Appl. Phys.* **97** (2005) 10G107.
- [142] X. Zuo, A. Yang, C. Vittoria, and V. G. Harris, *J. Appl. Phys.* **99** (2006) 08M909.
- [143] K. E. Kuehn, D. Sriram, S. S. Bayya, J. J. Simmins and R. L. Snyder, *J. Mater. Res.* **15** (2000) 1635 – 1641.
- [144] H. Chen and C. Yang, *Scandinavian J. Metallurgy* **30** (2001) 238–241.
- [145] A. E. Baranchikov, V. K. Ivanov, G. P. Murav'eva, N. N. Oleinikov and Yu. D. Tretyakov, *Doklady Chemistry* **397** (2004) 146–148.
- [146] D. K. Xia and C. A. Pickles, *Metal. Mater. Trans. B* **28B** (1997) 671-677.
- [147] S. Bera, A. A. M. Prince, S. Velmurugan, P. S. Raghavan, R. Gopalan, G. Panneerselvam and S. V. Narasimhan, *J. Mater. Sci.* **36** (2001) 5379 – 5384.
- [148] W. Schiessl, W. Potzel, H. Karzel, M. Steiner, G. M. Kalvius, A. Martin, M. K. Krause, I. Halevy, J. Gal, W. Schafer, G. Will, M. Hillberg and R. Wappling, *Phys. Rev. B* **53** (1996) 9143.
- [149] J. F. Hochepped, P. Bonville, and M. P. Pileni, *J. Phys. Chem. B* **104** (2000) 905-912.
- [150] C. Yao, Q. Zeng, G. F. Goya, T. Torres, J. Liu, H. Wu, M. Ge, Y. Zeng, Y. Wang and J. Z. Jiang, *J. Phys. Chem. C* **111** (2007) 12274-12278.
- [151] L. D. Tung, V. Kolesnichenko, G. Caruntu, and D. Caruntu. *Physica B* **319** (2002) 116-121.
- [152] X. Chu, X. Liu and G. Meng, *Sens. Actuators, B* **55** (1999) 19.
- [153] B. H. Sohn and R. E. Cohen, *Chem. Mater.* **9** (1997) 264.
- [154] S. Sun and C. B. Murray, *J. Appl. Phys.* **85** (1999) 4325-4330.

- [155] K Tanaka, M. Makita, Y. Shimizugawa, K. Hirao and N. Soga, *J. Phys. Chem. Solids* **59** (1998) 1611–1618.
- [156] Y. T. Pavljukhin, Y. Y. Medikov and V. V. Boldyrev, *Mater. Res. Bull.* **18** (1983) 1317–1327.
- [157] T. Sato, K. Haneda, M. Seki and T. Iijima, *Appl. Phys. A* **50** (1990) 13–16.
- [158] T. M. Clark and B. J. Evans, *IEEE Trans. Magn.* **33** (1997) 3745–3747.
- [159] Y. Zhihao and Z. Lide, *Mater. Res. Bull.* **33** (1998) 1587–1592.
- [160] J. A. Toledo-Antonio, N. Nava, M. Martinez and X. Bokhimi, *Appl. Catal. A: General* **234** (2002) 137–144.
- [161] A. Kundu, C. Upadhyay and H.C. Verma, *Phys. Lett. A* **311** (2003) 410–415.
- [162] Y. Ahn, E. J. Choi, S. Kim, D. H. An, K. U. Kang, B-G. Lee, K. S. Baek and H. N. Oak, *J. Korean. Phys. Soc.* **41** (2002) 123–128.
- [163] I. H. H. Hamdeh, J. C. Ho, S. A. Oliver, R. J. Willey, G. Oliveri and G. Busca, *J. Appl. Phys.* **81** (1997) 1851–1857.
- [164] J. Plocek, A. Hutlova, D. Niznansky, J. Bursik, J.-L. Rehspringer, and Z. Micka, *J. Non-Cryst. Solids* **315** (2003) 70–76.
- [165] P. Cheng, W. Li, T. Zhou, Y. Jin and M. Gu, *J. Photochem. Photobio. A: Chem.* **168** (2004) 97–101.
- [166] F. S. Li, L. Wang, J. B. Wang, Q. G. Zhou, X. Z. Zhou, H.P. Kunkel and G. Williams, *J. Magn. Mater.* **268** (2004) 332–339.
- [167] C. Gong, D. Chen and X. Jiao, *J. Sol-Gel Sci. Tech.* **35** (2005) 77–82.
- [168] M. Atif, S. K. Hasanain and M. Nadeem, *Solid State Comm.* **138** (2006) 416–421.
- [169] F. Li, H. Wang, L. Wang and J. Wang, *J. Magn. Mater.* **309** (2007) 295–299.
- [170] S. Komarneni, M. C. D'Arrigo, C. Leonelli, G. C. Pellacani and H. Katsuki, *J. Am. Ceram. Soc.* **81** (1998) 3041–3043.
- [171] J. C. Ho, H. H. Hamdeh, Y. Y. Chen, S. H. Lin, Y. D. Yao, R. J. Willey and S. A. Oliver, *Phys. Rev. B* **52** (1995-II) 10122–10126.
- [172] G. F. Goya and H. R. Rechenberg, *J. Magn. Mater.* **196-197** (1999) 191–192.
- [173] G. F. Goya, H. R. Rechenberg, M. Chen and W. B. Yelon, *J. Appl. Phys.* **87** (2000) 8005–8007.
- [174] C. N. Chinnasamy, A. Narayanasamy, N. Ponpandian, K. Chattopadhyay, H. Guerault and J-M. Greneche, *J. Phys.: Condens. Matter* **12** (2000) 7795–7805.
- [175] F. J. Burghart, W. Potzel, G.M. Kalvius, E. Schreier, G. Grosse, D.R. Noakes, W. Schafer, W. Kockelmann, S.J. Campbell, W.A. Kaczmarek, A. Martin, and M.K. Krause, *Physica B* **289-290** (2000) 286–290.
- [176] S. Bid and S.K. Pradhan, *Mater Chem. Phys.* **82** (2003) 27–37.
- [177] H. Ehrhardt, S. J. Campbell and M. Hofmann, *Scripta Materialia* **48** (2003) 1141–1146.
- [178] S. D. Shenoy, P. A. Joy and M. R. Anantharaman, *J. Magn. Mater.* **269** (2004) 217–226.
- [179] M. Hofmann, S. J. Campbell, H. Ehrhardt and R. Feyerherm, *J. Mater. Sci.* **39** (2004) 5057–5065.
- [180] S. Ozcan, B. Kaynar, M. M. Can and T. Firat, *Mater Sci Eng. B* **121** (2005) 278–281.
- [181] V. Berbenni, C. Milanese, G. Bruni, A. Marini and I. Pallecchi, *Thermochimica Acta* **447** (2006) 184–189.
- [182] J. H. Shim, S. Lee, J. H. Park, S-J. Han, Y. H. Jeong, and Y. W. Cho, *Phys. Rev. B* **73** (2006) 064404.

- [183] H. M. Widatallah, I. A. Al-Omari, F. Sives, M. B. Sturla and S. J. Stewart, *J. Magn. Magn. Mater.* **320** (2008) e324–e326.
- [184] S. Ammar, N. Jouini, F. Fievet, Z. Beji, L. Smiri, P. Moline, M. Danot and J. Greneche, *J. Phys.: Condens. Matter* **18** (2006) 9055–9069.
- [185] Z. Jiao, M. Wu, J. Gu and Z. Qin, *IEEE Sensors J.* **3** (2003) 435–438.
- [186] A. Kundu, S. Anand and H.C. Verma, *Powder Technology* **132** (2003) 131–136.
- [187] M. K. Roy, B. Haldar and H C Verma, *Nanotechnology* **17** (2006) 232–237.
- [188] H. Xue, Z. Li, X. Wang, and X. Fu, *Mater. Lett.* **61** (2007) 347–350.
- [189] J.M. Yang and F.S. Yen, *J. Alloys and Comp.* **450** (2008) 387–394.
- [190] I. Mohai, J. Szepvolgyi, I. Bertoti, M. Mohai, J. Gubicza and T. Ungar, *Solid State Ionics* **141–142** (2001) 163–168.
- [191] C. Yao, Q. Zeng, G. F. Goya, T. Torres, J. Liu, H. Wu, M. Ge, Y. Zeng, Y. Wang, and J. Z. Jiang, *J. Phys. Chem. C* **111** (2007) 12274–12278.
- [192] J. Jung, Y. Jung, E. Kim, S. Min, J. Jun, L. M. Malkinski Y. Barnakov, L. Spinu and K. Stokes, *IEEE Trans. Magn.* **41** (2005) 3403.
- [193] A. Yan, X. Liu, R. Shi, N. Zhang, R. Yi, Y. Li, G. Gao, and G. Qiu, *Solid State Comm.* **146** (2008) 483–486.
- [194] A. Yan, X. Liu, R. Yi, R. Shi, N. Zhang, and G. Qiu, *J. Phys. Chem. C* **112** (2008) 8558–8563.
- [195] W. Jiang, Z. Cao, R. Gu, X. Ye, C. Jiang and X. Gong, *Smart Mater. Struct.* **18** (2009) 125013.
- [196] P. Y. Lee, H. Suematsu, T. Nakayama, W. Jiang and K. Niihara *J. Magn. Magn. Mater.* **312** (2007) 27–31.
- [197] M. Sivakumar, T. Takami, H. Ikuta, A. Towata, K. Yasui, T. Tuziuti, T. Kozuka, D. Bhattacharya and Y. Iida, *J. Phys. Chem. B* **110** (2006) 15234–15243.
- [198] Z. Cvejic, S. Rakic, S. Jankov, S. Skuban and A. Kapor, *J. Alloys Comp.* **480** (2009) 241–245.
- [199] M. Thomas and K. C. George, *Indian J. Pure & Appl. Phys.* **47** (2009) 81–86.
- [200] S-H. Yu, T. Fujino and M. Yoshimura, *J. Magn. Magn. Mater.* **256** (2003) 420–424.
- [201] C. N. Chinnasamy, A. Narayanasamy, N. Ponpandian and K. Chattopadhyay, *Mater. Sci. Eng. A* **304–306** (2001) 983.
- [202] C. N. Chinnasamy, A. Narayanasamy, N. Ponpandian, K. Chattopadhyay, H. Guerault and J-M. Greneche, *Scripta Mater.* **44** (2001) 1407.
- [203-a] K. Tanaka, S. Nakashima, K. Fujita and K. Hirao, *J. Phys.: Condens. Matter* **15** (2003) L469.
- [203-b] S. Capdeville, P. Alphonse, C. Bonningue, L. Presmanes, and Ph. Tailhades, *J. Appl. Phys.* **96** (2004) 6142.
- [204] V. Sepelak, S. Wißmann and K. D. Becker, *J. Mater. Sci.* **33** (1998) 2845.
- [205] J. Z. Jiang, P. Wynn, S. Morup, T. Okada and F. J. Berry, *Nanostruct. Mater.* **12** (1999) 737.
- [206] S. A. Oliver, H. H. Hamdeh and J. C. Ho, *Phys. Rev. B* **60** (1999) 3400.
- [207] W. Potzel, W. Schafer and G. M. Kalvius, *Hyperfine Interactions* **130** (2000) 241.
- [208] H. Ehrhardt, S. J. Campbell and M. Hofmann, *J. Alloys Compd.* **339** (2002) 255.
- [209] P. Druska, U. Steinike and V. Sepelak, *J. Solid State Chem.* **146** (1999) 13.
- [210] W. Schafer, W. Kockelmann, A. Kirfel, W. Potzel, F. J. Burghart, G. M. Kalvius, A. Martin, W. A. Kaczmarek and S. J. Campbell, *Mater. Sci. Forum* **321–324** (2000) 802.

- [211] B. Jeyadevan, K. Tohji and K. Nakatsuka, *J. Appl. Phys.* **76** (1994) 6325.
- [212] S. A. Oliver, V. G. Harris, H. H. Hamdeh and J. C. Ho, *Appl. Phys. Lett.* **76** (2000) 2761.
- [213] X. Li, G. Lu and S. Li, *J. Alloys Comp.* **235** (1996) 150-155.
- [214] D. Sibera1, U. Narkiewicz, N. Guskos and G. Żolnierkiewicz, *J. Phys.: Conference Series* **146** (2009) 012014.
- [215] S. Ammar, N. Jouini, F. Fievet, O. Stephan, C. Marhic, M. Richard, F. Villain, C. Cartier, S. Brice and P. Sainctavit, *J. Non-Cryst. Solids* **245/246** (2004) 673.
- [216] Bluncson, G. K. Thompson and B. J. Evans, *Hyperfine Interact.* **90** (1994) 353.
- [217] T. Kamiyama, K. Haneda, T. Sato, S. Ikeda and H. Asano, *Solid State Comm.* **81** (1992) 563.
- [218] N. Wakiya, K. Muraoka, T. Kadowaki, T. Kiguchi, N. Mizutani, H. Suzuki and K. Shinozaki, *J. Magn. Magn. Mater.* **310** (2007) 2546–2548.
- [219] Y. Zhihao and Z. Lide, *Mater. Res. Bull.* **33** (1998) 1587–1592.
- [220] X. Niu, W. Du and W. Du, *Sensors and Actuators B* **99** (2004) 405–409.
- [221] M. Pineda, J. M. Palacios, E. Garcia, C. Cilleruelo and J. V. Ibarra, *Fuel* **76** (1997) 567-573.
- [222] N. Ikenaga, Y. Ohgaito, H. Matsushima and T. Suzuki, *Fuel* **83** (2004) 661–669.
- [223] C. S. Xavier, R. A. Candeia, M. I. B. Bernardi, S. J. G. Lima, E. Longo, C. A. Paskocimas, L. E. B. Soledade, A. G. Souza and I. M. G. Santos, *J. Thermal Analysis Calorimetry* **87** (2007) 709–713.
- [224] S. Nakashima, K. Fujita, K. Tanaka and K. Hirao, *J. Phys.: Condens. Matter* **17** (2005) 137–149.
- [225] K. Tanaka, S. Nakashima, K. Fujita and K. Hirao, *J. Appl. Phys.* **99** (2006) 106103.
- [226] S. Nakashima, K. Fujita, K. Tanaka, K. Hirao, T. Yamamoto and I. Tanaka, *J. Magn. Magn. Mater.* **310** (2007) 2543–2545.
- [227] S. Nakashima, K. Fujita, K. Tanaka, K. Hirao, T. Yamamoto and I. Tanaka, *Phys. Rev. B* **75** (2007) 174443.
- [228] S. Nakashima, K. Fujita, A. Nakao, K. Tanaka, Y. Shimotsuma, K. Miura and K. Hirao, *Appl. Phys. A* **94** (2009) 83–88.
- [229] S. B. Ogale and R. Nawathey, *J. Appl. Phys.* **65** (1989) 1367-1369.
- [230] D. Ravinder, *Bull. Mater. Sci.* **22** (1999) 765-768.
- [231] M. Sorescu, L. Diamandescu, R. Swaminathan, M. E. McHenry and M. Feder, *J. Appl. Phys.* **97** (2005) 10G105.
- [232] M. Bohra, Shiva Prasad, N. Kumar, D. S. Misra, S. C. Sahoo, N. Venkataramani and R. Krishnan, *Appl. Phys. Lett.* **88** (2006) 262506.
- [233] Y. F. Chen, D. Spoddig and M. Ziese, *J. Phys. D: Appl. Phys.* **41** (2008) 205004.
- [234] H. Yahiro, H. Tanaka, Y. Yamamoto and T. Kawai, *Solid State Comm.* **123** (2002) 535–538.

CHAPTER-2

Experimental Techniques and Procedures

This chapter deals with the experimental techniques of material synthesis and property measurements

2.1 Material Preparation methods

The method of material preparation plays a very important role in determining the chemical, structural, electrical and magnetic properties of spinel ferrites. Magnetic ferrites MFe_2O_4 (where M: Cu, Zn and their mixture) were prepared by different physical and chemical methods. These include ceramic method (solid state reaction) for bulk samples, chemical methods (coprecipitation) for nanoparticle samples, and deposition methods (RF-magnetron sputtering) for nanocrystalline thin film samples.

2.1.1 Ceramic processing of spinel ferrites (bulk form)

The most widely used method for the preparation of bulk oxides is by reaction of solid components in the correct molar proportion at elevated temperature over a long period. The preparation of materials by this method requires the care to avoid excess quantity of reagents as this method involves treatment of the whole lattice and the material cannot be purified after the synthesis [1].

2.1.1.1 Reaction mechanism

The knowledge of the reaction mechanism for spinel ferrites is necessary to understand the behavior of oxide mixtures during calcination or sintering. The spinel phase reaction $MO + Fe_2O_3 = MFe_2O_4$ is formed at the interface of MO and Fe_2O_3 by *counter-diffusion* of the cations M^{2+} and Fe^{3+} in the ratio 3:2 through practically rigid lattice of oxygen anions (Figure

2.1). In this reaction, the flux of the cations is coupled to maintain electro-neutrality. This reaction may also be accompanied by release or absorption of oxygen at the interface between oxide and ferrite [2–4].

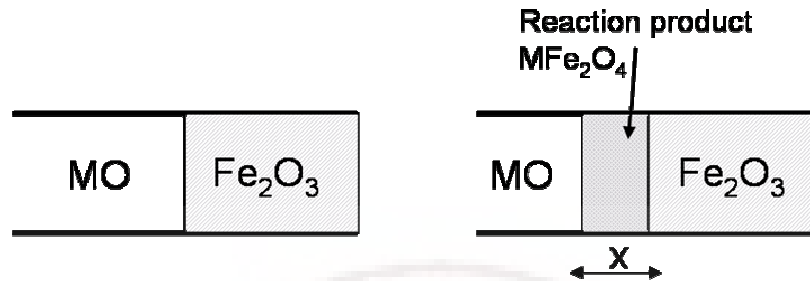


Figure 2.1: Schematic drawing of solid-state reaction in spinel ferrite.

In practice the diffusion coefficients of the ions differ widely. In spinel ferrites, diffusion of the large O²⁻ ions is rather slow when compared to cationic diffusion so that the most likely mechanism is the *counter-diffusion* of cations. The reaction between ZnO and Fe₂O₃ to form ZnFe₂O₄ is reported to occur by the counter-diffusion mechanism in which the cations Zn²⁺ and Fe³⁺ migrate in opposite directions and the oxygen ions remain essentially stationary [4]. Same mechanism is applicable for CuFe₂O₄.

Preparation process of bulk ferrite can be achieved by adjusting four major steps. These steps are powder preparation, pressing powder into a pellet, sintering and finishing or machining [5]. Sintering is the final and the most critical step. A brief discussion of sintering process is given below.

2.1.1.2 Sintering process

When a compacted powder is heated at an elevated temperature which is below the melting point, powder particles fuse together, voids between the particles decrease, and eventually a dense solid body is obtained. This phenomenon is called *sintering process* [6]. Sintering process has been used and still a very important process for producing ceramic materials.

The driving force of sintering is the excess surface free energy of a powder compact. When heated, system tries to decrease its surface free energy by decreasing its total surface area. This is reached by mass transport that joins the powder particles together. There is a chemical potential difference between surfaces of dissimilar curvature within the system. A concave

surface has a negative free energy and a convex surface a positive free energy. As a consequence, mass transport occurs from the particle surface (convex) to the inter-particle necks or pores (concave) (figure 2.2). The greater the curvature, i.e., the finer the particles, the greater the driving force sintering [2]. During sintering, mass transport can occur by solid-state, liquid-phase and vapor-phase mechanisms individually, or in combination.

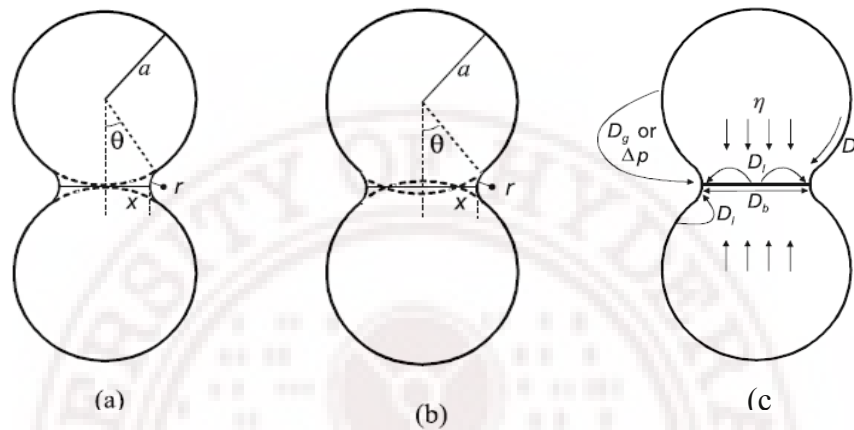


Figure 2.2: Two-particle model for initial stage sintering (a) without shrinkage and (b) with shrinkage. (c) Material transport paths during sintering process [6, 7].

The development of microstructures during sintering may be distinguished in three stages (Figure 2-3) [2, 3]

Initial stage: Initially, material is transported from higher-energy convex particle surfaces to the lower-energy concave intersections between adjacent particles to form necks (“neck growth”). The powder particles fuse together and the area of contact increases gradually. Since mass is only transported from convex to concave areas, the total pore volume and the distance between the particle centers remain about constant, and shrinkage of the green body is only about 3 - 5%. In this stage, the relative density, which is the density of the powder compact, is about 50 – 60% of its theoretical density (Figure 2.3).

Intermediate stage: In this stage, interparticle necks grow, the area of grain boundaries (the interface plane shared by two grains) increases, interparticle contacts flatten, and the pore diameters decrease. The distance between the particle centers and the volume of compact decreases (shrinkage of 5% to 20%), i.e. densification occurs. The density increases to about 95% of its theoretical X-ray density value.

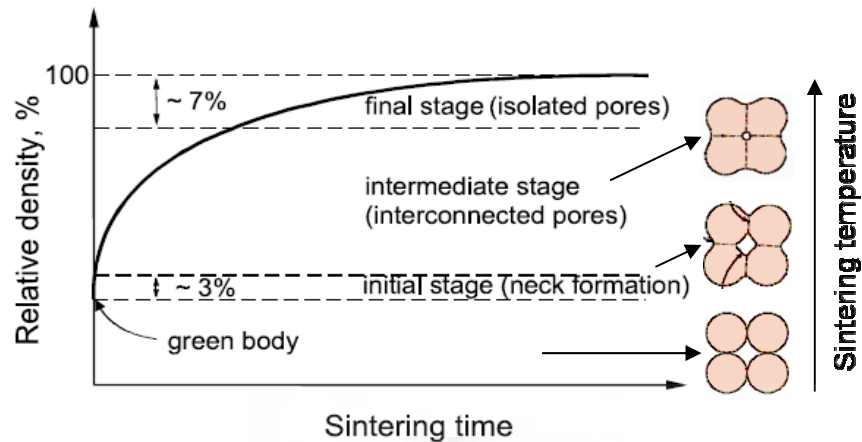


Figure 2.3: Schematic diagram showing the densification curve of a powder compact and the three sintering stages. A two-dimensional sphere model illustrating the first two stages during sintering [7, 8].

Final stage: When the relative density increases above 0.95, isolated spherical pores remain only at triple points (intersection lines where three grains meet) or inside the grain matrix. In the final stage, these pores are gradually eliminated and the relative density increases further.

The most important powder physical characteristics that can affect sintering are particle size, particle packing, and particle shape [2, 3].

Particle size: Material transport occurs faster over shorter distances, and less material needs to be transported to fill small pores. Furthermore, very fine particles have high surface energies. Therefore, smaller powder particles speed up the sintering process and lower the sintering temperatures and pressure. Due to the thermodynamic considerations, larger grains grow at the expense of smaller ones. Consequently, as sintering progresses, the average size of the grains increases (“coarsening”), and the size distribution becomes narrower. Since coarsening is much slower than sintering, grain growth can occur especially in the final stage.

Particle packing: Improved particle packing increases the number of contact points between adjacent particles and the relative density of the compact. Consequently, densification occurs faster (better material transport) and with less volume. One of the most important reasons for non-particle packing is the formation of aggregates.

Particle shape: Irregular-shaped particles, which have high surface area to volume ratio, have a higher driving force for densification and sinter faster than equiaxed particles. Particles that pack poorly sinter poorly.

2.1.1.3 Bulk Sample preparation

The bulk ferrite samples of $\text{Cu}_{1-x}\text{Zn}_x\text{Fe}_2\text{O}_4$ ($0 \leq x \leq 1$) were prepared by utilizing traditional solid state reaction method. The starting materials were high purity (99.9%) of Zinc (II) Oxide (ZnO), Copper (II) oxide (CuO) and Iron (III) oxide (Fe_2O_3). The sequence of the preparation procedure is as follows:

The oxide powders (CuO, ZnO and Fe_2O_3) were weighed as per required stoichiometric percentage. The powders were mixed thoroughly using agate mortar and pestle to yield a homogeneous powder. The oxide mixture showed a characteristic red color. The mixture was calcined in air at 750 °C for 12 hr followed by furnace cooling to form partial ferrite phase.

The calcining reaction itself is critical to the future properties of the ferrite because it determines the reactivity of the powder and the final shrinkage in the subsequent sintering step [9]. The result of the calcining process is a powder that is grounded further to homogenize its composition and improve reactivity by having a uniform small particle size.

It is necessary to provide the binding force among the calcined particles in order to make a green ceramic pellet of ferrite. The calcined ferrite powder and approximately 1.5 wt % of polyvinyl alcohol (PVA) were mixed together in the mortar. After granulating the mixture with a spatula and pestle about 2 gms of powder was used for making a single pellet. The ferrite powder was pressed using a cold uniaxial hydraulic press for 3 minutes to produce a green ceramic pellet with a diameter of 13 mm.

Finally, the green color pellets were placed in furnace and heated slowly until a temperature of 500 °C at which most of PVA decomposition was reached. After 3 hours of hold at 500°C, the temperature was raised to 1000 °C. After 12 hours of sintering, the samples were furnace cooled to room temperature by switching off the furnace. The sintering process is the most critical step. If carefully executed, it provides certain amount of bonding between the particles and yields the desired crystal structure, oxidation state, microstructure and physical properties of ferrites [5]. Some copper ferrite samples were quenched from high temperature to room temperature in air to study the effect of quenching on its structure and magnetic properties. Figure 2.4 shows the flow chart of the ceramic processing of bulk $\text{Cu}_{1-x}\text{Zn}_x\text{Fe}_2\text{O}_3$.

Solid state reaction method

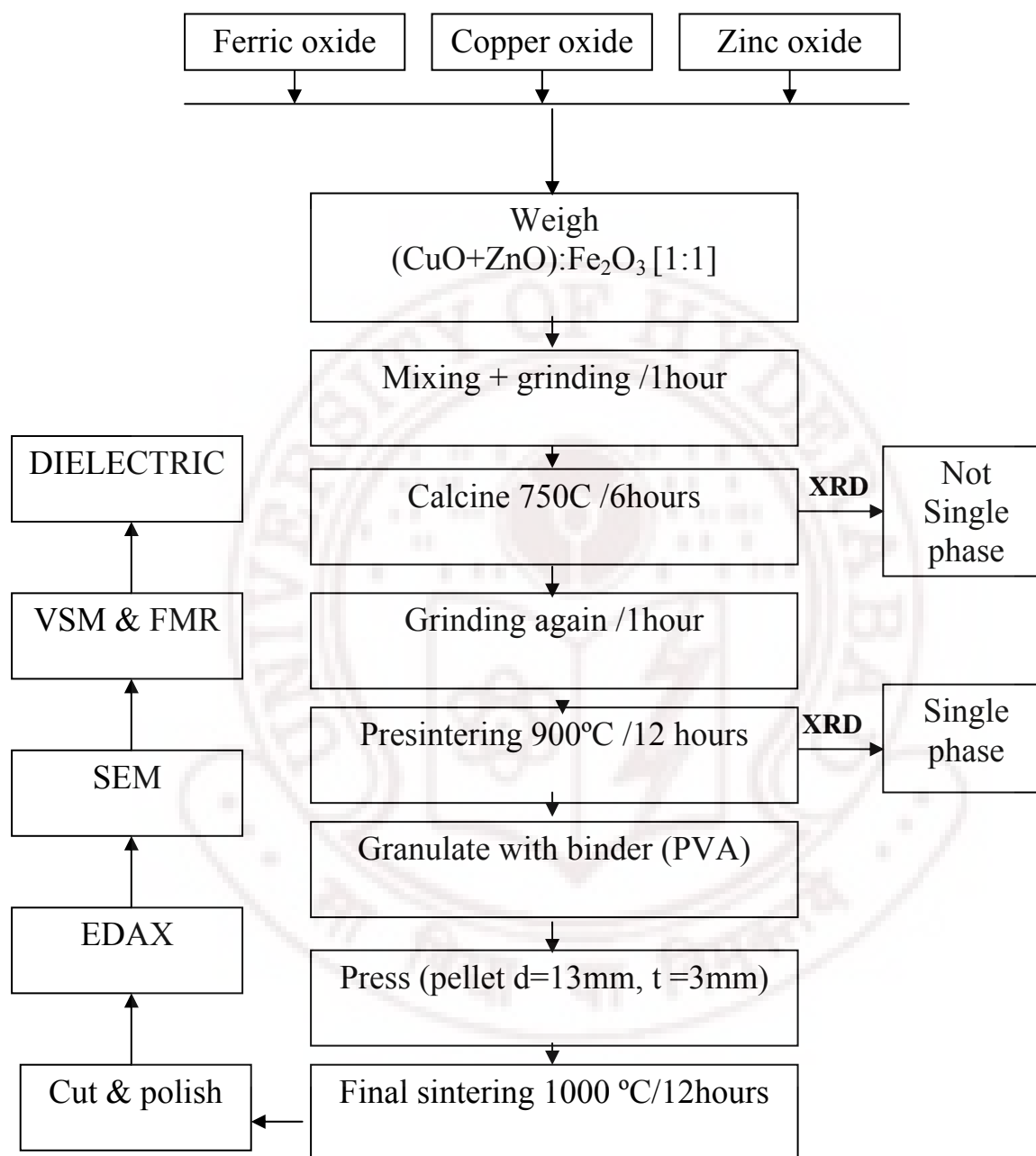


Figure 2.4: flow chart for conventional ceramic processing of bulk $\text{Cu}_{1-x}\text{Zn}_x\text{Fe}_2\text{O}_4$

2.1.2 Synthesis of Cu-Zn ferrite nanoparticles

Nanoparticles of spinel-ferrites offer great advantages and applications in many important areas. Decreasing the size of the particles to nanometer size (less than 100 nm) leads to increase in the surface-to-volume ratio which in turn strongly influences the physical and chemical properties of these materials [10]. Nanosized oxides give higher sintered density at relatively lower sintering temperatures, without considerable grain growth [11]. An ideal synthesis of nanocrystals has to provide the desired particle sizes over the largest possible range, narrow size distributions, high crystallinity, control of shape, and desired surface properties [12]. In the synthesis of nanoferrites, the precursors play a very important role [13]. The use of a particular precursor may affect the materials' structure on a molecular level. Using appropriate precursors ensures the homogeneity and the highly dispersed state of the resultant material.

Several methods are used for the synthesis of nanosized spinel-type oxides especially the ferrite materials, in view of the potential applications of these nanosized materials in different technological areas, as well as to study the intriguing properties of the nanomaterials [13-15]. Synthesis techniques for the preparation of ferrite nanoparticles can be basically divided into the chemical, mechanical and physical methods. Chemical techniques starting from atomic or molecular precursors are mainly focused on the coprecipitation, sol-gel technique, polymeric precursor method from organometallic complex, microemulsion processing, and hydrothermal synthesis. The physico-chemical methods are mainly focused on spray pyrolysis, gas condensation, freeze-drying and ultrasonic methods, which can have significant importance in the preparation of nanostructured ceramic materials [13-18].

The important methods used to prepare spinel ferrite nanoparticles especially the coprecipitation method used to synthesized Cu-Zn ferrites are described below.

2.1.2.1 Ball Milling

Ball milling is a mechanical alloying method used to manufacture oxide by vigorous mixing of the starting powder material and milling balls in a vial for several hours [19, 20]. The vigorous shaking action permits the starting material caught between milling balls to be crushed during collision of the balls. The repetitive collision generates enough energy to produce non-equilibrated nanostructures, usually in an amorphous or quasi-crystalline state

[21]. This technique has been employed to synthesize several magnetic spinel ferrites such as ZnFe_2O_4 [22, 23]. Mechanical methods based on mechanical attrition, grinding and milling lead to the formation of highly phase-dispersed materials typical for metal powders or oxide based materials (mechanical activation) or the formation of new products because of a solid-state reaction (mechanochemical synthesis) [24]. Although this is a method that can produce large quantities of nanomaterials with cost efficiency, it lacks the ability to produce monodispersed and crystalline magnetic nanoparticles.

2.1.2.2 Sonochemical Method

Sonochemical process uses ultrasound to assist or enhance a chemical reaction. Nanoparticles can be produced using sonochemical methods that involve the process of cavitation [25]. Cavitation is best described as the formation, growth, and collapse of bubbles. When acoustic waves are introduced in liquids, the decompression cycle of the acoustic waves can generate bubbles [26]. During the decompression or expansion cycle, negative pressure exerted on the liquid pulls molecules apart and eventually exceeds the local tensile strength of the liquid creating a cavity or bubble. Bubbles then grow in the decompression phase by absorbing energy from the acoustic radiation. Once bubbles have grown to a critical size (varies with different liquid), they can no longer efficiently absorb energy and this allows the surrounding liquid to enter the bubble (compression) causing it to implode. During the implosion or collapse of these bubbles, a short-lived hot spot can be generated.

2.1.2.3 Sol-gel process

The synthesis of oxide nanoparticles by this procedure is based upon the hydrolysis and condensation of metal alkoxide $\text{M}(\text{OR})_n$, where M is the metal, O is the oxygen and R is the organic group [27]. Since the metal alkoxide and water are not soluble in each other, they are required to be dissolved in a common alcoholic solvent in order to carry out their reaction. The solution is then mixed with water, which causes gelation due to hydrolysis of the alkoxides into a branched network. With the sol-gel method it is possible to achieve mixing at the atomic level and homogeneous materials can be achieved. The high reactivity of water with the metal alkoxide is explained by that the alkoxide group, being highly electronegative, creates a positive charge on the central metal atom. On the other hand, in the water molecule,

there exists a partial negative charge on the oxygen atom. As a result, the water molecule attacks the metal atom from the alkoxide and results in the hydrolysis of the alkoxide [28].

During the synthesis, two equal parts of alcoholic solutions are made. In one part, water and an organic polymer as a surfactant are dissolved in appropriate proportions in the alcoholic solvent. The second part of the alcoholic solution is prepared by dissolving completely the metal alkoxide in the common solvent. After homogenizing both the solutions, they are mixed rapidly. The order of mixing the two solutions does not affect the properties of the reaction product. The process is carried out in a dry-nitrogen glove box to avoid any premature reaction of atmospheric moisture with the alkoxide. The following reactions immediately take place upon mixing the two parts of the solutions [27, 28]



Here M represents the metal atom, R is the alkoxide group and O is the oxygen atom. The result is the formation of the M–O–M bond within the solution. The kinetics of hydrolysis and condensation reactions is governed mainly by the ratio of molar concentrations of water to alkoxide (*R*). In general, low *R* values (<3) are suitable for fiber and thin-film formation while large *R* values (>3) generate powder particles. The oxide nanoparticle size and its distribution and particle surface morphology are hence affected by this *R* value [28].

The high degree of mixing allows the precursor to form the required crystal phase during calcination at a very low temperature and high surface areas can therefore be achieved. However, it is important that the rate of hydrolysis of the different metal alkoxides match. Otherwise inhomogeneities will be formed, which might lead to phase segregation and lowering of surface area of the final material. Although the sol-gel method is very powerful for the preparation of materials with high surface area, it presents some drawbacks. The alkoxide precursors are expensive and often require moisture and oxygen-free atmosphere during synthesis [29]. This complicates the possibility of industrial scale-up.

2.1.2.4 Microemulsion

Microemulsion is defined as a system of single-phase and thermodynamically stable isotropic solution composed of water, oil and surfactant that brings down the water/oil interfacial tension to a very low value [30]. The process of microemulsion to produce nanoparticles is unique in the sense that it can produce monodispersed particles and has capability to control not only the size but also the shape of the nanoparticles [28]. The internal structure of a microemulsion, at a given temperature, is determined by the ratio of its constituents. If the concentration of oil is low, a microemulsion with a continuous water phase can be formed, a so-called oil-in-water (o/w) microemulsion. If more oil is added a bi-continuous phase, which has no defined shape, will be formed. If oil is continued to be added until the water concentration becomes low, water-in-oil (w/o) microemulsion can eventually be formed. The surfactant molecules in o/w and w/o microemulsions arrange themselves to form clearly defined shapes (often spherical) called micelles [31]. The micelles can host water droplets. Every microemulsion system has a certain region where the concentration of the components is right to form a microemulsion [32].

2.1.2.5 The Hydrothermal Method

A hydrothermal process is an effective approach to obtain highly crystalline ferrites from aqueous solutions, eliminating the annealing step, consists of heating the reaction mixture in a sealed container at moderate temperatures [16, 33 Byrappa]. In such conditions, a high pressure is built up inside the bomb-type reactor, thereby increasing the temperature of the solution high enough to promote the chemical reactions between the precursors and to produce ferrite powders with good crystallinity. As the pressure inside the reaction vessel increases, significant changes on the physical properties of the solvent are observed over a wide temperature interval. Thus, the polarity and density of the water decrease, whereas its temperature increases rapidly to reach values much higher than the boiling point. Additionally, its solvent properties are greatly enhanced, thereby enabling the complete dissolution of various compounds, both organic and inorganic, which otherwise have a sparse solubility in aqueous media. Finally, when the temperature and pressure attain the so-called “critical values” ($T_C = 374\text{ }^{\circ}\text{C}$, $P_C = 218\text{ atm}$), the dissimilarities between the gaseous and liquid phases disappear completely and a new phase known as supercritical water is formed.

In the supercritical state, water combines the individual characteristics of the liquid and gas phases making it very attractive as reaction medium for various chemical reactions. However, such a behavior is not restricted only to water; other many nonaqueous solvents can serve as reaction media under similar conditions. Thus, when the chemical reactions take place in aqueous solutions the process is known as hydrothermal, whereas for non-aqueous solvents the technique is called solvothermal. Under such extreme conditions, chemical reactions can occur in both sub-critical and super-critical regime, thereby resulting into highly crystalline single-phase products which do not necessitate post-synthesis annealing [18, 26]. However, although the hydrothermal/solvothermal process is a one-pot, highly efficient “green-chemistry” preparative route for various ferrite materials, it allows only for a limited control of the nucleation and growth processes usually yielding particles with irregular shapes, relatively large sizes and a wide size distribution. Yu and coworkers [34] noted that hydrothermal heating at 180°C of an ammoniacal FeCl₂ solution containing metallic Zn leads to the formation of octahedrally-shaped ZnFe₂O₄ nanoparticles with an average size of 300 nm. While the purity of the ferrite material is controlled by the reaction time and temperature, its crystallinity was found to be significantly enhanced by increasing the concentration of ammonia in the reaction solution. The reaction time and temperature as well as the dielectric constant of the reaction medium were also found to exert a significant effect on both the particle size and the crystallinity of the hydrothermally-prepared nanophase ferrites [16].

2.1.2.6 Combustion method

The “combustion synthesis,” also known as “self-propagating high-temperature synthesis” (SHS) represents a rapid process of solid combustion of reagents [35, 36]. The combustion method has been used in the preparation of a large number of technologically important oxides (refractory oxides, magnetic, semiconducting oxides, insulators, catalysts, sensors, etc.). There is a growing interest in the combustion synthesis of materials because this method is simple, fast, economic, and yields high purity products [13, 14].

The SHS method uses the energy produced by the exothermic redox decomposition of a mixture of metal nitrates with an organic compound. In the combustion, the mixtures of nitrates and organic compounds behave similarly to conventional oxidants and fuels. The reaction is carried out by dissolving metal nitrates and fuel in a minimum amount of water

and heating the mixture to evaporate water in excess. The resulting viscous liquid ignites and undergoes self-combustion, producing ashes that contain the oxide products. During the combustion, exothermic reactions take place. Gases such as N_2 , H_2O , and CO_2 evolve, favoring the formation of fine particle ashes [13, 14, 35].

2.1.2.7 Coprecipitation method

The co-precipitation method is based on simultaneous precipitation of two or more metals [18, 29]. The precipitation is performed mostly through the hydrolysis at low temperatures (25 -100 °C) of metal-nitrates solutions, such as zinc nitrate, copper nitrate and ferric nitrates. The starting point is to dissolve the metal salt precursors in water. The solution is then added slowly under vigorous stirring to a solution containing precipitating agent such as NaOH for all metals. It is important that all metals precipitate simultaneously so that a good degree of mixing of the metals is obtained. The stirring assures that there is no region where the amount of precipitating agent is low. If the stirring is inadequate local regions can form in the solution where the concentration of a precipitating agent slowly increases which could result in metals not precipitating simultaneously, which results in poor mixing of the metals [16].

Co-precipitation is the most commonly used method to prepare mixed metal oxides in the industry since the metals salts are easy to handle and relatively inexpensive. Powders prepared by this technique usually show narrow size distributions (good homogeneity), with averages size on the order of a few tenths of a nanometer (fine particles). The high purity of ferrites obtained by this procedure, the greater reactivity, the elimination of calcining step, and the versatility in the type of precursors represent the main advantages of this method. Several papers have been reported on the preparation of ferrite through coprecipitation approach and finally converted into fine ferrite powders by thermal treatment.

2.1.2.7.1 Co-precipitation mechanism

The thermodynamics requirement for the precipitation of a solid phase is that the product of the reactants' activities is greater than the solubility of the solid phase. This condition is achieved when the solution exceeds a critical level of super-saturation [18]. In the formation of zinc ferrite nanoparticles, the product of ferric and zinc ions activities must be greater than

the solubility of ZnFe_2O_4 and those conditions are attained at elevated temperature and high pH level. The precipitation of solid phase relieves the level of supersaturation in solution.

As shown in Figure 2.5, there are three pathways for the formation of small particles in solution [37]. In the first path, particles nucleate and then grow by diffusion. The distinct separation of the nucleation and growth processes results in the production of mono-disperse particles. In the second pathway, primary particles form during nucleation and then assemble into aggregates. In the third pathway, nucleation and growth stages are not distinct and result in polydisperse particles. However, if Ostwald ripening occurs during the aging of the particles, the smaller particles preferentially dissolve and larger particles will grow at their expense until all particles reach an equilibrium size [37].

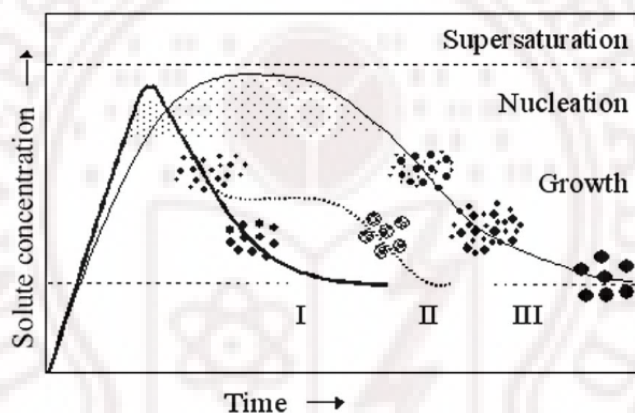
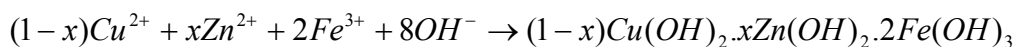


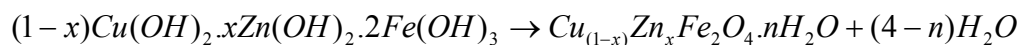
Figure 2.5: Mechanism of formation of colloids. Three possible pathways for particle formation, reproduced from Tartaj *et al.* [37].

The co-precipitation reaction takes place in two steps [38]:

Step 1: At first solid hydroxides of metals in the form of colloidal particles are obtained by the *coprecipitation* of metal cations in alkaline medium (coprecipitation step). For the case of Cu-Zn ferrite, this reaction is as follows:



Step 2: Then this product is subjected to heating in the precipitation alkaline solution to provide the transformation of solid solution of metal hydroxides to the Cu-Zn ferrites (ferritization step) as follows



where n is an integer.

A particular feature of “the co-precipitation method” is that the product contains a certain amount of associated water even after several hours of heating in alkaline solution. The rate of mixing of reagents plays a vital role in the size of the resultant particles. The relative rates of these two processes determine the size and polydispersity of obtained particles. Polydispersed colloids are obtained as a result of simultaneous formation of new nuclei and growth of the earlier formed particles. Less dispersed in size colloid is formed when the rate of nucleation is high and the rate of particles growth is low. This situation corresponds to a rapid addition and a vigorous mixing of reagents in the reaction. Slow addition of reagents in the coprecipitation reaction leads to the formation of bigger nuclei than rapid one. It must be also taken into account that in the case of slow addition of the base to solution of metal salts a separate precipitation takes place due to the different pH of precipitation for different metals. Separate precipitation may increase the chemical inhomogeneity in the particles. To obtain ferrite particles of a smaller size, less dispersed in size and more chemically homogeneous the mixing of reagents must be performed as fast as possible [38].

An increase in temperature (in the range 20-100°C) significantly accelerates formation of ferrite particles. The activation energy for formation of ferrites of different metals is not equal. Auzans [38] concludes that the heating at temperatures close to 100 °C is preferable for an easier and more rapid formation of the Mn-Zn ferrite particles.

2.1.2.8 Experimental procedure for synthesis of Copper-Zinc Ferrite nanoparticles

The nanoparticles of Cu-Zn ferrites were synthesized by co-precipitation method. The process description is as follows:

(a) Starting materials

Metal nitrates (Zinc nitrate hexahydrate $Zn(NO_3)_2 \cdot 6H_2O$ and copper nitrate hexahydrate $Cu(NO_3)_2 \cdot 6H_2O$) and Iron (III) nitrate nonahydrate $Fe(NO_3)_3 \cdot 9H_2O$ and Sodium hydroxide (NaOH) was utilized to chemically precipitate M-ferrite (MFe_2O_4) from a mixture of M-nitrate and iron nitrate. (M = Cu, Zn or Cu + Zn).

(b) The sequence of the procedure

The metal nitrates were weighed in required ratio for producing M-ferrite. The initial molar proportion (M^{2+}/Fe^{3+}) is always taken as the stoichiometric $\frac{1}{2}$. Then the metal nitrates (M-nitrate and iron nitrate) were dissolved in proper amount of distilled water and stirred constantly with a high-speed magnetic stirrer until dissolved. Sodium hydroxide is dissolved in distilled water until a pH greater than or equal to 12 was reached. The nitrate solution was poured into NaOH solution with vigorous stirring at 80 °C. This results in precipitating of solid particles from the solution (figure 2.6).

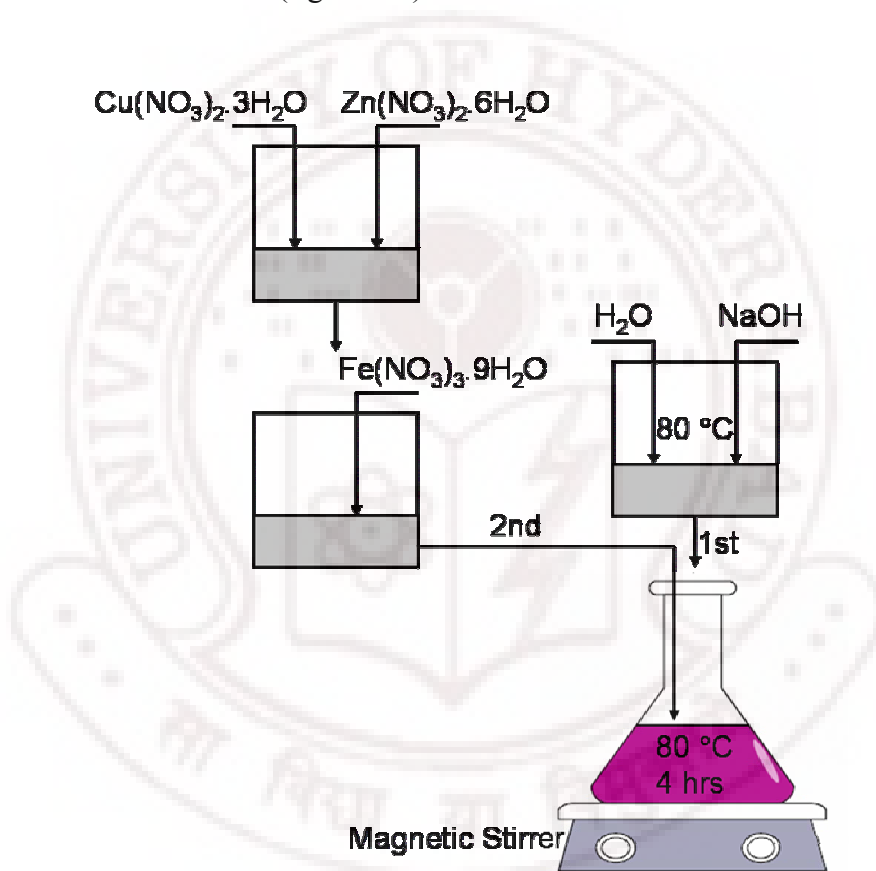


Figure 2.6: Schematic of the coprecipitation process of $Cu_{1-x}Zn_xFe_2O_4$ ferrite nanoparticles.

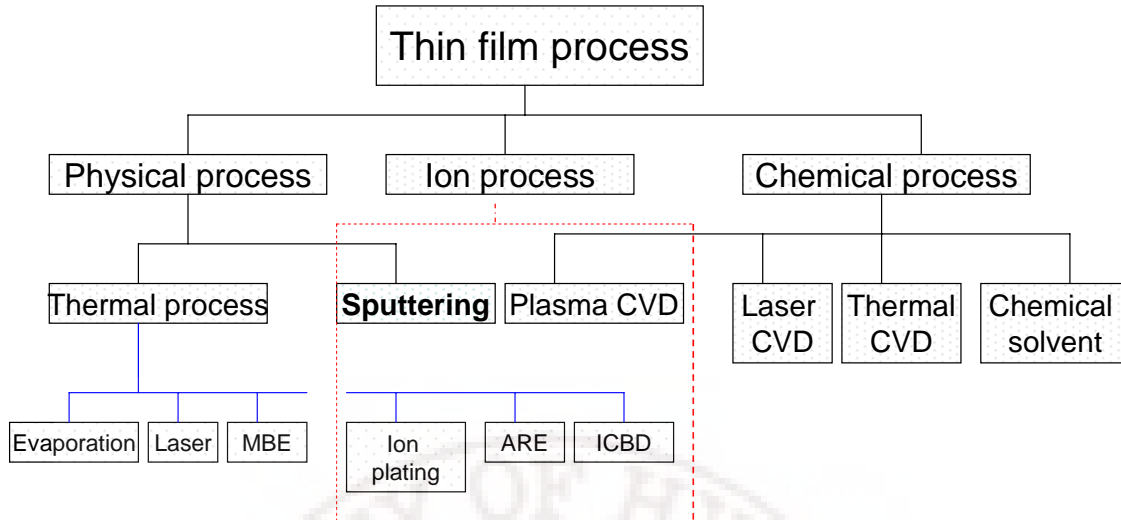
The solution (precipitate included) was centrifuged and the liquid was discarded. The precipitate was rinsed with distilled water and centrifuged again. The precipitate was then dried in oven at 80 °C for 12 hrs, ground using a mortar and pestle and calcined at 500, 700 and 850 °C for 6 hours. The XRD studies confirmed the formation of the M-ferrite phase in the calcined samples.

2.1.3 Thin films of Cu-Zn ferrites

Ferrite thin films can be prepared by chemical vapor deposition (CVD) or physical vapor deposition (PVD) techniques. In both CVD and PVD methods, one of the most critical deposition factors is the kinetic energy of the vapor phase particle, which can generally be divided according to the range of typically reported energies [39, 40], into three regimes.

1. Thermal regime ($0 \sim 0.3$ eV), in which particles have low energy. Techniques within this range include chemical vapor deposition and thermal evaporation;
2. Mediate regime ($1 \sim 100$ eV), in which particles have energies ranging from the bonding strength to the lattice penetration threshold. Techniques within this range include sputtering deposition and arc vapor deposition;
3. Implantation regime (> 100 eV) in which particle energies are well able to cause surface penetration and implantation. Technique within this range is ion implantation.

Figure 2.7 summarizes the main preparation methods for thin film processes [41]. Different techniques have been used by researchers for the preparation of ferrite thin films. These include chemical vapor deposition (CVD), magnetron sputtering, laser ablation, thermal evaporation, screen plating, ion beam deposition and ion implantation.



ARE: Activated reactive evaporation
 MBE: Molecular beam epitaxy
 ICBD: Ionized cluster beam deposition
 PVD: Physical vapor deposition
 CVD: chemical vapor deposition

Figure 2.7: thin film deposition processes [41]

2.1.3.1 Thermal Evaporation

The thermal evaporation process comprises evaporating source materials in a vacuum chamber below 1×10^{-6} Torr and condensing the evaporated particles on a substrate [41, 42]. The important methods of evaporation are resistive heating, flash evaporation, electron beam evaporation, laser evaporation, arc evaporation, and radio frequency (rf) heating. Two types of thermal evaporation processes are shown in figure 2.8. Resistive heating is most commonly used for the deposition of thin films. The source materials are evaporated by a resistively heated filament or boat, made of W, Mo, or Ta. Crucibles of quartz, graphite, alumina, beryllia, boron-nitride, or zirconia are used with indirect heating. The refractory metals are evaporated by electron-beam deposition since simple resistive heating cannot evaporate high melting point materials.

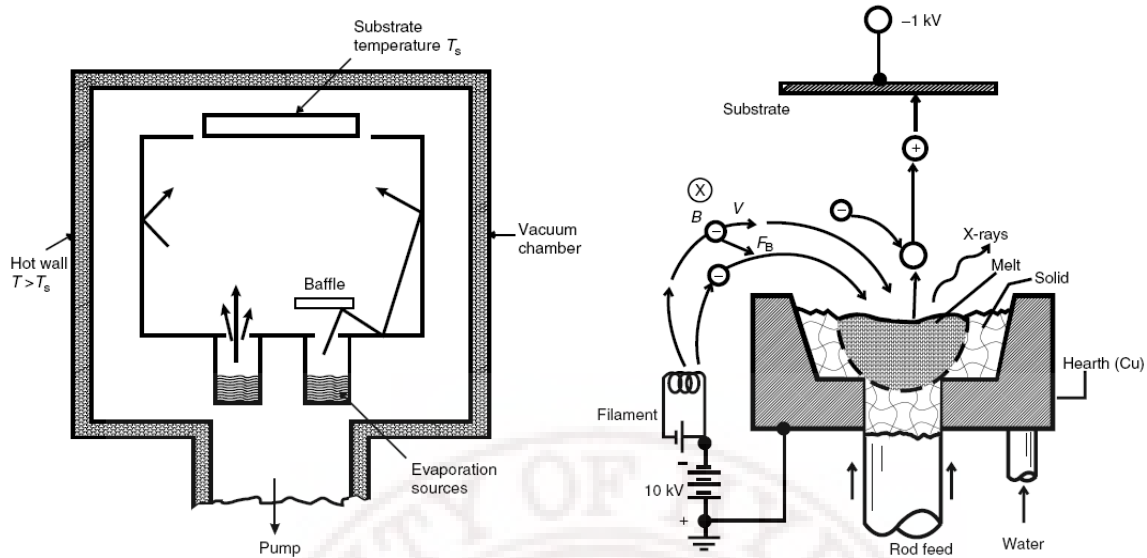


Figure 2.8: Thermal evaporation process utilizing: (Left) Resistive heating and (Right) electron beam [43].

2.1.3.2 Pulsed laser deposition (PLD)

PLD is an improved thermal process used for the deposition of alloys and/or compounds with a controlled chemical composition [41]. In laser deposition [44], a high-power pulsed laser such as the KrF excimer laser (1 J/shot) is irradiated onto the target of source materials through a quartz window. A quartz lens is used to increase the energy density of the laser power on the target source. Atoms that are ablated or evaporated from the surface are collected on nearby sample surfaces to form thin films. A typical PLD system is shown in figure 2.9. The target material is locally heated to the melting point, melted, and vaporized in a vacuum. The laser pulse may also provide photoemitted electrons from the target to make a plasma plume and the evaporation mechanism may be complex since the process includes the thermal process and the plasma process.

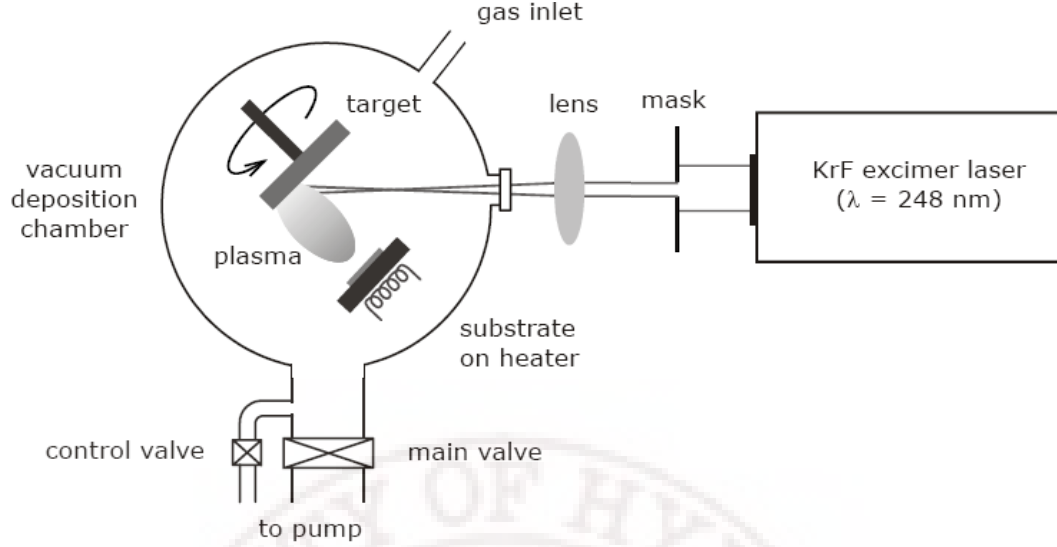


Figure 2.9: Pulsed laser deposition (PLD) uses a laser to ablate the source material from a target. The material is collected on substrates (S) in the form of thin films [41].

The PLD has the advantage of being simple in design, and the target has many forms such as a powder, sintered pellet, and single crystal. The mechanism of evaporation is simply discussed using the thermal evaporation model. The irradiated laser power is absorbed on the surface of the target. The optical absorption depth, L_o , of an ultraviolet laser is on the order of 10 nm. The depth, L_o , is given by [41]

$$L_o = 1 / \alpha$$

where α is the optical absorption constant of the target. The thermal diffusion depth, L_t , will govern the heating of the target; this is given by

$$L_t = \left(2\delta t \frac{K}{cn_{mol}} \right)^{1/2}$$

where δt is the pulse duration of the laser light, κ is the thermal conductivity of the target, c is the molar heat capacity of the target, and n_{mol} is the molar density of the target. The L_o and L_t characterize the mode of the heating as follows:

$$L_o \gg L_t \quad (\text{weakly absorbing})$$

$$L_o \ll L_t \quad (\text{strongly absorbing})$$

The values of L_t for Cu and Si are typically in micrometers. The targets of the insulator and wide-bandgap semiconductors show weak absorption. Metal targets and narrow-bandgap semiconducting targets show strong absorption. The strong absorption effectively melts the

target and thermally evaporates it. The laser irradiation may photoemit electrons from the target accompanied by photoionized atoms of target materials. The photoionized atoms create the plasma plume.

2.1.3.3 Sputtering

Sputtering is a Physical Vapor Deposition (PVD) process, which etches materials from a ceramic target [45]. When a solid surface is bombarded with energetic particles such as accelerated ions, surface atoms of the solid are scattered backward due to collisions between the surface atoms and the energetic particles as illustrated in Figure 2.10. This phenomenon is called *back-sputtering*, or simply *sputtering* [42]. Sputtering has become one of the most versatile techniques in thin film technology for preparing thin solid films of almost any material. Some of the main advantages of sputtering as a thin film preparation technique are (a) high uniformity of thickness of the deposited films, (b) good adhesion to the substrate, (c) better reproducibility of films, (d) ability of the deposit to maintain the stoichiometry of the original target composition, and (e) relative simplicity of film thickness control [42].

2.1.3.3.1 Sputtering process

The sputtering process can be summarized as follows [46]: an external potential is applied from an outside power source, charging the target with high negative voltage (3 to 5 kV). A gas is introduced into the vacuum chamber between the target and the grounded substrate and chamber wall. The large potential difference causes the ionization of introduced gas in the high electric field that forms *plasma*.

The ionization results in a negatively charged electron and positively charged ion pairs, whereas the plasma itself retains net neutral charge. Positively charged ions are attracted to the negatively charged target and accelerated by electric field, resulting in a collision with the target material. When an ion approaches the surface of a solid (target), one or all of the following phenomena may occur (figure 2.10) [47].

- The ion may be reflected, probably being neutralized in the process.

- The impact of the ion may cause the target to eject an electron, usually referred to as a *secondary electron*.
- The ion may become buried in the target. This is the phenomenon of *ion implantation*.
- The ion impact may also be responsible for some structural rearrangements in the target material.
- The ion impact may set up a series of collisions between atoms of the target, possibly leading to the ejection of one of the neutral atoms from the material by *momentum transfer*. This ejection process is known as *sputtering*. The sputtered atoms leave the target surface with relatively high energies (~ 10 eV) compared with evaporation atoms (~ 0.1 eV). This ejected flux of target atoms, which has a main direction, is then transported through the space towards the substrate where they condense and form a thin film [48].

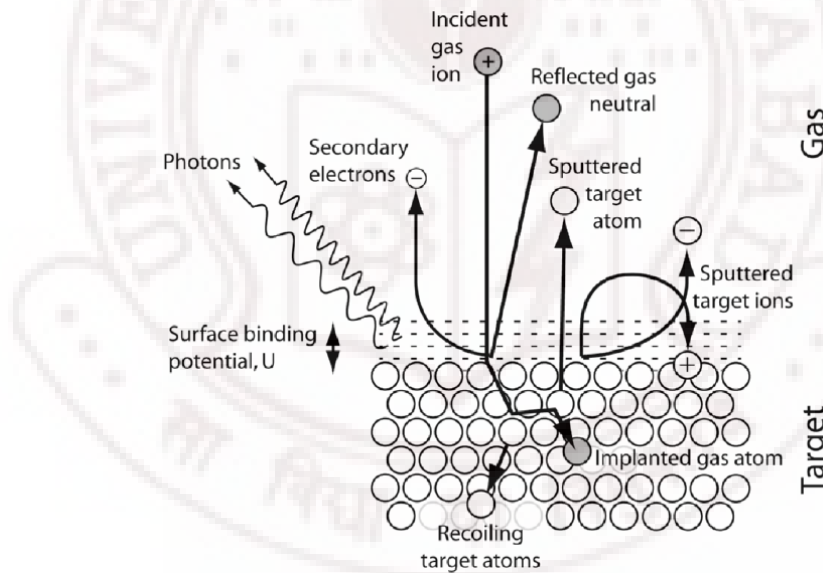


Figure 2.10: A schematic of the physical sputtering process [49]

The average number of the atoms ejected from the surface per incident ion is called the *sputtering yield* [50]. The sputtering yield S depends on many factors, such as the mass and the energy of the incident particles; the mass and the binding energy of the sputtered atoms; the crystallinity of the target; etc. and it can be described as [51, 52]:

$$S = \text{const}(E_{\text{ion}} - E_{\text{thers}}) = \text{const} \times e(V_p - V_{dc} - V_{\text{thers}})$$

where E_{ion} is the energy of the incident ion, E_{thres} is a threshold energy $E_{\text{thers}} = 8U_s(M_1 / M_2)^{2/5}$, V_p is the plasma potential, V_{dc} is the dc voltage on the target (discharge voltage), U_s is the surface potential barrier and M_1 and M_2 are the mass number of the ion and the target, respectively.

The deposition rate R is proportional to the sputtering yield S , and $I(1 - \gamma)$, with I the discharge current and γ the secondary electron emission coefficient [52]:

$$R = \text{const} \times SI(1 - \gamma)$$

The principle of *momentum transfer* used to deposit materials has made the sputtering technique very attractive. Using this technique it is easy to deposit materials which could not be easily deposited using other techniques. This includes even refractory materials.

Depending on the gas pressure and the distance between substrate and target, the flux will be more or less scattered by the gas. The average distance an atom can travel before a collision is called the *mean free path* (λ). The mean free path λ can be estimated through [49]

$$\lambda = \frac{kT_g}{\sqrt{2}\pi P_g d_g^2}$$

where k is the Boltzmann constant, T_g and P_g the gas temperature and pressure respectively, and d_g the diameter of the gas molecule ($d_{Ar} = 0.364$ nm). During sputtering process, the film surface is ion bombarded. Because of the high-energy state of plasma, sputtered particles have enough energy to migrate on the film surface which can densify the growing film by enhancing the surface atom mobility [53]. In addition, ion bombardment of the growing film can restrict the grain growth and permit the formation of nanocrystalline [54]. The size and crystallographic orientation of grains can be controlled by the energy of bombarding ions [55].

2.1.3.3.2 Effect of magnetic field (Magnetron sputtering)

The ionization efficiency is improved by using a magnetic field parallel to the cathode surface and thus restraining the primary electron motion to the vicinity of the cathode [56]. These electrons thus trapped move inside the orbit gain a higher mean free path and collisionally scatter before reaching the anode. Consequently magnetron sputtering requires lower gas

pressures to sustain the plasma compared to that of the diode sputtering technique. Reduced scattering and increased electron usage efficiency leads to a better deposition rate and reduced applied voltage to sustain plasma in this technique. Along with these advantages, this technique has the disadvantage of the discharge being swept to one side by the $\mathbf{E} \times \mathbf{B}$ force [45]. This is avoided by using cylindrical cathodes that allow these drift currents to close on themselves.

On the basis of the type of magnets used, magnetron sputtering is classified into different categories like cylindrical magnetron, hollow cathodes, cylindrical-post, cylindrical-hollow and planar magnetrons [41].

2.1.3.3.3 Film growth

Thin film formation includes the processes of nucleation and growth. During the earliest stage of film formation, a sufficient number of vapor atoms or molecules condense and establish a permanent residence on the substrate. There are three basic growth modes [55]: (1) island mode (or Volmer-Weber), (2) layer by layer mode (or Frank-van der Merwe), and (3) mixed mode (Stranski-Krastanov), which are illustrated schematically in Figure 2.11. Island growth occurs when the smallest stable clusters nucleate on the substrate and grow in three dimensions to form island. This island growth happens when atoms and molecules in the films are more strongly bound to each other than to the substrate. Many systems of metals on insulators, alkali halide crystals, and graphite are good examples of this growth mode.

The opposite characteristics are displayed during layer growth. In the layer growth mode, the atoms are more strongly bound to the substrate than to each other. The first complete monolayer is then covered with a somewhat less tightly bound second layer, providing the decrease in binding energy is continuous toward the bulk crystal value. The layer growth mode is sustained. The most important example of this growth mode involves single crystal epitaxial growth of semiconductor films. The layer plus island or mixed growth mechanism is an intermediate combination of both aforementioned modes. In this case, after forming one or several monolayers, subsequent layer growth becomes unfavorable and islands form. The growth of ferrite films prepared using sputtering system could be attributed to the third mode.

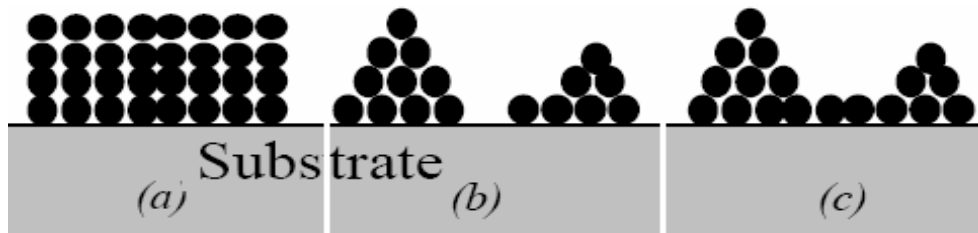


Figure 2.11: Basic modes of thin films growth (a) layer by layer growth mode, (b) island growth mode and (c) mixed growth mode [55].

2.1.3.3.4 Film microstructure

The most important parameters which influence the final grain structure of a vapor-deposited film for a given material are substrate temperature and growth flux. The growth flux is a quantity that represents the mass or volume flow rate onto the growth surface. In general, increasing the rate of deposition tends to promote formation of a finer scale microstructure, while increasing the substrate temperature tends to promote a coarser microstructure or single crystal growth [54]. Polycrystalline films are commonly described in terms of their grain structure, which is usually understood to include some measure of grain size, grain boundary morphology (typical grain shape), and film texture (distribution of crystallographic orientations). Thornton [57] proposed a four-zone model which is illustrated in Figure 2.12. In zone 1, tapered or fibrous grains and voided boundaries form where the structure is influenced by the shadowing effect and by the roughness of the substrate surface on which deposition is made. The transition zone is marked by dense grain boundary arrays and a film with a high dislocation density. Columnar grains evolve in zone 2, where the evolution of the structure is aided by surface diffusion processes. The transition from surface diffusion to bulk diffusion, as well as recrystallization and grain growth lead to the formation of an equiaxed grain structure in zone 3. As a general trend, similar structures evolve at higher temperatures in sputtered films as compared to evaporated films [43, 54, 57, 58].

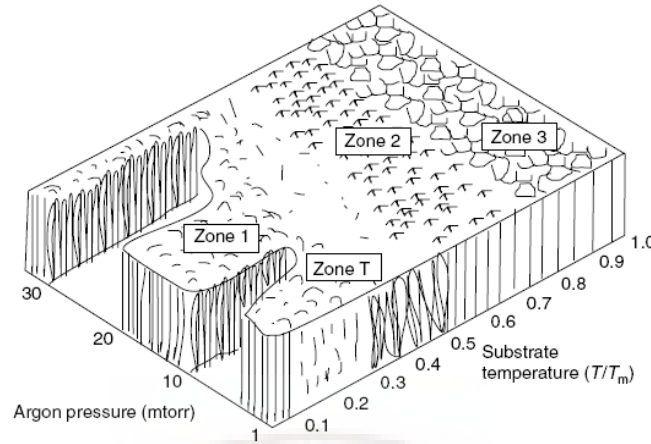


Figure 2.12: Structure evolution in polycrystalline films as a function of substrate temperature and argon gas pressure, following the four-zone model of Thornton [43, 57].

3.1.3.3.5 Deposition Equipment (Sputtering system)

Sputtering is a type of Physical Vapor Deposition (PVD) as it uses the principle of momentum transfer to remove neutral atoms from a target. Several sputtering systems are proposed for thin-film deposition including dc diode, rf diode, magnetron, and ion-beam sputtering. The simplest model is the dc-diode sputtering system. The dc-sputtering system is composed of a pair of planar electrodes. One of the electrodes is a cold cathode and the other is the anode. The front surface of the cathode is covered with target materials to be deposited. The substrates are placed on the anode. The sputtering chamber is filled with sputtering gas, typically argon gas at 5 Pa (4×10^{-2} T). The glow discharge is maintained under the application of dc voltage between the electrodes. In the dc sputtering system, the target is composed of metal since the glow discharge (current flow) is maintained between the metallic electrodes. The schematic diagram of the dc-sputtering system is shown in figure 2.13.

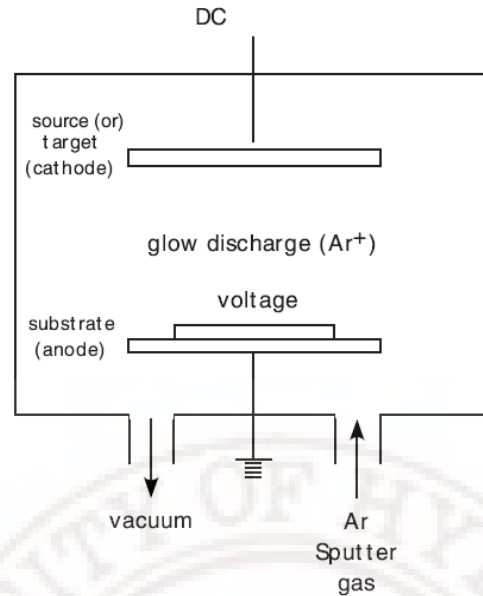


Figure 2.13: Schematic showing the basic features of a dc-sputter deposition system [54]

By simple substitution of an insulator for the metal target in the dc sputtering discharge system, the sputtering discharge cannot be sustained because of the immediate buildup of a surface charge of positive ions on the front side of the insulator. To sustain the glow discharge with the insulator target, rf voltage is supplied to the target. This system is called rf-diode sputtering. In the rf-sputtering system, the thin films of the insulator are sputtered directly from the insulator target.

RF sputtering makes it possible for dielectric materials to be sputtered at relatively low voltages. However, due to the inherent difficulty of passing current through a dielectric, sputtering rates for oxides are extremely slow and inefficient. Magnetron sputtering helps alleviate this problem by introducing a magnetic field in addition to the usual electric field present in the plasma Figure 2.14. This helps confine electron motion to the target area, improving plasma intensity and thus deposition rate. The fact that the plasma is more confined to the area between the target and the substrates improves the efficiency by reducing the amount of material wasted during deposition.

In magnetron sputtering, a magnetic field is superposed on the cathode and glow discharge, which is parallel to the cathode surface. The electrons in the glow discharge show cycloidal motion, and the center of the orbit drifts in the direction of $\mathbf{E} \times \mathbf{B}$ with the drift

velocity of E/B , where \mathbf{E} and \mathbf{B} denote the electric field in the discharge and the superposed transverse magnetic field, respectively.

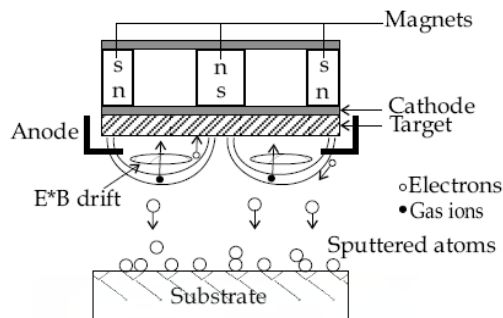


Figure 2.14: Simplified Cross Section of a Sputtering System.

The magnetic field is oriented such that these drift paths for electrons form a closed loop. This electron trapping effect increases the collision rate between the electrons and the sputtering gas molecules. This enables one to lower the sputtering gas pressure as low as 10^{-5} torr, but more typically 10^{-2} torr. In the magnetron sputtering system, the magnetic field increases the plasma density which leads to increase in the current density at the cathode target, effectively increasing the sputtering rate at the target. Due to the gas's low working pressure, the sputtered particles traverse the discharge space without collisions, which results in a high deposition rate.

When a reactive gas species such as oxygen or nitrogen is introduced into the chamber, thin films of compounds (i.e., oxides or nitrides) are deposited by the sputtering of the appropriate metal targets [59]. This technique is known as *reactive sputtering* and may be used in either the dc or rf mode. Reactive sputtering is used in practice for the high-rate deposition of insulating metal oxide films. In these glow-discharge systems, sputtering gas molecules, during thin-film growth, irradiate the sputtered films. This causes the inclusion of the gas molecules in the sputtered films [60].

In a planar magnetron, the magnetic flux on the cathode surface is terminated to the magnetic core as shown in Figure 2.15 a. The magnetron is called a *balanced* magnetron. When an additional magnetic flux is superposed to the balanced magnetron shown in Figure 2.15 b, the magnetron is called an *unbalanced* magnetron.

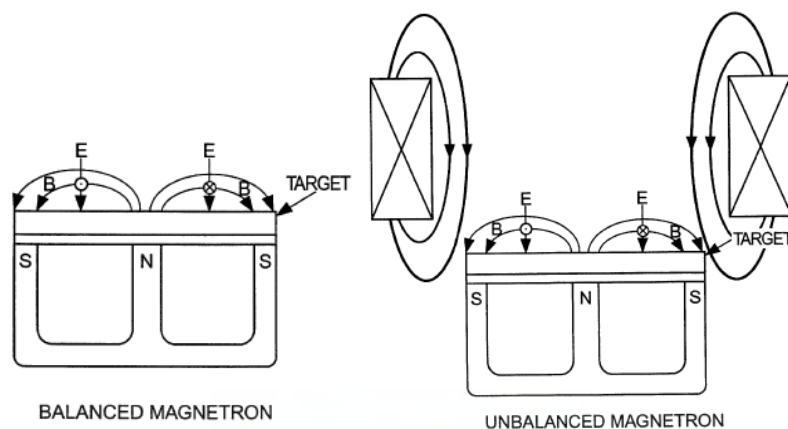


Figure 2.15: (a) Balanced (Left) and (b) unbalanced magnetron sputtering (Right) [41].

2.1.3.3.6 RF-magnetron Sputtering System

Ferrite films were deposited by employing TORR R300 rf-magnetron sputtering system as shown in figure 2.16. The deposition equipment is composed of two 2-inch planar high performance water-cooled magnetrons, a stainless steel chamber, high vacuum system, switch cabinet, a heated rotatable substrate holder etc. The equipment was provision of cooling water supply to cathode, power supply and turbo pump. The schematic diagram of the construction of the sputtering system is displayed in figure 2.17.

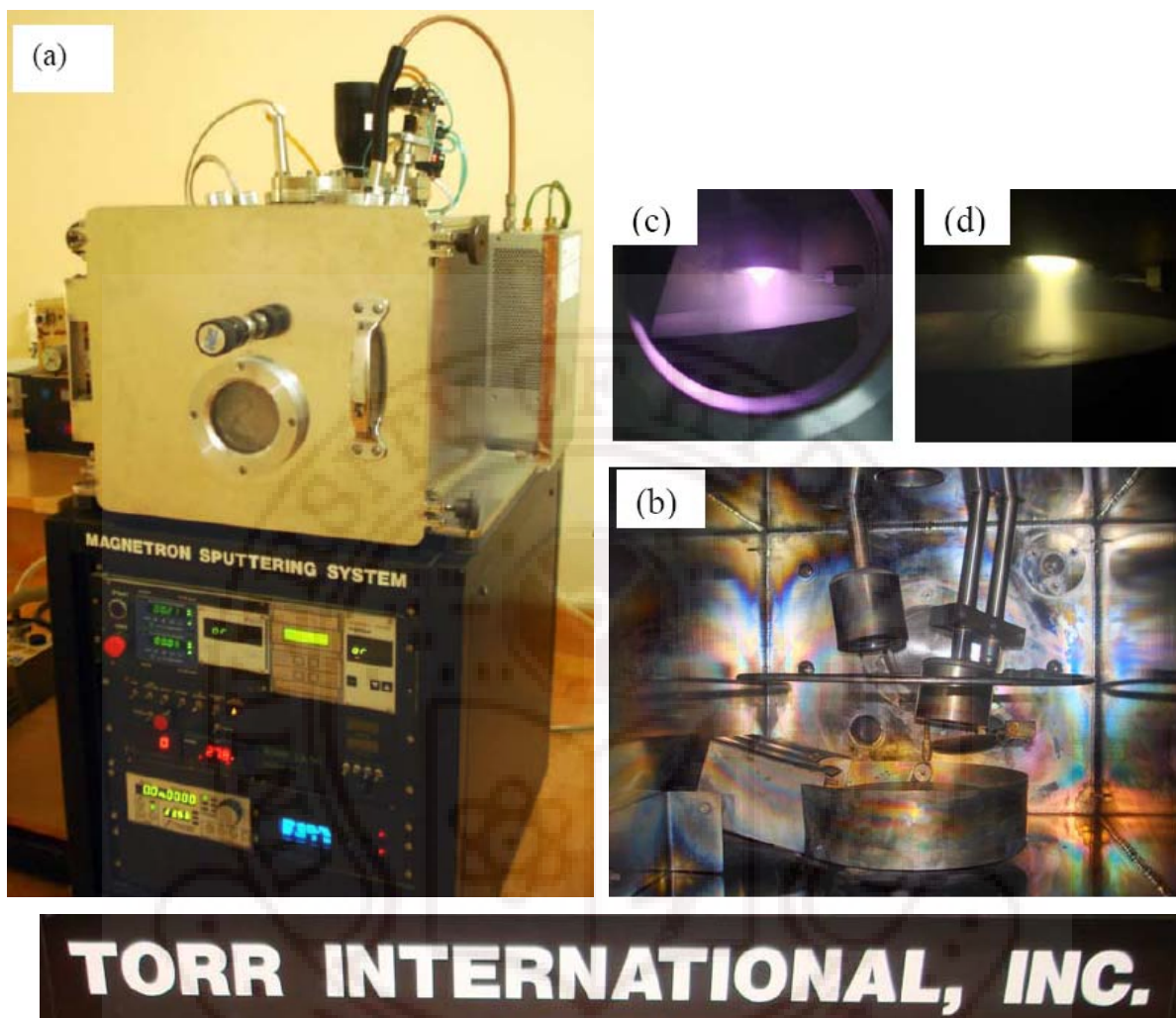


Figure 2.16: (a) The photograph of sputtering system used in this work, (b) view of the deposition chamber having two electron guns and (c) Plasma created during deposition process of ferrite thin films in Ar and (d) O_2 gas.

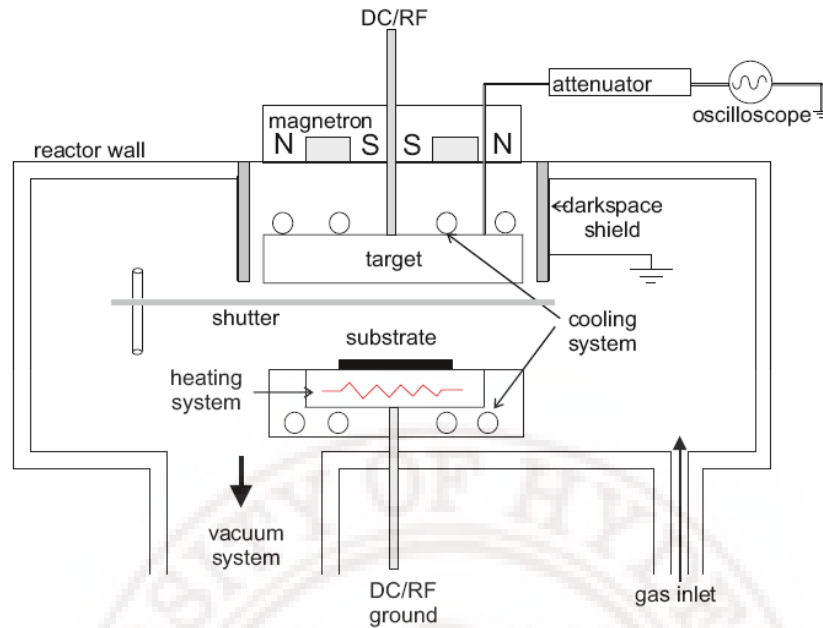


Figure 2.17: Schematic diagram of the sputtering system with magnetron [61]

The material to be deposited (target) acts as the cathode and is connected to a negative voltage RF power supply. The substrate is placed on a substrate holder and could be grounded, floating, biased, heated, cooled, or could be a combination of these. The substrates are placed exactly below the target which makes 15° with the normal to the substrate. This setup is placed inside a vacuum system which is pumped down and maintained at high vacuum. An inert gas like Argon is introduced into the system as the medium for glow discharge. This is because an inert gas like Argon has its meta-stable energy greater than its first ionization potential which helps in producing a sufficient supply of ions for self-sputtering. When this glow discharge is initiated, ions with high kinetic energy strike the cathode (target). Then sputtering process starts. The main parts of the deposition system are described in more details as follows.

1. Process Chamber

The sputtering chamber used to deposit the ferrite oxide films is made up of electro-polished stainless steel chamber of dimensions 16 inch \times 14 inch \times 16 inch. These materials are non corrosible, non-magnetic, easy to weld and clean, highly malleable and have good out-gassing characteristics. It is vertical mounted inside, where the sputter-down-mode is available. The

process chamber contains feed-throughs for power, waterlines (for supplying cooling water to the sputter guns and crystal monitor), thermocouple, gas lines and other purposes. Rubber O-rings act as vacuum sealant between the feed-throughs and the chamber. The chamber contains a rotatable substrate holder around a central axes supported by an external motor connected to the chamber through one of the feed-throughs. It also contains two rf sputtering guns above the substrate holder. The typical base pressure that could be maintained using this setup is in the low 10^{-6} Torr range. The sputtering system used to deposit the films for our experiments is made by TORR Company, USA. Figure 2.16 depicts the vacuum chamber used to deposit the ferrite films. Vacuum inside the chamber is created using a combination of Varian rotary vane mechanical pump and Turbo-molecular pump.

2. Vacuum system

The vacuum inside a sputtering chamber is created and maintained using a pumping assembly. There are various factors that are to be considered when choosing a pumping system. The pumping rate, ultimate pressure that can be achieved, ability to handle gas loads and potential for oil contamination of the pump are some of them. The pumping system used in this work is a combination of a rotary vane pump (Varian DS 302) for roughing the system to a pressure of 10^{-3} Torr and a Varian turbo-molecular pump (300 l/s) for maintaining a high vacuum in the system. This pump has the capability to pump the system down to a pressure in the microtorr range. The vacuum system is also composed of a choke (for reducing the volume flow rate during sputtering) and a full-range compact pressure sensor.

3. Source and RF-Sputtering power supply

The system is attached with two 2 inch Angstrom Sciences magnetron guns, each with innovative integral shutter and shield for depositing metals and dielectric target materials. The guns are at a tilt angle and focus at the center of the substrate stage. The guns are retractable up to 6 inch while keeping the focal point the same. The electrical system of rf sputtering for ferrite deposition involves an rf generator operated at 13.56 MHz, an rf switching control, an rf selector switch and two matchboxes (figure 2.18). The output of the rf generator is up to 300 W. Figure 2.14 shows the sputtering cathode with cross-sectional schematic diagram of planar magnetron sputter gun. It consists of target, backing plate, target holder, ground shield,

permanent magnet, pole piece, ceramic insulator and cooling water inlet. The entire gun is oriented $\sim 15^\circ$ from the substrate normal and 5-6 cm center to center distance of the target to the substrate. Also highlighted are the magnetic field lines with respect to the target surface. The electrical connections show how the target is isolated from the grounding shield which is at common ground with the substrate stage via the chamber walls.

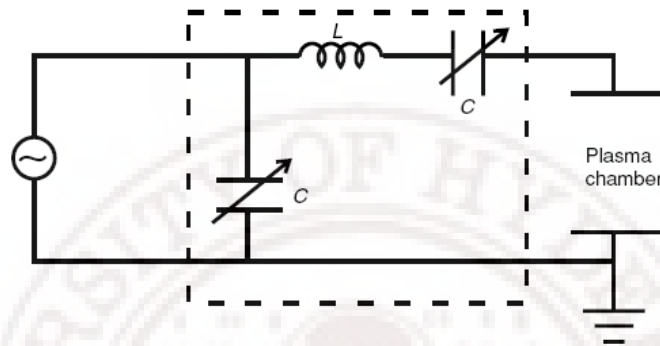


Figure 2.18: A typical “L” matching network used on an rf diode sputtering system [43].

Further attachments

1. Substrate heater

The substrates are heated using quartz lamp heating arrangement to heat the sample stage up to 400°C . The temperature is controlled and maintained digitally through a PID controller on front panel using a thermocouple as a sensor.

2. Pressure Gauges

Deposition pressure is one of the important parameters that could affect the properties of the film. . A full range combination cold cathode and Pirani gauge measuring from 760 to 10^{-8} Torr is provided.

3. Mass flow controller

There are two mass flow controllers with shutoff valves for Argon and Oxygen. A unique gas shower ring is provided inside the chamber for uniform gas distribution during sputtering process.

4. RF Power supply

The RF power supply is capable of delivering up to 300W . The RF supply is with an auto-matching network in order to minimize the reflected power. Both the total and reflected power

is shown digitally on displays. The amount of power supplied to the gun controls the amount of ions produced during the sputtering of the target material and thus their density.

2.1.3.3.7 Experimental Procedure

1. Target preparation

The source for the material to be deposited, the sputtered target, is a 2-inch ferrite ceramic target matching the size of the gun. The target preparation is similar to that explained in chapter 2 part-1 with minor modifications. The M-ferrite sputter target was loaded into the sputtering gun.

2. Substrate cleaning

All the films were deposited on glass substrates. The glass substrates were subjected to a sequential cleaning process before being loaded for deposition. The substrates were rinsed in flowing distilled water to remove dust particles. They are then cleaned with acetone to remove any organic impurities followed by subsequent cleaning step using isopropyl alcohol. The glass substrates were ultrasonically cleaned with distilled water. Complete drying is achieved by baking the substrates in an oven at 40°C for 30 minutes.

3. In order to produce an edge for the thickness measurement by a profilometer, a glass slide was fixed on the glass substrate before coating and removed later together with the material deposited on top of it.

4. The substrates are loaded onto circular stainless steel substrate holder. This setup is then mounted on the rotary sample holder assembly. This rotary assembly aids in placing the substrate exactly under the ferrite target.

5. Chamber evacuation

The vacuum chamber was evacuated down to a base pressure of 2×10^{-6} mTorr prior to the deposition.

6. The gun shutter to the M-ferrite target is opened. The RF power to the sputtering gun is turned on and the target was pre-sputtered for 10 min. in the chosen Ar/O₂ mixture.

7. The substrate was brought under the target and kept in this position for the entire sputtering process.

8. All the films were deposited for duration of 60 minutes.

2.2 Characterization techniques

The characterization of materials requires obtaining information about the spatial arrangement of the atoms and identifying precisely which atoms occupy which particular sites in the crystal structure. It also includes the specification of imperfections, impurities, inhomogeneities, and so on. Often, it involves measuring some particular electronic or optical properties. This chapter includes the description of the physical principles of a set of tools that have been used to characterize the prepared samples with details of the experimental procedure. Some tools produce pictures of the material in real space. These include the scanning-electron microscope (SEM) and the atomic force microscope (AFM). Other complementary tools take pictures in momentum space or wave-vector space rather than in real space such as x-ray diffraction (XRD).

Additional tools provide information about the dynamical response of a material. Included among the numerous techniques available in frequency space are the optical spectroscopies: infrared, visible, and ultraviolet spectroscopy. It also describes briefly on transport measurements of AC electrical resistivity and impedance analyzer. There are spectroscopic techniques in which both the electrons and photons play a significant role. Included among the spectroscopic tools we have used extensively in this study is the electron-spin resonance (ESR). This chapter also describes static magnetic characterization tools like vibrating sample magnetometer (VSM).

The characterization techniques of the ferrite Films and powders have been used in this work are as follows

1. X-ray diffraction (XRD) (θ -2 θ scan)
2. Scanning electron microscopy (SEM)
3. Electron dispersive of X-Ray Analysis (EDAX)
4. Thickness measurement (Profilometer)
5. Atomic force microscopy (AFM)
6. Vibrating sample magnetometer (VSM)
7. Ferromagnetic resonance (FMR)
8. Transmission Spectrum Measurement Spectrophotometer
9. Impedance analyzer

2.2.1 X-Ray Diffraction (XRD) (θ - 2θ Scan)

X-ray diffraction (XRD) is a powerful technique used for analyzing the structure, geometry, and phase identification of unknown materials. It can be used on single crystal materials or for the determination of preferred orientation, defects, and stresses in thin films as well as polycrystalline materials [51]. XRD techniques are based on the scattering of x-rays from crystals. Scattering is defined as the deflection of either waves or particles randomly as a result of collisions. In the case of x-ray radiation, the waves are scattered by electrons surrounding atoms. The total scattering of a system is the combination of the scatter from an individual atom in the solid summed over the contributions of all related in the lattice [62].

Diffraction effect is observed when electromagnetic radiation impinges on periodic structures with geometrical variations on the length scale of the wavelength of the radiation. The interatomic distances in crystals and molecules amount to 0.15 – 0.4 nm which correspond in the electromagnetic spectrum with the wavelength of x-rays having photon energies between 3 and 8 keV. Accordingly, phenomena like constructive and destructive interference should become observable when crystalline and molecular structures are exposed to x-rays. When a monochromatic X-ray radiation is incident upon the sample, a part of the radiation is scattered from the sample atoms. Scattered X-rays may constructively interfere when certain conditions are satisfied. This phenomenon is known as diffraction of X-rays (figure 2.19) and the condition is known as the Bragg law [63]

$$n\lambda = 2d_{hkl} \sin \theta$$

Two incident rays are scattered from two atomic planes of the crystal. The traveling difference of two rays is equal to the double product of the inter-atomic plane distance d_{hkl} and the sin function of the incident angle θ ($\sin\theta$). The Bragg law says that if the traveling difference is equal to an integer number of the incident X-ray wavelength then the constructive interference of the diffracted beam occurs and a sharp diffraction peak can be observed.

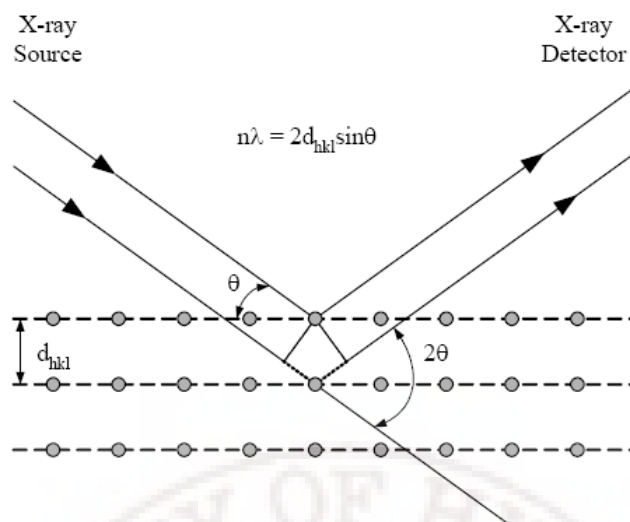


Figure 2.19: Reflection of X-rays from different atomic planes illustrating Bragg's law [63]

The key components of a modern diffractometer include a monochromatic radiation source, sample stage (goniometer), radiation detection system, enclosure, and safety features. One of the most common configurations is the θ – θ upright. This type of diffractometer has a movable detector and X-ray source, rotating about the circumference of a circle centered on the surface of a flat powder specimen.

Figure 2.20 shows the beam path schematically. The intensity of a diffracted beam is measured directly by an electronic solid-state detection system. The scattered X-rays dissipate energy by generating electron–hole pairs in the detector. The electronic system converts the collected charge into voltage pulses. The electronics counts the number of pulses per unit of time, and this number is directly proportional to the intensity of the X-ray beam entering the detector.

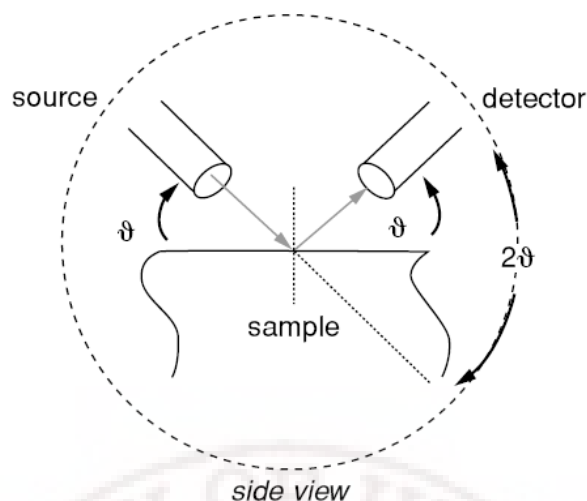


Figure 2.20: Schematic of a θ – θ upright shows how the source and detector each move at a constant rate of θ/s relative to the sample. Hence, the source and detector move at constant rate of $2\theta/s$ relative to one another [64].

The technique can be used to characterize powders as well as polycrystalline materials. The material of interest is ground to produce a fine, randomly orientated powder, with each particle in the powder consisting of small single crystals or an aggregate of crystals 10 μm or less. The powder is placed into a recess of a plastic sample holder and leveled flat in the sample holder with a straight edge.

In brief, a sample is irradiated by monochromatic X-rays, which will be diffracted according to Bragg's Law. In our experiments we have used X'Pert Philips PW 1730 Cu- K_α source ($\lambda = 0.15406 \text{ nm}$) and Co- K_α ($\lambda = 0.17898 \text{ nm}$) Inel XRG 3000 France. The diffraction intensity is measured continuously during a detector scan of 2θ , coupled to a specimen rotation of θ as shown in Figure 2.21. The recorded results are presented in the form of a diffractogram where I , the intensity, is plotted as a function of 2θ . The recorded results are then compared with theoretical calculations and literature.

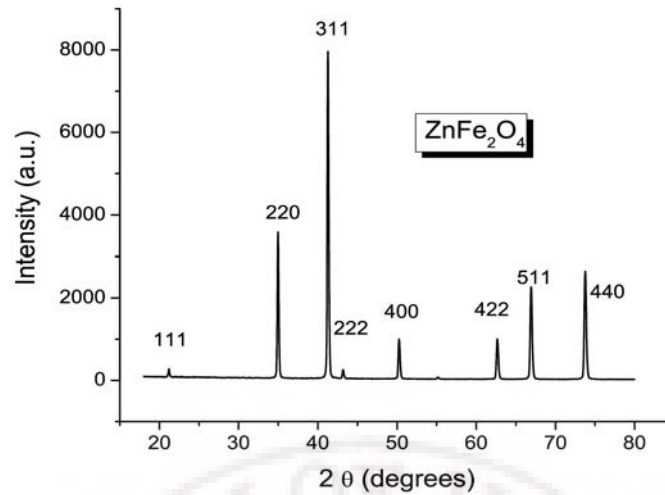


Figure 2.21: XRD patterns of powder ZnFe_2O_4 obtained in this work.

The diffraction data were fitted with a Lorentzian function to determine the location of each peak 2θ (figure 2.22). Using Bragg's law, the interplanar lattice spacing, d_{hkl} , was calculated. The variation of the average lattice spacing, i.e. the slight shift of the (hkl) peak position, in the direction normal to the plane of the films gives the strain on films; it is either compressive or tensile. The strain on films is calculated using the following formula:

$$\text{Strain}(\%) = \frac{\Delta d}{d} \times 100 \quad (2.1)$$

where d is the lattice spacing. A characteristic shift towards lower angle compared to the reflex of ideal crystals indicates a lattice expansion. The broadening due to strain (ϵ) can be written as $\Delta\beta = -\epsilon \tan\theta$ where $\epsilon = \Delta d / d$. The XRD line width and particle size are

connected through the Scherrer equation [63] $D = \frac{0.9\lambda}{\beta_1 \cos\theta}$ where, D is particle diameter, λ

the wavelength of the X-ray radiation, β_1 a measure of the broadening of diffraction line due to size effect.

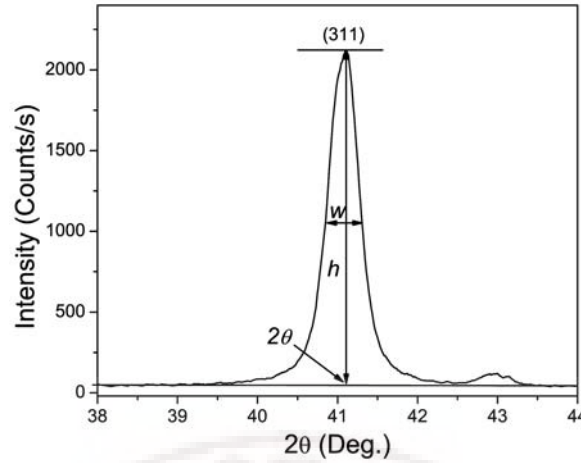


Figure 2.22: The (311)-reflex of XRD for ZnFe_2O_4 nanoparticles obtained in this work

Now if both the effect of “particle-size broadening” and “strain-broadening” is taken into consideration, then the total broadening (β) can be expressed as follows [36]:

$$\beta = \beta_1 + |\Delta\beta| = \frac{\lambda}{D \cos \theta} + \varepsilon \tan \theta$$

$$\frac{\beta \cos \theta}{\lambda} = \frac{1}{D} + \frac{\varepsilon \sin \theta}{\lambda} \quad (2.2)$$

where β is the full width at half maxima (FWHM) of the XRD peaks of the sample, D is the effective particle size, ε is the effective strain. A plot of $\frac{\beta \cos \theta}{\lambda}$ vs. $\frac{\sin \theta}{\lambda}$ will be a straight line, slope of which will give the estimation of the effective strain, whereas the intercept on $\frac{\beta \cos \theta}{\lambda}$ axis will carry the information of the particle size.

Usually, the polycrystalline is such a crystal aggregates whose orientations may deviated widely from complete randomness, which is said to possess texture. In order to compare the reflex intensities of different orientations they are usually normalized with the tabulated peak heights of the powder diffractograms (PDF1991). The X-ray density for each composition was calculated using the relation [63] $d_x = \frac{ZM}{NV} \text{ g/cm}^3$, where, Z is the number of molecules per unit cell ($Z = 8$ for spinel structure), M the molecular weight, N the Avogadro's number and V the theoretical value of the unit cell volume.

2.2.2 Scanning electron microscopy (SEM)

The scanning electron microscope (SEM) is a widely used instrument to obtain information on bulk specimens. It is also an indispensable and powerful tool for analyzing and constructing new nanomaterials [65, 66]. The scanning electron microscope (SEM) is one of the most versatile instruments available for the examination and analysis of the microstructure morphology, thickness and growth structure, particle size and shape and chemical composition characterizations [65, 66].

In this work, a Philips XL30 high / low vacuum scanning electron microscope was used for low magnification analyses. A schematic drawing of a conventional SEM representing the Philips XL30 ESEM is shown in Figure 2.23.

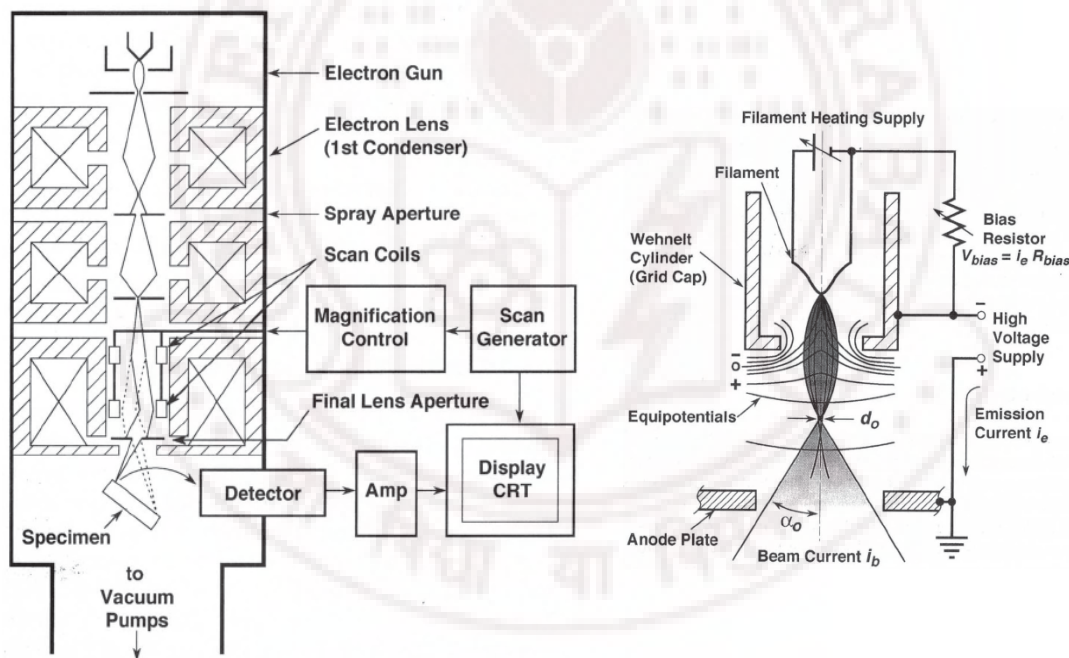


Figure 2.23: (left) Schematic drawing of the electron column showing the electron gun, lenses, the deflection system and the electron detector. (right) Schematic drawing of a conventional self bias thermionic tungsten hairpin electron gun [66, 67]

The main task of the electron gun is to provide a stable beam of electrons with adjustable energy. There are several types of electron guns available and these are mainly categorized by

their ability to produce an amount of current into a small spot, the stability of the emitted current and the lifetime of the source. The Philips XL30 ESEM was fitted with a tungsten thermionic emitter. The tungsten thermionic emitter is fairly reliable and inexpensive and is commonly used for low magnification imaging. A schematic is shown in Figure above.

The principle of a SEM [67] is to scan the specimen surface with a focused electron beam. When primary electrons strike a specimen surface, a wide range of useful interactions can occur, causing various charged particles and photons to be generated. The different emitted signals can be collected and used to form an electron image that contains useful 3D information of the surface. The image formed is displayed on a cathode ray tube (computer monitor) at the same scanning rate as the electron beam scans the specimen. In addition, for thin specimens, primary electrons can be transmitted through the material and similarly utilized. Typical signals of the electron beam - specimen interactions are shown schematically in Figure 2.24 [67].

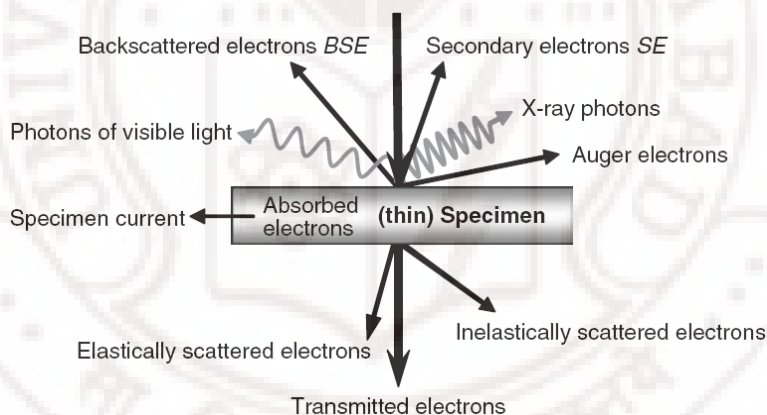


Figure 2.24: Some of the useful signals that are generated when a focused electron beam strikes a specimen. Note that, for a ‘thick’ specimen, i.e. more than a few hundred nanometres, electrons become absorbed within the specimen and hence are not transmitted [67]

All signals generated are emitted simultaneously and each carries different information. Both Secondary electrons (SE) and Backscattered electrons (BSE) are used for imaging while X-rays are used for chemical analysis. Secondary electrons are generated as a result of interaction and transfer of energy of both incoming primary electrons and outgoing

backscattered electrons with atoms within the material. Secondary electrons have low energy, approximately less than 50 eV, and as a result come from the outer surface of the material from where they have enough energy to escape.

BSEs are generated as a result of primary electrons coming from the electron beam that have been rebounded after collisions with the specimen. These have higher energy than SE, (greater than 50 eV) and come from a larger volume of the specimen (between the surface and 0.1 ~ 0.5 μm deep). BSEs provide information on surface topography as well as atomic number contrast. The backscattering coefficient increases monotonically with Z and areas with a high average atomic number appear brighter in contrast. As a result, BSE provide information on compositional uniformity within the specimen. Additional to SE and BSE, radiation in the form of X-ray photons is generated. This radiation provides chemical information when analyzed using energy dispersive X-ray spectrometry (EDAX) [67, 68].

2.2.3 Energy dispersive X-ray spectrometry (EDAX)

As already seen in the SEM, the bombardment of a specimen with an electron beam leads to the generation of X-rays. These can be used to determine the elemental composition of different regions or features within the specimen [68].

Basically, electrons in the inner shells of an atom are ejected and the atom is ionized. The excited atom returns to its stable state by an electron in one of its outer shells releasing its excess energy in the form of X-rays and filling the hole. The emitted X-rays have a characteristic energy for the shells involved in the activity and are characteristic of the given element. They may be used to gain chemical information about the specimen [69].

The X-rays can be detected by Si-crystal which produces electrical pulses with amplitude proportional to the energy of the incoming photon. The pulse amplitudes are measured and then stored in a multi-channel analyzer where each channel corresponds to a certain interval of pulse heights. A spectrum is then plotted showing the number of counts per energy channel. Peaks which form at certain energy levels in the spectrum can be identified and are proportional to the element(s) present within the specimen with that X-ray energy. The concentration of a given element can be determined by carrying out a quantitative analysis. A typical EDAX spectrum after collection is shown in Figure 2.25.

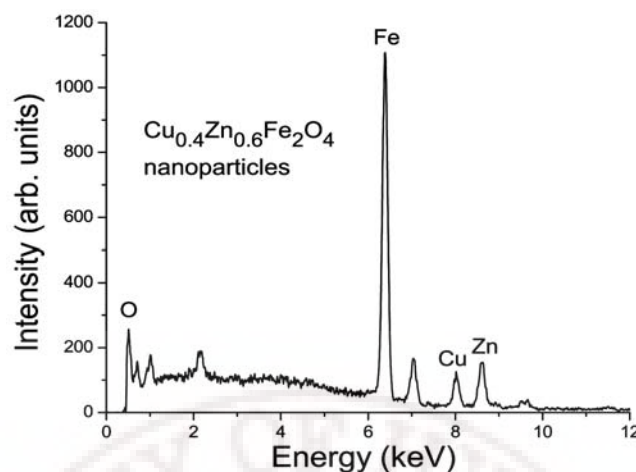


Figure 2.25: Typical EDAX spectrum obtained from $\text{Cu}_{0.4}\text{Zn}_{0.6}\text{Fe}_2\text{O}_4$ obtained in this work.

2.2.4 Profilometry

Insulating thin films are semitransparent, thus can be easily measured using optical techniques such as spectrophotometer and ellipsometry [51]. The thickness of the films in this work was measured by a profilometer, with a vertical resolution of 5\AA . Profilometry describes a class of techniques for measuring surface topography. The general operating technique is shown in Figure. 2.26.

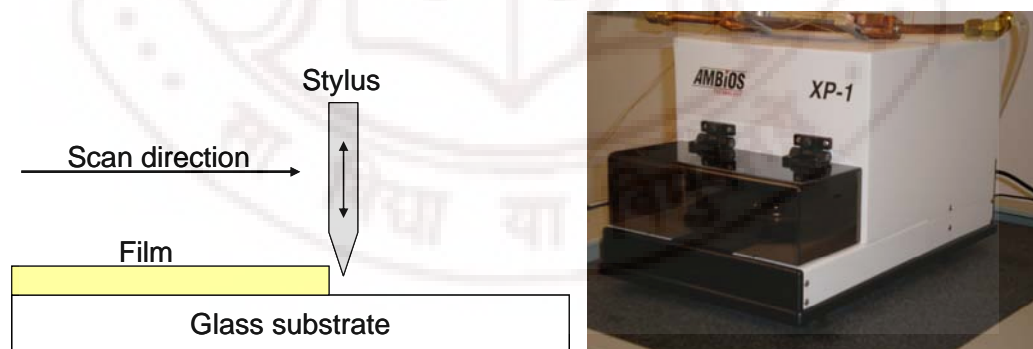


Figure 2.26: Operating Concept for a Stylus Profilometer

A mechanical diamond tip stylus is scanned across the film surface in a straight line and height is recorded. Several measurements per sample were performed to average over variations in the film thickness. The probe generates a measurable signal response, typically electrostatic or the deflection of a laser signal, proportional to the change in height of the

sample surface. These results in a direct contour trace of the sample surface with primary limitations on resolution attributed to the scratching of the film surface, substrate roughness, and vibration during measurement [51]. Stylus based profilometers can be accurate to a resolution of roughly 1 nm. This primary drawback to the profilometry technique is that a step must be patterned into the film to allow for the measurement of film thickness. For the purpose of this study the thickness measurement of ferrite films was performed using surface stylus profilometer (Ambios tech model XP-1). The samples were partially masked in order to obtain a step height between the glass substrates and the films. The thickness of ferrite thin films was measured at three different positions and averaged. Standard deviation was calculated from these.

2.2.5 Atomic force microscopy (AFM)

Atomic force microscope (AFM) [70], a non-destructive analytical technique, can be used to visualize the surface morphology and roughness of film samples with a resolution down to the atomic level. One of the major advantages of this technique is that the image obtained directly corresponds to the surface profile. It is therefore possible to extract quantitative data such as the concentration of particles, particle size, particle size distribution and surface roughness or terrace step height about the surface from the image. AFM images were obtained by scanning a probe needle over a rectangular area of the surface.

Different SPM scanning modes can be classified by the forces that they monitor and the distance between the tip and the sample surface over which the forces operate as shown in the force–distance curve in Figure 2.27. There are three primary possible operational modes with these devices: contact, intermittent contact or non-contact modes [71]. In contact-AFM mode an AFM tip makes soft physical contact with the sample where a constant normal force, typically in the nN-range, is maintained via a regulation loop. The net force measured is the sum of the attractive and repulsive forces. On the other hand, in the noncontact mode the influence of the force gradient between probe and surface on a vibrating cantilever is utilized to measure the topography. The tip-sample separation is large, typically between 1 and 100 nm. In contrast to the contact mode, the noncontact mode is less destructive. The net force detected is the attractive force between the tip and the sample [72, 73]. With intermittent

contact, or tapping mode, the probe is oscillated close to the surface where it repeatedly comes into and out of contact with the surface.

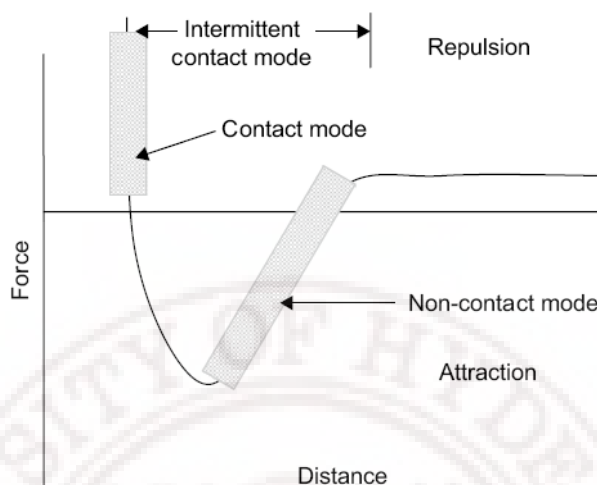


Figure 2.27: A typical force-distance curve experienced by a probe tip as it approaches a surface [70].

In this study, Nanopics 1000, SPI3800N with SPA400 (Seiko Instruments, Japan) microscope was used both in non-contact dynamic mode force microscopy (DFM) and contact mode atomic force (AFM) microscopy.

Working principle of AFM

The image is produced [72] by dragging a vibrating cantilever with a Si_3N_4 tip across the surface. When a sample brought close to a vibrating cantilever, a weak interaction force exists between the tip and the film surface that cause the tip to deflect from its equilibrium position, resulting in an amplitude change and a phase shift. A laser beam is reflected off the back of the cantilever and is detected with a split photodiode and onto a piezoelectric transducer. The degree of deflection of the tip can be measured by using this piezoelectric transducer together with a feedback loop. By adjusting the tip height during a scan so that there is no loss of vibration amplitude, a profile of the surface and topographic image can be obtained. Simplified block diagram of the atomic force microscope is shown in figure 2.28.

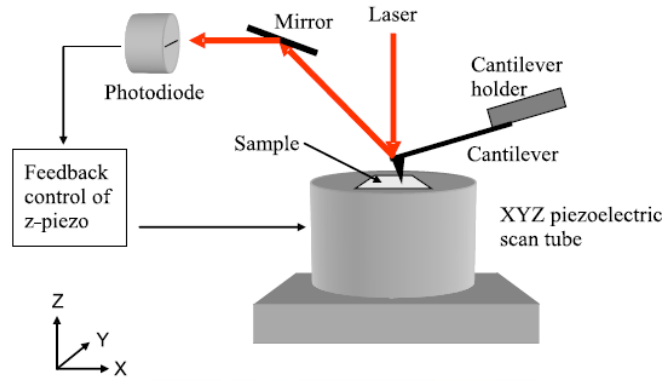


Figure 2.28: Schematic diagram of an atomic force microscope (AFM).

The resolution of the system is determined by the diameter of the tip and it is routinely possible to achieve nm-order spatial resolution. The lateral resolution is of the order of a few nanometres and the resolution in the vertical direction is better than 0.1 nm.

Two surface roughness quantities are commonly determined by the AFM: average roughness (RA) and root-mean-square roughness (RMS). For N measurements of height z and average height \bar{z} of the scanned area, the average roughness is the mean deviation of the height measurements

$$RA = \frac{1}{N} \sum_{i=1}^N |z_i - \bar{z}|$$

and the root-mean-square roughness is the standard deviation

$$RMS = \left[\frac{1}{N} \sum_{i=1}^N (z_i - \bar{z})^2 \right]^{1/2}$$

2.2.6 Vibrating Sample Magnetometer (VSM)

The vibrating sample magnetometer (VSM) is a basic instrument which was developed in 1956 by S. Foner and Van Oosterhart for characterization of the magnetic materials [74]. The VSM method is based on Faraday's law, which states that an emf will be generated in a coil when there is a change in the flux going through the coil [75]. When a material is placed within a uniform magnetic field a vibrator mechanism vibrates the sample in the magnetic

field. This causes the sample to undergo sinusoidal motion and creates a change in the magnetic flux, which is detected by pickup coils as an induction voltage. For a coil with n turns of cross-sectional area a , the emf (V) is related to dB/dt , given as [76]

$$V = -na \frac{dB}{dt}$$

Since $\Delta B = \mu_0 M$, when we place a magnetic sample into the coil, this relationship becomes

$$V = -na\mu_0 M / dt$$

The output measurement displays the magnetic moment M as a function of the field H . A schematic of the VSM system is shown in Figure 2.29. It has a pair of electromagnets that generate a DC magnetic field, and a pick-up coil that acquires the sample signals. When a sample has a net magnetization, it produces magnetic flux in its vicinity. During VSM measurements, the sample is mechanically vibrated (up and down) at a fixed frequency (generally 82Hz). This vibration produces a flux change, which generates an AC voltage proportional to the magnetic moment of the sample in the pick-up coil. A lock-in amplifier is then used to measure the voltage. The AC signal picked up by the coil is proportional to the frequency and amplitude of the sinusoidal motion and the total magnetic moment of the sample at that applied magnetic field.

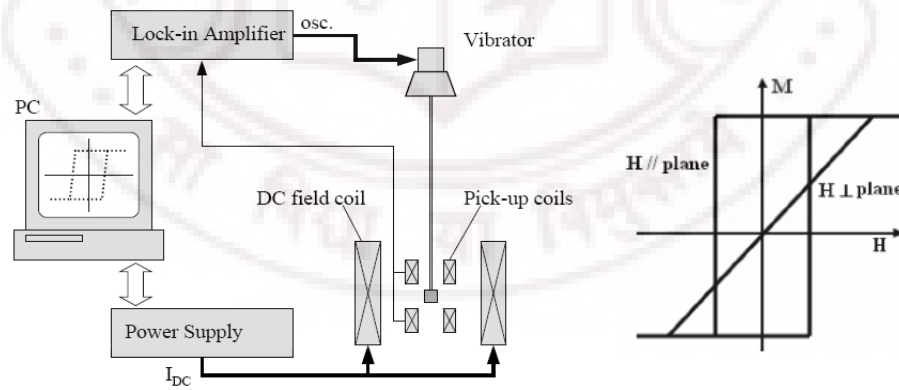


Figure 2.29: Magnetic measurements (a) block diagram of the VSM (b) idealized M-H-curves of a ferrite thin film with easy magnetization axis parallel to the film plane.

The frequency and amplitude of the sinusoidal motion are held constant, which is controlled by a capacitor (reference signal generator). By feeding the signals from the pick-up coils and the reference signal into a demodulator, the magnetic moment of the sample is

extracted [77]. The system is calibrated with a magnetic material with a known saturation magnetization, e.g. Ni. A Hall probe was used in order to determine the values of the applied field. Using the computer interface, the magnetic field and the signal proportional to the magnetic moment can be simultaneously recorded (hysteresis loops). The magnetic moment determined by VSM is given in terms of the basic electromagnetic unit (or, emu), which can be related to the magnetization, susceptibility, and Bohr magneton. VSM provides a fast and easy technique for the measurement of the magnetic properties of a material [74]. The sensitivity of VSM manufactured by Lake Shore is in the range of 10^{-6} emu which is sufficiently accurate for the samples used in this dissertation

2.2.7 Ferromagnetic resonance (FMR)

Ferromagnetic resonance (FMR) is a powerful and useful tool for studying magnetic materials [78]. It is extremely informative method to study magnetic thin films because parameters of FMR depend strongly on thin film properties which have various physical origins. FMR can be detected using a conventional electron spin resonance (ESR) spectrometer. ESR spectrometer operating at X-band frequency is commonly used instruments to measure such parameters as damping factor, gyromagnetic ratio or to observe temperature dependent phase transitions. However, comprehensive characterization of ferromagnetic materials encompasses study of various kinds of magnetic anisotropy, phase transitions with respect to magnetic field, domain wall motion etc.

The high frequency properties of the films were characterized using ferromagnetic resonance (FMR). FMR spectra were recorded using JEOL (JES-FA200) ESR Spectrometer operating at a standard X-band frequency ($\nu = 9.16$ GHz). The modulation of the magnetic field was done with a frequency of 100 kHz and amplitude 10 Oe. The first derivative dP/dH of the power absorption P was recorded as a function of applied field H in the range 0 – 8 kOe. We used 3×5 mm size samples for FMR measurements. Measurements were carried out at room temperature with two orientations of the magnetic field: in parallel and perpendicular to the film plane. The temperature dependent study of the resonance line parameters (line position, shape and width) was also carried out in the temperature range 120 to 470K with a temperature stability of ± 1 K.

For a fixed frequency of the spectrometer, the dynamic susceptibility of the sample was recorded as a function of the strength and direction of the applied field. With the spectrometer used, the reference resonance field is $H_0 = \omega_0/\gamma = 3.3$ kOe. For a given sample the field H_{res} was registered as the field for which $dP/dH = 0$. The distance between the bounding peaks of the first derivative of the absorption line was taken as the experimental width of the resonance line (see figure 2.30 for the typical resonance spectrum at X-band).

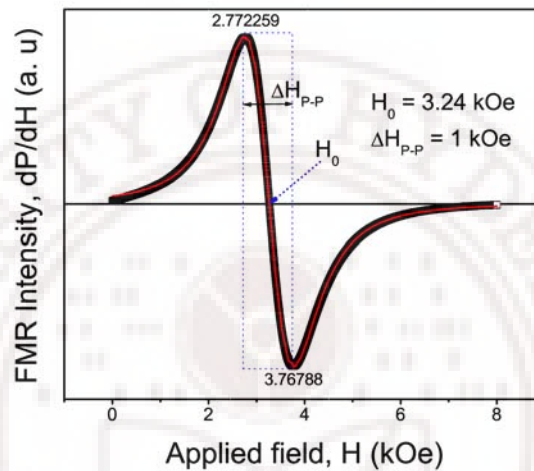


Figure 2.30: typical FMR signal of ferrite thin films recorded in this work.

The Experimental Set-Up of ESR Spectrometer

X-band ESR is widely used since the sample volume is convenient (tube diameter ~ 4 mm), giving enough information from the obtained spectra. In order to manage a successful experiment each individual sub-system must function properly. A cold temperature ESR experiment requires much preparation in the instrumental setup. A brief explanation of the crucial instruments that are necessary and their individual contribution in acquiring reasonable spectra follows.

The experimental set-up of the main components of a standard X-band EPR spectrometer used is outlined in the figure 2.31. Generally, the main components of an EPR spectrometer are listed below [79-81]:

1. Microwave Bridge
2. Cavity

3. Electromagnets
4. Signal Channel (Console)
5. User interface (Computer)

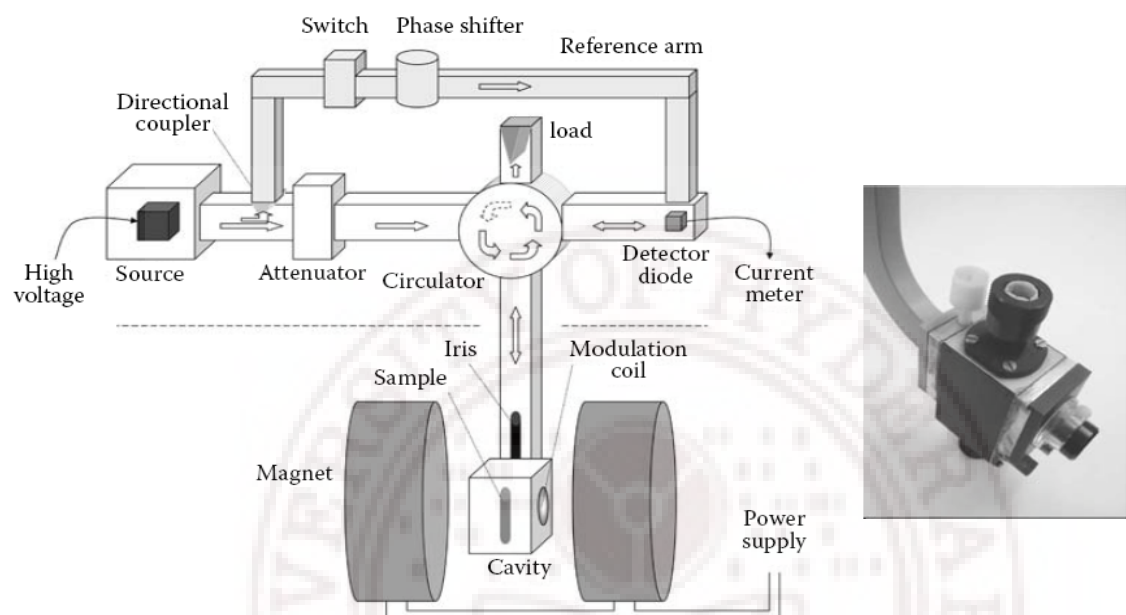


Figure 2.31: Schematic drawing of an X-band EPR spectrometer, (right) X-band cavity resonator [79].

1. The Microwave Unit

The microwave bridge functions both as a microwave source and a detector of the transmitted waves from the cavity. The microwaves are generated through a gun-diode semiconductor oscillator which is widely used to produce lower power ratio signals at X-band frequencies ($\nu = 9.2 \text{ GHz}$). The produced radiation is transferred by means of a rectangular, hollow waveguide to an attenuator where the power (200 mW) can be reduced typically by a factor between 1 and 10^6 . The output of the attenuator is transferred with a waveguide to a circulator that forces the waves into the downward waveguide to reach the resonator containing the sample. The signal microwave frequency is not permanent and adjustments can be done during the tuning process before each experiment.

The microwave radiation from the cavity is reflected to the detector, which consists of a diode that converts the microwave power to electric current, via a circulator that acts as traffic

circle by changing the route of the microwaves. The reflected microwaves are directed only to the detector and not to the source. Detection is further improved by modulating the signal. If the modulation is less than the absorption signal linewidth, the detector is sensitive to the phase of the signal, and then the derivative of the absorption signal appears. Any remaining radiation that reflects back from the detector is forced by the circulator into the upward waveguide that ends in a wedge, or taper, or “choke” to convert the radiation into heat, so that no radiation can return to the source. To control the power output of the microwave source there exists a variable attenuator that blocks the flow of microwave radiation. Thus one can more accurately determine and control the amount of microwave power exposed to the sample.

2. The Cavity

The sample is held in a microwave cavity which consists of a metal box (figure 31) that aids the amplification of weak signals from the sample. The cavity is itself positioned into a cryostat that remains under vacuum in the system. The sample which is surrounded by two large magnetic coils is swept with a magnetic field through the resonance condition.

The energy dissipation per cycle represents the amount of energy loss in one microwave period. The higher the energy loss, i.e. Q decreases, the lower the sensitivity of the spectrometer. Some of the microwave energy can be lost to the side walls of the cavity since electric currents are generated, which contribute to heat production. In order to reduce the origin of electric currents inside the cavity, the sample is placed in an electric field minimum and a magnetic field maximum. Thus bigger signals and higher sensitivities can be obtained.

The amount of microwave radiation into the cavity and the transmission back to the detector is determined by the iris. This is a hole that operates by carefully controlling the impedance (resistance) of the cavity and the waveguide. There exists a screw in front of the cavity where adjustments of the iris can be made.

3. The Signal Channel

The signal channel is built into the console which contains the required electronics for phase sensitive detection. Phase sensitive detection with magnetic field modulation increases the system sensitivity. The magnetic field is continuously modulated sinusoidally at the modulation frequency. When an EPR signal occurs, the field modulation sweeps through the signal and the transmitted microwaves from the cavity becomes amplitude modulated at the

same frequency. A reference signal, which is sensitive to signals with the same modulation frequency and phase as the field modulation, is compared to the modulated signal. The signals which do not fulfill these requirements are suppressed.

If higher modulation amplitudes give rise to increased intensities, too high modulation amplitudes can subject broadening and distortion of the signal. A good rule of thumb is to use modulation amplitude that is less than the linewidth of the signal. Otherwise, difficulties in resolving signals from each other may occur.

4. The Magnetic Field Controller

The magnetic field controller is used to control the magnetic field sweep through the sample. The controller sets the field values, the sweep time and the current that flows in each magnet coil (windings). The controller regulates the magnetic field by receiving a reference value, in numerous times, which correspond to the magnetic field value. In between the two magnets a Hall probe is placed. This is influenced by the magnetic field such that it produces a voltage which is dependant of the field. The controller can then regulate the field by comparing the voltage produced by the Hall probe with the previously set reference voltage. Whenever there is a difference in voltage the magnetic power supply changes the amount of current that flows through the magnets and hence the magnetic field.

5. The User (operator) Interface

The JEOL ESR-spectrometer has Acquisition Software configured for various types of measurements, i.e. different resonators. The knobs of the spectrometer are all switches in the software of the spectrometer's computer. The computer software is active (i.e. setting, regulating, and calibrating the spectrometer). The functions to set and their main parameters in parentheses are the microwave (frequency, attenuated intensity), the magnet (center field, scan range), the modulation system (strength, frequency), the amplifier (gain), and the data recorder (scan rate and damping time constant). The temperature of the optional cooling (or heating) system is set on a separate control system.

2.2.8 Optical transmittance

The transmission spectra of the films were recorded on a UV-Vis-NIR spectrophotometer (JASCO -V570 & V670). The spectrophotometer features an all-reflecting, double-

monochromator optical system. The components are coated with silica for durability. Holographic gratings are used in the monochromator for the ultra-violet and visible light range and near infrared range.

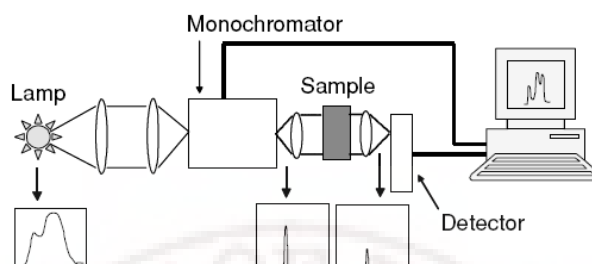


Figure 32: Schematic diagram of the UV-Vis-NIR spectrophotometer [82]

Figure 2.32 is a schematic diagram illustrating the operation of a spectrometer. Basically, the instrument has two radiation sources that cover the full operating wavelength of the spectrometer from 190 nm to 3000 nm, a monochromator that is responsible for passing monochromatic light to the sample, and two photodetectors for measuring the transmittance at different wavelength regions. The deuterium lamp and halogen lamp are the two radiation sources. The later is in charge of the wavelength in the visible to near infrared region, i.e. from 300 nm to 3300 nm, while the other is in charge of those wavelengths from 185 nm to 350 nm.

The monochromator uses reflection gratings and entrance-and-exit slits to pass monochromatic light to the sample. The transmittance of the monochromatic light that passed through the sample is measured by a photomultiplier operating in the ultraviolet and visible region and a lead sulfide (PbS) detector operating in the near infrared region. One thing to note here is that all transmittance values shown by the instrument are in relative terms. It shows what percentage of light, from 0% to 100%, gets transmitted through the sample with respect to another parallel and unobstructed reference beam.

Reflectivity spectra provide similar and complementary information to the transmission and absorption measurements. For instance, absorption coefficients corresponding to the fundamental absorption are as high as $10^5 - 10^6 \text{ cm}^{-1}$, so that they can only be measured by using very thin samples (thin films). In these cases, the reflectivity spectra $R(\nu)$ can be very advantageous, as they manifest the singularities caused by the absorption process but with the

possibility of using bulk samples [82-84]. The reflectivity at each frequency is defined by

$$R = \frac{I_R}{I_0} \text{ where } I_R \text{ is the reflected intensity.}$$

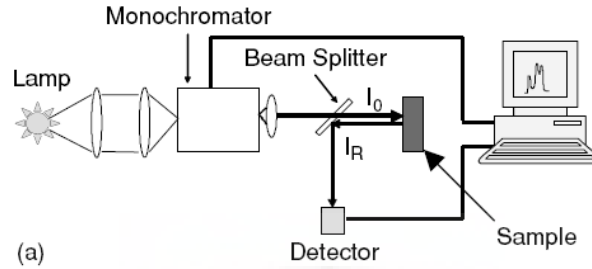


Figure 2.33: An experimental arrangement used to measure direct reflectivity spectra [82].

Reflectivity spectra can be registered in two different modes [82] *direct reflectivity* or *diffuse reflectivity*. Direct reflectivity measurements are made with well-polished samples at normal incidence. Diffuse reflectivity is generally used for unpolished or powdered samples. For direct reflectivity measurements (Figure 2.33), monochromatic light (produced by a lamp and a monochromator) is passed through a semitransparent lamina (the beam splitter). This lamina deviate the light reflected in the sample toward a detector.

2.2.9 Dielectric measurements

In addition to the magnetic properties, ferrite materials also exhibit good dielectric properties. The dielectric properties determine the response of a material when placed in an electric field [85, 86]. For most applications of ferrite materials, the dielectric constant (ϵ') and dielectric loss ($\tan\delta$) are important practical parameters. Studies of the dielectric properties provide a great deal of information about the suitability of the material for various applications. Dielectric properties (ϵ_r) are always presented relative to the dielectric constant of the vacuum (ϵ_0). The dielectric properties of ferrite materials are determined by the electrical permittivity (ϵ') also known as the dielectric constant and the electrical conductivity (σ)

$$\epsilon' = C_p t / \epsilon_0 A$$

where ϵ_0 is the permittivity of the free space, t is the thickness of the sample and A is the surface area of the sample [87]

$$\rho_{AC} = \frac{1}{\epsilon' \epsilon_0 \omega \tan \delta}$$

In figure 2.34 the permittivity is presented as a capacitor. The capacitor is placed parallel to the resistor, the latter presenting the conductivity.

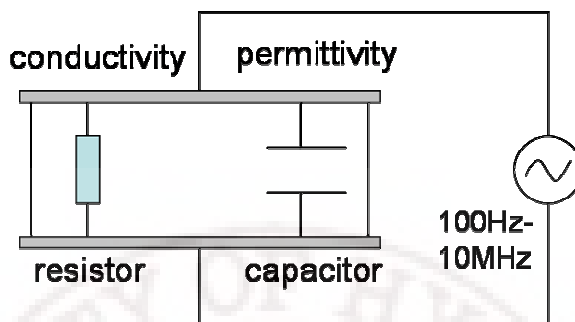


Figure 2.34: Dielectric measurement setup. A parallel plate condenser with dielectric

Dielectric measurements (dielectric constant, loss) were carried out using Agilent 4294A impedance Analyzer interfaced to a PC. Signal of 0.5V was applied to the samples. The Agilent 4294A Precision Impedance Analyzer provides highly accurate 4-terminal-pair impedance measurement in a wide frequency range of 40 Hz to 110 MHz and extremely small variation in component characteristics that can be precisely evaluated with sweep measurements of 0.08% basic accuracy. This instrument is very good for component evaluation like capacitors, inductors, resonators, semiconductors and for material evaluations like toroidal cores and it also has a wide range of measurement parameters.

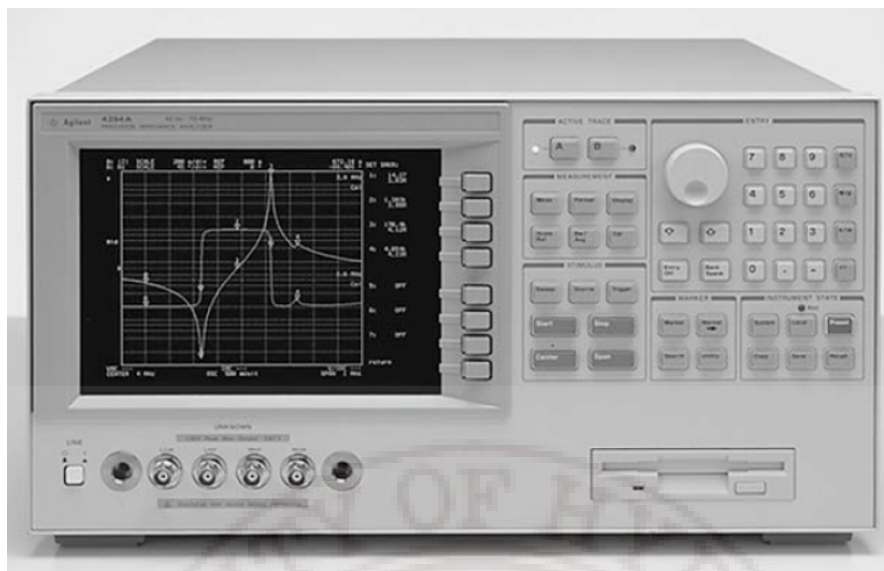


Figure 2.35: Agilent 4294A Precision Impedance Analyzer front panel (40Hz–110 MHz).

The front panel of the Agilent 4294A provides several blocks of hardkeys and an LCD display with a series of softkeys along its right-hand edge. Also, there are a number of test connectors and a power switch beneath the LCD display. Figure 2.35 shows the front panel of the Agilent 4294A.

Measurements on the samples were done at room temperature as a function of frequency and composition. The electrical contacts were made by using silver paste electrodes on bulk ferrite pellets to study the electrical properties of ferrite ceramics. The sintered pellets were polished to a smooth finish and cleaned thoroughly. The flat surfaces of pellets were coated with silver paste, which gives the metal-insulator-metal structure to the pellets which are ready for electrical measurements.

The AC impedance was also measured in the frequency range 100 kHz to 13 MHz. The impedance $|Z|$ and the phase difference (θ) between the voltage and current were measured as a function of frequency for the given sample. Analysis of the data is carried out by plotting the imaginary part of the impedance $Z'' = |Z| \cos\theta$ against the real part $Z' = |Z| \sin\theta$ on a complex plane called the impedance plot. An impedance plot with linear scale is used to analyze the equivalent circuit. The intercept on the Z' axis on the low frequency side gives the room temperature DC resistance [88].

References

- [1] S. E. Dann, *Reactions and Characterization of Solids*, The Royal Society of Chemistry, Great Britain (2000).
- [2] U. Schubert and N. Husing, *Synthesis of inorganic materials*, 2nd Ed. Wiley-VCH Verlag, Germany (2005).
- [3] G. Winkler, *Crystallography, chemistry and technology of ferrites*, In: Magnetic properties of materials Ed. by J. Smit, McGraw-Hill, USA, (1971).
- [4] M. Paulus, *Preparation conditions of the ferrites in Preparative methods in solid state chemistry* Ed. by P. Hagenmuller, Academic Press, New York (1972).
- [5] B. B. Ghate and A. Goldman, *Ferrimagnetic ceramics*, In: Materials science and technology, Vol 11 “structure and properties of ceramics Ed by M.V. Swain” Ed R.W. Cahn, P Haasen and E.J. Kramer (1994).
- [6] M. N. Rahaman, *Ceramic processing and sintering* 2nd Ed. Marcel Dekker, New York (2005).
- [7] S-J. L. Kang, *Sintering: densification, grain growth and microstructure*, Elsevier, Butterworth-Heinemann, GB (2005).
- [8] J. S. Reed, *Principles of Ceramics Processing*, 2nd Ed. John Wiley, New York (1995).
- [9] J. Zhu and K. J. Tseng, *IEEE Trans. Magn.* **40** (2004) 3339 – 3345.
- [10] R.H. Kodama, Magnetic nanoparticles, *J. Magn. Magn. Mater.* 200 (1999) 359-372.
- [11] H. Nathani, S. Gubbala and R. D. K. Misra, *Mater. Sci. Eng. B* 121 (2005) 126–136.
- [12] T. Hyeon, *Chem. Commun.* (2003) 927-934.
- [13] L. Patron, I. Mindru and G. Marinescu, *Magnetic Nanomaterials: Nonconventional Synthesis and Chemical Design*, In: Dekker Encyclopedia of Nanoscience and Nanotechnology, Marcel Dekker (2004).
- [14] K. C. Patil, M. S. Hegd, T. Rattan and S. T. Aruna, *Chemistry of Nanocrystalline Oxide Materials*, World Scientific, Singapore (2008).
- [15] A-H. Lu, E. L. Salabas, and F. Schth, *Angew. Chem. Int. Ed.* 46 (2007) 1222 – 1244.
- [16] M. A. Willard, L. K. Kurihara, E. E. Carpenter, S. Calvin and V. G. Harris, *International Mater. Rev.* 49 (2004) 125 – 170.
- [17] A. Goldman, *Modern Ferrite Technology*, 2nd Ed. Springer Science, New York (2006).
- [18] B. L. Cushing, V. L. Kolesnichenko and C. J. O'Connor, *Chem. Rev.* 104 (2004) 3893-3946.
- [19] C. Suryanarayana, *Mechanical Alloying and Milling*, Marcel Dekker, New York (2004).
- [20] M. S. El-Eskandarany, *Mechanical alloying for fabrication of advanced engineering materials*, Noyes, New York (2001).
- [21] C. Suryanarayana, *Non-equilibrium Processing of Materials*, Elsevier, (1999).
- [22] C. N. Chinnasamy, A. Narayanasamy, N. Ponpandian, K. Chattopadhyay, H. Guerault and J-M. Greneche, *J. Phys.: Condens. Matter* **12** (2000) 7795–7805.
- [23] M. Hofmann, S. J. Campbell, H. Ehrhardt and R. Feyerherm, *J. Mater. Sci.* **39** (2004) 5057 – 5065.
- [24] A. S. Edelstein, and R. C. Cammarata, ed., *Nanomaterials: Synthesis, Properties and Applications*, IoP, Bristol and Philadelphia (1996).
- [25] Suslick, K. S., Ed. *Ultrasound: Its Chemical, Physical, and Biological Effects*, Wiley-VCH, New York (1998).

- [26] C.N.R. Rao, P.J. Thomas and G.U. Kulkarni, *Nanocrystals: Synthesis, Properties and Applications*, Springer, Verlag, Berlin, Heidelberg (2007).
- [27] C. J. Brinker, and G. W. Scherer, *Sol–Gel Science: The Physics and Chemistry of Sol–Gel Processing*, Academic Press, San Diego (1990).
- [28] C. C. Koch, I. A. Ovidko, S. Seal and S. Veprek, *Structural Nanocrystalline Materials: Fundamentals and Applications*, Cambridge University Press, New York (2007).
- [29] J. A. Rodriguez and M. F.-Garcia (Ed.), *Synthesis, properties, and applications of oxide nanomaterials*, Wiley, New Jersey (2007).
- [30] M. Fanun, *Microemulsions: Properties and Applications*, Taylor & Francis, CRC Press (2009).
- [31] P. Kumar, *Handbook of Microemulsion Science and Technology*, Marcel Dekker Inc, New York (1999).
- [32] D. O. Shah, *Micelles, Microemulsions, and Monolayers: Science and Technology*, Marcel Dekker, New York (1998).
- [33] K. Byrappa and M. Yoshimura, *Handbook of Hydrothermal Technology*, NoYes, New Jersey (2001).
- [34] S-H. Yu, T. Fujino and M. Yoshimura, *J. Magn. Magn. Mater.* **256** (2003) 420–424.
- [35] A. Pathak and P. Pramanik, *Nanoparticles of oxides through chemical methods*, PINSA 67 (2001) 47-70.
- [36] A.I. Gusev and A.A. Rempel, *Nanocrystalline materials*, Cambridge Intern. Sci. Pub. (2004).
- [37] P. Tartaj, M. del Puerto Morales, S. Veintemillas-Verdaguer, T. Gonzalez-Carreno, and C. J. Serna, *J. Phys. D: Appl. Phys.* 36 (2003) R182-R197.
- [38] E. Auzans, *Thesis: Mn-Zn Ferrite nanoparticles for water and hydrocarbon based ferrofluids: preparation and properties*, Institute of Physics of Latvian University (1999).
- [39] A.A. Voevodin and M.S. Donley, *Surf. Coat. Technol.* **82** (1996) 199–213
- [40] S. Zhang and N. Ali, *Nanocomposite thin films and coatings*, Imperial College Press, London (2007).
- [41] K. Wasa, M. Kitabatake and H. Adachi, *Thin film materials technology: sputtering of compound materials*, William Andrew, New York (2004).
- K. Wasa and S. Hayakawa, *Handbook of Sputter Deposition Technology*, Noyes, New Jersey (1992).
- [42] J. George, *Preparation of thin films*, Marcel Dekker, New York (1992).
- [43] K. S. Sree Harsha, *Principles of vapor deposition of thin films*, Elsevier (2006)
- [44] R. Eason, *Pulsed laser deposition of thin films*, Wiley, New Jersey (2007).
- [45] R. A. Powell and S. M. Rossnagel, *PVD for Microelectronics: Sputter Deposition Applied to Semiconductor Manufacturing*, Academic Press, San Diego (1999).
- [46] J. A. Thornton and J. E. Greene, *Sputter deposition processes*, In: R. F. Bunshah, (ed.), *Deposition technologies for films and coatings*, 2nd ed. Noyes, New Jersey, (1994).
- [47] B. Chapman, *Glow discharge processes: Sputtering and plasma etching*, Wiley, New York (1980).
- [48] R. F. Bunshah, (ed.), *Deposition technologies for films and coatings*, 2nd ed. Noyes Publications, New Jersey, (1994).
- [49] A. Rockett, *The materials science of semiconductors*, Springer, New York (2008)
- [50] D. M. Mattox, *Handbook of physical vapor deposition processing*, Noyes Publications, New Jersey (1998).

- [51] M. Ohring, *The Materials science of thin films*, Academic Pres, San Diego (1992)
- [52] K. Ellmer, *J. Phys. D: Appl. Phys.* 33 (2000) R17-R32.
- [53] J. E. Mahan, *Physical vapor deposition of thin films*, John Wiley & Sons, New York (2000).
- [54] L. B. Freund and S. Suresh, *Thin film materials: Stress, Defect Formation and Surface Evolution*, (2003)
- [55] M. Ohring, *Materials science of thin films*, 2nd Ed. Academic Press, San Diego (2002).
- [56] K. Seshan, *Handbook of thin film deposition processes and techniques*, 2nd ed. NoYes, New Jersey (2002).
- [57] J. A. Thornton, *Annual Rev. Mater. Sci.* 7 (1977) 239-260.
- [58] C. V. Thompson, *Annual Rev. Mater. Sci.* 30 (2000) 159-190.
- C. V. Thompson and R. Carel, *J. Mech. Phys. Solids* 44 (1996) 657-673.
- [59] D. Depla, S. Mahieu and J. E. Greene, *Sputter Deposition Processes*. In: Ed. P. M. Martin, *Handbook of deposition technologies for films and coatings*, 3rd ed. Elsevier, USA (2010).
- [60] D. Depla and S. Mahieu, *Reactive Sputter Deposition*, Springer-Verlag, Berlin Heidelberg (2008).
- [61] G. Franz, *Low pressure plasmas and microstructuring technology*, Springer-Verlag, Berlin, Heidelberg (2009), p. 377.
- [62] M. Birkholz, P. F. Fewster and C. Genze, *Thin Film Analysis by X-Ray Scattering*, WILEY-VCH Germany (2009).
- [63] B.D. Cullity and S. R. Stock, *Elements of X-Ray Diffraction*, 3rd Ed., Prentice Hall, New Jersey, USA (2001)
- [64] T. L. Alford, L. C. Feldman and J. W. Mayer, *Fundamentals of Nanoscale Film Analysis*, Springer, New York (2007).
- [65] W. Zhou and Z. L. Wang, Ed. *Scanning Microscopy for Nanotechnology*, Springer, New York (2006).
- [66] J. Goldstein, D. Newbury, D. Joy, C. Lyman, P. Echlin, E. Lifshin, L. Sawyer and J. Michael, *Scanning Electron Microscopy and X-Ray Microanalysis*, 3rd. Ed., Plenum Publishers, New York, (2003).
- [67] D. J. Stokes, *Principles and practice of variable pressure/environmental scanning electron microscopy*, John Wiley & Sons, UK (2008).
- [68] W. Zhou and Z. L. Wang, Ed., *Scanning microscopy for nanotechnology*, Springer, New York (2006).
- [69] A. J. Garratt-Reed and D. C. Bell, *Energy-Dispersive X-Ray Analysis in the Electron Microscope*, BIOS Scientific, Oxford, UK (2003).
- [70] W. R. Bowen and N. Hilal, *Atomic force microscopy in progress engineering*, Elsevier, UK (2009).
- [71] AR Clarke and CN Eberhardt, *Microscopy techniques for materials science*, Woodhead, CRC, England (2002).
- [72] K.S. Birdi, *Scanning probe microscopes: applications in science and technology*, CRC Press, Florida, USA (2003).
- [73] H. S. Nalwa, Ed., *Advances in surface science*, Academic Press, San Diego (2001).
- [74] B. D. Cullity and C. D. Graham, *Introduction to magnetic materials*, 2nd ed. IEEE, New Jersey (2009)
- [75] H. Zijlstra, *Experimental methods in magnetism*, North-Holland Publishing, Amsterdam (1967).

- [76] K. H. J. Buschow and F. R. de Boer, *Physics of magnetism and magnetic materials*, Kluwer Academic, New York (2004).
- [77] F. Fiorillo, *Measurement and characterization of magnetic materials*, Elsevier, Amsterdam (2004).
- [78] A. P. Guimaraes and I. S. Oliveira, *Magnetism and magnetic resonance in solids*, Wiley, New York (1998).
- [79] W. R. Hagen, *Biomolecular EPR Spectroscopy*, Taylor & Francis Group, CRC Press, USA (2009).
- [80] C. P. jr. Poole, *Electron Spin Resonance*, A comprehensive treatise on experimental techniques, 2nd ed, John Wiley & Sons, New York (1983).
- [81] J. A. Weil and J. R. Bolton, *Electron paramagnetic resonance: elementary theory and practical applications*, 2nd Ed. John Wiley, New Jersey (2007).
- [82] J. G. Sole, L. E. Bausa and D. Jaque, *An introduction to the optical spectroscopy of inorganic solids*, John Wiley, New Jersey (2005).
- [83] H. Kuzmany, *Solid-State Spectroscopy*, Springer-Verlag Berlin Heidelberg (2009).
- [84] M. Fox, *Optical properties of solids*, Oxford University press, Great Britain (2001).
- [85] K. C. Kao, *Dielectric phenomena in solids*, Elsevier, USA (2004).
- [86] G. G. Raju, *Dielectrics in Electric Fields*, Marcel Dekker, New York (2003).
- [87] D. B. Sirdeshmukh, L. Sirdeshmukh and K. G. Subhadra, *Micro- and Macro-Properties of Solids: Thermal, Mechanical and Dielectric Properties*, Springer, New York (2006).
- [88] E. Barsoukov and J. R. Macdonald *Impedance Spectroscopy: Theory, Experiment, and Applications* 2nd Ed. Wiley, New Jersey 2005.

CHAPTER-3

Properties of bulk Cu-Zn ferrites

This chapter consists of studies of various properties of bulk $\text{Cu}_{1-x}\text{Zn}_x\text{Fe}_2\text{O}_4$. The results and discussion of the structural, magnetic and dielectric measurements on the samples are described in detail.

3.1 Crystal Structure

The crystal structure determination of the bulk ferrite samples was carried out using powder X-ray diffraction (XRD). The XRD patterns of $\text{Cu}_{1-x}\text{Zn}_x\text{Fe}_2\text{O}_4$ with ($x = 0.0, 0.2, 0.4, 0.6, 0.8$ and 1.0) are shown in figure 3.1. The patterns show sharp peaks corresponding to a single phase spinel structure. No impurity or secondary phase was detected. It can be seen that for the compositional range $0 < x \leq 1$ the index of reflection planes (111), (220), (311), (222), (400), (422), (511), and (440) are indications of the presence of the cubic symmetry whereas for $x = 0$ it shows tetragonal structure.

The lattice parameters (a) were computed using the d-spacing values, which were calculated using Bragg's law, and the respective (hkl) parameters. The values of lattice parameter found for CuFe_2O_4 ($a = 8.20$ (0.01), $c = 8.69$ (0.01) Å) and for ZnFe_2O_4 ($a = 8.44$ (0.003) Å) agree well with those reported in JCPDS (Joint Committee on Powder Diffraction Standards) card numbers 06-0545 and 22-1012, respectively. The compositional dependence of lattice parameter (a) is shown in Figure 3.2. It can be seen that the lattice parameter increases almost linearly with the increase in Zn-content (x) in accordance with the Vegard's law [1] suggesting the formation of a homogeneous solid solution between CuFe_2O_4 and ZnFe_2O_4 . This behavior has also been reported by Banerjee et al. [2]. The difference in the values of the lattice constant of Cu and Zn ferrite may be due to the different scattering source, sintering and preparation techniques.

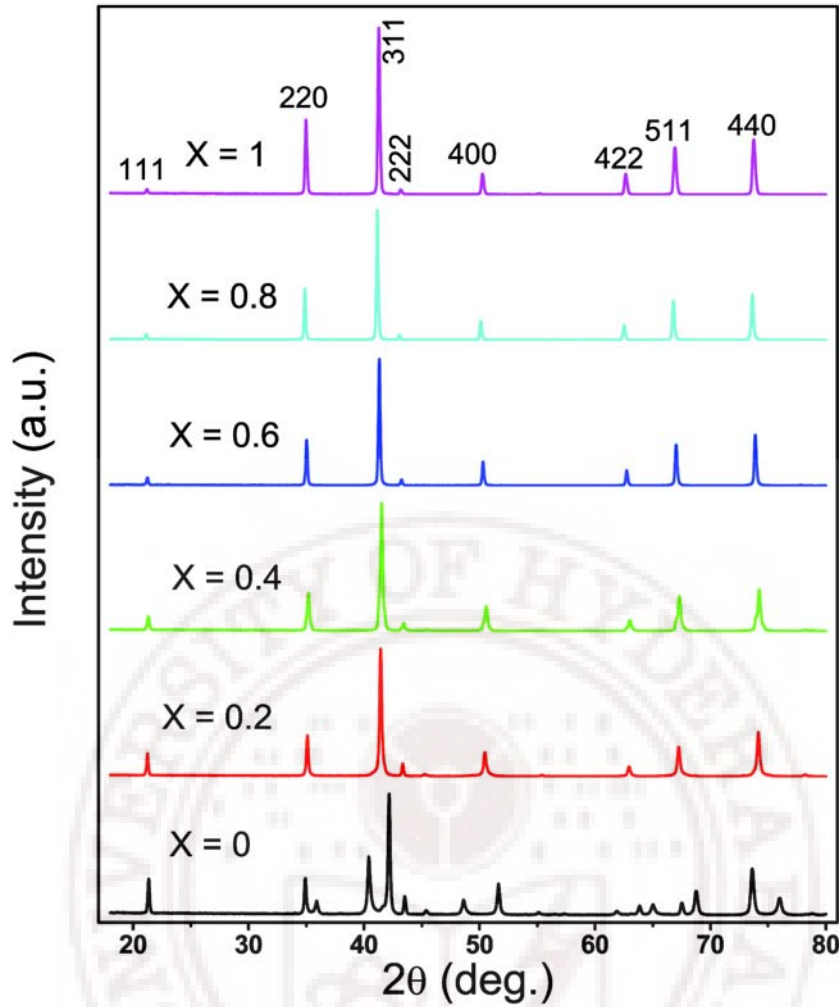


Figure 3.1: XRD patterns of bulk $\text{Cu}_{1-x}\text{Zn}_x\text{Fe}_2\text{O}_4$ system

It is reported that the Cu^{2+} ions have a marked preference for octahedral sites [3] due to their favorable fit of charge distribution of this ion in the crystal field of the octahedral site [4,5]. On the other hand, the Zn^{2+} ions have preference for tetrahedral sites [6,7] due to their readiness to form covalent bonds involving sp^3 hybrid orbit [8]. So the linear increase in lattice constant with zinc content can be attributed to the larger ionic size of Zn^{2+} (0.82\AA) compared to that of Cu^{2+} (0.70\AA) [9]. Such effects of cationic size differences are also reported by Mangalarga et al. [8] and Hirota et al. [10].

X-ray density (d_x) was calculated using the formula $d_x = nM / N_A a^3$ [11] where n is the number of molecules in a unit cell ($n = 8$ for spinel structure), M , N_A , and a are the molecular weight, Avogadro's number, and the lattice parameter, respectively. The X-ray density (d_x) depends on the lattice parameter and the molecular weight of the sample

whereas the bulk density (d) is being calculated from the geometry and mass of the samples. The compositional dependence of both densities d_x and d has been plotted in figure 3.2. It can be seen that both d and d_x decrease with increasing zinc concentration. The percentage porosity ($P\%$) of the samples was calculated using the following relation [10]:

$$P(\%) = \left[1 - \frac{d}{d_x} \right] \times 100$$

where d and d_x are the bulk density and X-ray density respectively. The porosity of the samples increases with increasing Zn-content.

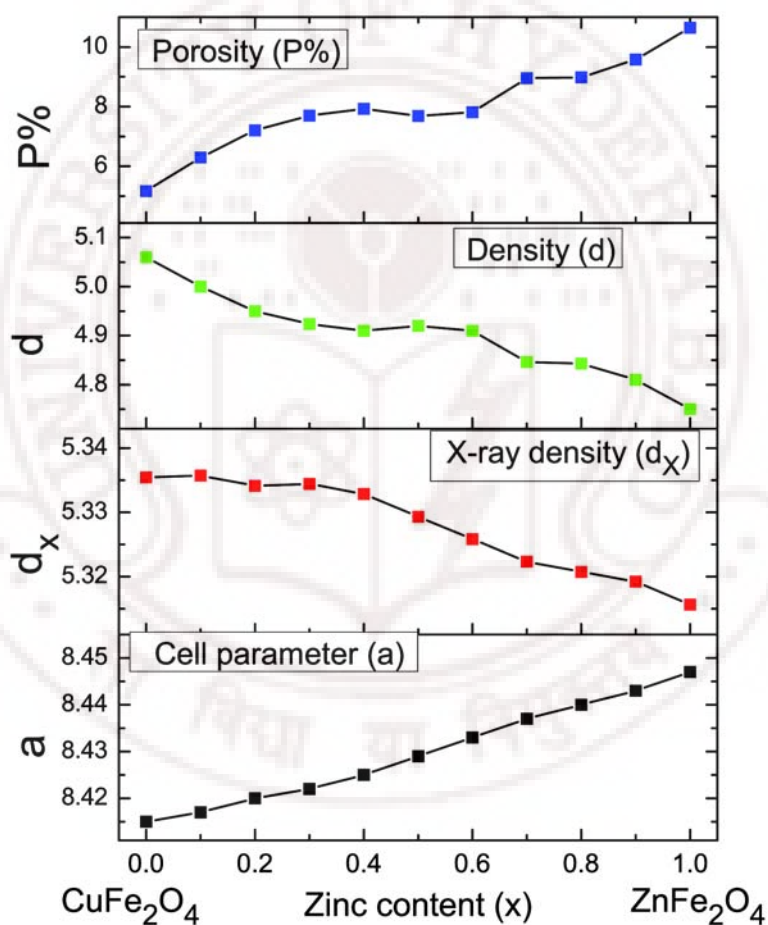


Figure 3.2: Variation of lattice parameter, density and porosity of $\text{Cu}_{1-x}\text{Zn}_x\text{Fe}_2\text{O}_4$.

3.2 Microstructure analysis

The Information about the microstructure of the bulk CuZn-ferrite samples was obtained from the SEM images taking in the secondary electron mode. SEM analysis is useful to study the microstructure of different compositions of ferrite and to identify the phases formed during sintering process. It is also useful to interpret the porosity percentage and estimate the grain size, shape and grain size distribution. The SEM images of the samples sintered at 1000 °C for 12 hrs are shown in figure 3.3. All the ferrite samples showed very good densification upon sintering. SEM of the surfaces of the sintered ferrites showed little or no intergranular porosity. It has been found that the porosity increases with increase in the grain size. It is to be noted here that there are some pores present; in the final structure that is unavoidable since 100% theoretical density is never achieved during any sintering process. The images show that the powder grains are free from anisotropy or secondary phase. The mean grain size of the samples increases drastically from about 1 μm for $x = 0$ to about 70 μm for $x = 0.8$. The magnetic, electrical and mechanical properties of ferrites are found to be dependent on the microstructure of the samples [3].

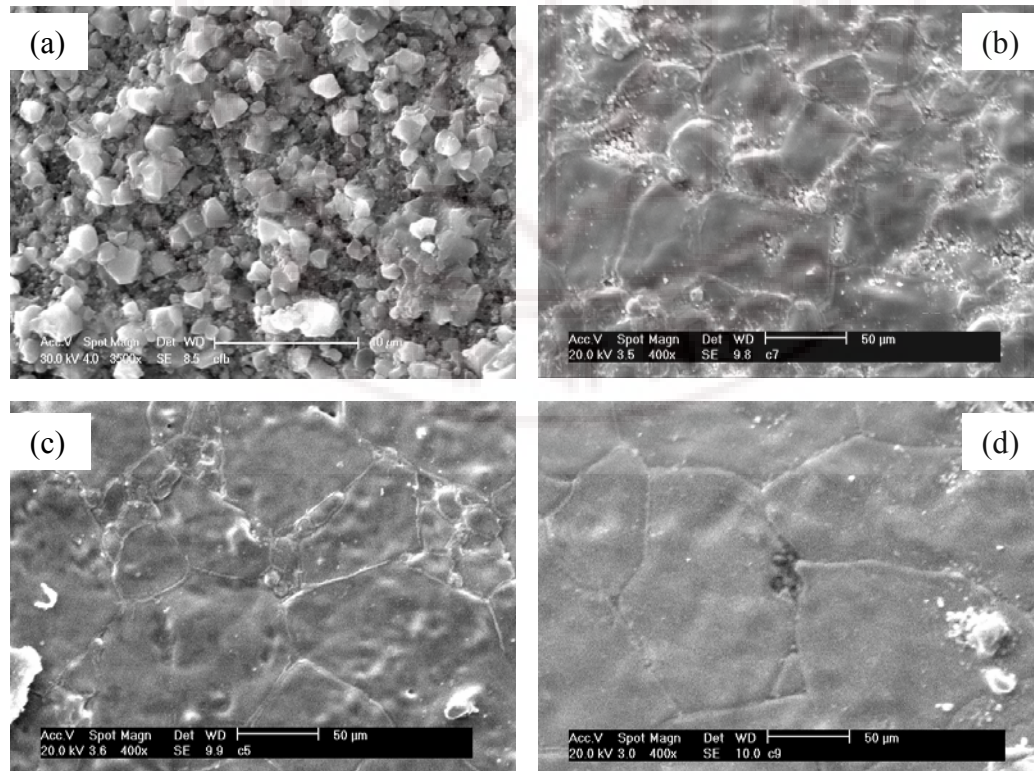


Figure 3.3: SEM images of $\text{Cu}_{1-x}\text{Zn}_x\text{Fe}_2\text{O}_4$ sintered at 1000°C for 12 hrs for $x =$ (a) 0, (b) 0.3, (c) 0.5 and (d) 0.8

The characterization of the Cu-Zn ferrite samples sintered at 1000 °C for 12 Hrs was completed by the EDAX analysis using systematic data collected from the samples. For each sample we have checked the homogeneity by averaging the readings at three different positions from the centre and the edges. The relative elemental concentration from EDAX spectra of figure 3.4 are given in table 3.1. The values are normalized to the nominal composition of the starting materials. The Cu/Zn/Fe/O ratios were found to be within ~ 3-6 % of the starting composition. It can be seen that the samples are iron rich and the concentration of iron increases with increasing zinc content which is attributed to loss of the divalent Zn ions during sintering process.

Table 3.1: The calculated and measured composition of the $\text{Cu}_{1-x}\text{Zn}_x\text{Fe}_2\text{O}_4$ ferrite system by EDAX analysis. (The atomic weight of Zn = 65.38, Cu = 63.546, Fe = 55.847, O = 15.9994)

Zinc content	M (g)	Cu		Zn		Fe		O	
		Cal.	Obs.	Cal.	Obs.	Cal.	Obs.	Cal.	Obs.
0	239.24	26.56	25.56	0	0	46.69	49.15	26.75	25.29
0.1	239.42	23.89	22.46	2.73	2.95	46.65	49.60	26.73	24.99
0.2	239.60	21.22	17.95	5.46	5.68	46.61	48.19	26.71	28.19
0.3	239.79	18.55	16.42	8.18	7.42	46.58	49.01	26.69	27.15
0.4	239.97	15.89	14.81	10.90	9.90	46.54	48.31	26.67	26.98
0.5	240.15	13.23	14.04	13.61	11.49	46.51	46.92	26.65	27.55
0.6	240.34	10.58	8.18	16.32	14.70	46.47	47.03	26.63	30.09
0.7	240.52	7.93	7.11	19.03	18.32	46.44	50.53	26.61	24.04
0.8	240.71	5.28	6.44	21.73	20.95	46.40	47.88	26.59	24.73
0.9	240.89	2.64	2.34	24.43	22.56	46.37	50.95	26.57	24.15
1.0	241.07	0	0	27.12	25.45	46.33	51.03	26.55	23.52

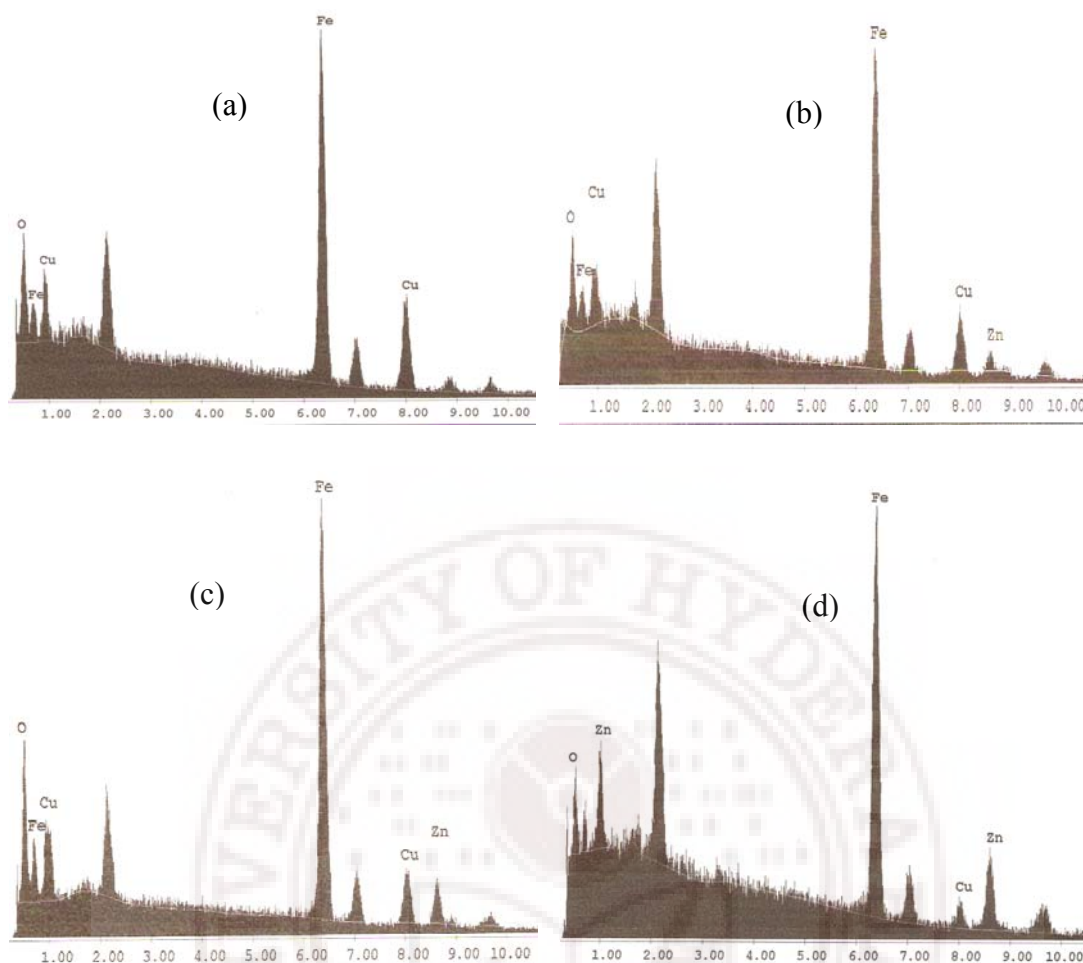


Figure 3.4: EDAX spectra of $\text{Cu}_{1-x}\text{Zn}_x\text{Fe}_2\text{O}_4$ sintered at 1000°C for 12 hrs for $x =$ (a) 0, (b) 0.3, (c) 0.5 and (d) 0.8

3.3 Magnetization studies

Figure 3.5 shows the M-H plots for the synthesized samples with concentrations ($X = 0.0, 0.1, 0.4, 0.6, 0.7$) obtained using vibrating sample magnetometer (VSM) at room temperature. For the sake of clarity the data for other compositions are not included in the figure. Each loop shows low coercivity H_C and low remanence (except for $x = 0$) indicating that the samples belong to the family of soft ferrites. The variation of coercivity H_C and saturation magnetic moment n_B as a function of Zn content are listed in table 3.2.

It is observed that H_C decreases with increasing Zn content. This may be attributed to the decreasing of the magnetic anisotropy due to increasing grain size with increasing Zn content. This is in accordance with the result states that the coercive force is inversely proportional to grain size and directly proportional to magnetocrystalline anisotropy

constant [12]. M_S and n_B increase with increase in Zn content up to 40%. For higher Zn content these parameters show decreasing trend.

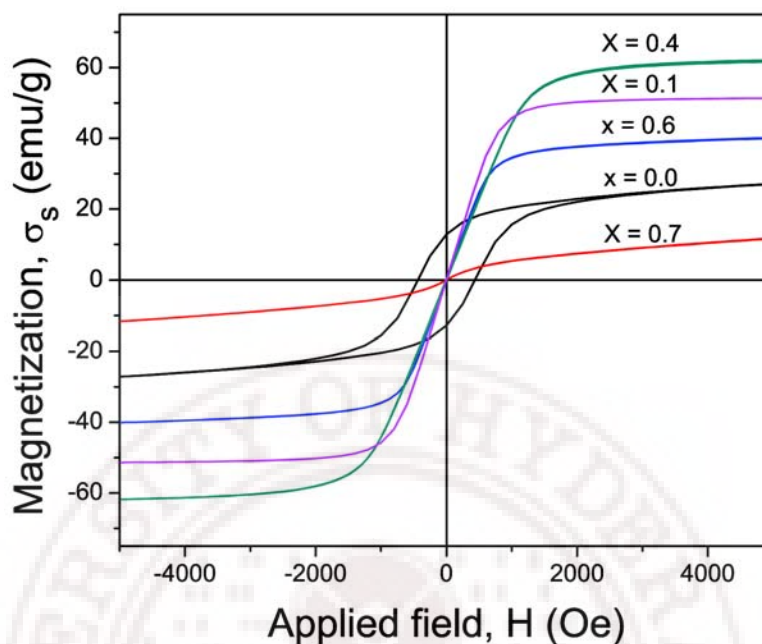


Figure 3.5: M-H Plots of $\text{Cu}_{1-x}\text{Zn}_x\text{Fe}_2\text{O}_4$ sintered at 1000°C for 10hrs

The magnetization in copper ferrite ($x = 0$) can be explained on the basis of Neel's model. Neel's two sublattices model explains the magnetic properties of ferrimagnetic materials based on the spin moments of the individual ions in the crystal.

Table 3.2: The magnetic parameters extracted from the M-H plots of $\text{Cu}_{1-x}\text{Zn}_x\text{Fe}_2\text{O}_4$

Zinc content (x)	Saturation Magnetization, M_S (emu/g)	Saturation magnetic moment, n_B (μ_B)	Coercivity, H_c (Oe)
0.0	38.29	1.64	440
0.1	51.38	2.20	1.7
0.2	58.48	2.51	1.8
0.3	60.92	2.61	1.0
0.4	62.17	2.67	0.8
0.5	55.84	2.40	0.7
0.6	40.17	1.73	0.5

Copper ferrite (CuFe_2O_4) crystallizes in inverse spinel structure. The magnetic ions (Fe^{3+} and Cu^{2+}) are distributed between the tetrahedral A-sites and the octahedral B-sites. These two sites constitute the two sublattices in the unit cell. According to this model, the magnetic properties in copper ferrites are governed by oxygen anion mediated exchange mechanisms namely antiferromagnetic superexchange between Fe^{3+} in the A site and Fe^{3+} in the B site (A-O-B interaction). The superexchange mechanism is depicted in Figure 3.6.

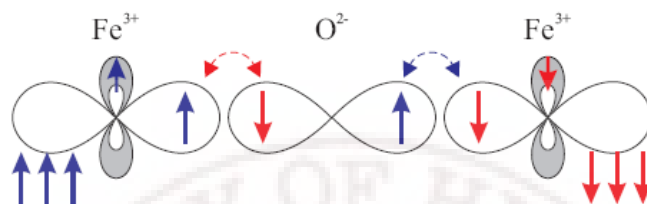


Figure 3.6: Illustration of super exchange between Fe^{3+} on the A site and Fe^{3+} on the B site mediated by an oxygen anion. Virtual hopping (dashed arrows), possible only in an antiferromagnetic configuration of the Fe^{3+} ions, leads to a lower ground state energy in perturbation theory.

Figure 3.7 shows the spin orientations of ions in a single copper ferrite unit cell. It can be seen that a cancellation of the spin moments between the Fe^{3+} ions on the A and B sites and hence, the magnetization per formula unit is only due to the Cu^{2+} ions. The Fe^{3+} ions on A & B sites are arranged anti-parallel.

The net magnetic moment n_B can be calculated as follows

$$M_B = M(\text{Fe}^{3+}) + M(\text{Cu}^{2+})$$

$$M_A = M(\text{Fe}^{3+})$$



The net magnetic moment $n_B = |M_B - M_A| = M(\text{Cu}^{2+}) = 1.73 \mu_B$

Measured moments for $\text{CuFe}_2\text{O}_4 = 1.64 \mu_B$

Figure 3.7: Magnetic moment configuration in copper ferrite (CuFe_2O_4) (inverse spinel)	
Tetrahedral (A-site) (Fe^{3+})	
Octahedral (B-site) [$\text{Fe}^{3+}\text{Cu}^{2+}$]	

In the case of zinc ferrite (ZnFe_2O_4) where all 8 Zn^{2+} ions occupy the A sites and all 16 Fe^{3+} ions occupy the B-sites (normal spinel), there can exist only antiferromagnetic

superexchange interactions between Fe^{3+} ions which orient themselves in an antiparallel manner so that ZnFe_2O_4 behaves as an antiferromagnet. Figure 3.8 shows the spin orientations of ions in a single zinc ferrite unit cell.

Figure 3.8: Magnetic moment configuration in zinc ferrite ZnFe_2O_4 (normal spinel)	
Tetrahedral (A-site) (Zn^{2+})	
Octahedral (B-site) [$\text{Fe}^{3+}\text{Fe}^{3+}$]	
For zinc ferrite ZnFe_2O_4 , it is normal spinel $(\text{Zn})_{\text{tet}}[\text{Fe}\downarrow\text{Fe}\uparrow]_{\text{octa}}\text{O}_4$ so the net magnetic moment is zero.	

The magnetic properties of Zn substituted ferrimagnetic copper ferrite can't be explained according to Neel's model that predicts increase in magnetic moment linearly with Zn^{2+} to reach maximum value of $10 \mu_B/\text{f.u.}$ at $x = 1$. Experimentally the situation is different (table 3.2) where the magnetic moment increases to reach a maximum at $x = 0.4$ and then decreases to 0 at $x = 0$.



The departure from the Neel collinear model of ferrimagnetism can be explain using three theoretical models as follows [13]:

- (i) a paramagnetic centre model in which the number of magnetic nearest neighbors determines whether a magnetic ion remains paramagnetic or contributes to the magnetization [14].
- (ii) a uniform spin canting relative to the average magnetization Y-K model [15] and
- (iii) a localized canting where the canting angle of a magnetic ion spin depends on the local magnetic environment [16].

The Y-K model [15] is an improvement of Neel's model, which successfully explains the experimental results by introducing the concept of canting of spin moments in the lattice when Zn^{2+} is substituted on the A-sites. The transition from the magnetic CuFe_2O_4 to the non-magnetic ZnFe_2O_4 can be explained in view of Y-K model as follows:

When a magnetic Cu^{2+} ion is substituted by a non-magnetic Zn^{2+} ion, the total magnetization rises to $2.2 \mu_B/\text{f.u.}$ This can be explained by the fact that Zn^{2+} ions have tendency to occupy the tetrahedral A-sites which leads to an increase in the number of Fe^{3+} on the B site, at the cost of Cu^{2+} ions, so as to maintain charge neutrality. When 4 magnetic Cu^{2+} ions are substituted by 4 non-magnetic Zn^{2+} ions, the total magnetization

risks to $2.67 \mu_B/\text{f.u}$ (figure 3.9). When more than five Cu^{2+} ions are substituted by equivalent number of Zn^{2+} ions at the A sites, one finds that the magnetization decreases in contradiction to the Neel's model. This is however in contradiction to the fact that ZnFe_2O_4 (ZFO) is an antiferromagnet with a zero net magnetic moment. It is assumed to be due to parallel arrangement of Fe^{3+} at the B-sites of ZFO (Figure 3.8). If there are only Fe^{3+} ions on the B-sites, one expects only a superexchange interaction and this should cause an antiparallel spin alignment at the B-sites. To avoid this contradiction, one has to supplement Neel's model with additional assumptions in order to correctly explain the transition from CuFe_2O_4 to ZnFe_2O_4 .

Figure 3.9: Magnetic moment configuration in $\text{Cu}_{0.6}\text{Zn}_{0.4}\text{Fe}_2\text{O}_4$ (mixed spinel)	
Tetrahedral (A-site) ($\text{Fe}^{3+}\text{Zn}^{2+}$)	
Octahedral (B-site) [$\text{Fe}^{3+}\text{Cu}^{2+}$]	

In summary, the observed variations in magnetic moment can be attributed to the tetrahedral site's strong preference for nonmagnetic Zn^{2+} ions, which causes the migration of Fe^{3+} ions from A- sites to B- sites, resulting in an increase in magnetic moment on B-sublattice and increase in the net saturation magnetization according to the formula

$$(\text{Zn}_x^{2+} \text{Fe}_{1-x}^{3+})_{\text{Tetra}} [\text{Cu}_{1-x}^{2+} \text{Fe}_{1+x}^{3+}]_{\text{Octa}} \text{O}_4^{2-}$$

The reduction of M_s and n_B for $x > 0.4$ can be explained in terms of spin structure changes from two sublattices Néel collinear structure to three sublattices with triangular arrangement having non collinear Yafet-Kittel canted spin structure on B-sublattice. For the samples with $x \geq 0.7$ the magnetization increases with the applied magnetic field so that the saturation magnetization could not be reached even in the applied field of 10kOe.

3.4 Dielectric properties

3.4.1 AC electrical resistivity

Figure 3.10 shows the variation of AC electrical resistivity ρ_{AC} with frequency for various $\text{Cu}_{1-x}\text{Zn}_x\text{Fe}_2\text{O}_4$ samples at room temperature. All samples show same behavior of ρ_{AC} decreasing with increasing frequency, which is known to be the normal behavior of AC properties in ferrites. The conduction process in ferrites can be explained in terms of the electron-hopping model of Heikes and Johnston [17]. The hopping exchange in these ferrites, which reflects the conduction process, can be explained on the basis of the charge carrier exchange interaction between ions of different valency state belonging to the same element and occupy equivalent crystallographic positions, viz. the octahedral sites, which permits a fairly easy exchange of carriers between the different ions [18].

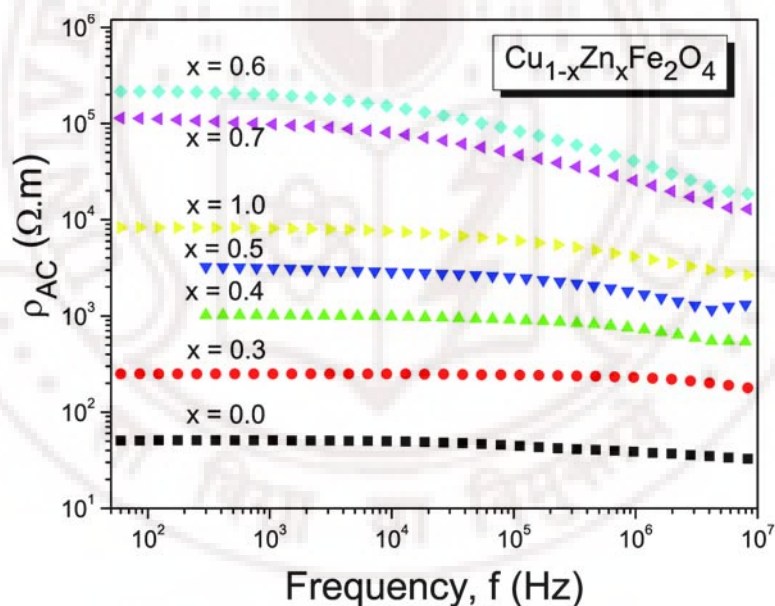


Figure 3.10: Frequency dependence of AC electrical resistivity of $\text{Cu}_{1-x}\text{Zn}_x\text{Fe}_2\text{O}_4$

In the present samples the charge carriers exchange $\text{Fe}^{2+} \rightleftharpoons \text{Fe}^{3+}$ and $\text{Cu}^{1+} \rightleftharpoons \text{Cu}^{2+}$ occurs by random transfer between adjacent octahedral sites (B-sites) in the spinel lattice. The magnitude of exchange, which controls the conduction in ferrites, depends upon the concentration of $\text{Fe}^{2+}/\text{Fe}^{3+}$ and $\text{Cu}^{1+}/\text{Cu}^{2+}$ ion pairs present on B-sites [19]. The concentration of these ion pairs for a given ferrite depends on the preparation conditions.

The formation of these ions occurs during the sintering process as per the following mechanism:

The volatilization of Zn^{2+} ion at high sintering temperature leads to a partial evaporation of Zn^{2+} from the sample surface. As a result the associated oxygen bonds become unsaturated. The unsaturated bonds get associated with the neighboring Fe^{3+} ions and convert it to Fe^{2+} ions. The presence of Fe^{2+} as well as Fe^{3+} on B-sites leads to the formation of low resistivity surface layer so that zinc ferrite behaves as n-type semiconductor [20,21]. A reduction of a small amount of Cu^{2+} ions that occupy B-sites to Cu^{1+} ions takes place at 900 - 950°C and copper ferrite behaves as p-type semiconductor [19].

The applied electric field induces the charge carrier to transfer from one ion to the adjacent one in chain steps causing the conduction in these materials. The increase in frequency of the applied electric field enhances the hopping of charge carriers resulting in decrease of resistivity. At higher frequency, AC resistivity decreases because of the fact that hopping frequency can no longer follow the frequency of the applied external field [22]. The ferrite resistivity increases at low frequency because motion of electrons occurs readily through grains under an electric field but interrupted as they reach the interfaces [23].

3.4.2 Dielectric constant

Figure 3.11 shows the variation of the dielectric constant ϵ' of $\text{Cu}_{1-x}\text{Zn}_x\text{Fe}_2\text{O}_4$ ferrites in the frequency range 60 Hz to 10 MHz at room temperature. It is observed that the dispersion behavior exhibited by these samples is normal i.e. the values of ϵ' decreases with increasing frequency. Similar behavior is observed for all compositions in the entire frequency range. The normal dielectric behavior has been reported in earlier works on ferrites [20, 24-26]. The decrease is rapid in the low frequency range followed by weak frequency dependence at higher frequency reaching a fairly constant value in MHz frequency range. The decrease in ϵ' takes place when the jumping frequency of electric charge carriers cannot follow the alteration of applied AC electric field beyond a critical frequency [27].

The high values of the order of 10^2 - 10^4 of the dielectric constant ϵ' as well as the low frequency dispersion in these polycrystalline ferrites can be explained in terms of Koops

theory [28], which is based on the Maxwell-Wagner type interfacial space charge polarization for inhomogeneous multi-layer dielectric structure [22,27]. The high values of ϵ' at low frequency has been also reported in earlier works on ferrite [20,22,25,29].

According to Koops' model the dielectric structure (ferrite) is composed of well conducting grains, which are separated by poorly conducting thin layer grain boundaries, such as an equivalent of a resistor and a capacitor (figure 3.12).

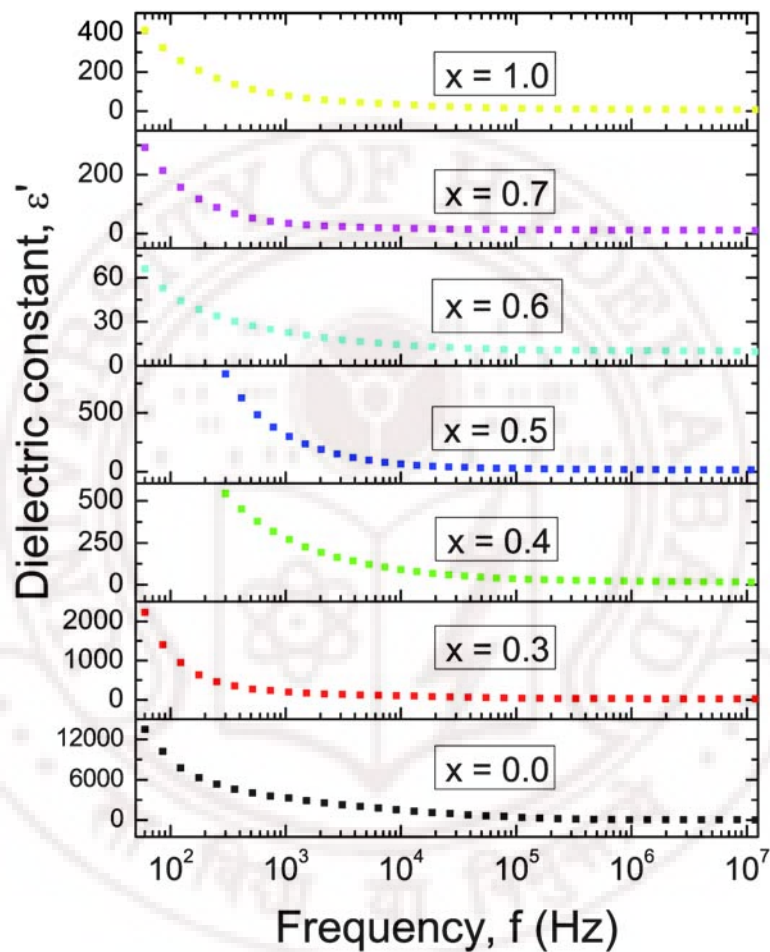


Figure 3.11: Frequency dependence of dielectric constant of $\text{Cu}_{1-x}\text{Zn}_x\text{Fe}_2\text{O}_4$

There are two types of charge carrier exchange in this system i.e. $\text{Fe}^{2+} \rightleftharpoons \text{Fe}^{3+}$ and $\text{Cu}^{1+} \rightleftharpoons \text{Cu}^{2+}$. When an electric field is applied, it could induce a local displacement of charge carriers through hopping to accumulate at the separating boundaries. The build up of charge carriers at the interfaces corresponds to a charge polarization and dielectric constant. At high frequencies, the jumping frequency of electric charge carriers cannot follow the alteration of applied AC electric field beyond a critical frequency and the

probability of charge carriers reaching the grain boundaries decreases resulting in decrease in the polarization and dielectric constant.

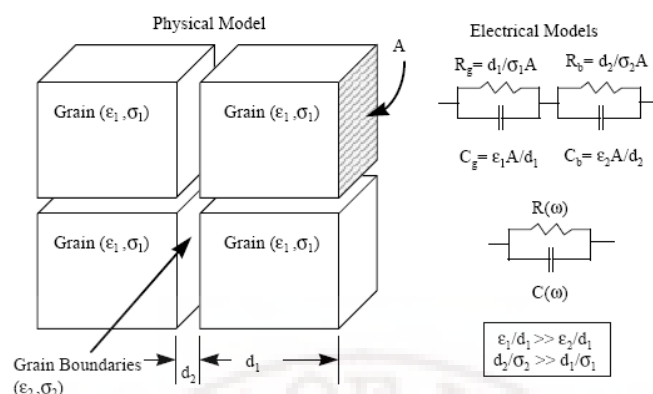


Figure 3.12: Dielectric structure composed of well conducting grains separated by poorly conducting thin layer grain boundaries, such as an equivalent of a resistor and a capacitor.

3.4.3 Dielectric loss tangent

The dielectric loss ($\tan\delta$) arises due to lag of the polarization behind the applied alternating electric field and is caused by the impurities and imperfections in the crystal lattice. The variation of loss angle ($\tan\delta$) with frequency is shown in figure 3.13. It can be seen that all the samples do not show relaxation peak behavior where $\tan\delta$ decreases with increasing frequency. The high values of $\tan\delta$ for some compositions of this system have been reported earlier in earlier work by Rezlescu [30]. The high values of loss tangent could be assigned to the higher concentration of charge carriers that form during sintering process. The dielectric loss in ferrites is generally reflected in the resistivity measurement, where the material with lower resistivity exhibit higher dielectric loss [31].

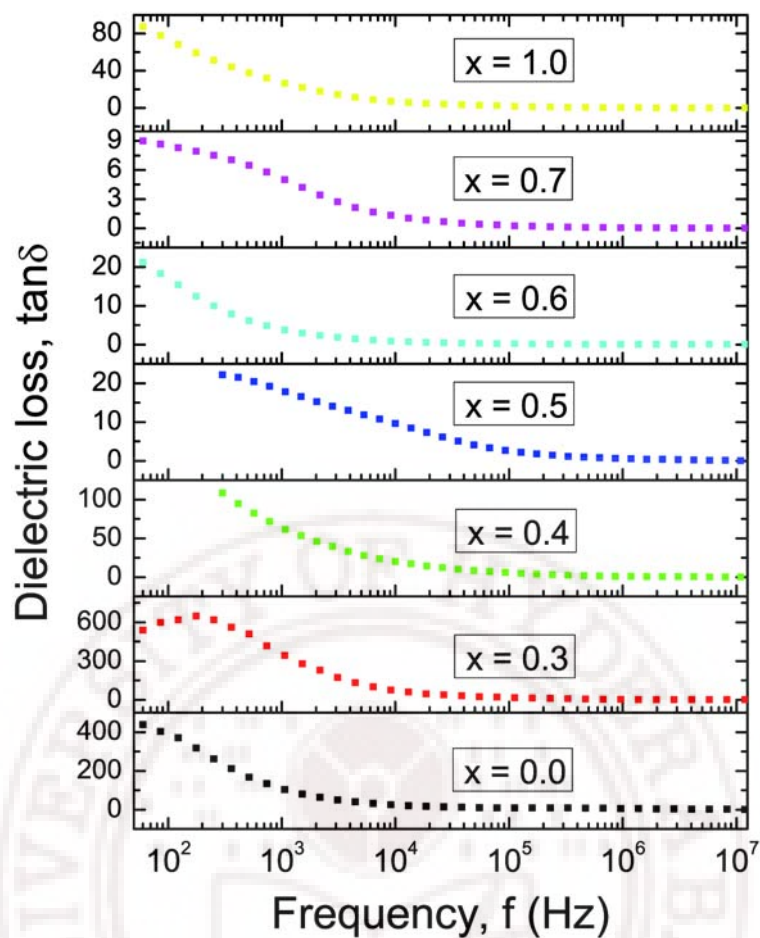


Figure 3.13: Frequency dependence of dielectric loss tangent of $\text{Cu}_{1-x}\text{Zn}_x\text{Fe}_2\text{O}_4$

3.4.4 Composition dependence of dielectric properties

Figure 3.14 shows the variation of ϵ' , $\tan\delta$ and ρ_{AC} with Zn concentration. It is observed that ϵ' and $\tan\delta$ decrease with increase Zn content up to $x = 0.6$ followed by an increasing trend with increase in Zn content. Similar behavior in the variation of ϵ' and $\tan\delta$ with zinc content has been reported earlier [24,22]. The variation of dielectric parameters with zinc content can be explained on the basis of two types of charge carriers' model [19].

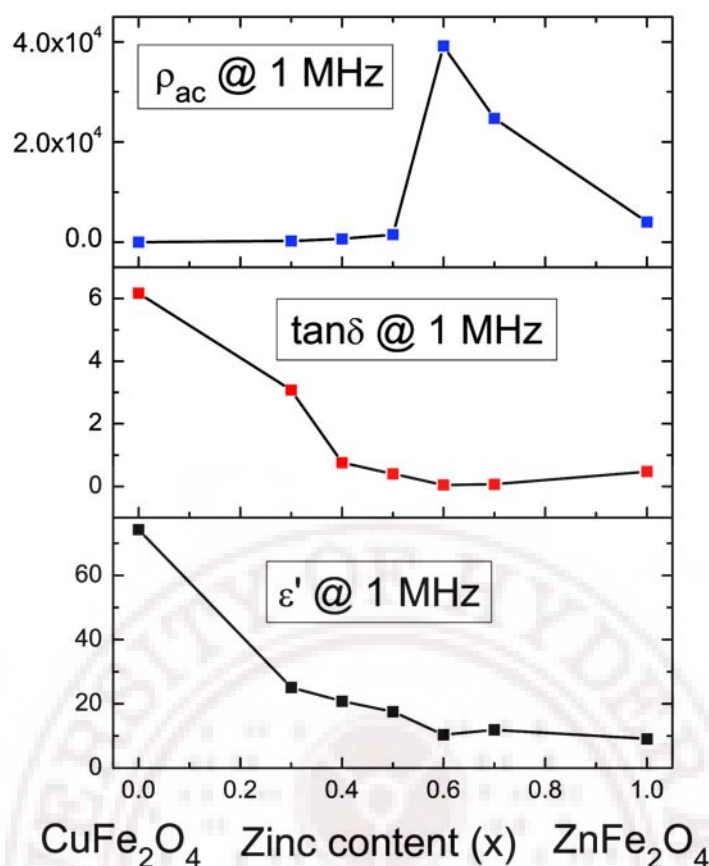


Figure 3.14: Compositional dependence of ϵ' , $\tan\delta$ and ρ_{AC} at a frequency of 1 MHz.

At low substitution of Zn^{2+} ($x \leq 0.6$) p-type charge carriers dominate. The n-type of carriers dominate for $x > 0.6$ which depends on the sintering temperature. As the sintering temperature is ~ 1000 °C, this is enough to produce a pair of Cu^{1+} and Cu^{2+} but it is too low to create a plenty of Fe^{2+} ions. Ferrite samples with low zinc concentration are likely to have low evaporation of Zn favoring the creation of more Cu^{1+} compared to Fe^{2+} ions. Therefore the major contribution to the conductivity of the present ferrite samples is from the p-type carriers.

It is well known that Cu^{2+} ions strongly prefer the occupation of B-site and Zn^{2+} ions strongly prefer the occupation of A-sites, while Fe^{3+} ions partially occupy both A- and B-sites. As Zn^{2+} ion substitution increases at (A-sites) replacing Cu^{2+} ions, some Fe^{3+} ions will be forced to migrate from A- sites to B- sites and the dielectric constant decreases. At higher concentration of Zn, the probability of increasing Fe^{2+} ions and Fe^{3+} ions on B-sites increases. Since Fe^{2+} ions are easily polarizable, the larger the number of Fe^{2+} ions the

higher would be the dielectric constant [32]. Ferrites prepared at higher sintering temperature are likely to have more Fe^{2+} ions and therefore, high dielectric constant and electrical conductivity [18]. Compositional non-stoichiometry is also an important requirement for obtaining high dielectric constant and dielectric loss.

The variation of AC electrical resistivity with composition for this system is similar to that for ceramic $\text{Ni}_{1-x}\text{Zn}_x\text{Fe}_2\text{O}_4$ where the resistivity increases with increasing zinc content [33]. The values of ϵ' and ρ_{AC} for $x = 0.5$ and its variation with frequency is similar to that reported in earlier works by Nam et al. [34].

3.5 Effect of quenching on properties of CuFe_2O_4

Heat treatment is a process involving heating a material to a high temperature followed by controlled cooling. The principal steps of any heat treatment are the heating stage, the holding time, and the cooling stage. The amount of time a sample is held at the holding temperature and the rate at which heat is removed from the sample are the most critical factors. It is necessary for the holding time to be sufficiently long to complete the required microstructural phase transformations. The cooling rate is equally important because different microstructural phases and their inherent properties are obtained at different cooling rates. [35].

Copper and copper containing ferrites have been a focus of continued interest because of their interesting electrical and magnetic properties and crystal structure changes due to its high sensitivity to heat treatment. Switching and memory phenomena are also exhibited by CuFe_2O_4 [36].

Figure 3.15 (a) shows XRD spectra of slow cooled (furnace cooled) copper ferrite powder. All peaks match with that of the standard bar pattern (JCPDS No. 34-0425) of copper ferrites with tetragonal structure. Figure (3.15b) is an XRD pattern of ferrite powder quenched from 900 °C. All major peaks match well with that of standard bar pattern of copper ferrite (JCPDS No. 70-0010) with cubic symmetry. The patterns show sharp peaks corresponding to a single phase spinel structure. No impurity or secondary phases were detected. It can be seen that for the quenched sample the index of reflection

planes are indications of the presence of the cubic symmetry whereas the slow cooled sample shows tetragonal structure.

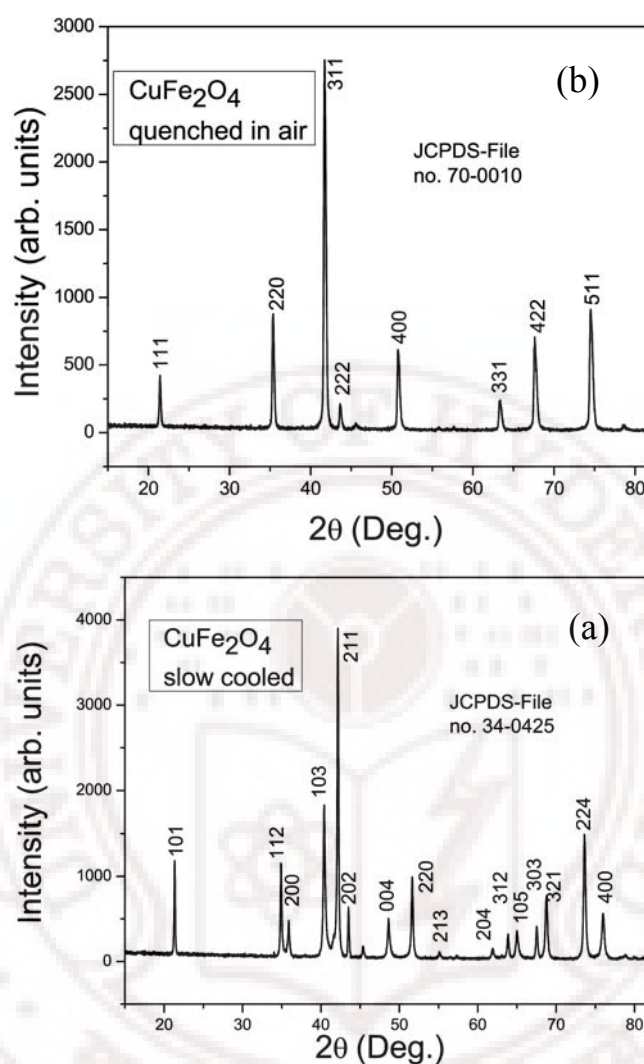


Figure 3.15: XRD patterns of CuFe_2O_4 (a) slow cooled with tetragonal structure (b) quenched in air with cubic symmetry.

The SEM images of both the samples show distinct differences (figure 3.16). Both the ferrite samples showed very good densification with little intergranular porosity. The mean grain size is $\sim 1 \mu\text{m}$ for slow cooled sample with good homogeneity. The mean grain size for the quenched sample is $\sim 7 \mu\text{m}$ with wide grain size distribution. EDAX measurements show the stoichiometric ratio between iron and copper within $\pm 5\%$ of the starting composition for both the samples.

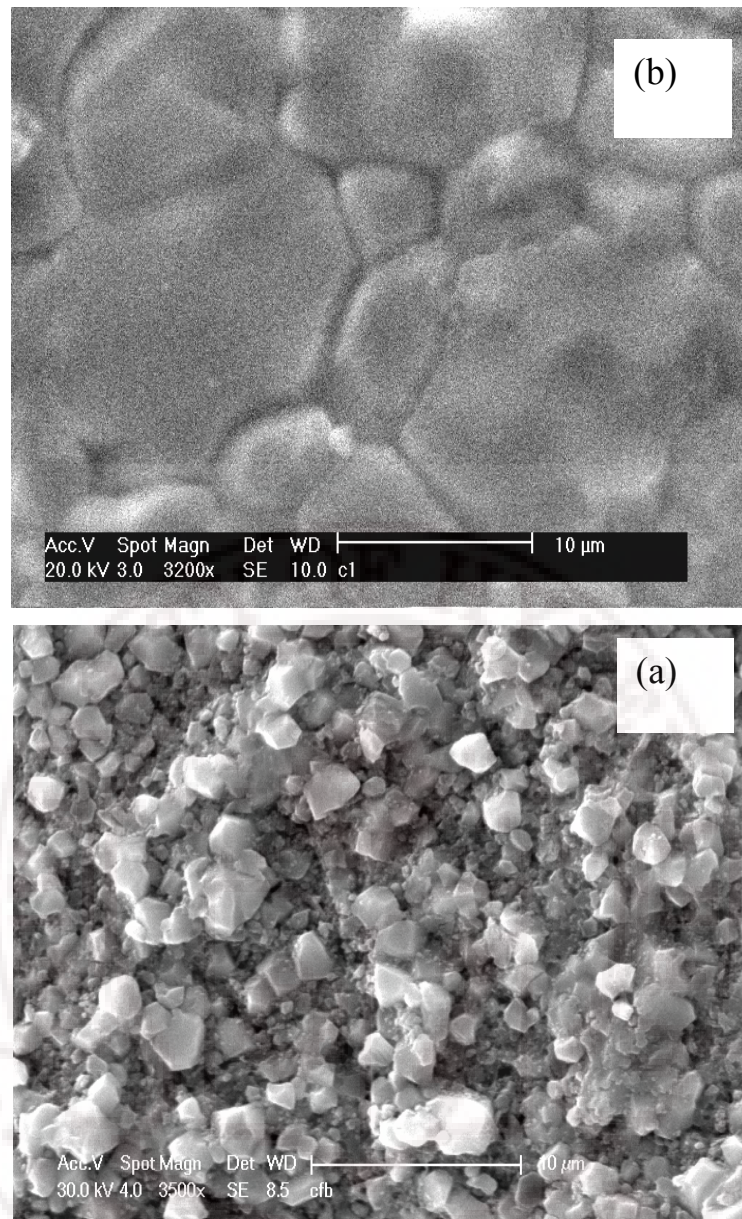


Figure 3.16: SEM images of CuFe_2O_4 (a) slow cooled and (b) quenched from 900 °C in air.

Figure 3.17 shows the M-H curves of slow cooled (sc) and quenched samples. It can be seen that the quenched sample show higher magnetization and lower values of retentivity and coercivity. The values of the magnetization are in close agreement with the earlier reported values for slow cooled and quenched CuFe_2O_4 samples [36,37].

The increase in M_s in the quenched sample as compared to the slow cooled sample can be explained by considering the fact that on quenching the sample from elevated temperatures the cation distribution between A- and B-sites is random and frozen. This

leads to change of structure from tetragonal to cubic where migration of cupric ions to tetrahedral site causes an increase in the magnetization. The hysteresis curve of the quenched sample is narrow compared to with that of slow cooled sample. This behavior can be assigned to the cubic symmetry of the quenched sample compared to the slow cooled sample which has tetragonal symmetry and consequently higher magnetic anisotropy.

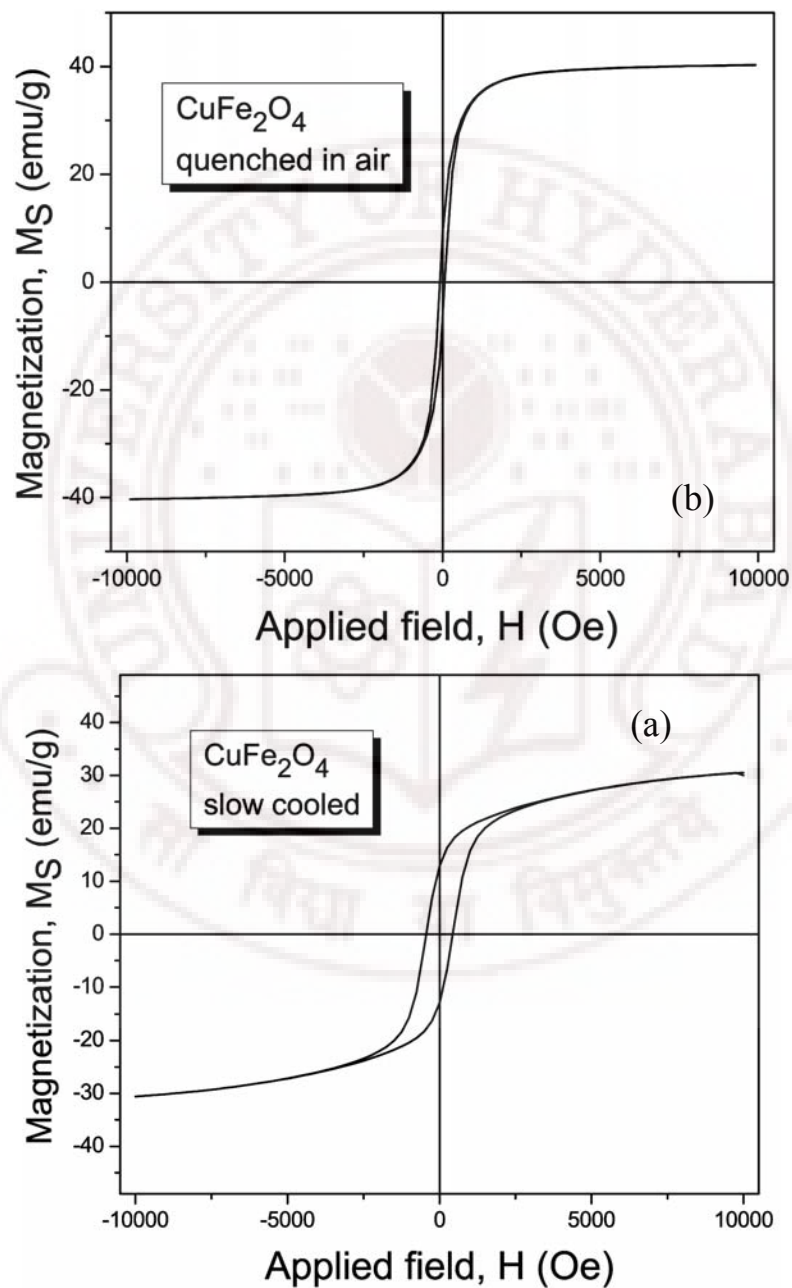
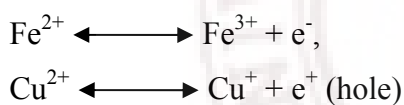


Figure 3.17: M-H plots of CuFe_2O_4 (a) slow cooled and (b) quenched from 900°C in air.

Figure 3.18 shows the variation of the dielectric constant (ϵ') and loss tangent ($\tan\delta$) with frequency for both slow cooled and quenched samples. The quenched sample show higher value of dielectric constant and dielectric loss tangent than the slow cooled sample. This behavior could be attributed to the formation of Cu^+ ions in the sample when quenched from high temperature. The presence of Cu^+ besides Cu^{2+} increases the number of charge carriers that contribute to conduction and consequently increase the polarization and dielectric constant. In the polarization process in ferrite containing copper there are two types of carriers (n and p) take part. The appearance of p-type carrier is due to Cu^{2+} - Cu^{1+} exchange that takes place in this ferrite [38].

The behavior of dielectric constant with frequency $\epsilon(f)$ can be explained based on the Rezlescu's model [19]. According to this model the $\epsilon(f)$ can be ascribed to the presence of collective contribution to the polarization from two different types of charge carriers. For the samples under investigation, the conduction process can be attributed to the presence of two types of charge carriers, n-type as electron transfer between Fe^{2+} and Fe^{3+} and p-type as a hole exchange between Cu^{1+} and Cu^{2+} at tetrahedral sites. These two coupling mechanisms can be represented by the following relations [29]:



Since the direction of displacement of electrons is opposite to that of the holes under the application of external field, the mobility of the holes is relatively very small compare to that of electrons. The resultant polarization of both types of charge carriers will give rise to peaking behavior as shown in the figure 3.18.

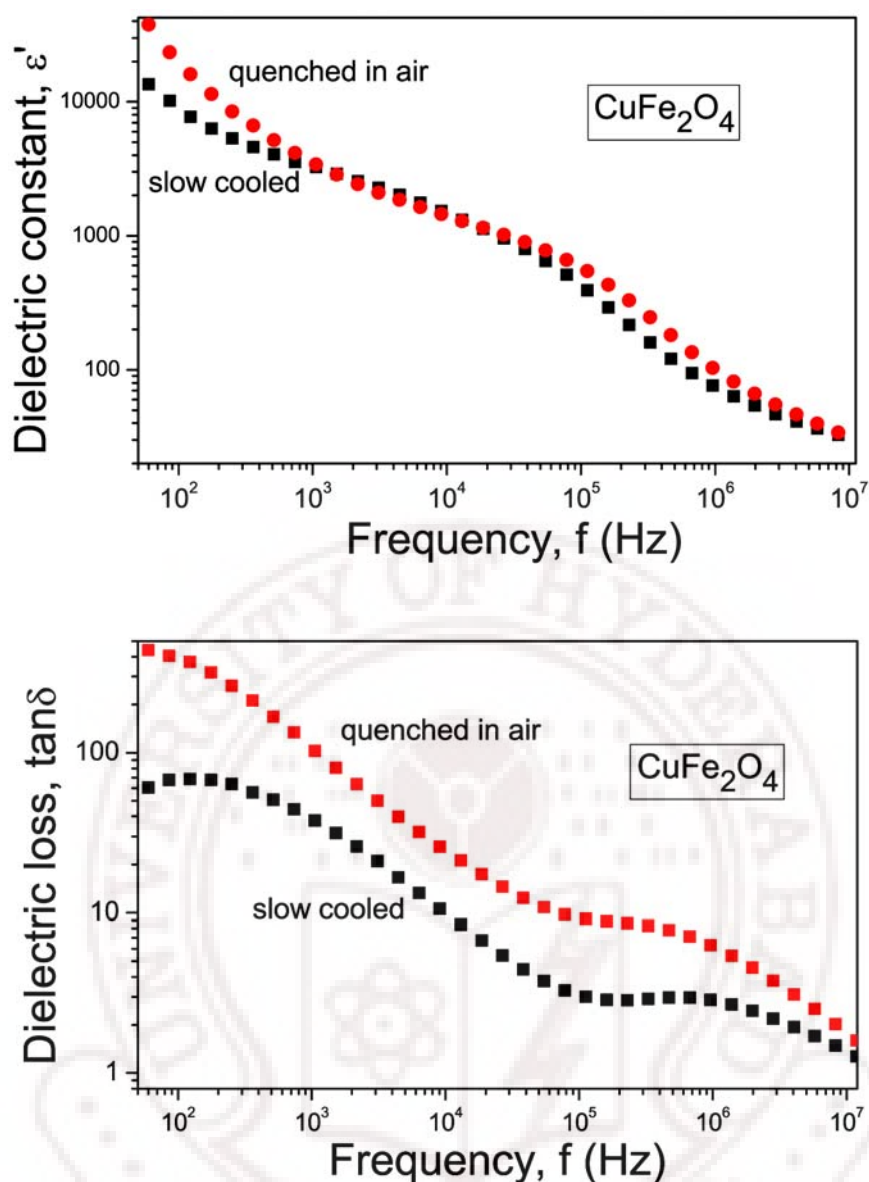


Figure 3.18: Dielectric constant and dielectric loss tangent of CuFe_2O_4 slow cooled and quenched from 900°C in air.

References

- [1] M. U. Rana, M.-ul Islam and T. Abbas, *Mater. Chem. Phys.* **65** (2000) 345–349.
- [2] M. Banerjee, N. Verma and R. Prasad, *J. Mater. Sci.* **42** (2007) 1833–1837.
- [3] A. Goldman, *Modern Ferrite Technology*, 2nd Ed. Springer Science, New York (2006).
- [4] M. Ul-Islam, T. Abbas and M. A. Chaudhry, *Mater. Lett.* **53** (2002) 30–34.
- [5] M. U. Rana and T. Abbas, *J. Magn. Magn. Mater.* **246** (2002) 110–114.
- [6] A. G. Angeles, G. Mendoza-Suarez, A. Gruskova, M. Papanova and J. Slama, *Mater. Lett.* **59** (2005) 26–31.
- [7] M. Sorescu, L. Diamandescu, R. Peelamedu, R. Roy and P. Yadoji, *J. Magn. Magn. Mater.* **279** (2004) 195–201.

- [8] R. V. Mangalarga, S. A. Kumar and P. Manohar, *Matter. Lett.* **58** (2004) 593 – 1596.
- [9] K. Hirota, T. Aoyama and S. Enomoto, *J. Magn. Magn. Mater.* **205** (1999) 283-289.
- [10] D. Ravinder, K. V. Kumar and B. S. Boyanov, *Mater. Lett.* **38** (1999) 22 -27
- [11] B.D. Cullity and S. R. Stock, *Elements of X-Ray Diffraction*, 3rd Ed., Prentice Hall, New Jersey, USA (2001).
- [12] G. M. Argentina, P. D. Baba, *IEEE. Trans. Microwave. Theor. Tech*, **20** (1974) 652.
- [13] J. L. Dormann and M. Nogues, *J. Phys.: Condens. Matter* **2** (1990) 1223-1237.
- [14] M. A. Gilleo, *Phys. Rev.* **109** (1958) 777.
- [15] Y. Yafet and C. Kittel *Phys. Rev.* **87** (1952) 290.
- [16] S. Geller, *J. Appl. Phys.* **37** (1966) 1408.
- [17] R. R. Heiks and W. D. Johnston, *J. Chem. Phys.* **26** (1957) 582 – 587.
- [18] E. J. W. Verwey, P. W. Haaijman, F. C. Romeijn and G. W. van Oosterhout, *Philips Res. Rep.* **5** (1950) 173–187.
- [19] N. Rezlescu and E. Rezlescu, *Phys. Stat. Sol. (a)* **23** (1974) 575–587.
- [20] L. G. Van Uitert, *Proc. IRE* **44** (1956) 1294–1303.
- [21] A. K. Singh, T. C. Goel, R. G. Mendiratta, O. P. Thakur and C. Prakash, *J. Appl. Phys.* **91** (2002) 6626–6629.
- [22] A. M. Abdeen, *J. Magn. Magn. Mater.* **192** (1999) 121-129.
- [23] W. D. Kingery, H. K. Bowen and D.R. Uhlmann, *Introduction to ceramics*, 2nd Ed, Wiley, Singapore (1976).
- [24] A. Y. Lipare, P. N. Vasambekar and A.S. Vaingankar, *J. Magn. Magn. Mater.* **279** (2004) 160–172.
- [25] A. A. Pandit, A. R. Shitre, D. R. Shengule and K. M. Jadhav, *J. Mater. Sci.* **40** (2005) 423–428.
- [26] A. Verma, T. C. Goel, R. G. Mendiratta and M. I. Alam, *Mater. Sci. Eng. B* **60** (1999) 156–162.
- [27] M. A. El Hiti, *J. Magn. Magn. Mater.* **192** (1999) 305–313.
- [28] C. G. Koops, *Phys. Rev.* **83** (1951) 12–124.
- [29] H. M. Zaki, *Physica B* **363** (2005) 232–244.
- [30] E. Rezlescu, *Phys. Stat. Sol. (a)* **17** (1973) K139–K141.
- [31] K. Iwauchi, *Japn J. Appl. Phys.* **10** (1971) 1520–1528.
- [32] R. G. Kharabe, R. S. Devan, C. M. Kanamadi and B. K. Chougule, *Smart Mater. Struct.* **15** (2006) N36–N39.
- [33] S. Sindhu, M. R. Anantharaman, B. P. Thampi, K. A. Malini and P. Kurian, *Bull. Mater. Sci.* **25** (2002) 599–607.
- [34] J. H. Nam, H. H. Jung, J. Y. Shin and J. H. Oh, *IEEE Trans. Magn.* **31** (1995) 3985–3987.
- [35] G. E. Totten, C. E. Bates and N. A. Clinton, *Handbook of quenchants and quenching technology*, ASM International, Ohio (1994).
- [36] S. R. Sawant and R. N. Patil, *Ind. J. Pure & Appl. Phys.* **21**(1983) 145-147.
- [37] S. R. Sawant and R. N. Patil, *Sol. Stat. Comm.* **40** (1981) 391-394.
- [38] V. R. Kulkarni and A. S. Vaingankar, *J. Mater. Sci.* **22** (1987) 4087-4092.

CHAPTER-4

Studies on Cu-Zn ferrite nanoparticles

The studies of nanoparticles of copper and copper containing ferrites have been of continued interest because of their interesting electrical and magnetic properties and crystal structure changes that take place due to heat treatment [1]. Chemical techniques are suitable for the synthesis of ultrafine materials with homogeneous composition and adequate morphology for their use in multiple technological purposes [2]. Coprecipitation method has been extensively used for the preparation of nanosized particles of spinel ferrite materials [3,4]. In this chapter the crystal structure and magnetic properties of Cu-Zn ferrite nanoparticles synthesized by coprecipitation method are presented. These studies have been very useful in finding out the role of Cu^{2+} and Cu^{1+} ions in controlling the magnetic and dielectric properties of these ferrites.

4.1 Crystal structure

Figure 4.1 shows the typical XRD patterns of the $\text{Cu}_{1-x}\text{Zn}_x\text{Fe}_2\text{O}_4$ ($0.0 \leq x \leq 1.0$) powder samples coprecipitated at 80 °C followed by heat treatment in air at 850 °C for 6 hrs. For all the samples, the spinel phase is obtained and the main peak is (311), which is in agreement with our studies on corresponding bulk samples [Chapter 3]. As can be seen from the XRD pattern no other phase is present. The average particle size of the as-coprecipitated $\text{Cu}_{1-x}\text{Zn}_x\text{Fe}_2\text{O}_4$ ($x > 0$) samples estimated using Scherrer formula vary in the range 8–12 (± 1) nm. The as-coprecipitated sample of CuFe_2O_4 ($x = 0$) is found to be amorphous.

The lattice parameters of the samples were calculated using the combination of Bragg's law of diffraction and the relation $a = d_{hkl} \sqrt{h^2 + k^2 + l^2}$ for cubic symmetry where h , k , and l are the miller indices, a represents lattice parameter and d_{hkl} is interplanar spacing. With increase in Zn content the lattice parameter increases similar to what is observed in the case of bulk samples. The estimated values of 'a' for the samples with $x = 0.4$ and 0.8 are

8.36 and 8.38 Å respectively. This can be attributed to the difference in radii of Zn^{2+} (0.82 Å) and Cu^{2+} (0.72 Å) which means that the larger the ion greater the lattice parameter [5]. The relative concentration of Cu and Zn in the ferrite structure not only influences the particle size and lattice parameter but also causes deviation in the distribution of cations at the lattice sites of the nanoparticles. The cation distribution is influenced by the strong chemical affinity of certain cations to occupy either A- or B-sites and the metastable cation distribution in nanosized particles. It is also influenced by change in the stoichiometry when large number of small ions replaces ions having larger radii.

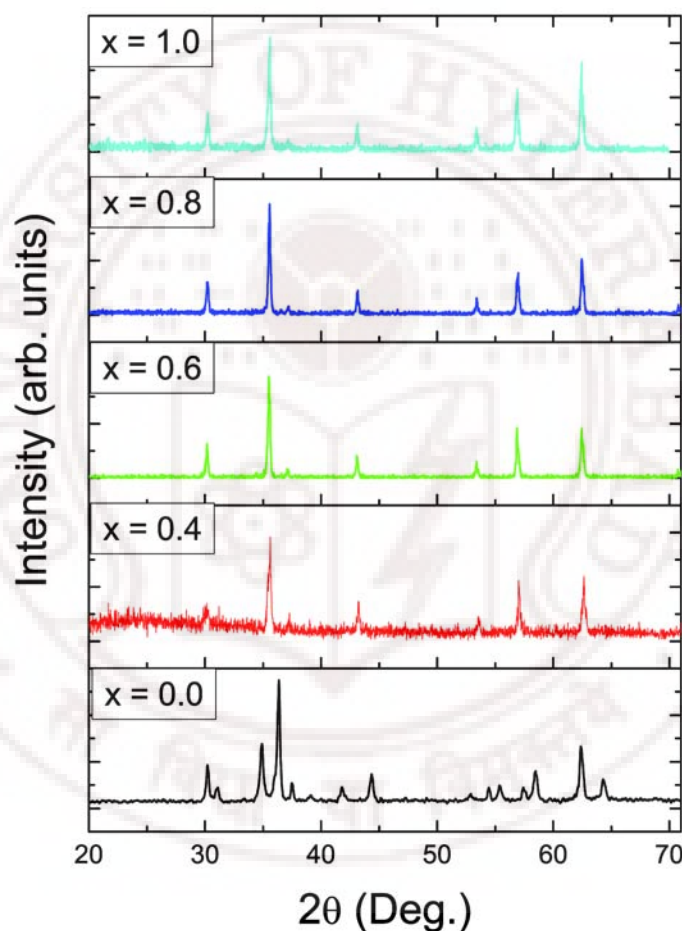


Figure 4.1: X-ray powder diffraction patterns of $\text{Cu}_{1-x}\text{Zn}_x\text{Fe}_2\text{O}_4$ synthesized by coprecipitation method and calcined at 850 °C for 6 hrs.

4.2 Microstructure analysis

The surface morphology of the calcined copper-zinc ferrite nanoparticles have been studied by scanning electron microscopy (SEM). Figure 4.2 represents the SEM images for the compositions with $x =$ (a) 0.0 (b) 0.4, (c) 0.6 and (d) 1.0. The difference in

microstructure is clearly seen in terms of grain size and morphology. The figure suggests the presence of aggregates of small grains at the surface of the higher Zn containing samples. The samples have a homogeneous microstructure of equiaxed grains. It can be seen that the morphology varies significantly with composition. Energy-dispersive x-ray spectroscopy (EDAX) was used to determine the final composition of the samples. The synthesis procedure was optimized until it produced samples with uniform microstructure and chemical homogeneity.

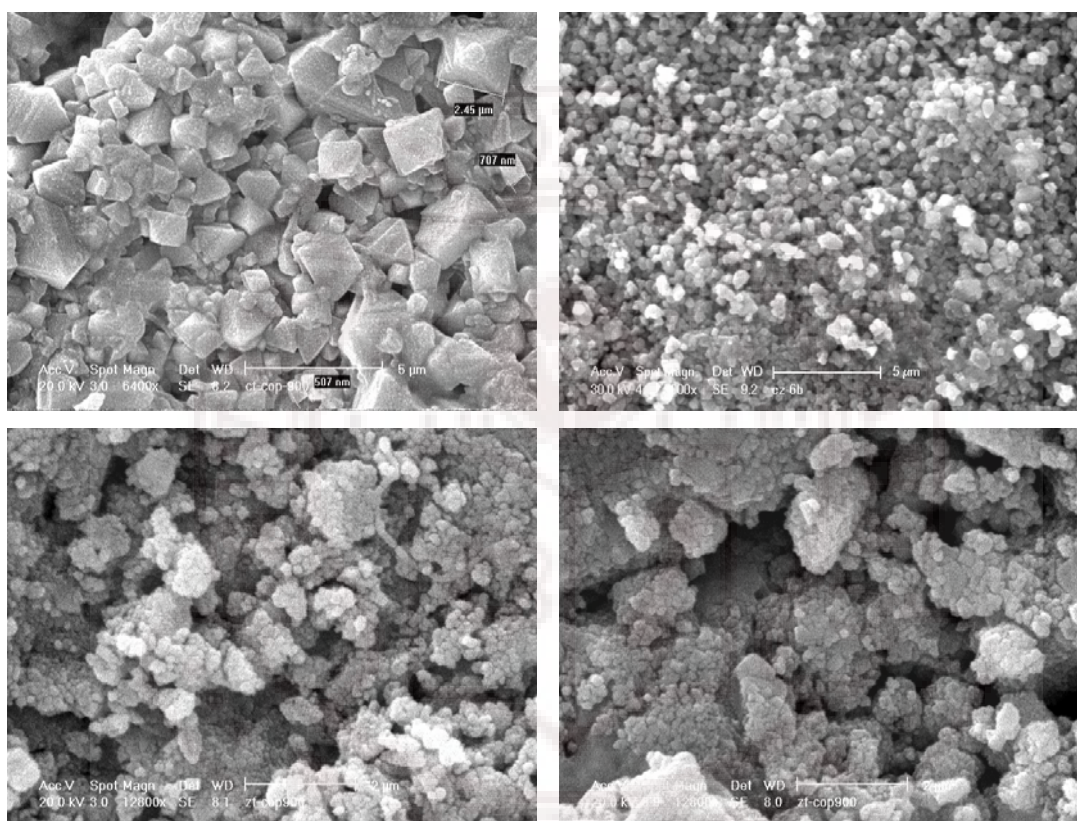


Figure 4.2: SEM photographs of calcined $\text{Cu}_{1-x}\text{Zn}_x\text{Fe}_2\text{O}_4$ samples at 850 C for 6 hrs with x value of (a) 0.0 (b) 0.4, (c) 0.6 and (d) 1.0

The EDAX measurements (Figure 4.3) performed randomly at several spots across the samples show no microphase separation or compositional inhomogeneities at a submicrometer level. It reveals that the Cu:Zn:Fe ratio in the matrix is close to the nominal compositions with an overall a slight excess of Fe observed. No trace of any impurities is found in the samples confirming the phase purity of the samples. The EDAX results suggest that the precursors have undergone the chemical reaction fully to form the expected ferrite materials.

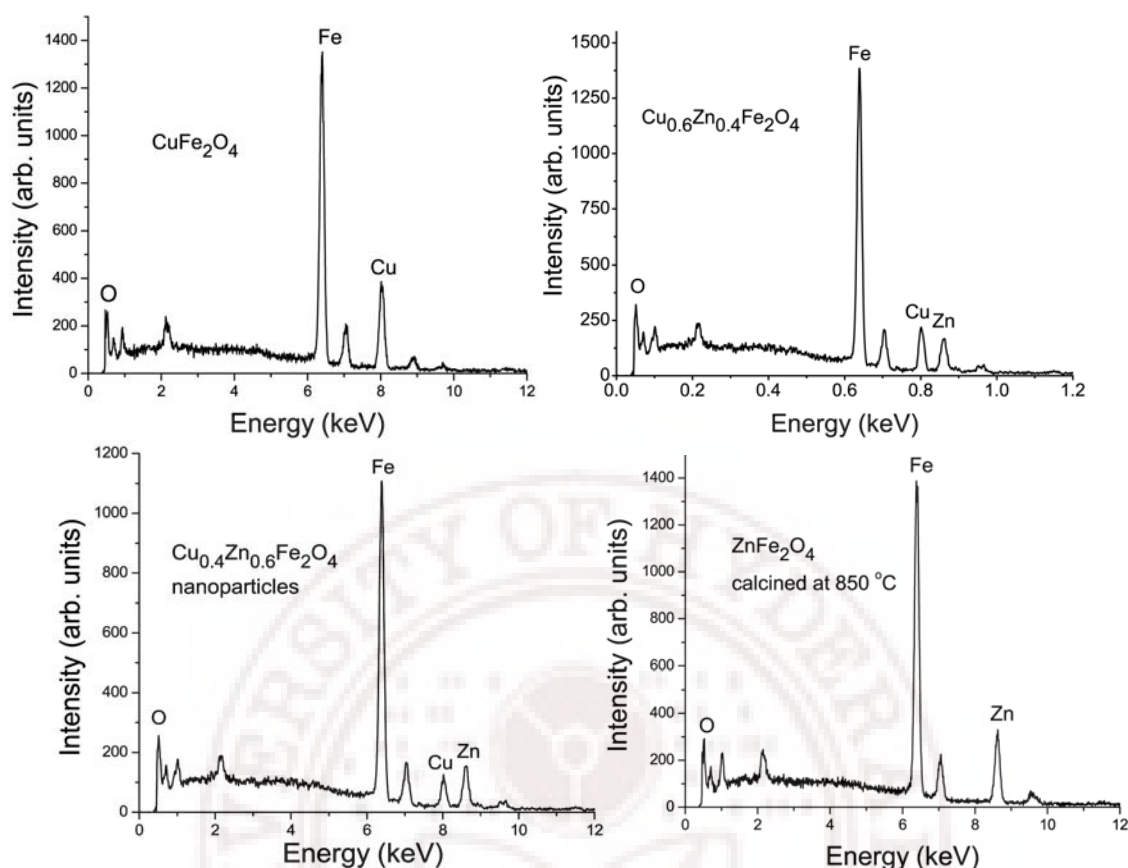


Figure 4.3: EDAX results confirm the formation of calcined $\text{Cu}_{1-x}\text{Zn}_x\text{Fe}_2\text{O}_4$ ferrite crystallites in the heat treated samples at 850 °C for 6 hrs with x value of (a) 0.0 (b) 0.4, (c) 0.6 and (d) 1.0.

4.3 Magnetic properties

Figure 4.4 indicates the composition dependence of the magnetization (M) vs. applied field (H) for $\text{Cu}_{1-x}\text{Zn}_x\text{Fe}_2\text{O}_4$ ($0.0 \leq x \leq 1.0$) samples synthesized by coprecipitation method followed by calcination at 850 °C for 6 hrs. With the increase in Zn content, the saturation magnetization (M_s) initially increases reaching the maximum value of about 67 emu/g at $x = 0.4$ followed by a decreasing trend with further increase in zinc content. This trend is similar to that of the bulk $\text{Cu}_{1-x}\text{Zn}_x\text{Fe}_2\text{O}_4$ samples (3rd chapter) and for M-Zn ferrite system (see for eg. [5,6]).

The improvement in M_s with the addition of Zn ions into the CuFe_2O_4 compound is attributed to the preferential occupation of nonmagnetic Zn^{2+} ions of A-sites and consequent displacement of equivalent number of magnetic Fe^{3+} ions to B-sites. The

increment of B-site population with the magnetic Fe^{3+} on account of displacement from A-sites develops the difference of magnetic moments which leads to the enhancement of $\text{Fe}^{3+}(\text{A})\text{-O-Fe}^{3+}[\text{B}]$ superexchange interaction and magnetization [7]. However, with further increase in zinc content ($x > 0.4$) after reaching a maximum, M_S starts to decrease irrespective of increase in the number of Fe^{3+} ions on B-sites. The increment of Fe^{3+} ions on B-sites leads to decrease in the superexchange interaction between A and B sites. At this stage the Fe^{3+} spins start canting on B-sites. The canting increases with increase in the zinc content leading to full antiparallel alignment at $x = 1$ (ZnFe_2O_4) [7-9].

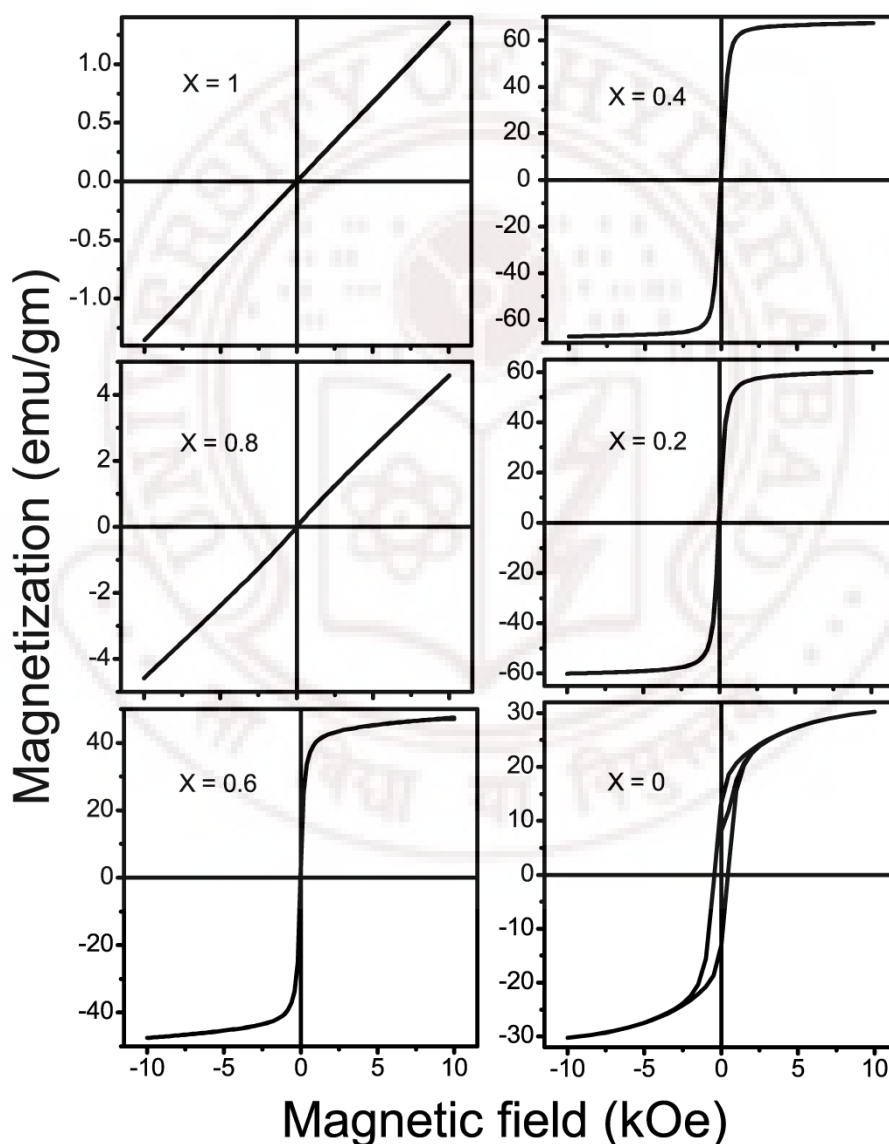


Figure 4.4: Magnetization vs. magnetic field curves at 300 K for the $\text{Cu}_{1-x}\text{Zn}_x\text{Fe}_2\text{O}_4$ samples prepared by coprecipitation method and calcined at 850 °C for 6 hrs.

With the increase in Zn concentration, the coercivity H_C decreases monotonously. The decline in coercivity can be due to decreasing crystal anisotropy with increase in Zn concentration [10]. Similar results have been reported in the literature for substitution of magnetic ions by non magnetic Zn in mixed ferrites [11].

The slightly higher M_S values for the nanoparticle compared to the bulk materials (Figure 4.5) can be attributed to the change in the cation distribution of the coprecipitated samples. For the bulk material Cu^{2+} ions are apt to locate in the octahedral sites while Zn^{2+} in the tetrahedral sites. However, in the coprecipitated samples some fraction of Cu^{2+} ions occupy the tetrahedral sites while fraction of Zn ions occupy the octahedral sites resulting in an increase in the magnetic moment [10].

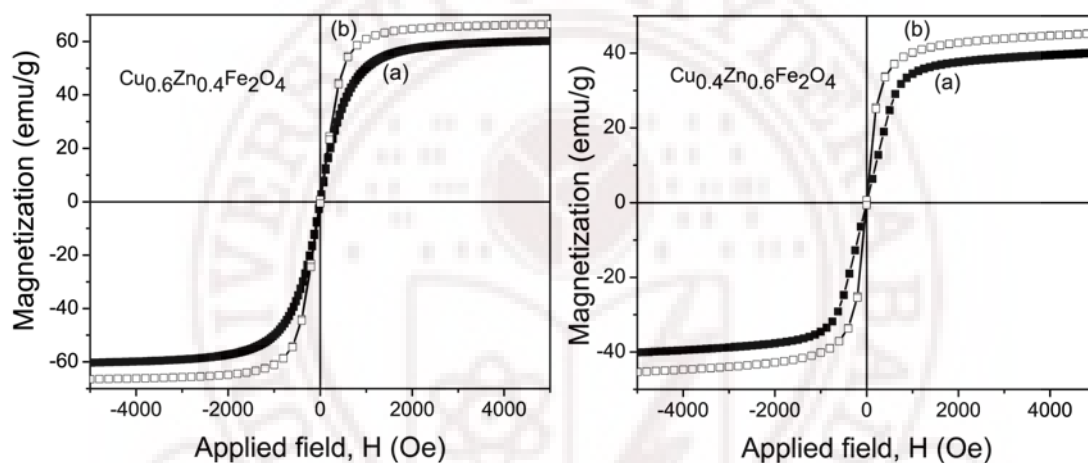


Figure 4.5: M-H plots of $\text{Cu}_{0.6}\text{Zn}_{0.4}\text{Fe}_2\text{O}_4$ and $\text{Cu}_{0.4}\text{Zn}_{0.6}\text{Fe}_2\text{O}_4$ (a) bulk sample prepared by solid state reaction at 1000 °C for 12hrs (b) nanoparticles synthesized by coprecipitation method with calcination at 850 °C for 6hrs.

4.4 FMR studies

Figures (4.6-4.8) show the temperature dependent ESR data for the as-coprecipitated $\text{Cu}_{1-x}\text{Zn}_x\text{Fe}_2\text{O}_4$ nanoparticle ($x = 0.4, 0.6, 0.7, 0.8$ and 1.0) samples with cubic shapes. It can be seen that ESR measurements show only one FMR signal at $g \sim 2$, in the high temperature range. The FMR signal splits into two resonances. The single FMR lines of Lorentzian shape at high temperature can be assigned to a paramagnetic (PM) phase. With decrease in temperature the resonance absorption appearing at lower field can be assigned to a ferromagnetic phase. The resonance at high field can be assigned to the presence of one or two magnetic phases (PM, spin glass or antiferromagnetic) [12].

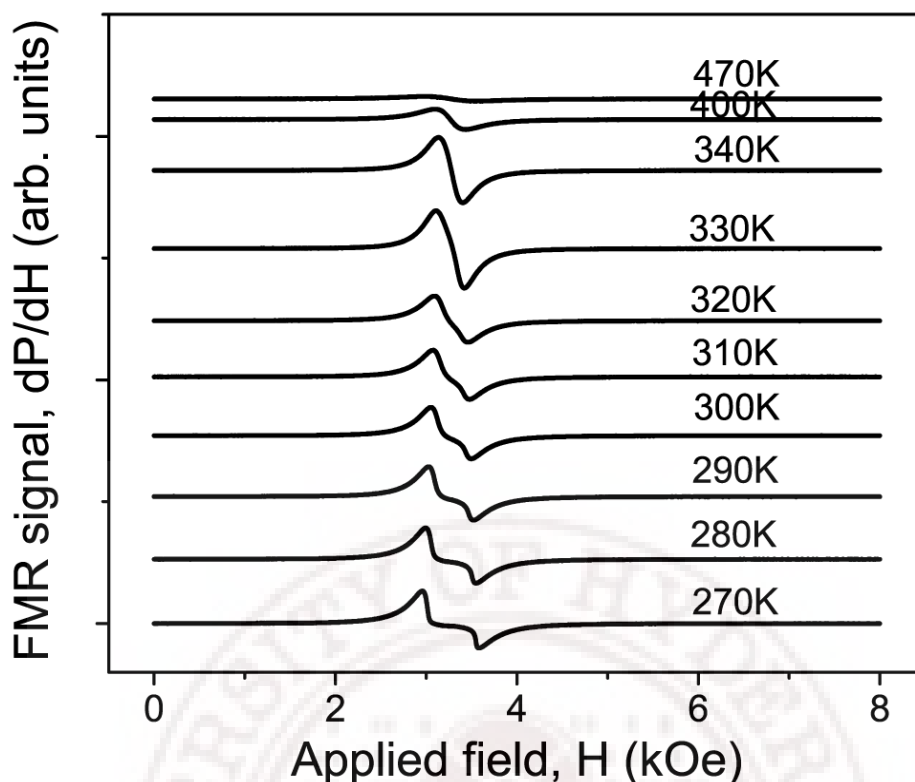


Figure 4.6: FMR spectra of as-coprecipitated ZnFe_2O_4 nanoparticles at pH value of 12.

In the present systems, the splitting of the FMR spectra at lower temperature can be assigned to the formation of ferromagnetic (FM) clusters in paramagnetic (PM) and antiferromagnetic (AFM) backgrounds. The preparation of these materials as nanosized particles leads to change in their magnetic properties. Some of Zn^{2+} and Fe^{3+} ions redistribute partially among A- and B-sites which cause local superexchange interactions via oxygen ions between Fe^{3+} ions on both sites leading to local ferromagnetic phases [13]. With decreasing temperature more FM centers form and consequently increase the FM phase. This indicates that the FM-PM transition is not complete. The PM phase may still survive in a certain temperature range below T_C . The formation of AFM phase could not be ruled out. We believe that the AFM phase plays a major role in the splitting of FMR signal. This is evident from the decrease signal intensity with decrease in temperature. The disappearance of the high-field signals in the sample containing high Cu content (Figure 4.8) where the Para-to-ferromagnetic phase transition occurs in a very narrow temperature range confirms the absence or the highly reduced AFM phase in these samples compared to the sample having high zinc content.

For zinc ferrite, the temperature dependence of FMR spectra (Figure 4.6) shows substantial changes near the transition temperature due to the existence of multi-magnetic phases (para-, ferro- and antiferromagnetic phases) over a wide temperature range. The splitting of the ESR signal could be due to the size distribution of the local effective magnetic fields (H_{eff}) which lead to the appearance of two or more preferred directions of the orientation of local magnetic moments (ensembles of particles with specific shape or size distributions). This leads to superparamagnetic behavior as can be understood from M-H and M-T plots shown in figures 4.22 and 4.23. When these ferromagnetic phases are formed, the resonance field H_R due to the spins in the ferromagnetic phase shifts towards the lower field with decreasing temperature due to the ferromagnetic exchange interaction. Whereas for the spins in the PM or AFM backgrounds H_R shifts towards the higher field with decreasing temperature due to the demagnetizing field from the ferromagnetic phases.

The presence of two well resolved absorption lines in a wide temperature below Curie point T_C was observed in La-manganite single crystal [14,15] and in polycrystalline samples [16]. The low field resonance is assigned to the FM state which appears below T_C . The decrease in the resonance field H_r with decreasing temperature is associated with anisotropic interactions, namely, with increasing magnetocrystalline anisotropy and shape anisotropy. The other line assigned to the paramagnetic state changes its position insignificantly and its resonance field H_r does not depend on the sample shape and the orientation of the external magnetic field. The slight increase in H_r with decrease in temperature may be associated with a change in the g factor caused by local lattice distortions initiated by strong electron-phonon coupling.

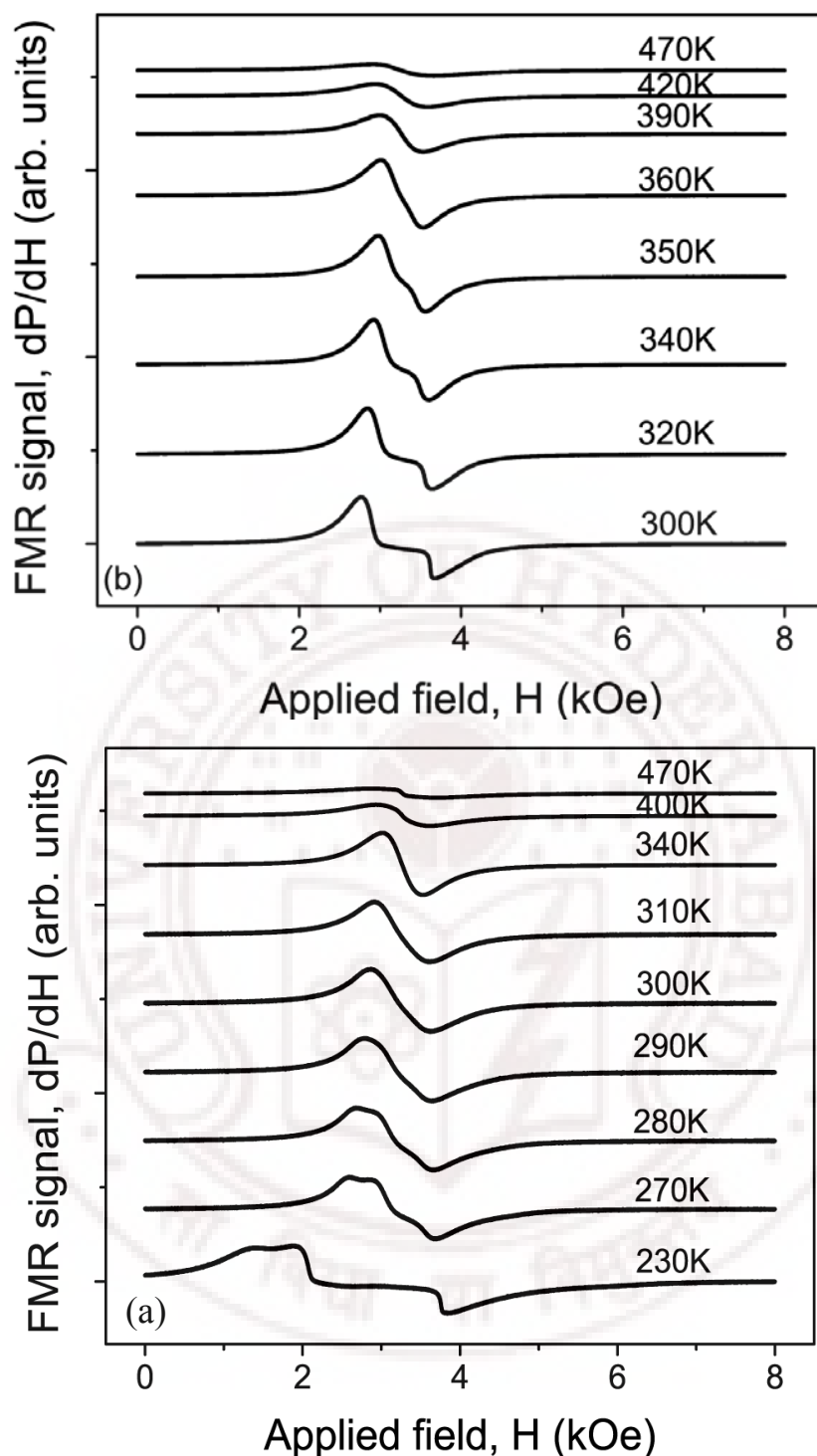


Figure 4.7: FMR spectra of (a) $\text{Cu}_{0.2}\text{Zn}_{0.8}\text{Fe}_2\text{O}_4$ and (b) $\text{Cu}_{0.3}\text{Zn}_{0.7}\text{Fe}_2\text{O}_4$ nanoparticles

The analysis of the resonance absorption of ESR signal for the samples of doped perovskite manganites (either single crystalline or polycrystalline) in which para- and ferromagnetic phases coexist over a wide temperature region was carried out by Dzhezherya and Tovstolytkin [12]. It was found that by taking into account the mutual

influence of coexisting phases gives rise to the appearance of substantial changes in the curves of line shape and H_R values of resonance fields, as well as to the geometry of a phase distribution dependent on an external magnetic field. Near the temperature boundaries of the phase coexistence region, the resonance field for the paramagnetic phase becomes dependent on the shape of the sample, the saturation magnetization and the fraction of ferromagnetic phase.

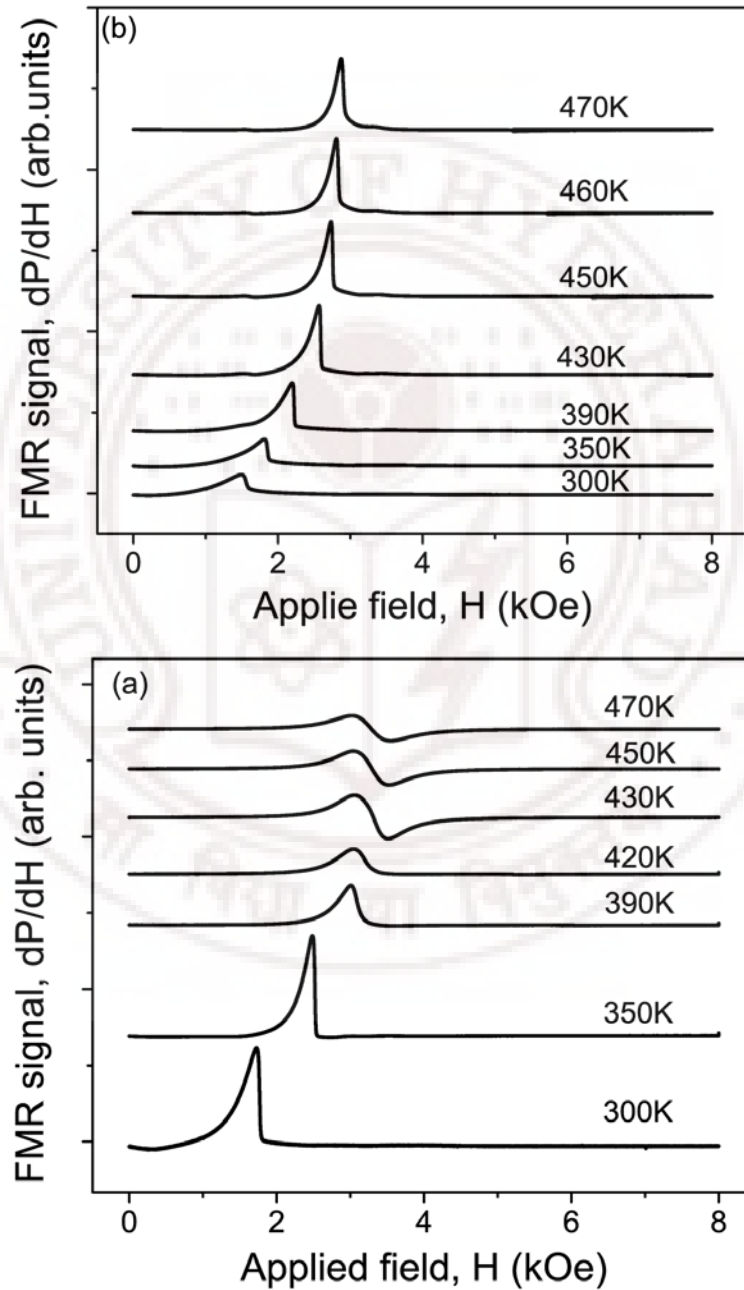


Figure 4.8: FMR spectra of (a) $\text{Cu}_{0.4}\text{Zn}_{0.6}\text{Fe}_2\text{O}_4$ and (b) $\text{Cu}_{0.6}\text{Zn}_{0.4}\text{Fe}_2\text{O}_4$ nanoparticles.

The ESR measurements carried out on spinel compounds $\text{Fe}_{1+x}\text{Cr}_{2-x}\text{S}_4$ by Z. Yang et al. [17] show that only one ESR signal, with a $g \sim 2$, appears at temperatures above T_C (the PM state). Below T_C ESR spectra splits into two resonances. The ESR spectra analysis indicates that the PM-FM transition is not complete and the PM phase may still survive in a certain temperature range below T_C .

This phenomenon was also observed in magnetic ferrofluids. One of the first experimental results regarding the effect of the particle size distribution on the ferromagnetic resonance line was reported by Sharma and Waldner [18]. They showed that at room temperature the ferromagnetic resonance line of some magnetic fluids has a two line pattern, consisting of a narrow line superposed to a broad line. They assumed that the broad line is due to the large particles within the magnetic fluid and the narrow line is due to the small particles, which are in superparamagnetic state. Similar experimental results were reported in Ref. [19,20].

The influence of the temperature on the ferromagnetic resonance behavior of magnetic fluids was investigated by different authors [20–23]. The experimental results have shown that by increasing the temperature, the ferromagnetic resonance line becomes narrower and the resonance field shifts towards larger values. The explanation to the mentioned experimental results was supplied by the effective-field model of Raikher et al. (RSS model) [24,25]. The particles are assumed to be ultrafine (several nanometers in size), hence single-domain and considerably influenced by superparamagnetism. Under these circumstances the shape of the FMR absorption line is determined as interplay of two main mechanisms: thermofluctuational motion of particle magnetic (homogenous broadening) and orientational spreadout of the particle anisotropy axes (inhomogeneous broadening). These sources of the line shape have different temperature and field dependences.

The thermal and the particle size distribution effects on the ferromagnetic resonance of diluted magnetic fluids were theoretically investigated by Marin [26], neglecting possible effects due to the viscosity of the carrier liquid. The model originates from the theory of the ferromagnetic resonance of single-domain particle systems, which was modified in order to take into account the orientation mobility of the particles within the fluid and the finite size of magnetic particles. Under these circumstances the shape of the resonance line, the resonance field and the line width of magnetic fluids are found to be strongly affected by the temperature and by the particle size distribution.

Figure 4.9 shows the temperature dependence of FMR spectra of the as-coprecipitated CuFe_2O_4 nanoparticles in the temperature range 300 to 470K. The FMR data shows a single resonance line fitted by a Lorentzian function corresponding to a g-value of 2.044 at room temperature. Beside the main resonance line there is a very weak signal corresponding to $g \sim 4.3$ for residual Fe^{3+} ions in close contact with spinel Cu-ferrites. The FMR data support the superparamagnetic nature in this sample.

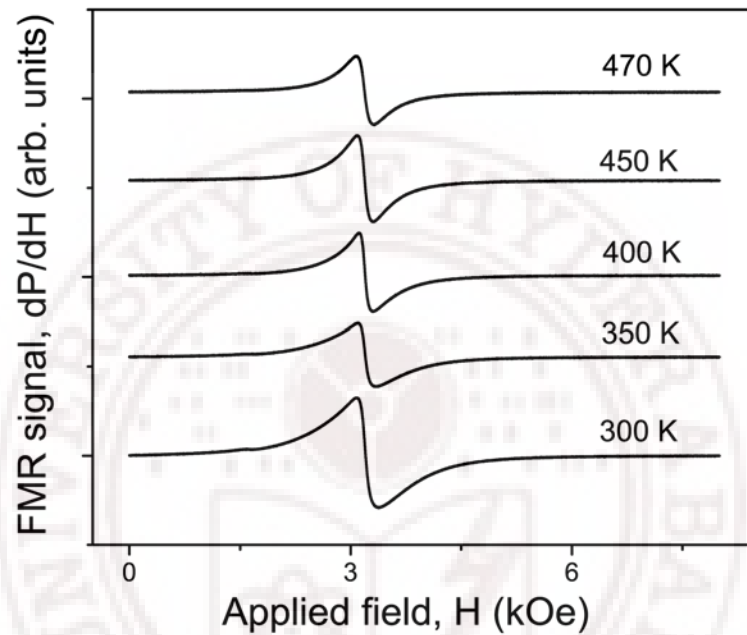


Figure 4.9: FMR spectra of as-coprecipitated CuFe_2O_4 nanoparticles recorded at various temperatures.

Figure 4.10 displays the temperature dependence of resonance field (H_r) and peak-to-peak linewidth (ΔH_{pp}) of the as coprecipitated CuFe_2O_4 nanoparticles. It is found that ΔH_{pp} decreases with increase in temperature up to 370K followed by increasing trend with further increase in temperature. The peak to peak width (ΔH_{pp}) of the FMR signal depends on the magnetic interactions and relaxation times which in turn are influenced by the microstructure of the ferrite material [27]. It could be the slight weakening of magnetic moment that is responsible for the observed reduction in the linewidth when temperature increases to 370 K. The increase of ΔH_{pp} above 370 K could be due to thermal broadening. The resonance field H_r plotted in Figure 4.10 shows weak temperature dependence throughout the temperature range. This is in agreement with the magnetization data which shows that the sample is weak superparamagnet at room temperature.

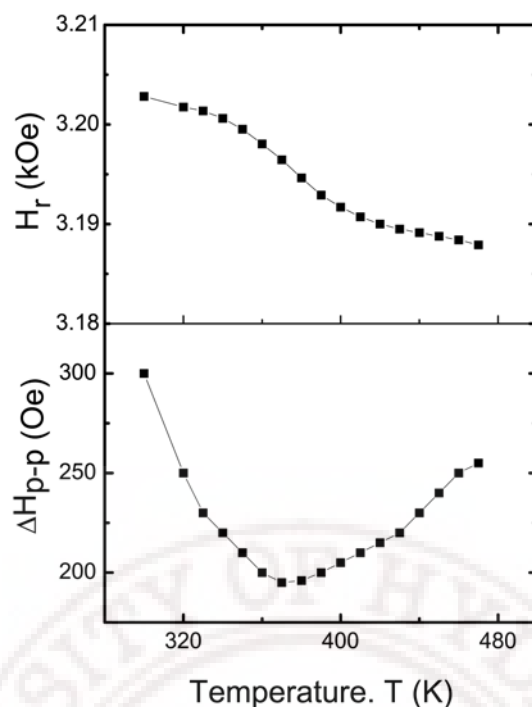


Figure 4.10: Temperature dependence of FMR parameters of CuFe_2O_4 nanoparticles

4.5 Dielectric properties

The variation of the dielectric constant (ϵ') and dielectric loss tangent ($\tan\delta$) of the Cu-Zn ferrite nanoparticle samples has been done as a function of frequency and composition as presented in figure 4.11 and figure 4.12. All the samples show normal behavior where both ϵ' and $\tan\delta$ decrease with increasing frequency. The values of ϵ' and $\tan\delta$ decrease with increase in frequency rapidly in the lower frequency range and marginally in the MHz frequency range. This behavior can be explained on the basis of Koops' model [28] which is based on the Maxwell-Wagner type interfacial space charge polarization for inhomogeneous multi-layer dielectric structure [29,30]. According to this model, the dielectric structure (ferrite) is composed of well conducting grains, which are separated by poorly conducting thin layer grain boundaries, such as an equivalent of a resistor and a capacitor.

There are two types of charge carrier exchange in this system i.e. $\text{Fe}^{2+} \rightleftharpoons \text{Fe}^{3+}$ and $\text{Cu}^{1+} \rightleftharpoons \text{Cu}^{2+}$. When an electric field is applied, it could induce a local displacement of charge carriers through hopping to accumulate at the separating boundaries. The building up of charge carriers at the interfaces corresponds to charge polarization and dielectric constant. At high frequencies, the jumping frequency of electric charge carriers cannot

follow the alteration of applied AC electric field beyond a critical frequency and the probability of charge carriers reaching the grain boundaries decreases resulting in decrease of polarization and dielectric constant [30-32].

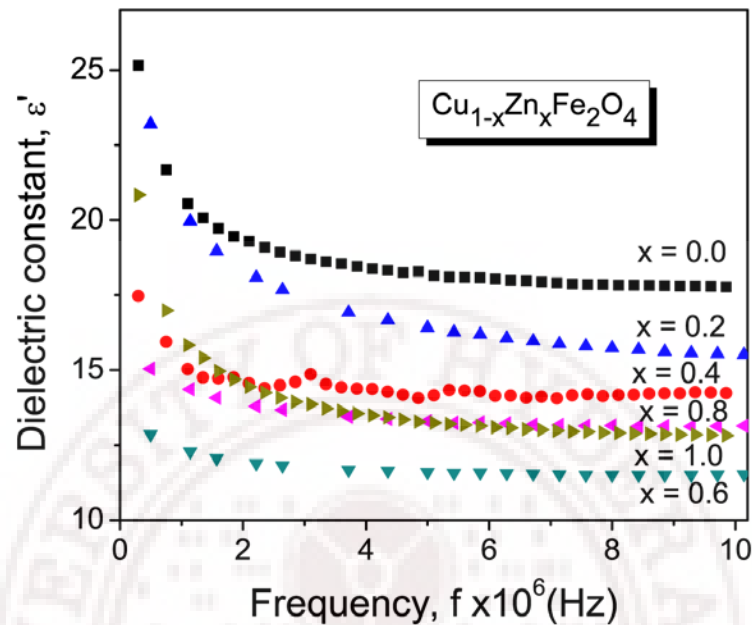


Figure 4.11: Frequency dependence of dielectric constant of $\text{Cu}_{1-x}\text{Zn}_x\text{Fe}_2\text{O}_4$ nanoparticles.

The Loss factor decreases with the increase in frequency as shown in Figure 4.12. The values of $\tan \delta$ depend on a number of factors such as stoichiometry, Cu^+ and Fe^{2+} contents and structural homogeneity, which in turn depend on the composition and sintering temperature of the samples [29]. The initial decrease of $\tan \delta$ with an increase in frequency can also be explained on the basis of Koops' phenomenological model [28].

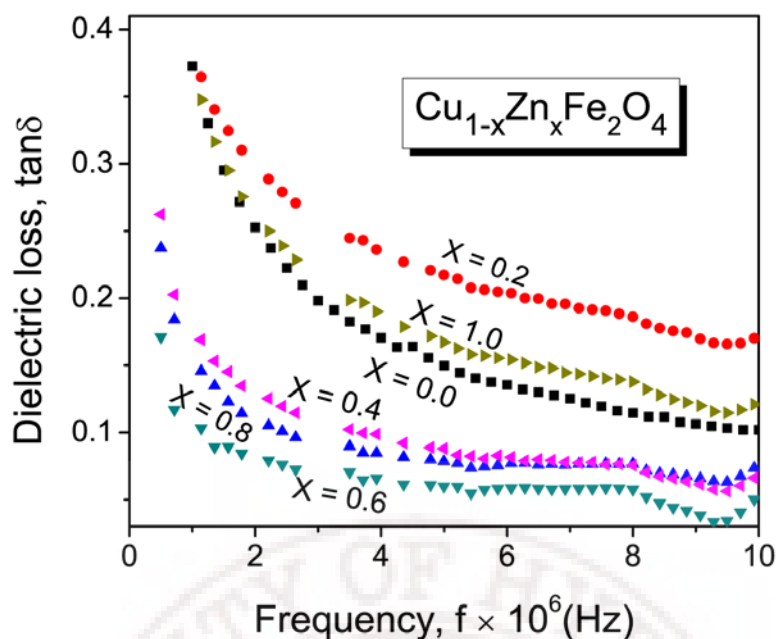


Figure 4.12: Frequency dependence of dielectric loss tangent ($\tan\delta$) of $\text{Cu}_{1-x}\text{Zn}_x\text{Fe}_2\text{O}_4$ nanoparticles.

Figure 4.12 shows that the ϵ' and $\tan\delta$ decrease with increase in Zn content up to $x = 0.6$ followed by increasing trend with further addition of Zn. The variation of dielectric parameters with zinc content can be explained on the basis of two types of charge carrier model [33]. The decrease in ϵ' and $\tan\delta$ with increase in Zn content can be assigned to the decrease in Cu charge carriers. The increase in the ϵ' values with increasing Zn content ($x > 0.6$) suggests the presence of increasing concentration of Fe^{2+} ions [34]. The Fe^{2+} ions being more easily polarizable than the Fe^{3+} ions, an increase in Fe^{2+} concentration would result in an increase in dielectric constant.

The real part of complex permittivity (ϵ') of the nanocrystalline copper and zinc ferrites prepared by solid state reaction (bulk) and coprecipitation methods (nanoparticles) is shown in Figure 4.13 (a) and (b). The frequency dependence of dielectric constants (ϵ') for the coprecipitated samples show little dispersion unlike for the corresponding bulk ferrites. The figure also shows the low values of dielectric constant observed in the coprecipitated CuFe_2O_4 sample compared to those obtained for ferrite bulk ceramics. Different behavior is obtained for the ZnFe_2O_4 where the coprecipitated sample shows higher values compared to the bulk one. The higher values could be attributed to the nanometer size effect of the particles. The dielectric enhancement is attributed to dipoles associated with the interfaces of the nanometer-sized particles. These dipoles result from different types of point defects at the particle interfaces [35]. The effect of particle size on the dielectric

constant of nanocrystalline ZnFe_2O_4 has been studied by Ghatak et al. [36] where ϵ' is high for the smallest particles.

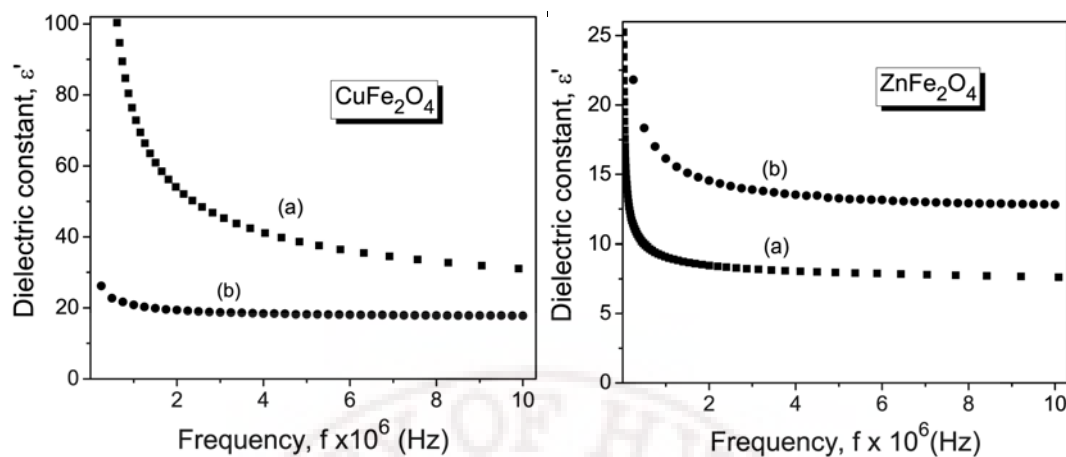


Figure 4.13: Frequency dependence of ϵ' of (a) bulk samples sintered at 1000 °C/12h and (b) coprecipitated samples calcined at 850 °C/6h of CuFe_2O_4 and ZnFe_2O_4 .

4.6 Effect of heat treatment

4.6.1 Copper ferrite nanoparticles

4.6.1.1 Crystal structure

The XRD patterns of CuFe_2O_4 nanoparticles synthesized by coprecipitation method are shown in figure 4.14. It can be seen that the as-synthesized powder does not show any XRD peaks which is an indication of amorphous nature of the sample. The as-coprecipitated powder is not expected to be pure CuFe_2O_4 as it may contain some adsorbed water and amorphous copper and iron hydroxides. Similar behavior has been reported by Tao et al. [37] and Sun et al. [38].

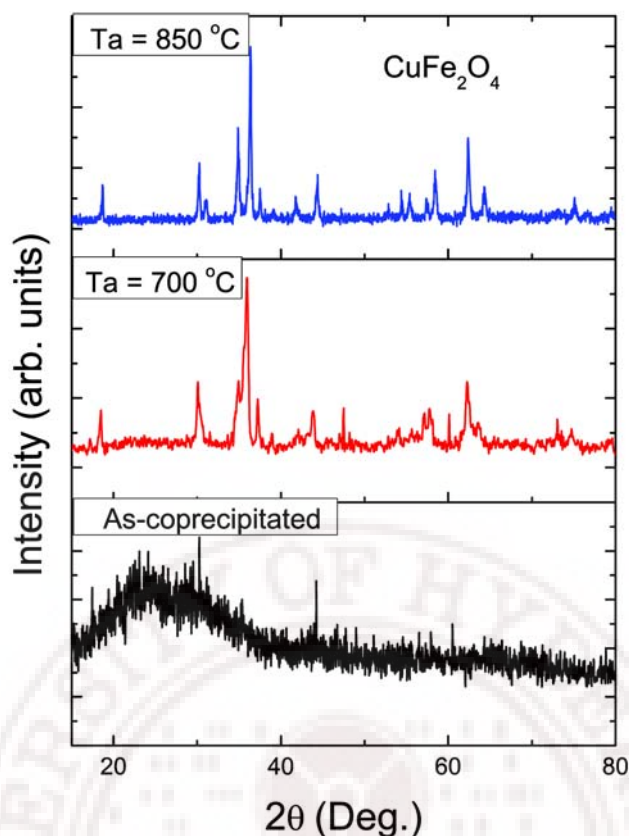


Figure 4.14: the calcination effect on the XRD patterns of CuFe_2O_4 nanoparticles prepared by coprecipitation method.

The crystalline phase of the powder improves when the calcination temperature is increased. Diffraction patterns of the calcined powder show that the crystallization process starts when the calcination is done for 6 hrs at temperatures between 700 and 850 °C. This result is in good agreement with that obtained using metal citrate precursor [2]. The sample calcined at 850 °C is highly crystalline and the position and the relative intensity of peaks match well with that of standard tetragonal CuFe_2O_4 pattern (JCPDS N0. 34-0425) where the patterns display the fundamental peaks of tetragonal structure with $I4_1/amd$ space group regarded as a distorted cubic spinel structure. The d^9 electronic configuration state in Cu^{2+} ions favors the Jahn-Teller effect due to the elongation of the ligand axis along the d orbital [2,39]. The lattice parameters $a = 8.232 \text{ \AA}$ and $c = 8.618 \text{ \AA}$ (for standard $a = 5.844$, $c = 8.630$) were calculated from the position of the principal peaks using a standard least squares routine. The results are also in good agreement with values obtained by other workers [39-41]. We were not able to estimate the average particle size

from the Debye–Sherrer formula due to the amorphous state of the as prepared sample and the large crystallite size of the calcined sample as observed in SEM images ($\langle D \rangle \sim 1 \mu\text{m}$).

4.6.1.2 Microstructural analysis

Figure 4.15 shows the SEM micrographs of as-coprecipitated and calcined samples at 850 °C for 6 hrs. The SEM micrographs show that the as-coprecipitated samples have dominant spherical polydispersed particles with some monodispersed grains linked together with average particle sizes of the order of 60 nm.

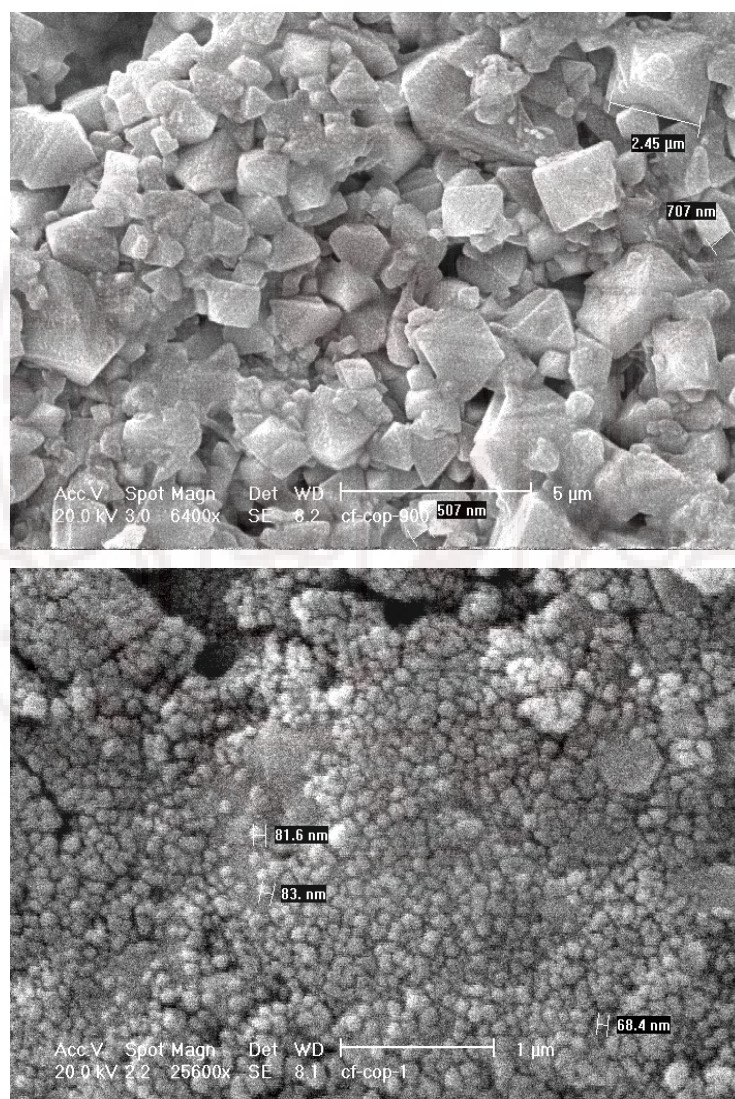


Figure 4.15: SEM micrographs of CuFe_2O_4 nanoparticles. (down) as coprecipitated (above) calcined at 850 °C for 6 hrs.

The calcined sample shows changes in the microstructure from a non-uniform agglomeration to highly crystalline structure. The average grain size is about $1\mu\text{m}$ and density $\sim 5\text{ g/cm}^3$ which is close to that of bulk sample obtained by sintering at $1000\text{ }^\circ\text{C}$ for 12 hrs [Chapter 3] and higher than that obtained for samples synthesized by ball milling and sintered at higher temperature [42]. The grain coarsening is mainly attributed to sintering that forms dense structure. Similar effect was observed by Sun et al. [38].

The EDAX data of the as-coprecipitated sample shows that the Fe/Cu ratio deviates from the stoichiometry at different position in the sample. However, the chemical composition of the sample CuFe_2O_4 heat treated at $850\text{ }^\circ\text{C}$ is found to confirm the chemical homogeneity. The chemical signatures obtained are identical within experimental accuracy (5-8%) and only Cu, Fe, and O elements are observed with the expected molar ratio for CuFe_2O_4 .

4.6.1.3 Magnetic properties

The magnetic properties of ferrite materials are mainly dependant on the preparation method, particle size, sintering temperature, measuring temperature, microstructure and external field. Nanocrystalline ferrites are characterized by a lack of long range atomic order, similar to that of the liquid state. The lack of crystallinity causes nanocrystalline materials to have a very low magnetic anisotropy [43] and lower coercivity.

Figure 4.16 shows the effect of annealing temperature on the M-H plots of CuFe_2O_4 nanoparticles. The magnetization of the as-coprecipitated sample is much smaller than the corresponding bulk sample and it shows superparamagnetic behavior at room temperature with zero coercivity and remanance. The substantial reduction of the magnetization could be related to the large surface area that arises in the imperfect structure of nanosized particles [44]. This leads to possible local canting of magnetic ions and formation of magnetic dead layer on the surface of particles [45,46]. The spherical nanoparticle can be thought of having core-shell structure with shell of finite and constant thickness made of weak-magnetic layer i.e. magnetically dead layer. It has been found that the shell layer can have thickness approximately equal to one lattice constant, which means that the magnetic nature of the first crystalline layer on the nanoparticles is weakened by surface adsorption of nonmagnetic ions but the magnetic properties of the core remains intact and resembles

to bulk magnetization [47]. The superparamagnetic behavior of the sample suggests that the thermal energy can overcome the anisotropy energy barrier of a single particle, and the net magnetization of the particle assemblies in the absence of external magnetic field is zero [48].

Table 4.1: Magnetic parameters of copper ferrite prepared by coprecipitation method.

CuFe_2O_4	M_s (emu/cc)	H_C (Oe)	M_R
As coprecipitated	1.92	0.35	0
Calcined at 700 °C	30	350	8
Calcined at 850 °C	33	450	13
Bulk	35	435	13.5

The samples calcined at 700 and 850 °C exhibit hysteresis behavior at RT typical of ferrimagnetism, with coercivity, H_C , of 350 and 450 Oe, remanence, M_R , of 8 and 13 emu/g, and saturation magnetization, M_s , of 30 and 33 emu/g respectively. The M_s values obtained by extrapolating the high field region of the $M(H)$ curve to infinite field (M vs. $1/H$ to $1/H = 0$). The values of H_C , M_s and M_R/M_s (squareness) ratio for sample calcined at 700 °C are less than the corresponding values for the bulk sample whereas the values obtained for the sample calcined at 850 °C are close to the bulk sample values. For the calcined copper ferrite, the improvement in magnetic properties such as saturation magnetization, remanent magnetization and coercivity are attributed to the increase in grain size, decrease in the defects and impurities and change in cation distribution[49]. This suggests that the calcination at 850 °C for 6 hrs is optimum for this compound to be synthesized by coprecipitation method. The larger value of H_C for the sample calcined at 850 °C compared to that of the bulk sample could be due to several sources including magnetic anisotropy, shape, stress, and surface effects.

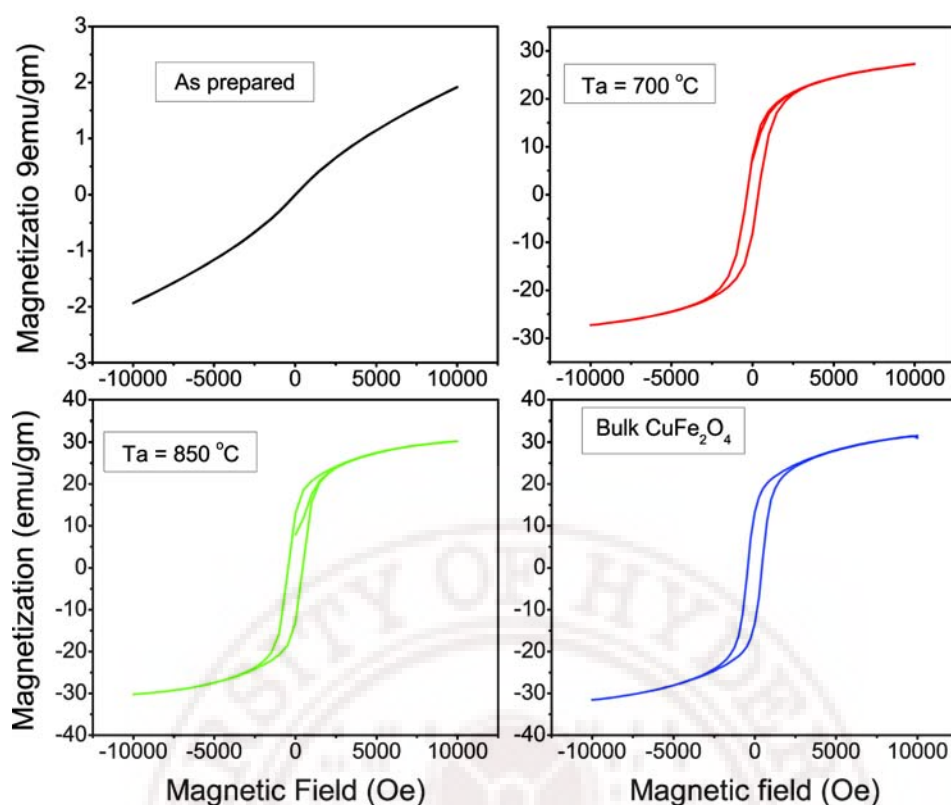


Figure 4.16: M-H plots of CuFe_2O_4 nanoparticles measured at room temperature-The annealing effect.

The magnetization vs magnetic field plots for as-prepared and calcined CuFe_2O_4 nanocrystalline samples 80 and 300K are shown in Figure 4.17. The as-coprecipitated sample does not show hysteresis even at 80 K and does not saturate in applied field up to 10 kOe suggesting that the as-prepared sample is superparamagnetic at RT and 80 K. The relatively low magnetization (M) values found at high fields may be linked to the magnetic disorder due to the poor crystalline state of the CuFe_2O_4 [50].

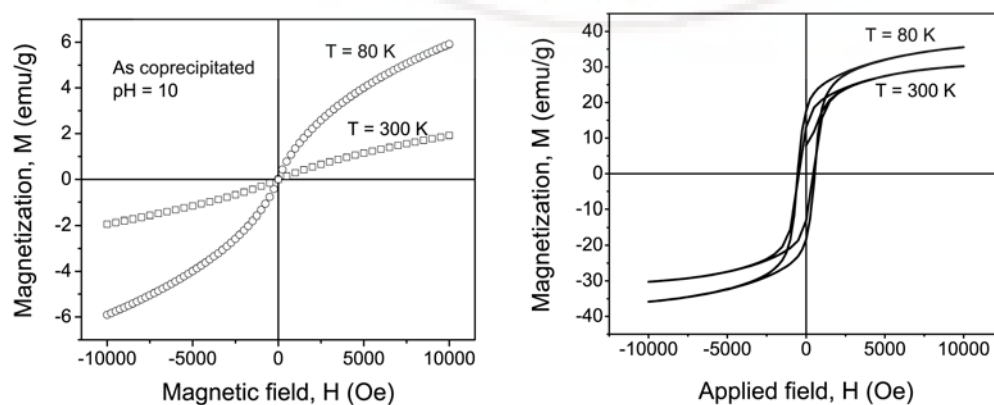


Figure 4.17: M-H plots of CuFe_2O_4 nanoparticles annealed at 850 °C.

The EDAX data of the as-coprecipitated sample does not show the stoichiometric ratio of 1:2 between Cu and Fe for various pieces of the sample. This could be due to the presence of residual CuO and Fe₂O₃ phases in close contact with spinel Cu-ferrite as confirmed by ESR spectra (Figure 4.9) which show weak signal corresponding to isolated Fe³⁺ ions. The magnetization loop measured at 300 K displays a smaller H_C, a reduction of ~ 20% of the value at 80 K. The reduction in H_C and M_S indicates the existence of residual disorder in the sample.

4.6.2 Zinc ferrite nanoparticles

4.6.2.1 Crystal structure (XRD analysis)

To study the effect of particle size on the properties, the as-coprecipitated ZnFe₂O₄ samples were calcined at 500, 700 and 850 °C for 6hrs. XRD patterns of the as-prepared, heat treated and the bulk samples are shown in figure 4.18. The XRD patterns for all the samples display the characteristic peaks of ZnFe₂O₄ which match well with cubic spinel Franklinite [JCDPS file No. 22-1012]. The fundamental peaks of ZnFe₂O₄ as shown in the figure are indexed as (111), (220), (311), (222), (400), (422), (511) and (440). The cell parameters of the samples calculated from the position of the principal peaks using a standard least squares routine are listed in table 4.2. The lattice parameter value of as-synthesized ZnFe₂O₄ particles is 8.47 Å which is larger than the JCPDS table value of 8.441 Å. The cell parameter of the calcined samples decreases with increase in calcination temperature reaching a value of 8.447 Å which is comparable to the value of 8.44 Å obtained for sample synthesized by ceramic method [chapter 3]. These results agree very well with earlier reports [51,52].

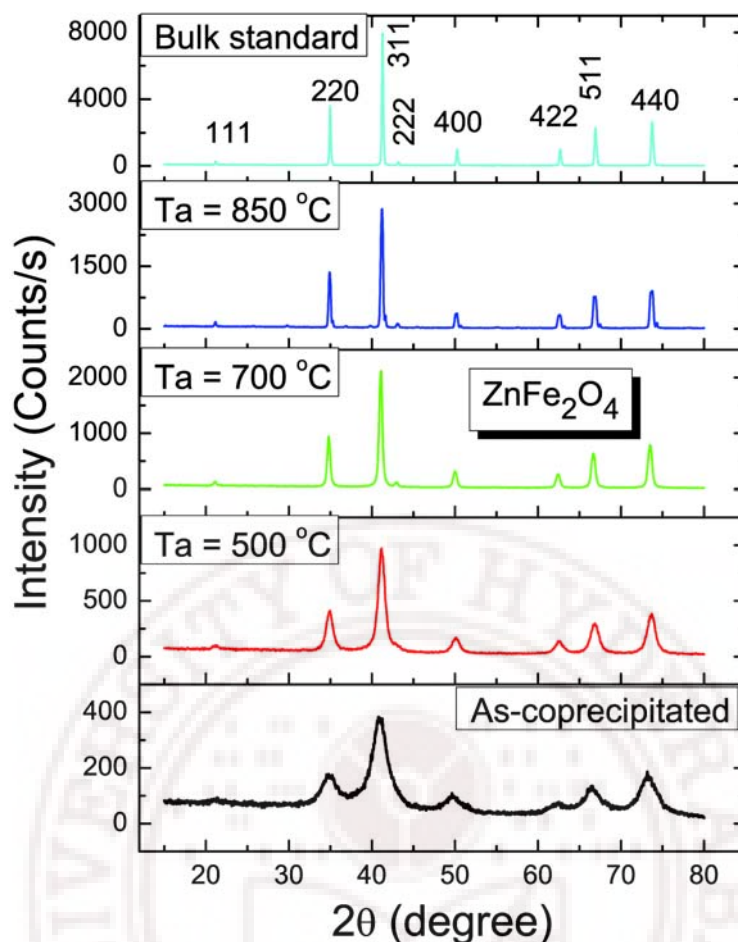


Figure 4.18: XRD patterns of ZnFe_2O_4 nanoparticles- annealing effect

Broad XRD peaks corresponding to single-phase spinel zinc ferrite are observed. The broadening in XRD peaks may come from other sources in addition to the main contributions from the reduced particle size and strain in the crystal. The broadening decreases as heat treatment temperature increases. This indicates the improvement of crystallinity in the powders as well as the particle size growth with increase in heat treatment temperature. The mean particle size $\langle D \rangle$ of the crystallites was estimated from the full width at half maximum of the most intense reflection peak using Scherrer's

formula $\langle D \rangle = \frac{0.9\lambda}{\beta_{1/2} \cos \theta}$ [53] where $\langle D \rangle$ is the average particle size, λ is the wavelength, θ

is the diffraction angle of the most intense peak (311) and $\beta_{1/2}$ is given

by $\beta_{1/2} = \sqrt{(\beta_{1/2})_0^2 - b_0^2}$ [53] where $(\beta_{1/2})_0$ is the full width at half maximum (FWHM) of

the (311) peak and B_0 is same for larger crystallites. The value of $(\beta_{1/2})_0$ was obtained

from the fitting of the (311) peak to the Lorentzian function. The uncertainty in particle

size determination was estimated from the errors in the fitting procedures, which is in the range ± 1 nm. These studies reveal that with the increase in the calcination temperature the crystallite size gradually increases for all the powder samples. The estimated average particle size for various powder samples calcined at different temperatures are listed in Table 4.2.

Table 4.2: Effect of heat treatment on the particle size and lattice parameter of ZnFe_2O_4 nanoparticles prepared by coprecipitation method.

Calcination temperature (°C)	Particle size (nm)	Lattice parameter (Å)
As prepared (80)	8	8.471
500	15	8.461
700	20	8.455
850	30	8.447
Ceramic Standard (1000)	5 μm	8.440

4.6.2.2 Microstructural analysis

Figure 4.19 shows EDAX spectra of various samples. The chemical signatures for Zn, Fe and O are within the expected stoichiometry of ZnFe_2O_4 with an experimental error of (3-6%). This confirms the formation of ferrite crystallites in the as-synthesized sample. XRD and EDAX studies demonstrate that the as-coprecipitated samples were nanoparticles of crystalline ZnFe_2O_4 ferrite.

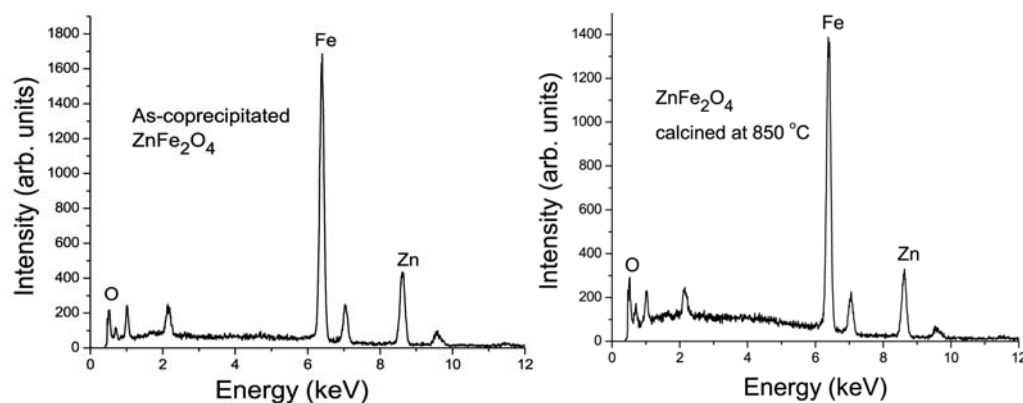


Figure 4.19: EDSX results confirm the formation of ferrite crystallites in the as-synthesized sample. The chemical signatures obtained are identical.

The Figure 4.20 shows the SEM micrographs of as-coprecipitated and the samples calcined at 500 °C, 700 °C and 850 °C for 6 hrs.

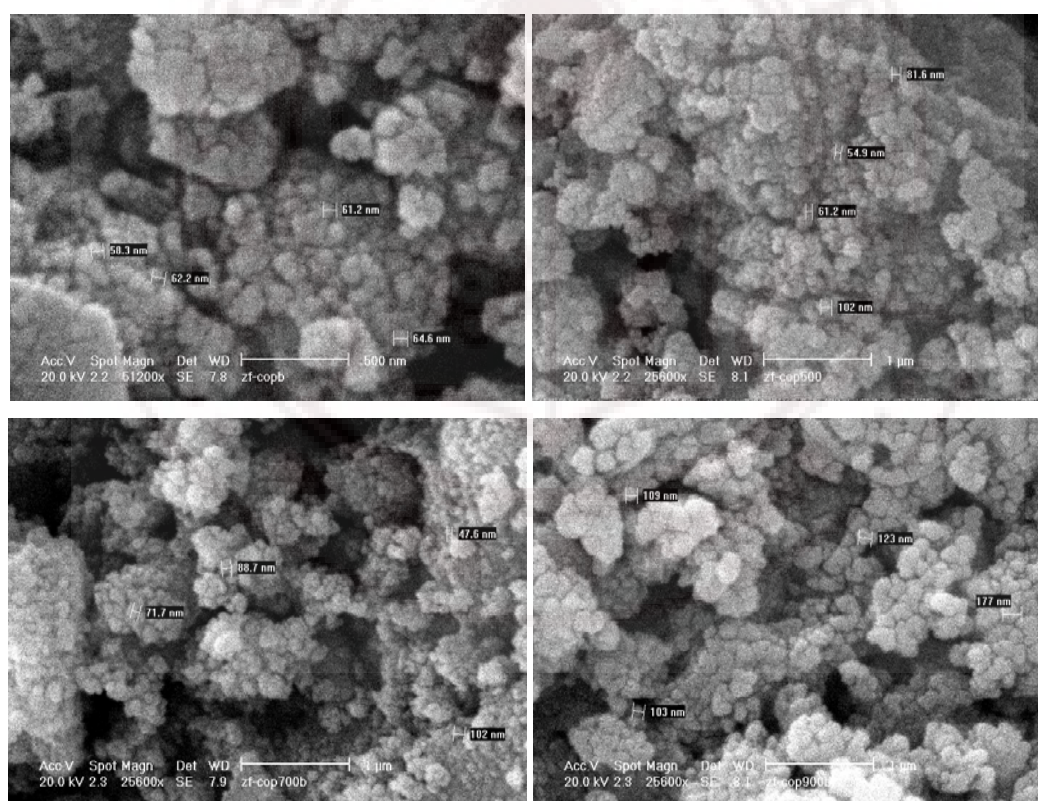


Figure 4.20: SEM micrographs of ZnFe_2O_4 nanoparticles (pH = 10) as a function of heat treatment (a) as-coprecipitated, and calcined at (b) 500, (c) 700 and (d) 850 °C.

The SEM micrographs show that the samples have nanocrystalline structures with average particle sizes ~ 50 nm. The samples calcined at 500- 850 °C show changes in the

microstructure from a uniform agglomeration to grain coarsening without densification. The grain coarsening is mainly attributed to sintering process.

4.6.2.3 Magnetic properties

Figure 4.21 shows room temperature magnetization (M) measurements of coprecipitated and calcined samples of ZnFe_2O_4 prepared at pH values of 10 and 12. It can be seen that the magnetization of as-prepared samples does not saturate up to a magnetic field of 10 kOe. The M values at 10 kOe are 2 and 8 emu/g for the samples synthesized at pH values of 10 and 12 respectively. At RT the sample is paramagnetic having slightly higher M values compared to the bulk sample. This could be due to the existence of ferromagnetic mixed phases in paramagnetic background [54]. The heat treatment significantly decreases the magnetization value. The figure shows large decrease in M value for sample calcined at 850 °C. The higher value of M for sample prepared at pH 12 could be attributed to the redistribution of Zn^{2+} and Fe^{3+} cations in the ZnFe_2O_4 lattice sites. The value of magnetization is related to the inversion parameter δ . Higher magnetization corresponds to higher inversion parameter δ . The cation redistribution has changed from normal to the mixed spinel type structure. Hence, some percentage of Fe^{3+} cations are pinned in tetrahedral sites due to small size effect, which cause the formation of A-B exchange interaction between Fe^{3+} ions on both the sites to give rise to ferrimagnetic ordering of small clusters depending on the inversion parameters. These results are in good agreement with the data on ZnFe_2O_4 nanoparticles reported earlier [54-57].

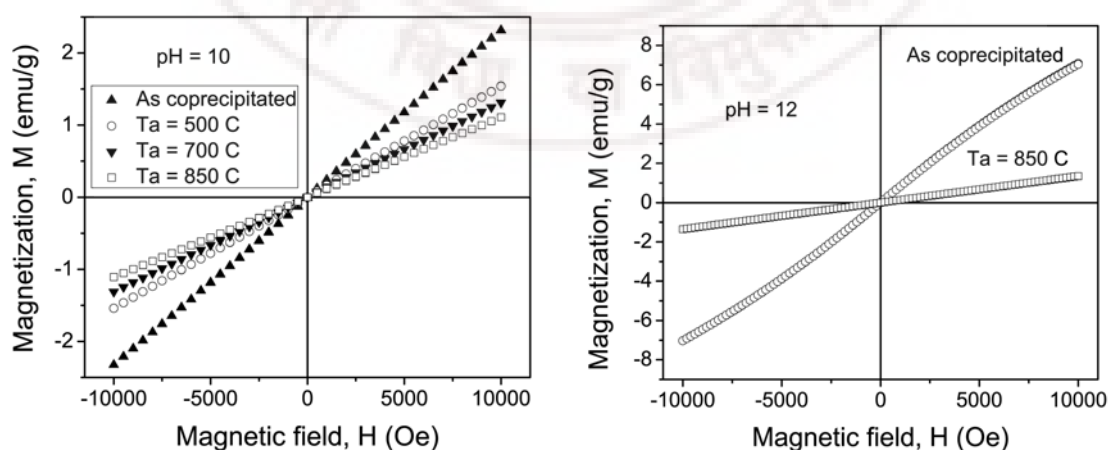


Figure 4.21: Room temperature M-H plots of ZnFe_2O_4 nanoparticles (pH = 10 and 12) as a function of heat treatment.

Figure 4.22 shows the M-H plots of as-coprecipitated and calcined ZnFe_2O_4 nanoparticles (pH = 10 and 12) recorded at 80 and 300 K. The M-H curves at 80 K show high values of M with H_C and M_R close to zero suggesting that the samples are superparamagnets [58]. Similar behavior was observed by Upadhyay et al. [59].

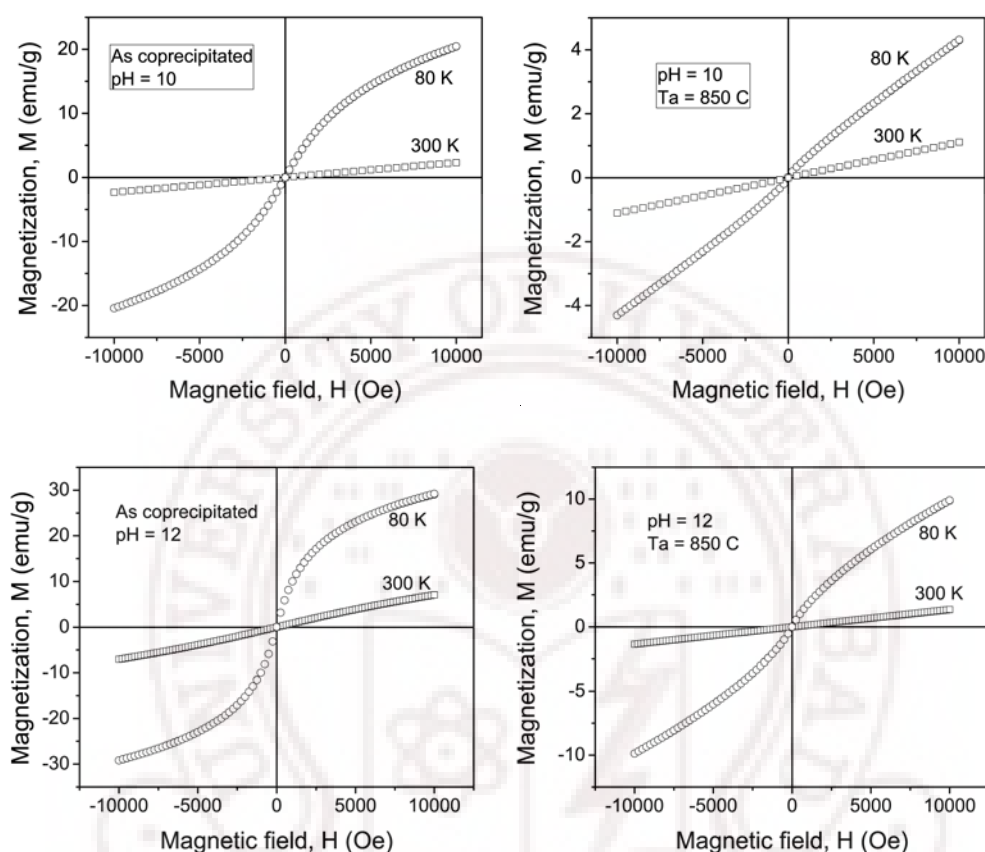


Figure 4.22: M-H plots of as-coprecipitated and calcined ZnFe_2O_4 nanoparticles (pH = 10 and 12) recorded at 80 and 300 K.

Figure 4.23 shows the magnetization (M) as a function of temperature (80-300 K) for the as-prepared sample at pH value of 12 at constant magnetic fields (H_{dc}) of 20, 100 and 5 kOe in the FC-ZFC modes. In this temperature range the superparamagnetic blocking temperature is not observed and it could be below 80 K. The nanoparticles trapped inside magnetic pores show superparamagnetic behavior.

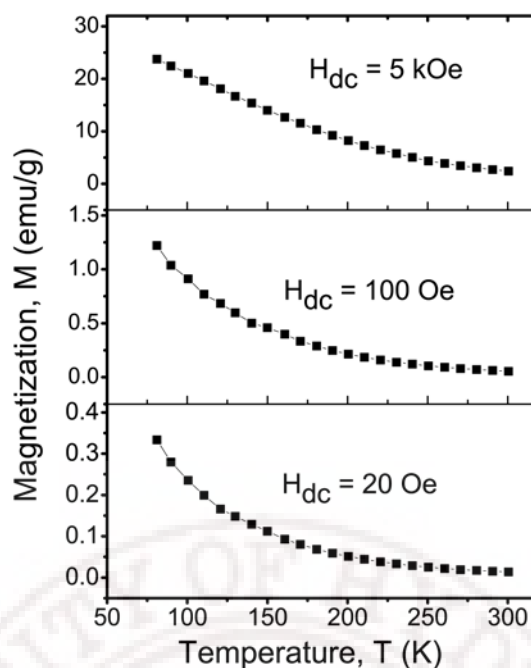


Figure 4.23: M-T curves for ZnFe_2O_4 nanoparticles prepared at pH value of 12

Figure 4.24 shows the effect of pH-value on the magnetic properties of ZnFe_2O_4 nanoparticles. The magnetization value (M) of the as-coprecipitated ZnFe_2O_4 nanoparticles increased significantly by increasing the pH-value. This result can be explained by the fact that the cationic distribution in the nanocrystalline ZnFe_2O_4 is disordered: Zn^{2+} ions occupy B sites and Fe^{3+} ions occupy both A and B sites in the AB_2O_4 spinel structure. The occupation of Fe^{3+} ions on both sites leads to super-exchange spin interaction between A and B sites which give rise to a weak ferrimagnetic behavior. The disorder of cations increases with pH-value and thereby increases the magnetic moment. However, disordered Zn and Fe ions move back to their thermodynamically stable sites during subsequent heat treatment leading to disappearance of ferrimagnetism and ZnFe_2O_4 becoming normal spinel like the corresponding bulk sample.

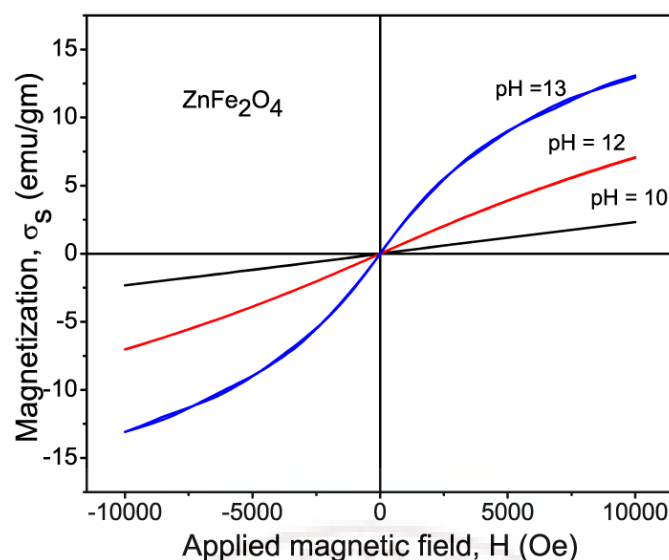


Figure 4.24: Room temperature M-H plots of as-coprecipitated ZnFe_2O_4 nanoparticles prepared at pH = 10, 12 and 13.

4.6.2.4 ESR study

Figure 4.25 shows the ESR spectra of zinc ferrite nanoparticles as a function of particle size. All the spectra show a single broad signal indicating the complete formation of the compound and absence of isolated Fe^{3+} ions. The peak to peak resonance linewidth (ΔH_{pp}) increases with increase in particle size. There is no significant change in g-value as a function of particle size. A good correlation is noticed between ΔH_{pp} and particle size in this compound.

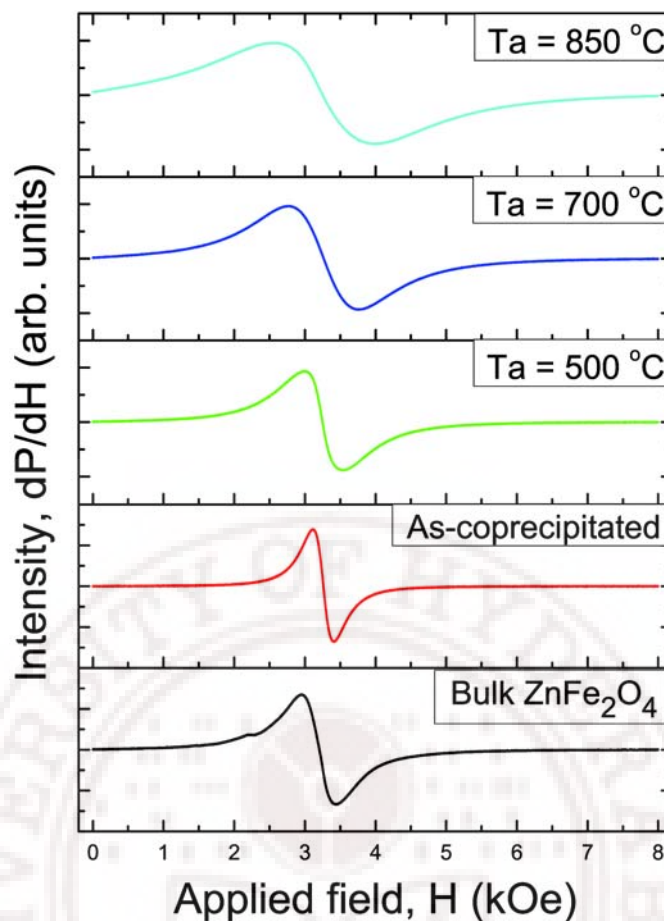


Figure 4.25: EPR spectra of zinc ferrite nanoparticles coprecipitated at a pH-value of 10 as a function of thermal heat treatments.

The temperature dependence of ΔH_{pp} and resonance field H_r for sample with 8 nm particle size is shown in figure 4.26. The ΔH_{pp} decreases with increasing temperature up to 250K followed by increasing trend with further increase in temperature. The reduction in ΔH_{pp} with decreasing temperature is due to the variation of both the magnetization and anisotropy [60]. The large values of ΔH_{pp} and g-factor at low temperature are attributed to stronger dipole-dipole interactions. With increasing temperature, this interaction decreases resulting in decreasing of ΔH_{pp} and increase in H_r . The increase of ΔH_{pp} with temperature above room temperature could be due to thermal broadening. The resonance field H_r decreases slightly with decreasing temperature down to 230 K followed by a rapid decrease at lower temperatures (Figure 4.25). The non-linear temperature dependency of H_r in nanometer size $ZnFe_2O_4$ suggests that the surface anisotropy becomes dominant on the magneto-dynamics of nanoparticles when the

diameter of the nanoparticle is smaller than the critical size (the effect of large surface area to volume ratio) [23].

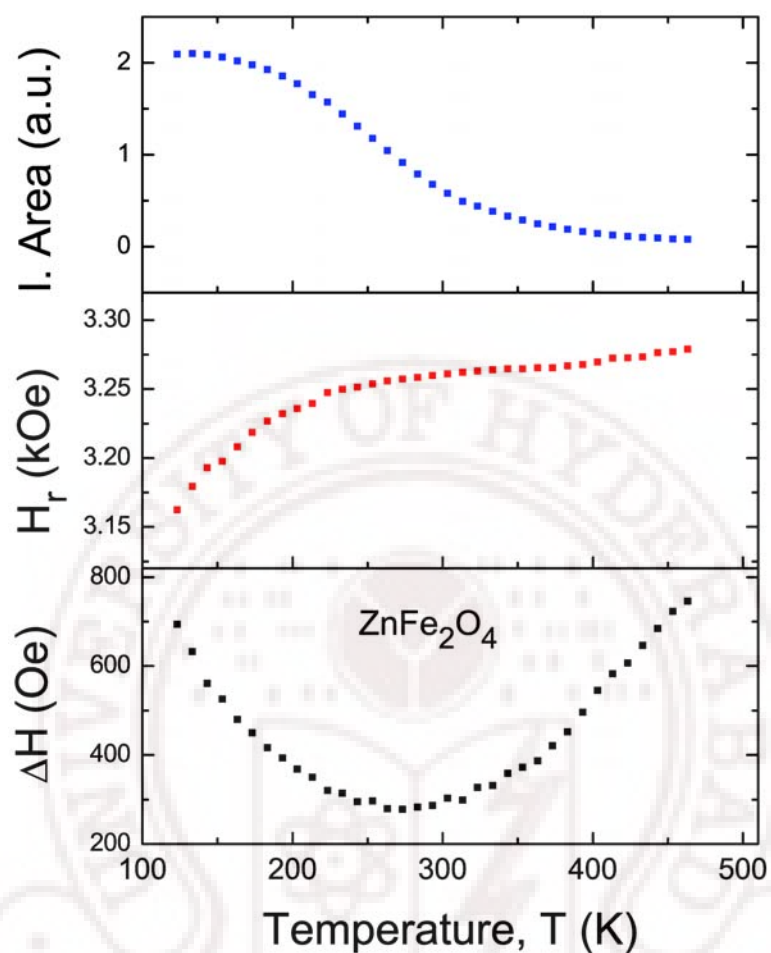


Figure 4.26: Temperature dependence of EPR parameters of Zn-ferrite nanoparticles-Effect of annealing.

References

- [1] G. F. Goya, H. R. Rechenberg and J. Z. Jiang, *J. Appl. Phys.* **84** (1998) 1101-1108.
- [2] M. Bomio, P. Lavela and J. L. Tirado, *J. Solid State Electrochem.* **12** (2008) 729-737.
- [3] M.U. Islam, T. Abbas, S. B. Niazi, Z. Ahmad, S. Sabeen and M. A. Chaudhry, *Solid State Comm.* **130** (2004) 353-356., S. Roy and J. Ghose, *J. Appl. Phys.* **87** (2000) 6226-6228.
- [4] Z. J. Zhang, Z. L. Wang, B. C. Chakoumakos and Jin S. Yin, *J. Am. Chem. Soc.* **120** (1998) 1800- 1804.
- [5] M. Banerjee, N. Verma and R. Prasad, *J. Mater. Sci.* **42** (2007) 1833-1837.
- [6] J. Gao, Y. Cui and Z. Yang, *Mater. Sci. Eng. B* **110** (2004) 111-114.
- [7] M. A. Willard, Y. Nakamura, D. E. Laughlin and M. E. McHenry, *J. Am. Ceram. Soc.* **82** (1999) 3342-3346.
- [8] Y. Yafet and C. Kittel, *Phys. Rev.* **87** (1952) 290-294.
- [9] R. G. kulkarni and U. V. Patil, *J. Mater. Sci* **17** (1982) 843-848.
- [10] A. Goldman, *Modem Ferrite Technology*, 2nd Ed. Springer Science, New York (2006).
- [11] S. Ounnunkad, P. Winotai and S. Phanichphant, *J. Electroceram.* **16** (2006) 363-368.
- [12] Y. I. Dzhzherya and A. I. Tovstolytkin, *J. Phys.: Condens. Matter* **19** (2007) 246212.
- [13] H. H. Hamdeh, J. C. Ho, S. A. Oliver, R. J. Willey, G. Oliveri and G. Busca, *J. Appl. Phys.* **81** (1997) 1851- 1857.
- [14] K. W. Joh, C. H. Lee, C. E. Lee, N. H. Hur and H-C. Ri, *J. Phys.: Condens. Matter* **15** (2003) 4161-4167.
- [15] N. V. Volkov, G. A. Petrakovskii, V. N. Vasilev and K. A. Sablina, *Phys. Solid State* **44** (2002) 1350-1354.
- [16] H-D. Zhou, G. Li, S-J. Feng, Y. Liu, T. qian, X-J. Fan and X-J. Li, *Solid State Comm.* **122** (2002) 507-510.
- [17] Z. Yang, S. Tan and Y. Zhang, *Solid State Comm.* **115** (2000) 679-682.
- [18] V. K. Sharma, F. Waldner, *J. Appl. Phys.* **48** (1977) 4298.
- [19] I. Hrianca, I. Malaescu, F. Claici and C. N. Marin, *J. Magn. Magn. Mater.* **201** (1999) 126-128.
- [20] P. C. Morais, G. R. R. Goncalves, A. F. Bakuzis, K. S. Neto and F. Pelegriini, *J. Magn. Magn. Mater.* **225** (2001) 84.
- [21] F. Gazeau, J-C. Bacri, F. Gendron, R. Perzynski, Yu. L. Raikher, V. I. Stepanov and E. Dubois, *J. Magn. Magn. Mater.* **186** (1998) 175-187.
- [22] P. C. Morais, M. C. F. L. Lara, A. L. Tronconi, F. A. Tourinho, A. R. Pereira, F. Pelegriini, *J. Appl. Phys.* **79** (1996) 7931.

- [23] R. Berger, J-C. Bissey, J. Kliava, H. Daubric and C. Estornes, *J. magn. Magn. Mater.* **234** (2001) 535-544.
- [24] Y. L. Raikher and V. I. Stepanov, *Phys. Rev. B* **50** (1994) 6250-6259.
- [25] Y.L. Raikher and V.I. Stepanov, *J. Magn. Magn. Mater.* **149** (1995) 34-37.
- [26] C. N. Marin, *J. Magn. Magn. Mater.* **300** (2006) 397-406.
- [27] P. Chand, *Hyperfine Interact* **184** (2008) 195-200.
- [28] C. G. Koops, *Phys. Rev.* **83** (1951) 12-124.
- [29] M. Ajmal and A. Maqsood, *J. Alloys Comps.* **460** (2008) 54-59.
- [30] N. H. Vasoya1, V. K. Lakhani, P. U. Sharma, K. B. Modi, R. Kumar and H. H. Joshi, *J. Phys.: Condens. Matter* **18** (2006) 8063-8092.
- [31] M. A. El Hiti, *J. Magn. Magn. Mater.* **192** (1999) 305-313.
- [32] R. C. Kambale, P. A. Shaikh, C. H. Bhosale, K. Y. Rajpure and Y. D. Kolekar, *Smart Mater. Struct.* **18** (2009) 085014.
- [33] N. Rezlescu and E. Rezlescu, *Phys. Stat. Sol. (a)* **23** (1974) 575-587.
- [34] N. Gupta, A. Verma, S. C. Kashyap and D. C. Dube, *Solid State Comm.* **134** (2005) 689-694.
- [35] S. Berger, Dielectric Properties of Nanoparticles, In: *Encyclopedia of Nanoscience and Nanotechnology*, Edited by H. S. Nalwa, American Scientific, Vol. **2** (2004) 371-387.
- [36] S. Ghatak, M. Sinha, A. K. Meikap and S. K. Pradhan, *Physica E* **40** (2008) 2686-2693.
- [37] S. Tao, F. Gao, X. Liu and O. T. Sørensen, *Mater. Sci. Eng. B* **77** (2000) 172-176.
- [38] Z. Sun, L. Liu, D. Jia and W. Pan, *Sensors and Actuators B* **125** (2007) 144-148.
- [39] J. Darul and W. Nowicki, Radiation, *Phys. Chem.* **78** (2009) S109-S111.
- [40] R. K. Selvan, C. O. Augustin, C. Sanjeeviraja and D. Prabhakaran, *Solid State Comm.* **137** (2006) 512-516.
- [41] R. K. Selvan, C. O. Augustin, M. I. Oshtrakh, O. B. Milder and V. A. Semionkin, *Hyperfine Interact* **165** (2005) 231-237.
- [42] M. H. Khedr, A. A. Farghali, and A. A. Abdel-Khalek, *J. Anal. Appl. Pyrolysis* **78** (2007) 1-6.
- [43] C. D. Lokhande, S. S. Kulkarni, R. S. Mane and S-H. Han, *J. Magn. Magn. Mater.* **313** (2007) 69-75 73.
- [44] H. Nathani, S. Gubbala and R. D. K. Misra, *Mater. Sci Eng. B* **121** (2005) 126-136.
- [45] J. P. Chen, C. M. Sorensen, K. j. Klabunde, G. C. Hadjipanayis, E. Devlin and A. Kostikas, *Phys. Rev. B* **54** (1996) 9288.
- [46] J. M. D. Coey, *Phys. Rev. Lett.* **27** (1971) 1140-1142.
- [47] M. K. Rangolia, M. C. Chhantbar, A. R. Tanna, K. B. Modi, G. J. Baldha and H. H. Joshi, *Indian J. Pure Appl. Phys.* **46** (2008) 60-64.
- [48] C. Liu and Z. J. Zhang, *Chem. Mater.* **13** (2001) 2092-2096.
- [49] C. D. Lokhande, S. S. Kulkarni, R. S. Mane and Sung-Hwan Han, *J. Crystal Growth* **303** (2007) 387-390.

- [50] R. A. Borzi, S. J. Stewart, G. Punte, R. C. Mercader, G. Cernicciato and F. Garcia, *Hyperfine Interact* **148/149** (2003) 109–116.
- [51] H. H. Hamdeh, J. C. Ho, S. A. Oliver, R. J. Willey, G. Oliveri and G. Busca, *J. Appl. Phys.* **81** (1997) 1851.
- [52] J. Philip, G. Gnanaprakash, G. Panneerselvam, M. P. Antony, T. Jayakumar and B. Raj, *J. Appl. Phys.* **102** (2007) 054305.
- [53] B.D. Cullity and S. R. Stock, *Elements of X-Ray Diffraction*, 3rd Ed., Prentice Hall, New Jersey, USA (2001).
- [54] S. A. Oliver, V. G. Harris, H. H. Hamdeh and J. C. Ho, *Appl. Phys. Lett.* **76** (2000) 2761.
- [55] T. Sato, K. Haneda, M. Seki and T. Iijima, *Appl. Phys. A* **50** (1990) 13-16.
- [56] S. Ammar, N. Jouini, F. Fievet, Z. Beji, L. Smiri, P. Moline, M. Danot and J. Greneche, *J. Phys.: Condens. Matter* **18** (2006) 9055–9069.
- [57] A. Yan, X. Liu, R. Yi, R. Shi, N. Zhang, and G. Qiu, *J. Phys. Chem. C* **112** (2008) 8558–8563.
- [58] S. Bedanta and W. Kleemann, *J. Phys. D: Appl. Phys.* **42** (2009) 013001.
- [59] C. Upadhyay, H.C. Verma, V. Sathe and A.V. Pimpale, *J. Magn. Magn. Mater.* **312** (2007) 271–279.
- [60] P. Kirrani, R. V. Upadhyay and R. V. Mehta, *J. Magn. Magn. Mater.* **252** (2002) 35-38.

CHAPTER-5

Properties of Cu-Zn ferrite thin films

This chapter contains the experimental results on the growth, structure, magnetic and optical properties of ferrosipinel $\text{Cu}_{1-x}\text{Zn}_x\text{Fe}_2\text{O}_4$ ($x = 0, 0.4$ and 1) thin films deposited by rf-magnetron sputtering. The RF-Magnetron sputtering is a useful technique for getting very high deposition rate and homogeneous films with unique properties achieved by controlling the sputtering parameters [1]. The main objective is to study the influence of deposition environment on the structure and film growth as well as on the magnetic and optical properties of the sputtered films. These studies would be helpful in finding out the role of Cu^{2+} and Cu^{1+} ions in controlling the magnetic and optical properties of these ferrites. The Cu-ion valence state can be altered by using reducing or oxidizing environment while depositing the films. The studies on bulk $\text{Cu}_{0.5}\text{Fe}_{2.5}\text{O}_4$ ferrite show the ordering of the Cu^+ ions to the tetrahedral A-site when material is quenched from high temperature in a highly reducing atmosphere [2]. Our studies on bulk $\text{Cu}_{1-x}\text{Zn}_x\text{Fe}_2\text{O}_4$ ferrites show that highest magnetization of ~ 330 emu/cc is obtained for the composition $\text{Cu}_{0.6}\text{Zn}_{0.4}\text{Fe}_2\text{O}_4$ [3]. There is no report on the properties of copper-zinc ferrite thin films. The detailed study of crystal structure, magnetic and optical properties of Cu-Zn ferrite thin films are presented in this chapter.

The pure Argon (Ar), pure oxygen (O_2) and mixture of ($\text{Ar}+\text{O}_2$) were used as sputtering gases at pressure of 5, 8, 12 and 15 mTorr. The films were deposited on glass substrates mounted on a non-rotating, unheated platform placed at a distance of ~ 60 mm below the target inside a vacuum chamber with a turbo pump yielding a base pressure of 10^{-6} Torr. For all the films the deposition time was kept 60 minutes. The films were deposited using rf-power of 100 W at various working gas pressure of Ar , O_2 and $\text{Ar}+\text{O}_2$. We have used 2-inch diameter polycrystalline sintered targets prepared by ceramic method using high purity starting materials with final sintering at 900°C for 12 hrs.

5.1 Copper ferrite (CuFe₂O₄) thin films

Introduction

Thin films of spinel ferrites MFe₂O₄ (M = Mn, Cu, Zn, Ni, Co, Cd, etc.) exhibit excellent chemical stability and high corrosion resistivity and seem to be applicable as recording media and microwave absorbing layers [4]. In the spinel structure, the relatively large (1.4 Å) oxygen ions form a close packed f.c.c. lattice with two kinds of interstitial sites, the tetrahedral (A) sites and octahedral (B) sites that are surrounded by four and six oxygen ions respectively. The smaller transition metal cations (M²⁺ and Fe³⁺) occupy the interstices of oxygen ion lattice. The cation distribution among A and B sub-lattices determines to a large degree the magnetic and electronic properties of spinel ferrites. The general cation distribution can be indicated as: $(M_d^{2+}Fe_{1-d}^{3+})_{tetra}[M_{1-d}^{2+}Fe_{1+d}^{3+}]_{octa}O_4^{2-}$ where d = 1, 0 and 0 < d < 1 for normal, inverse and mixed spinel respectively [5].

Copper ferrite crystallizes in an inverse or mixed spinel structure depending upon the preparation conditions. Under slow cooling Cu-ferrite crystallizes in a tetragonal structure with lattice parameter ratio c/a of about 1.06. Tetragonal phase of Cu-ferrite has inverse spinel structure with almost all Cu²⁺ ions occupying octahedral sublattice, whereas Fe³⁺ ions divide equally between the tetrahedral and octahedral sublattices. There is a structural phase transition from tetragonal to cubic at a temperature of 390 °C due to disorientation of Jahn–Teller distortion as a result of thermal motion of lattice at high temperatures [6]. This transition is strongly affected by the distribution of Cu ions on the two sublattices and the oxygen stoichiometry. These parameters can be altered by adjusting preparation conditions such as sintering temperature, cooling rate, gaseous environment etc. With increasing the number of Cu²⁺ ions on tetrahedral sublattice the distortion decreases stabilizing the cubic symmetry with large magnetic moment at room temperature [7,8].

There have been a number of studies on Cu-ferrite thin films with the objective of enhancing magnetization for applications [9-12]. In these studies higher magnetization values were achieved either by substrate heating or annealing the films at high temperatures. Zuo et al. [13] predicted that a high magnetization may be achieved by increasing the number of Cu^{2+} ions on A-sublattice.

In this section, we have studied the effect of deposition environment on the structure, magnetic and optical properties of Cu-ferrite thin films. The films were deposited in pure Ar and pure O_2 at different working pressure. Then the films were deposited in a mixture of Ar and O_2 to understand the effect of oxidizing environment on their properties.

5.1.1 Effect of Ar- O_2 pressure

5.1.1.1 Structural analysis (XRD)

Figure 5.1 shows the XRD patterns for the as-deposited CuFe_2O_4 films. All the peaks belong to cubic spinel structure without any secondary phase. The diffraction (220) lines indicate the textured growth in the case of film deposited in Ar. With increase in oxygen content the intensity of (400) peak increases at the expense of (220) peak intensity. Ohnishi and Teranishi [7] reported that for spinel-ferrite the intensity ratios of planes I220/I400, I440/I400 and I422/I400 are considered to be sensitive to the cation distribution parameter (d). Our XRD data shows a strong dependence of these intensity ratios on the deposition environment. The higher values of these ratios for the as-deposited films in pure Ar indicate higher inversion parameter. The average crystallite size (D) of the films was estimated from XRD data using the Scherrer formula [14] $D = 0.9\lambda / \beta \cos \theta$, where λ is the wavelength of the used X-rays, β is the broadening of diffraction line measured at the half maximum intensity in radians and θ is the angle of diffraction. The values of the crystallite sizes are estimated to be about 15 ± 2 nm for the film deposited in Ar and decreases with increasing oxygen partial pressure to be about 10 ± 2 nm for the film prepared in pure oxygen.

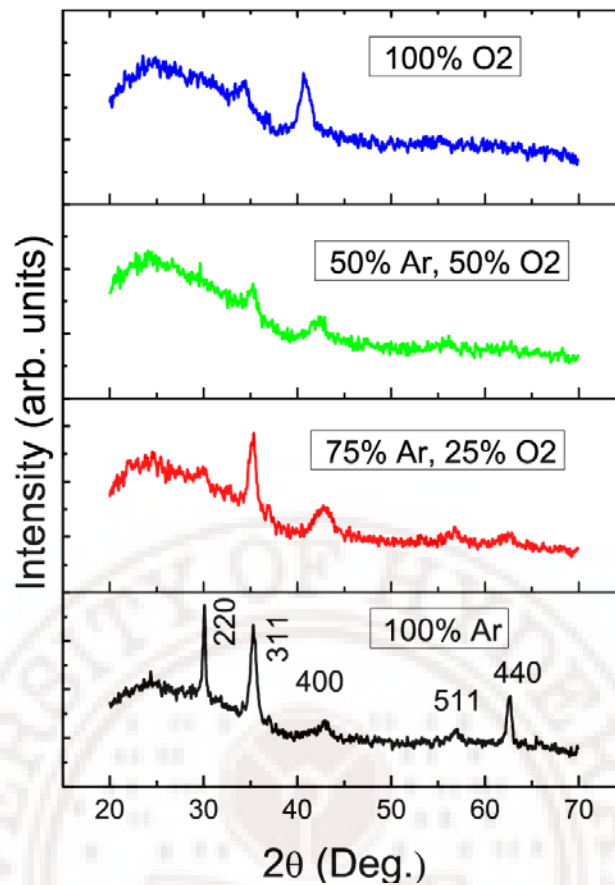


Figure 5.1: XRD patterns of as-sputtered Cu-ferrite films prepared under (Ar+O₂) at 12 mTorr.

5.1.1.2 Surface morphology (AFM)

Figure 5.2 shows the AFM images of the films. The film sputtered in Ar shows dense formation of oblong crystallites with partial alignment in one direction. The shape of grains becomes Y-shaped and their density decreases with increase in O₂ content. The average grain sizes and root mean square roughness (rms) values decreases with oxygen content (Table 5.1).

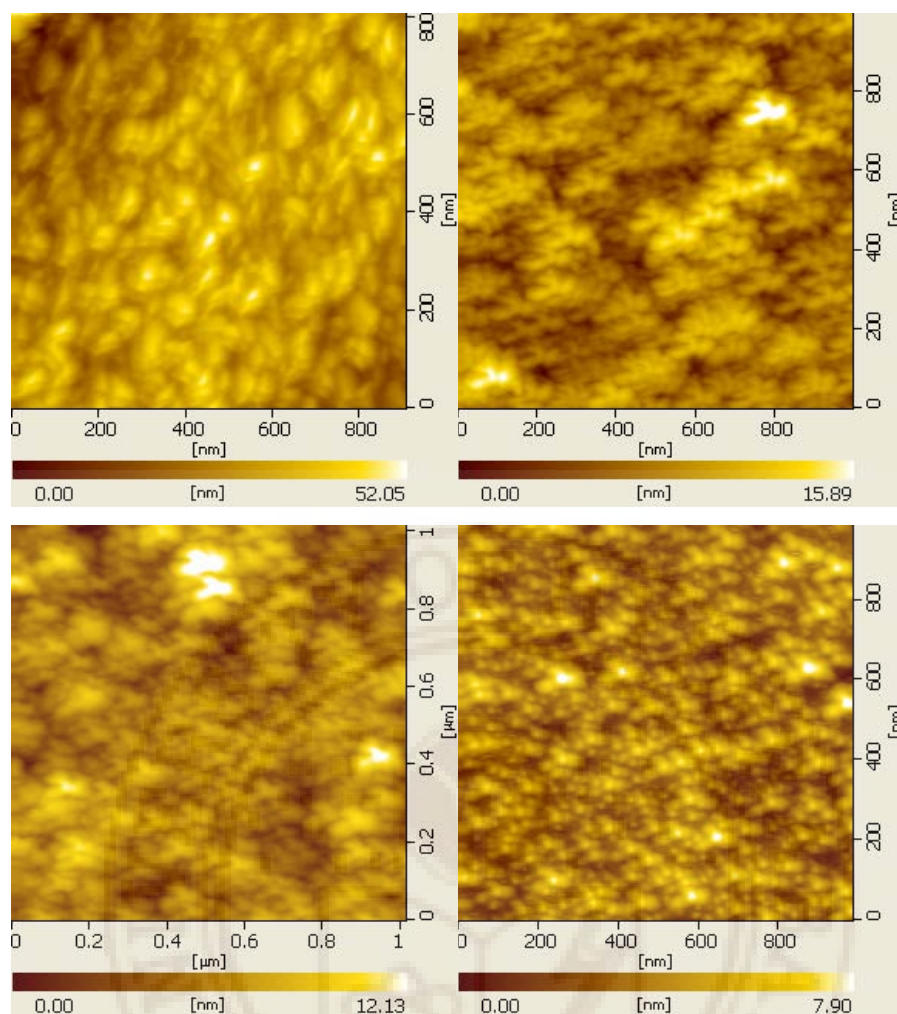


Figure 5.2: AFM images of as-sputtered Cu-ferrite films prepared under (Ar+O₂) at 12 mTorr.

The average composition of the films was determined by EDAX studies using systematic data collected from the centre and edges of the films. The relative elemental concentration was used to estimate the atomic composition of the as-deposited films by considering their values normalized to the nominal composition of the target. The composition of the films was found to be close to the composition of the target. Figure 5.3 presents the EDAX analysis for CuFe₂O₄ thin film deposited on a glass substrate. The Cu, Fe and O peaks appear along with a large Si substrate peak. The evolution of the oxygen peak in the EDAX spectra showed increasing values for the oxygen signal after thermal annealing at 500 °C.

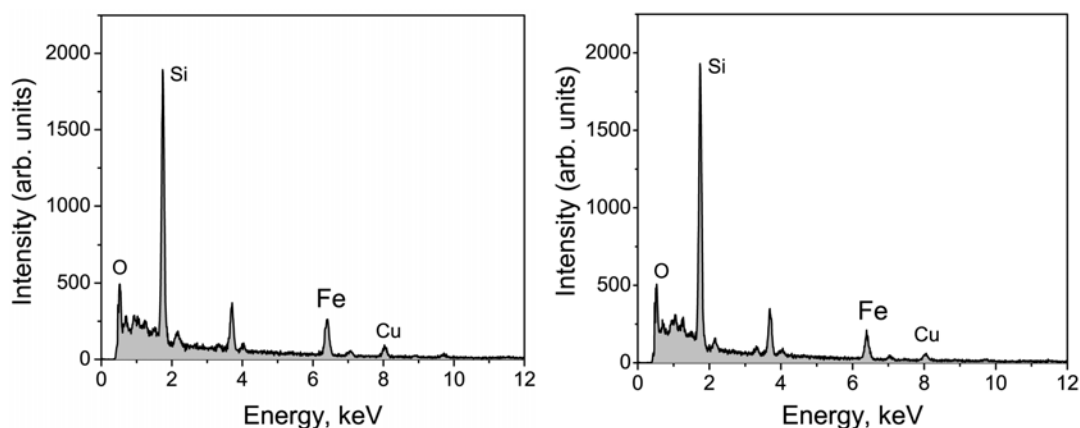


Figure 5.3: EDAX results confirm the formation of ferrite nanocrystallites in the as-deposited and annealed at 500 °C CuFe_2O_4 films. The chemical signatures obtained are identical. The films deposited on glass substrates and show prominent Si peaks.

Figure 5.4 shows the SEM micrographs of heat treated CuFe_2O_4 film at 500 °C for 3 hrs. The SEM micrographs show that the film has nanocrystalline structure with average grain sizes of about 80 nm. It can be observed that the grains of the CuFe_2O_4 film are dense and uniform after heat treatment.

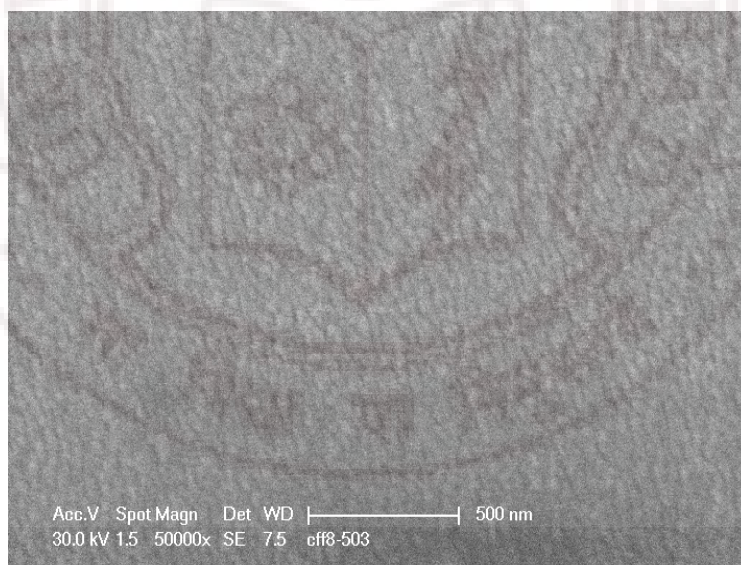


Figure 5.4: SEM images of CuFe_2O_4 thin films deposited at 12 mTorr Ar and annealed at 500 °C for 3 hrs.

5.1.1.3 Magnetization studies (*M-H* plots)

Figure 5.5 shows the *M-H* plots at RT for the Cu-ferrite films deposited under Ar gas environment with external field parallel (H_{\parallel}) and perpendicular (H_{\perp}) to the film planes.

The estimated magnetic parameters are summarized in Table 5.1. The films show large magnetization values and exhibit ferrimagnetic behavior with strong magnetic anisotropy. The saturation magnetization (M_S) for bulk Cu-ferrite target is found to be 170 emu/cm^3 [Chapter 3]. The magnetization value of the as-deposited film strongly depends on Ar gas pressure. The in-plane magnetization $M_{S\parallel}$ values of the as-deposited films are 120, 142, 264 and 247 emu/cm^3 at 5, 8, 12 and 15 mTorr of pure Ar gas respectively. Since $M_{S\parallel}$ value is found to be maximum for films deposited under 12 mTorr, the effect of O_2 addition was therefore studied by maintaining the (Ar+ O_2) pressure at this level. The magnetization values and coercivity (H_C) as a function of oxygen content are listed in Table 5.1.

The estimated deposition rate is $\sim 58 \text{ \AA /min}$ for the films prepared under pure Ar and it decreases to $\sim 17 \text{ \AA /min}$ in pure oxygen at pressure of 12 mTorr. The high deposition rate in pure Ar gas environment can lead to freezing of some Cu-ions on tetrahedral sites and equivalent number of Fe ions on octahedral sites during the deposition process. Furthermore, the deposition in reducing (argon) atmosphere may lead to the formation of Cu^+ ion, having larger ionic radius than the Cu^{2+} ion. The Cu^+ ions prefer occupation of the smaller four-coordinated tetrahedral site in the spinel structure and displace Fe^{3+} cations to occupy the octahedral sublattice [2]. This will increase octahedral Fe^{3+} ion concentration in expense of Cu^{2+} ions which in turn causes ferrimagnetic behavior with large magnetization.

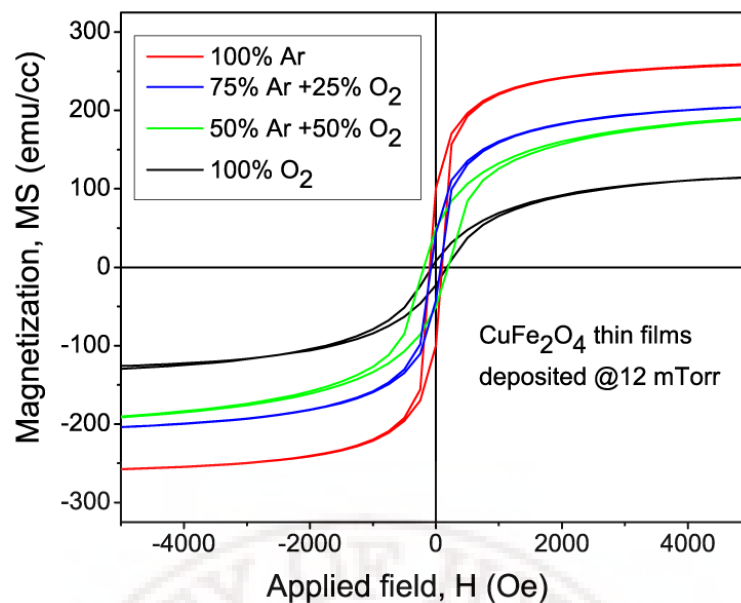
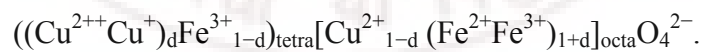


Figure 5.5: M-H curves of as-sputtered Cu-ferrite films prepared under (Ar+O₂) at 12 mTorr.

For the films sputtered under Ar atmosphere, the estimated magnetic moment is $2.1 \mu_B$ per formula unit, whereas it is $1.5 \mu_B$ per formula unit for the bulk target. The magnetization value of $2.3 \mu_B$ has also been reported for quenched bulk Cu-ferrite [15]. The higher value of M_S can therefore arise due to ordering of Cu^{2+} to tetrahedral A-sites. The decrease in M_S value with increase in oxygen content in (Ar+O₂) mixture is ascribed to decrease in growth rate and Cu^{2+} concentration which allow the cations to take up their preferable sites. The formation of Fe^{2+} cannot be ruled out in the spinel structure where a fraction of Fe^{3+} will be replaced by Fe^{2+} ions. So the general cation distribution for copper ferrite can be represented as



The strong magnetic anisotropy of the films may be due to weak coupling between Cu^{2+} on the A-sites and Fe^{3+} on B-sites as a result of ordering of the Cu^{2+} ions to tetrahedral A-sites.

Table 5.1: Structural and magnetic parameters of as-sputtered Cu-ferrite films prepared under (Ar + O₂) at 12 mTorr.

(Ar+O ₂) (%)	Thickness (nm)	Grain size (nm)	RMS (nm)	M _S (emu/cc)	M _{S⊥} (emu/cc)	H _C (Oe)	H _{C⊥} (Oe)
±5%							
100 + 0	350	126	3.7	264	188	100	107
75 + 25	210	112	2.6	212	150	77	110
50 + 50	130	98	2.2	202	110	196	210
0 + 100	100	68	1.3	118	58	125	150

The films sputtered in Ar environment were annealed in air at 500 °C for 3 h followed by slow cooling. This lowered the M_S value by about 30% of the as-deposited film (Figure 5.6). The coercivity however increases to a value of 330 Oe. The annealing removes the randomness of A-site and B-site cations and also oxidizes Cu⁺ to Cu²⁺ leading to lower magnetization value.

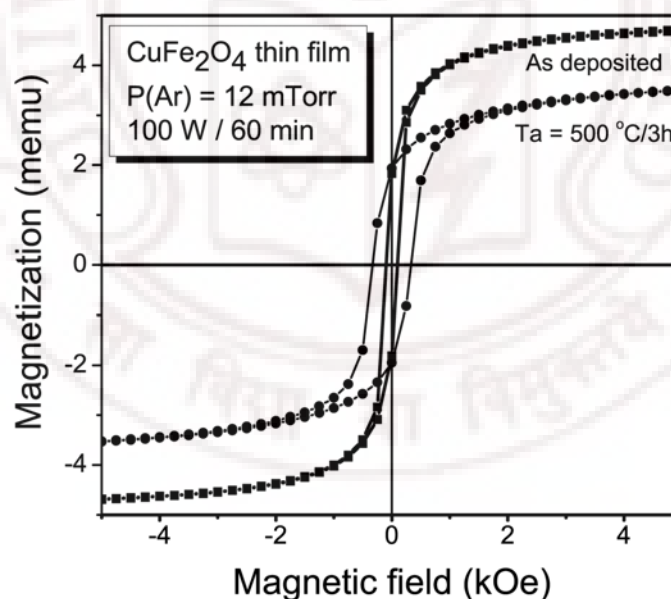


Figure 5.6: M–H plots at RT for as-sputtered CuFe₂O₄ film (P(Ar) = 12 mTorr) and film annealed at 500 °C for 3 h with field parallel to film surfaces.

Figure 5.7 shows room temperature hysteresis curves of the film magnetic moment versus the static applied field in both the in-plane and perpendicular to plane static field configurations. The in-plane and perpendicular-to-plane intrinsic coercivities are 100 and 132 Oe, respectively. The saturation flux density $4\pi M_S$ of the film is obtained as the value

of applied field H required saturating the sample in the perpendicular-to-plane configuration. This saturation field is 2.5–3 kOe. With the perpendicular to-plane demagnetizing factor equal to 4π for a thin film, $4\pi M_S$ is 2.5–3 kG. Note that this saturation field estimation of $4\pi M_S$ does not require the measurement of the film thickness [16]. This determination of the saturation magnetization is consistent with that obtained from the FMR measurements to be presented in the next section.

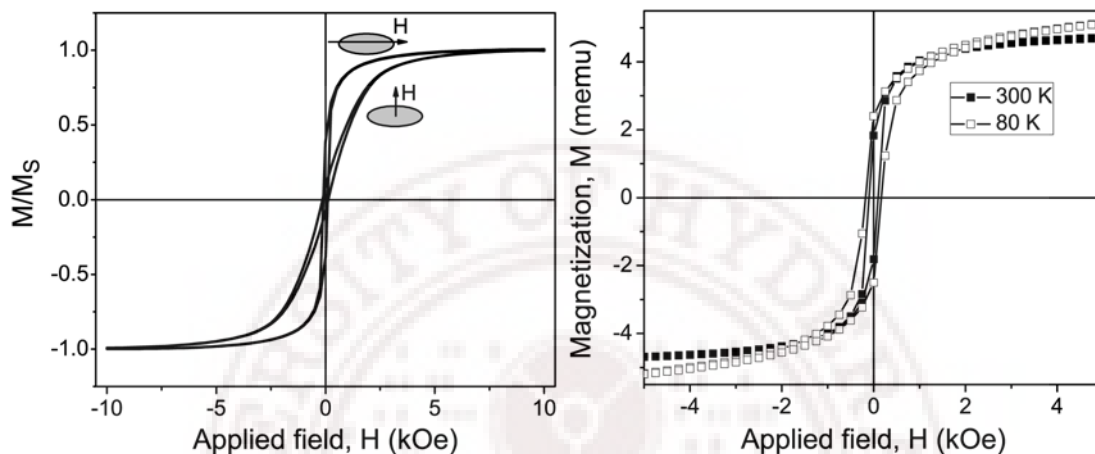


Figure 5.7: M–H plots (Left) recorded at RT with applied field in plane and out of plane configurations (Right) recorded at 300 and 80 K for as-sputtered CuFe_2O_4 film ($P(\text{Ar}) = 12$ mTorr) with field parallel to film surfaces.

Magnetization as a function of the external magnetic field, $M(H)$, are shown at 300 and 80 K for CuFe_2O_4 thin film in figure 5.7. The magnetization at 10 kOe is as high as 264 emu/cc at 300 K, and reaches 300 emu/cc at 80 K. The magnetic hysteresis loops are clearly observed in the low-field ranges. The hysteresis loop at 80 K ($H_C = 132$ Oe) is larger than that measured at 300 K ($H_C = 100$ Oe). The higher value of H_C at lower temperature can be assigned to the large disorder in the system.

5.1.1.3 Magnetization studies (ZFC-FC)

Figure 5.8 shows the magnetization-temperature (M-T) curves of as-sputtered CuFe_2O_4 thin films deposited at 12 mTorr of Ar, O_2 and Ar+ O_2 gas pressure under zero field cooling and field cooling (ZFC–FC) conditions. The ZFC/FC magnetization curves were measured in 100 Oe of external field in the temperature range 80–300 K. The zero-field cooled (ZFC) curves were obtained by cooling the CuFe_2O_4 films from 300 K to 80 K in

the absence of an external magnetic field, followed by the measurement of the magnetization under a magnetic field of 100 Oe as the temperature is raised back to room temperature. The field-cooled (FC) measurements were carried out in a similar way, except for the cooling process which was performed under an external magnetic field of 100 Oe.

It can be seen in figure 5.8 that the ZFC and FC curves for the as-deposited films show significant irreversibility. In the ZFC curve for CuFe_2O_4 films (Figure 5.7 a-c) no maximum can be seen up to 300 K. The mean blocking temperature for CuFe_2O_4 films is well above room temperature, which is also evident from the large coercivity field (see Figure 5.4). The larger coercivity field (magnetocrystalline constant K) of CuFe_2O_4 is well above the applied field of 100 Oe. Since the blocking temperature is closely related to the magnetic anisotropy energy E_A , one can evaluate the size of nanomagnets by the measured T_B .

The curves follow different trends as the temperature is decreased from 300 to 80 K. In the FC mode, the magnetization continues to increase with decreasing temperature without a tendency towards saturation demonstrating Curie-like behavior, whereas the ZFC magnetization shows a steady decrease to smaller values in the low temperature region. Such irreversibility observed in ZFC/FC curves originates from the anisotropy barrier blocking of the magnetization orientation in the nanoparticles cooled under zero field [17]. The magnetization direction of the nanocrystals is frozen in the initial state at high temperature, i.e., randomly oriented. At low temperature (80 K in our case) when a small magnetic field of 100 Oe is applied some small nanocrystals with low magnetic anisotropy energy flip in the field direction while the large ones do not. With increasing temperature, the thermal activation energy together with the field flips the larger particles. This process results in the increase in the magnetization in the ZFC curve with increasing temperature [17]. The size distribution of nanocrystals, i.e., the magnetic anisotropy is usually not uniform in the randomly arranged nanocrystal system. Larger the particles, higher the anisotropy energy (E_A), thus a larger $k_B T$ is required for the material to become superparamagnetic.

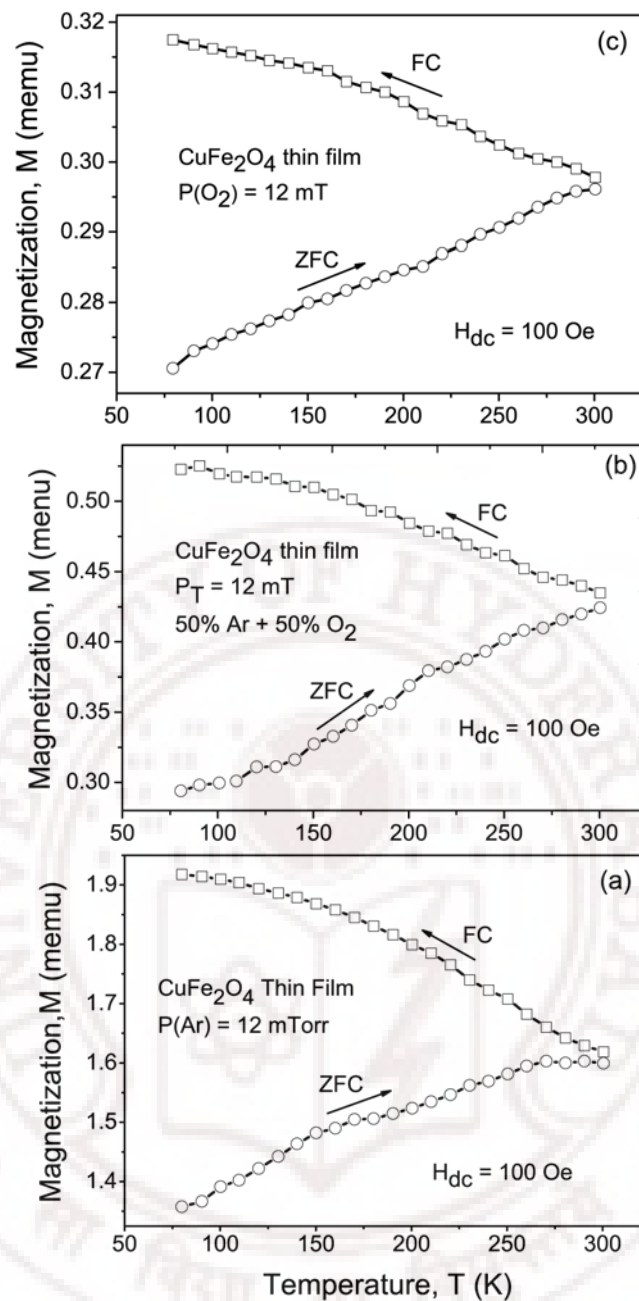


Figure 5.8: Field cooled (FC) and zero field cooled (ZFC) magnetization curves as a function of temperature taken in DC applied field of 100 Oe for the CuFe_2O_4 thin films deposited at 12 mTorr of (a) Ar (b) 50% Ar + 50% O_2 and (c) O_2 gas pressure.

The variation of magnetization (M) with temperature (T) for rf-sputtered CuFe_2O_4 films in oxygen atmosphere show that the films contain nanoscale crystals was reported by Ibrahim et al. [18]. The ZFC and FC curves separate at the spin freezing temperature (T_f). ZFC/FC magnetization measurements show superparamagnetic behavior of the nanocrystalline CuFe_2O_4 ferrite prepared by coprecipitation in a polymer matrix [19]. The ZFC and FC magnetization curves on nanocrystalline CuFe_2O_4 and $\text{CuFe}_2\text{O}_4/\text{SnO}_2$

nanocomposites synthesized by reaction of urea–nitrate combustion method show the blocking temperature. These materials are superparamagnetic at ambient temperature and ferrimagnetic at lower temperatures [20]. The blocking above room temperature has also been reported in spinel ferrite NiFe_2O_4 and CoFe_2O_4 nanocrystals embedded inside a ZnO matrix by Zhou et al. [17] and for pulsed laser deposited MgFe_2O_4 thin films by Yamamoto et al. [21].

5.1.1.4 FMR studies

Figure 5.9 shows room temperature FMR spectra of CuFe_2O_4 thin film deposited at 12 mTorr of Ar gas pressure at different orientations between external field and film surface from perpendicular to parallel orientations. The results show the shift in the signal position from the high-field region towards the low field regions as the polar angle θ_H increases. The lowest resonance field H_R is 2.2 kOe. The symmetric Lorentzian line is observed when the magnetic field is applied in the film plane. The subsequent azimuthal angular measurements show that the value of H_R and the lineshape are not changed if the applied magnetic field is rotated in the film plane.

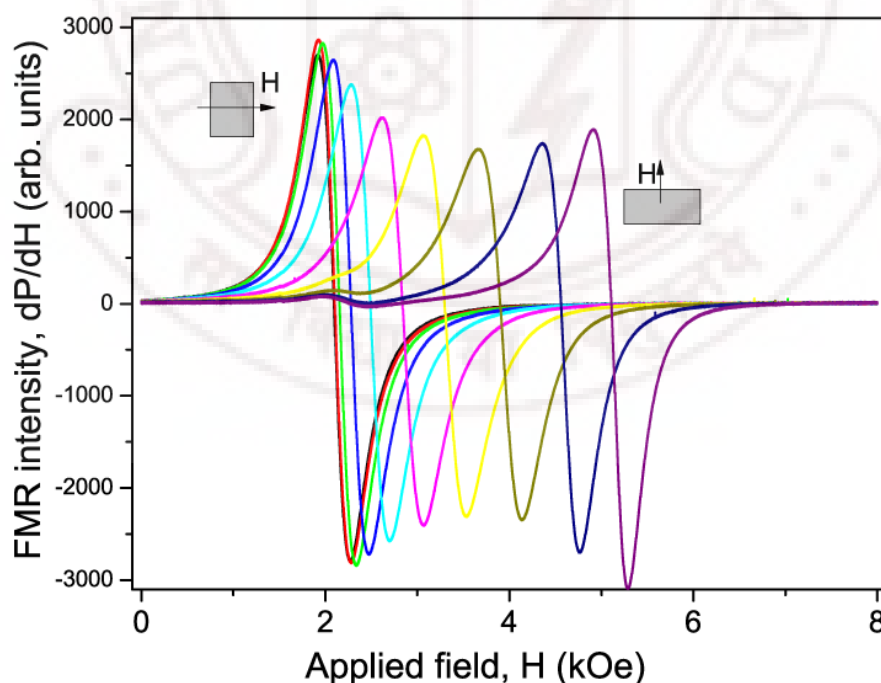


Figure 5.9: Angular dependent FMR signal of as-sputtered CuFe_2O_4 thin films at 12 mTorr of Ar gas pressure.

Figure 5.10 shows the out of plane angular dependence of FMR linewidth (ΔH) and resonance field (H_R) of as-sputtered CuFe_2O_4 thin films at 12 mTorr of Ar gas pressure. The effective saturation magnetization ($4\pi M_{\text{eff}}$) and the effective g-value (g_{eff}) were determined from the data on the resonance fields for static fields parallel and perpendicular to the film plane using Kittel relations [22]:

$$\left(\frac{\omega}{\gamma}\right) = H_{\perp} - 4\pi M_{\text{eff}} \quad (\text{for } H \perp \text{ the film plane}) \quad (5.1-a)$$

$$\left(\frac{\omega}{\gamma}\right)^2 = H_{\parallel} (H_{\parallel} + 4\pi M_{\text{eff}}) \quad (\text{for } H \parallel \text{ the film plane}) \quad (5.1-b)$$

The estimated g-value of 2.1 agrees well with the reported value of 2.06 - 2.2 for the bulk ferrimagnetic Cu-ferrite [23] and for amorphous Cu-ferrite film [24].

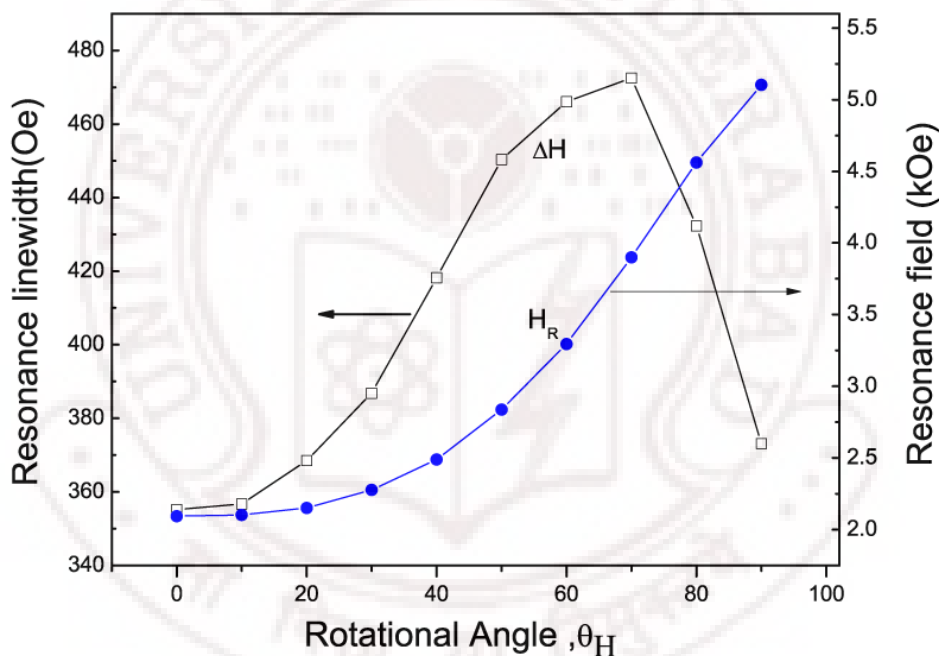


Figure 5.10: Angular dependent FMR linewidth (ΔH) and resonance field (H_R) of as-sputtered CuFe_2O_4 thin films at 12 mTorr of Ar gas pressure.

In order to see an inhomogeneous broadening of the linewidth, the peak to peak linewidth was measured as a function of the out-of-plane angle. The inhomogeneous contribution to the total linewidth arises from the broadening induced by magnetic inhomogeneities, such as the internal static magnetic fields and the orientation of the crystallographic axis or anisotropy axis. Figure 5.10 shows the ΔH versus θ_H curves of the FMR signal for the Ar-deposited film. The shape of the curves implies that the linewidth is

composed of a homogeneous part and an inhomogeneous part. The homogeneous part is due to an intrinsic damping mechanism that is always present in the samples, whereas the inhomogeneous part is usually written as [25]

$$\Delta H_{inhom} = \left| \frac{\partial H_r}{\partial \theta_H} \right| \Delta \theta_H + \left| \frac{\partial H_r}{\partial \phi_H} \right| \Delta \phi_H + \left| \frac{\partial H_r}{\partial H_{int}} \right| \Delta H_{int}, \quad (5.2)$$

where $\Delta \theta_H$ and $\Delta \phi_H$ represent the spread in the orientation of the crystallographic axes and ΔH_{int} represents the variations of the internal magnetic fields throughout the sample.

Figure 5.11 presents the temperature dependence of the FMR spectra for the Ar-deposited CuFe_2O_4 film at 12 mTorr recorded between 120 and 320 K. The magnetic field was applied along the in-plane direction. The corresponding FMR spectra consist of a single symmetric line, of almost ideal Lorentzian lineshape. In figure 5.11 H_R shifts towards smaller values with decreasing temperature because the magnetic field is applied along the in-plane easy axes.

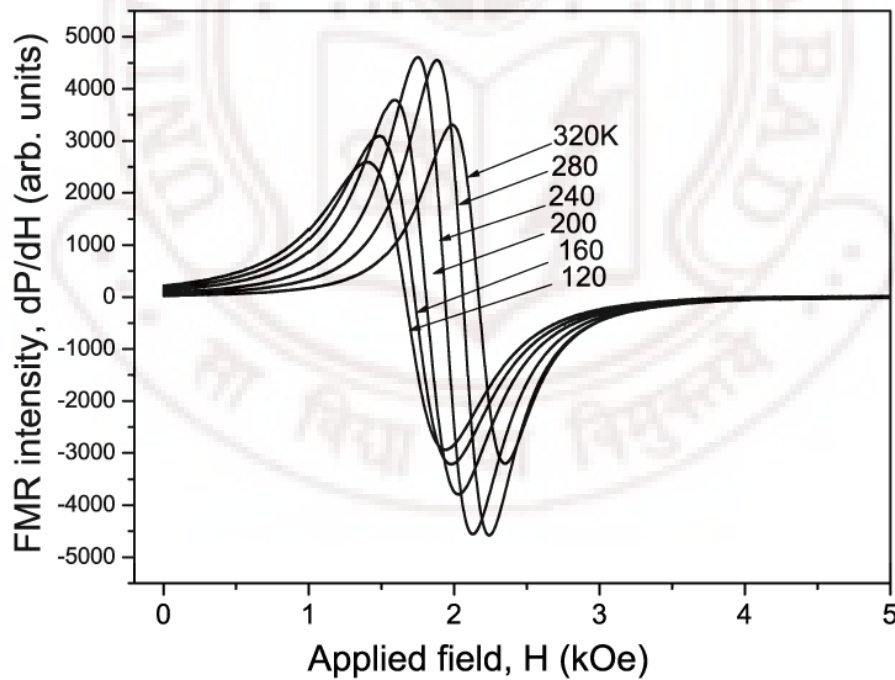


Figure 5.11: In-plane resonant microwave absorption spectra of as-sputtered CuFe_2O_4 thin films ($P(\text{Ar}) = 12$ mTorr) for selected temperatures in the 120–320K range.

Ferromagnetic resonance measurements at X-band frequencies were performed to study the effects of spin freezing on high-frequency magnetic parameters for the films.

The temperature dependence of the linewidth (ΔH) for representative sample sputtered in Ar at 12 mTorr is plotted in Figure 5.12. The variation of ΔH_{\parallel} and ΔH_{\perp} with T is quite similar where both of them increase with decreasing T to saturate at lower T. A relatively large ΔH is measured for H perpendicular to the film. The decrease in ΔH with T could be attributed to the weakening of the internal field (H_i) where both superexchange and anisotropy decrease as a result of increased thermal vibrations [26]. This trend in the Cu-ferrite film is very similar to that reported previously for NiZnCu ferrite films prepared using RF-magnetron sputtering [27]. It is also similar to our data obtained on Cu-Zn ferrite and ZnFe_2O_4 films reported in the subsequent sections. Above RT, ΔH_{\parallel} and ΔH_{\perp} coincide. At lower temperatures a slight difference between parallel and normal configurations has been observed which can be understood in terms of an effective magnetization M_{eff} of superparamagnetic particle ensemble variation with temperature. The variation of ΔH_{\parallel} and ΔH_{\perp} in the low temperature range could also be related to spin freezing as seen in the magnetization data in Figure 5.8.

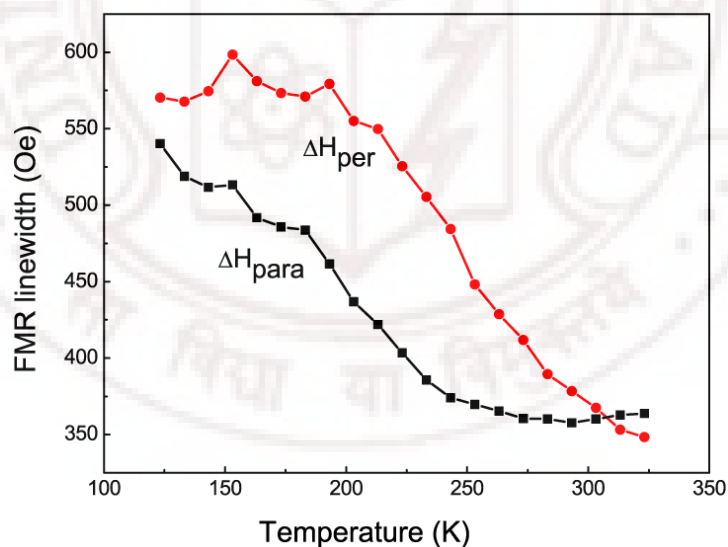


Figure 5.12: Temperature dependence of FMR linewidth of CuFe_2O_4 thin films

Figure 5.13 shows the temperature dependence of the resonance field (H_R) for static field parallel (H_{\parallel}) and perpendicular (H_{\perp}) to the film plane for argon-sputtered thin film. The resonance field H_{\perp} is larger than H_{\parallel} at all temperatures. One observes an increase in

the resonance fields H_{\parallel} and decrease in H_{\perp} as the temperature is increased similar to that reported by Han et al. [27] for NiZnCu ferrite system. A monotonous increase of H_{\parallel} from about 1.65 to 2.2 kOe is observed as the temperature increases from 120 K to 320K. At $T = 220$ K, $H_{\parallel}(T)$ shows a kink above which the resonance field increases rapidly with temperature.

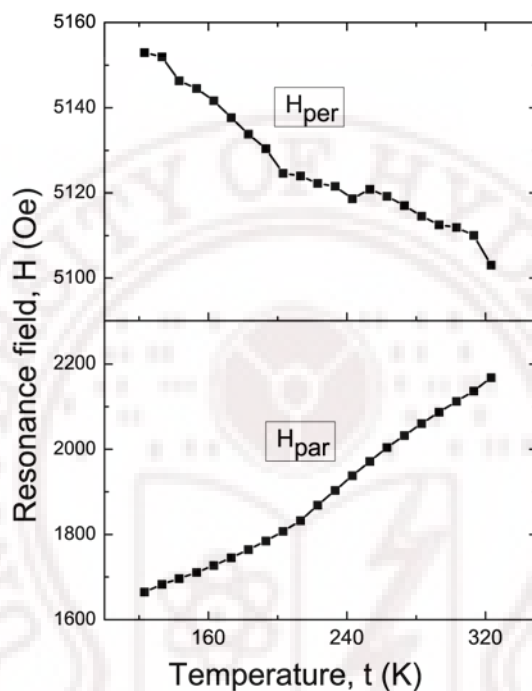


Figure 5.13: Temperature dependence of FMR resonance fields of 12 mTorr Ar-deposited CuFe_2O_4 thin films recorded in the in-plane and out-of-plane configurations.

The temperature dependence of the effective saturation induction ($4\pi M_{\text{ef}}$) and effective (g_{eff}) is shown in Figure 5.18. A room temperature g_{eff} of 2.14 is estimated for the film. As mentioned earlier, the corresponding g -value of 2.1 is in good agreement with the value reported for divalent copper ions in octahedral sites. The data indicate an increase in g_{eff} as T decreases. Such strong temperature dependence for g_{eff} is usually observed around the compensation point in ferrimagnetic crystalline oxides where the sublattice magnetizations cancel each other.

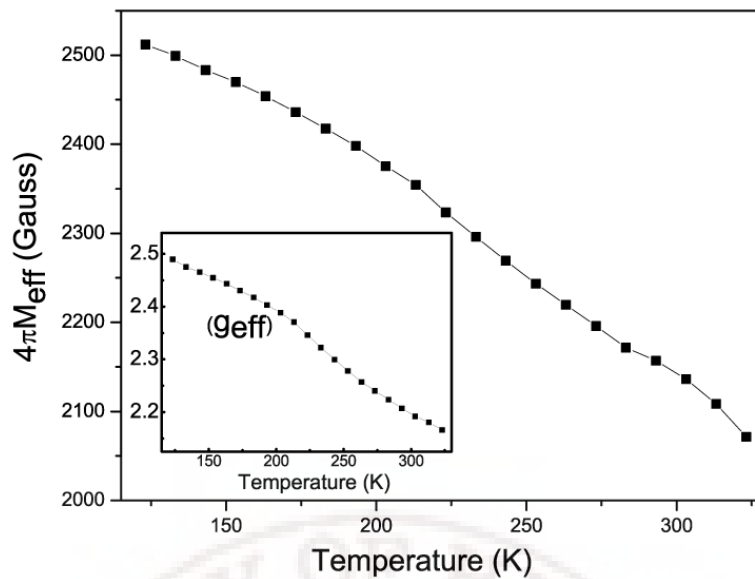


Figure 5.14: The effective saturation magnetization ($4\pi M_{\text{eff}}$) and the effective g-value (g_{eff}) (inset) were determined from data on the resonance fields for static fields parallel and perpendicular to the film plane using Kittel relations.

5.1.1.5 Optical properties

The variation of (Ar/O₂) ratio influences the optical properties of the ferrite films. Figure 5.18 shows the transmittance spectra measured at RT for the as-grown CuFe₂O₄ films deposited in 12 mTorr of Ar, O₂ and mixture of (Ar+ O₂) gas pressure. The transmittance spectra show that all the films have sharp absorption edges which vary between 570 and 700 nm with increase in Ar percentage. The Ar-deposited films show less transmittance due to the higher thickness. With increase in the O₂ percentage the film thickness decreases, absorption edge shifts towards lower wavelengths and transmittance is enhanced. This can also be due to the decrease of average grain size and formation of pores in the films. The compositional dependence of transmittance for films having same thickness shows that copper ferrite films have less transmittance. Zinc ferrite films show higher transmittance and blue shift.

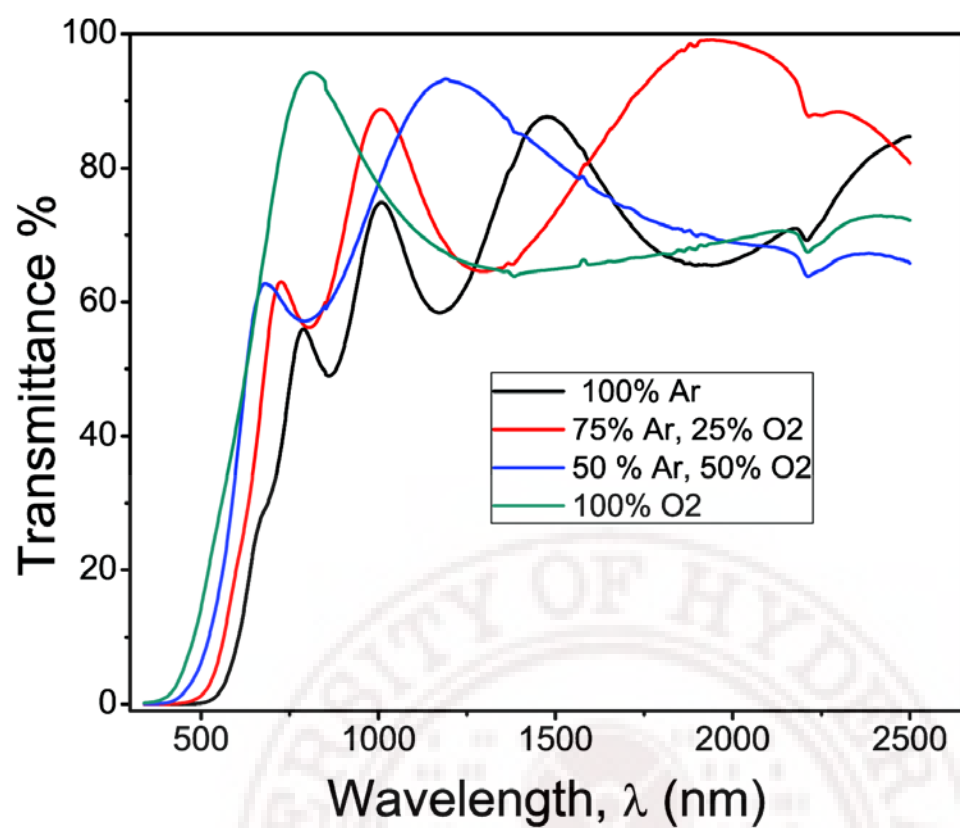


Figure 5.15: Optical transmittance of as-sputtered Cu-ferrite films prepared under (Ar+O₂) at 12 mTorr.

5.2 Zinc ferrite (ZnFe_2O_4) thin films

Thin films of zinc ferrite were deposited by RF-Magnetron sputtering from a sintered target of ZnFe_2O_4 on glass substrates. The rf-power used was 100W. The films were sputtered under argon, oxygen and (argon + oxygen) mixture at various pressures. The structural characterization of the films was done using X-ray diffraction (XRD). The information about microstructure, surface morphology, chemical composition, grain size and surface roughness were obtained from atomic force microscope (AFM), scanning electron microscope (SEM) and energy dispersive X-ray analysis (EDAX) studies. The static magnetic properties of the films were studied at RT and 80 K in applied fields up to 10 kOe using Vibrating Sample magnetometer (VSM). Field cooled (FC) and zero field cooled (ZFC) magnetization measurements and the temperature and orientation dependence of magnetic resonance data provide strong evidence of superparamagnetic character at room temperature and the occurrence of ferrimagnetic or ferromagnetic ordering at low temperature in the present nanocrystalline zinc ferrite films. The optical properties of the films were studied as a function of pure O_2 pressure. The optical constants of the films were extracted from the transmission spectra by the envelope method. The effect of annealing on structural, optical, and magnetic properties of the films was investigated for the films annealed at temperatures from 200 to 500 °C.

5.2.1 Effect of working gas pressure

5.2.1.1 Structural analysis (XRD)

Figure 5.16 shows the XRD patterns of the ZnFe_2O_4 thin films sputtered under pure Ar and oxygen at various working pressure. The patterns were indexed to the cubic spinel structure belonging to Zn-ferrites. Three main peaks were observed with orientations along the (311), (400) and (511) directions in all the films. Using Bragg's law, the interplanar lattice spacing, $d_{(311)}$, was calculated. The lattice parameters, a , calculated by using $a = \sqrt{11}d_{311}$ are listed in table 5.2. The lattice parameter is higher for the film deposited at lower pressure and decreases with increase in pressure. At lower pressure (8 mTorr), the diffraction peaks are broad and slightly shifted towards lower angle as

compared to the spectra for the bulk Zn-ferrite powder sample. The shift is more for the films prepared under Ar gas. This can be attributed to the internal stress caused by the trapped Ar atoms into the film and its consequent effect on the interaction between the grains and the substrate. The XRD peak shift for the films deposited under oxygen is lower and it decreases with the increase in the oxygen pressure. The XRD spectra peaks for the films deposited at 31 mTorr are very close to the corresponding peak positions of the bulk Zn-ferrite powder [Chapter 3, figure 3.1] indicating considerably lower stress in these films. The average crystallite size (D) of the films was estimated from XRD data using the Scherrer formula [14] $D = 0.9\lambda / \beta \cos \theta$, where λ (1.54056 Å) is the wavelength of the used X-rays, β is the broadening of the diffraction line measured at the half maximum intensity in radians and θ is the angle of diffraction. The values of the crystallite size as a function of the sputtering gas pressure are listed in table 5.2. The crystallite size is smaller for the films deposited at 8 mTorr pressure of argon or oxygen. There is a slight increase in crystallite size with increase in oxygen pressure.

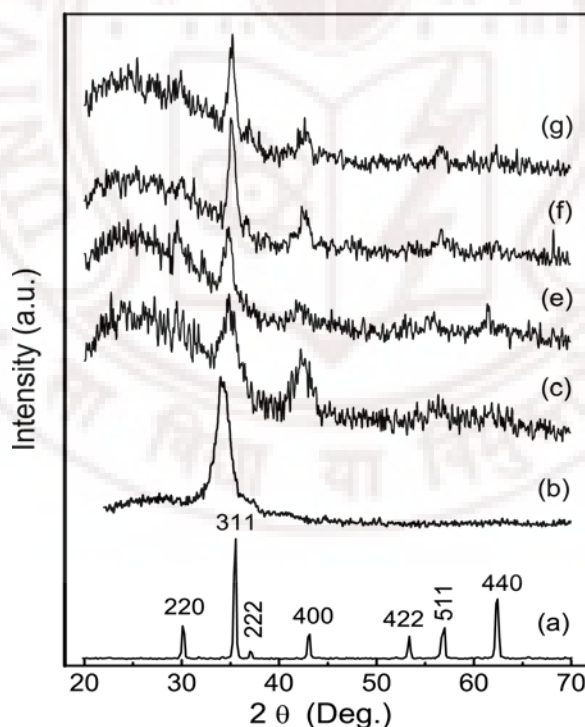


Figure 5.16: The XRD patterns of ZnFe_2O_4 (a), powder sample and thin films deposited at a pressure of (b) 8mTorr Ar, (c) 8mTorr O_2 , (d) 18mTorr O_2 , (e) 27mTorr O_2 and (f) 31mTorr O_2 .

5.2.1.2 *Film surface morphology (AFM)*

The surface morphology of the Zn-ferrite thin films was analyzed using the non-contact mode of AFM. Figure 5.17 displays AFM images of the Zn-ferrite films grown on glass substrates at 8mTorr of Ar and 8–31mTorr of O₂. It can be seen that the topography of the ferrite films depends on the sputtering gas type and pressure. The film deposited under Ar exhibits a dense microstructure compared with those sputtered in the O₂ environment. The average grain sizes and surface roughness (root mean square (RMS)) values are listed in table 5.2. The increase in roughness is consistent with the increase in crystallinity with oxygen pressure during deposition. This result is supported by XRD patterns as shown in Figure 5.16. The film deposited under Ar shows higher RMS values compared with that sputtered at the same pressure of the oxygen environment. The average RMS roughness increased from 1.7 to 2.7 nm as the oxygen pressure increases. This is due to variation in the distribution of incident angles and energy of the depositing atoms at low and high deposition pressures [28]. At low deposition pressure few collisions occur within the plasma; therefore incident angles tend to be close to normal and bombarding energy tends to be high. The high bombarding energy leads to a high adatom mobility (atoms present at the surface of the layer) and thus, to a higher film density. However, the increase in oxygen pressure results in focusing the particles ejected from the target on a small area, which leads to an increase in the number of collisions occurring in the space between the target and the substrate (plasma) leading to an increase in the incident angles of the particles. This causes a shadowing effect leading to the formation of clusters and voids within the growing layer [29, 30]. This makes the films porous. The increase in the surface roughness could be attributed to the formation of clusters of particles with voids in between due to the variation in the distribution of incident angles and energy of the depositing atoms at low and high gas pressures. These results support the optical refractive index variation with oxygen pressure.

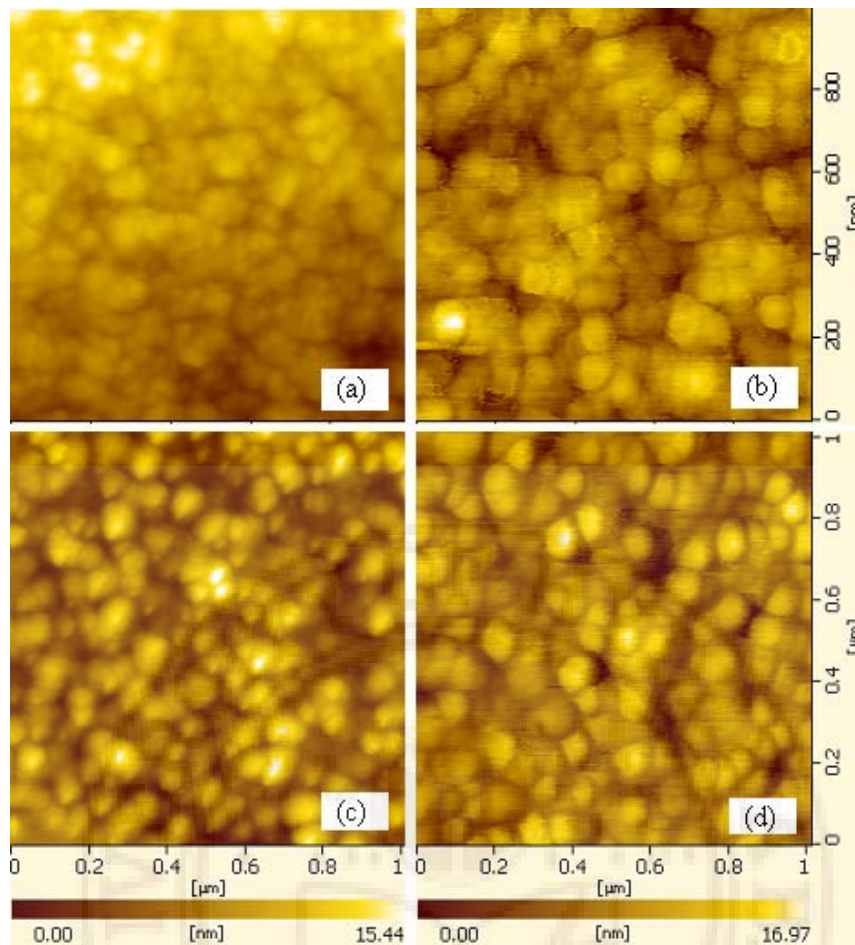


Figure 5.17: AFM images of ZnFe_2O_4 thin films deposited at a pressure of (a) 8mTorr Ar, (b) 8mTorr O_2 , (c) 27mTorr O_2 and (d) 31mTorr O_2 .

Table 5.2: Structural parameters of the films deposited under Ar and O_2 environments. t_1 and t_2 refer to film thicknesses as estimated from the profilometer and the optical transmission spectra, respectively.

Sample	P (mT)	RMS (nm)	Grain Size (nm)	Crystallite Size (nm)	Lattice Parameter (\AA)	t_1 (nm)	t_2 (nm)
		± 0.1	± 5	± 2	± 0.002	± 15	± 15
ZF-Ar8	8	4.2	55	11	8.68	420	450
ZF-O8	8	1.7	70	11	8.55	300	320
ZF-O18	18	2.3	66	13	8.53	280	265
ZF-O27	27	2.7	60	15	8.46	240	250
ZF-O31	31	2.6	72	15	8.45	200	230

5.2.1.3 Optical properties

5.2.1.3.1 Spectral transmittance

Figure 5.18 shows the optical transmission spectra, as a function of photon energy in the wavelength range 350–2500 nm, of ZnFe_2O_4 thin films deposited on glass substrates in argon and oxygen at room temperature. The films have strong band edge absorption in the wavelength region of less than 600 nm. The fringes in the transmission spectra result from the interference of the incident light at the air–film, film–substrate and substrate–air interfaces. The optical transmittance of the films prepared in O_2 is more than 80% above the band edge and higher than the film deposited in argon. Zhi-hao *et al.* [31] reported a band edge of 700 nm for ZnFe_2O_4 nanoparticles and Wu *et al.* [32] reported 650 nm for the ZnFe_2O_4 film prepared by spray pyrolysis.

The optical properties of any material are characterized by parameters such as the refractive index (n), extinction coefficient (k) and absorption coefficient (α). There are a number of methods that can be used for the routine determination of the wavelength dependent complex refractive index of thin films, using simple spectrophotometric equipment [33]. We have used the envelope method proposed by Manifacier *et al.* [34] and developed by Swanepoel [35] to evaluate the optical constants from the transmission spectra. The envelopes are constructed by curve fitting to connect the maxima (T_M) and minima (T_m) in the transmission spectra (Figure 5.18) using equations [35]

$$T = \frac{Ax}{B - Cx \cos \varphi + Dx^2} \quad (5.3)$$

where

$$A = 16n^2n_s, \quad B = (n+1)^3(n+n_s^2), \quad C = 2(n^2-1)(n^2-n_s^2), \\ D = (n-1)^3(n-n_s^2), \quad \varphi = 4\pi nd / \lambda \quad \text{and} \quad x = \exp(-\alpha d)$$

The extremes of the interference fringes can be obtained from equation (1) by setting the interference condition $\cos \varphi = +1$ for maxima T_M and $\cos \varphi = -1$ for minima T_m and can be written as

$$T_M = \frac{Ax}{B - Cx + Dx^2} \\ T_m = \frac{Ax}{B + Cx + Dx^2} \quad (5.4)$$

The interference maxima T_M and minima T_m can be considered to be a continuous function of λ and experimentally determined by the envelopes as shown in figure 5.18.

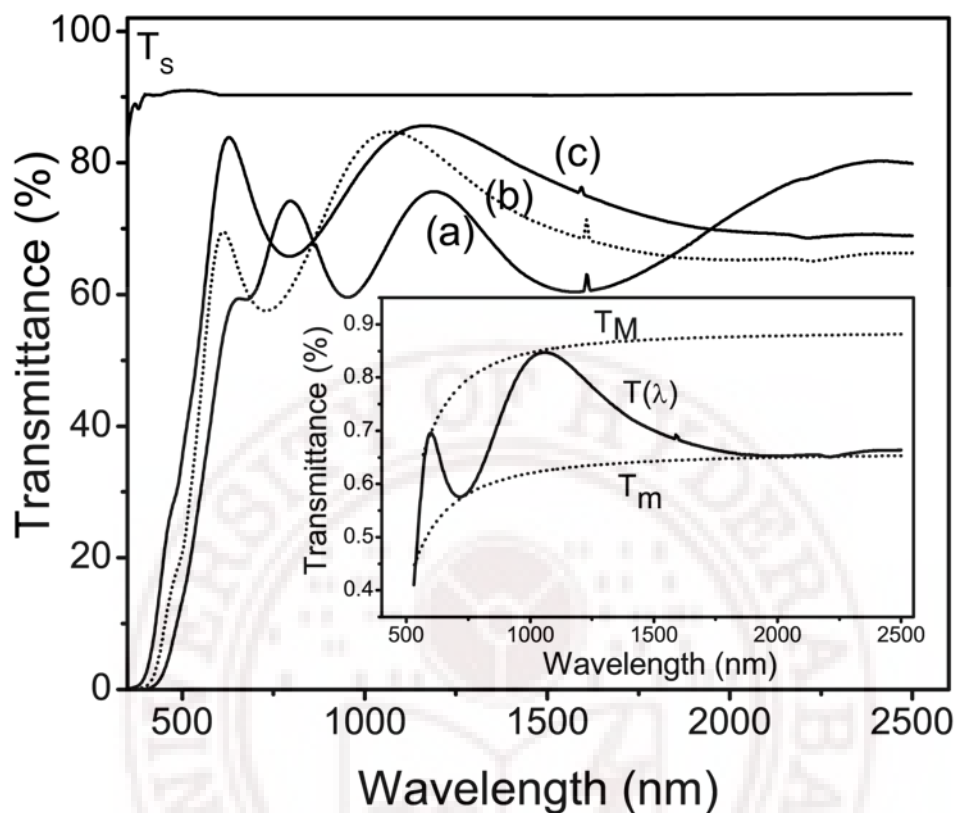


Figure 5.18: Spectral transmittance of Zn-ferrite thin films prepared under (a) 8 mT of Ar (b) 8 mT of O₂, (c) 31 mT of O₂. The inset shows the envelope for the data for film prepared under O₂ at 8 mT. The curve T_s is for glass substrate.

5.2.1.3.2 Refractive index

Using Swanepoel's method, the refractive index n values were calculated from the transmission spectra of the films. A typical transmission spectrum at normal incidence has two spectral regions: the region of weak and medium absorption and the strong absorption region. In the weak and medium absorption region, a first approximation of the real part of the refractive index, n , of the film can be calculated by the following expression:

$$n = \left[N + \sqrt{N^2 - n_s^2} \right]^{1/2} \quad (5.5)$$

where

$$N = 2n_s \left[\frac{T_M - T_m}{T_M T_m} \right] + \frac{n_s^2 + 1}{2}$$

where T_M and T_m are the transmission maximum and the corresponding minimum at a certain wavelength, λ , and n_s is the refractive index of the substrate used (for glass $n_s = 1.51$).

Figure 5.19 shows the spectral dependence of the refractive index for the films deposited in different environments of argon and oxygen. The variation in the refractive index follows the normal dispersion law where it decreases with increasing wavelength. The refractive index of the films deposited in the argon atmosphere is higher than the films deposited in oxygen. It decreases as the oxygen pressure increases. This can be correlated with the variation of the microstructure of the films. As the oxygen pressure is increased the films become more porous which leads to a decrease in the refractive index.

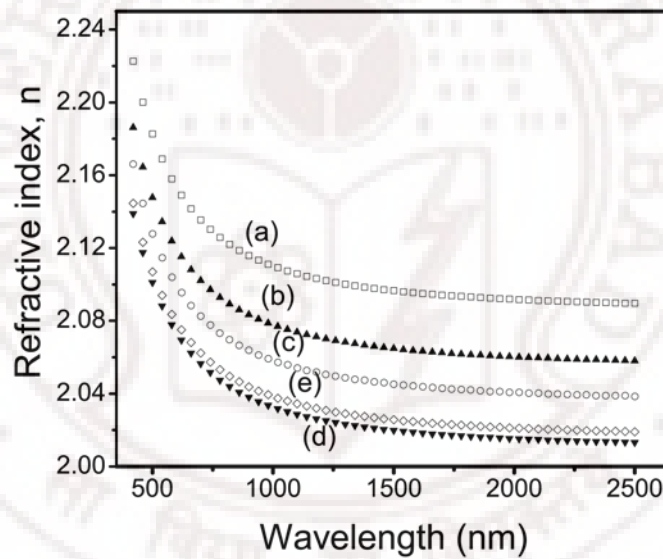


Figure 5.19: Refractive index of Zn-ferrite thin films deposited at a pressure of (a) 8 mT Ar, (b) 8mT O₂, (c) 18mT O₂, (d) 27mT O₂ and (e) 31mT O₂.

According to a single-oscillator model of Wemple–DiDomenico (WD) model [36], the relation between the refractive index, n , and photon energy, $h\nu$, can be written as follows:

$$n^2(h\nu) - 1 = \frac{E_o E_d}{E_o^2 - (h\nu)^2} \quad (5.6)$$

where $h\nu$ is the photon energy, E_d is the dispersion energy or the oscillator strength and E_o is the oscillator energy. The first parameter measures the average strength of the interband

optical transitions, associated with the changes in the structure of the material. The second one can be correlated with the optical band gap by the empirical formula $E_0 = 2E_g$.

Figure 5.20 shows $(n^2 - 1)^{-1}$ against $(h\nu)^2$ plots. E_0 and E_d can be determined directly from the slope $(E_0 E_d)^{-1}$ and the intercept E_0/E_d on the vertical axis of the straight line fits these plots.

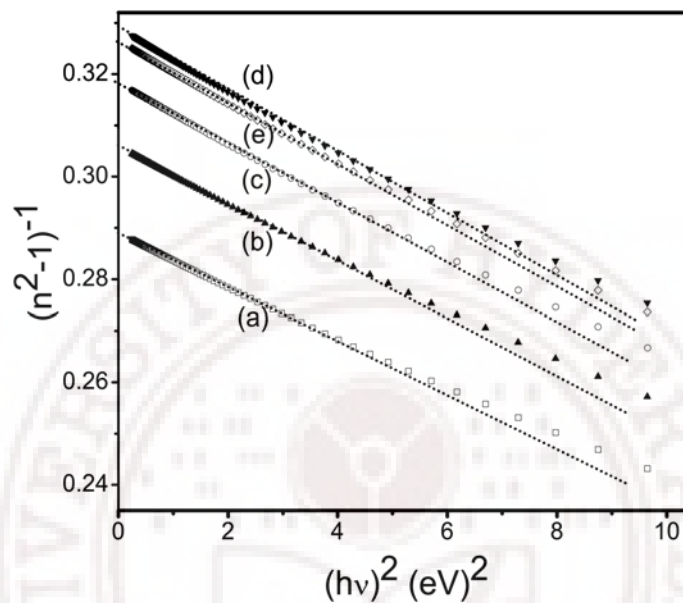


Figure 5.20: $(n^2 - 1)^{-1}$ versus $(h\nu)^2$ plots with linear fits for Zn-ferrite thin films prepared under (a) 8 mT Ar, (b) 8mT O₂, (c) 18mT O₂, (d) 27mT O₂ and (e) 31mT O₂.

The optical band gap obtained from the WD-model gives an estimation of the direct band gap of zinc ferrite. The estimated values are 3.8 eV and 3.76 eV for the films deposited at 8mTorr of argon and oxygen pressure, respectively. These values are higher than the estimated values of 2.43 and 2.48 eV obtained from Tauc relation (equation 5.10).

Table 5.3 summarizes the estimated values of the oscillator parameters, E_0 , E_d along with that of the static refractive index, $n(0)$, for $(h\nu) \rightarrow 0$, extrapolated from the WD single oscillator fit. An important achievement of the WD model is that it relates the dispersion energy E_d to other physical parameters of the material, through an empirical formula $E_d = \beta N_c Z_a N_e$ (eV), where N_c is the coordination number of the cation nearest neighbor to the anion, Z_a the formal chemical valency of the anion, N_e the total number of valence electrons per anion and β is a two-valued constant ($\beta_i = 0.26 \pm 0.03$ eV and $\beta_c = 0.37 \pm 0.04$ eV, for ionic and covalent compounds, respectively). The estimated values of β for the present films are also listed in table 5.3.

Table 5.3: Optical parameters of ZnFe₂O₄ thin films.

Sample name	E _g (eV)	E _d (eV)	E ₀ (eV)	β (eV)	N(0)	k@ 600 ×10 ⁻²
ZF-Ar8	2.43	26.2	7.60	0.27	2.11	7.3
ZF-O8	2.48	24.6	7.52	0.26	2.06	5.9
ZF-O18	2.52	23.5	7.45	0.25	2.04	5.1
ZF-O27	2.54	22.4	7.16	0.23	2.01	5.7
ZF-O31	2.61	22.9	7.40	0.24	2.02	4.5

5.2.1.3.3 Absorption and extinction coefficients

The absorption coefficient (α) was evaluated from transmission data using the following relation [35]:

$$x = \exp(-\alpha t), \quad \alpha = -\frac{1}{t} \ln[x] \quad (5.7)$$

where t is the film thickness and x is absorbance. In the region of weak and medium absorption, the parameter x is given by

$$x = \frac{E_M - [E_M^2 - (n^2 - 1)^3 (n^2 - n_s^4)]^{1/2}}{(n - 1)^3 (n - n_s^2)} \quad (5.8)$$

where

$$E_M = \frac{8n^2 n_s}{T_M} + (n^2 - 1)(n^2 - n_s^2)$$

The extinction coefficient, k , was calculated from the relation $k = \alpha\lambda/4\pi$

Figure 5.21 shows the dependence of the extinction coefficient (k) on wavelength, λ , for the thin films. The extinction coefficient is slightly affected by the change in oxygen working pressure. From the plot, it is clear that films deposited at high oxygen working pressure had a lower extinction coefficient (i.e. more transmissive) than those deposited at low oxygen pressure. This behavior is probably due to the higher porosity of the films deposited in the oxygen gas atmosphere. This factor plays a significant role in optical absorption processes. The variation of the extinction coefficient can be related to the

variation of the transmittance [37]. As the oxygen pressure is increased the transmittance increases and results in a decrease in the extinction coefficient.

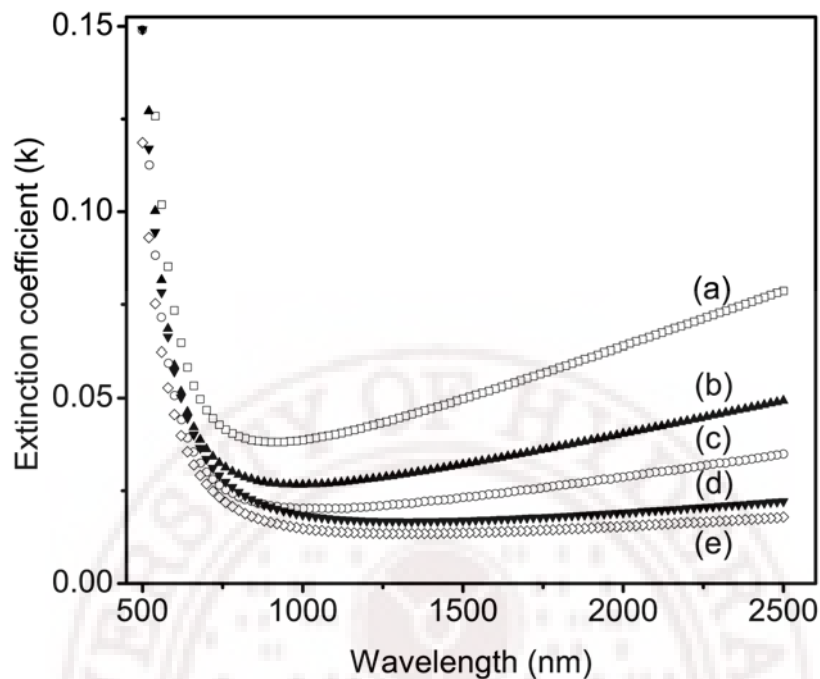


Figure 5.21: Variation of the extinction coefficient (k) with wavelength for Zn-ferrite thin films prepared under (a) 8 mT Ar, (b) 8mT O₂, (c) 18mT O₂, (d) 27mT O₂ and (e) 31mT O₂ gas pressure.

5.2.1.3.4 Film thickness

Film thickness (t_1) was measured using a surface stylus profilometer (table 5.2). The thickness (t_2) of the films was also estimated from the interference fringes of transmission data by calculating the refractive index of the thin film corresponding to two adjacent maxima (or minima) given as $n(\lambda_1)$ at λ_1 and $n(\lambda_2)$ at λ_2 [38]:

$$t = \frac{\lambda_1 \lambda_2}{2(n(\lambda_1)\lambda_2 - n(\lambda_2)\lambda_1)} \quad (5.9)$$

where $n(\lambda_1)$ and $n(\lambda_2)$ are the refractive indices in two consecutive maxima (or minima) and λ_1 and λ_2 the corresponding wavelengths. The film thicknesses estimated from the transmission data are comparable to the values obtained using a surface stylus profilometer (table 5.2) within an experimental error of about ± 15 nm. The deposition rate

is maximum in the Ar environment and it is reduced considerably if Ar is replaced by oxygen with the same working pressure. The decrease in the thickness of the film with the increase in oxygen pressure is an indication of the decrease in the deposition rate due to the shadowing effect.

5.2.1.3.5 Optical energy gap

The optical band gap E_g for both the films can be estimated from the absorption coefficient α using the Tauc relation [38, 39] which is given by

$$\alpha h\nu = A(h\nu - E_g)^q \quad (5.10)$$

where A is a constant which depends on the transition probability, $(h\nu)$ is the energy of the incident photon and q is an index that characterizes the optical absorption process and is theoretically equal to 2, 1/2, 3 or 3/2 for allowed indirect, allowed direct, forbidden indirect and forbidden direct electronic transitions, respectively, depending on the nature of the electronic transition responsible for the reflection [40].

We plotted in figure 5.22 $(\alpha h\nu)^{1/q}$ versus $h\nu$ and obtained linear fits for $q = 1/2$, indicating a direct allowed transition. The band gap energy E_g , of the film was obtained by extrapolating the linear portion of the plot to $(\alpha h\nu)^2 = 0$. The band gap values are listed in table 5.3. The optical band gap is lower for the film deposited under Ar than under oxygen at the same gas pressure. It increases with the increase in oxygen gas pressure. This increase might be due to the enhanced stoichiometry and decrease in the oxygen vacancies by increase in the oxygen pressure. The band gap values obtained in this study are lower compared with the reported value of 2.70 eV for ZnFe_2O_4 films deposited by spray pyrolysis [32].

The absorption in a wavelength range from 400 to 500 nm is attributed to the $3d^5 \rightarrow 3d^4 4s^1$ transition of Fe^{3+} ions, where the $4s$ orbital of Fe^{3+} is thought to contribute to the conduction band.

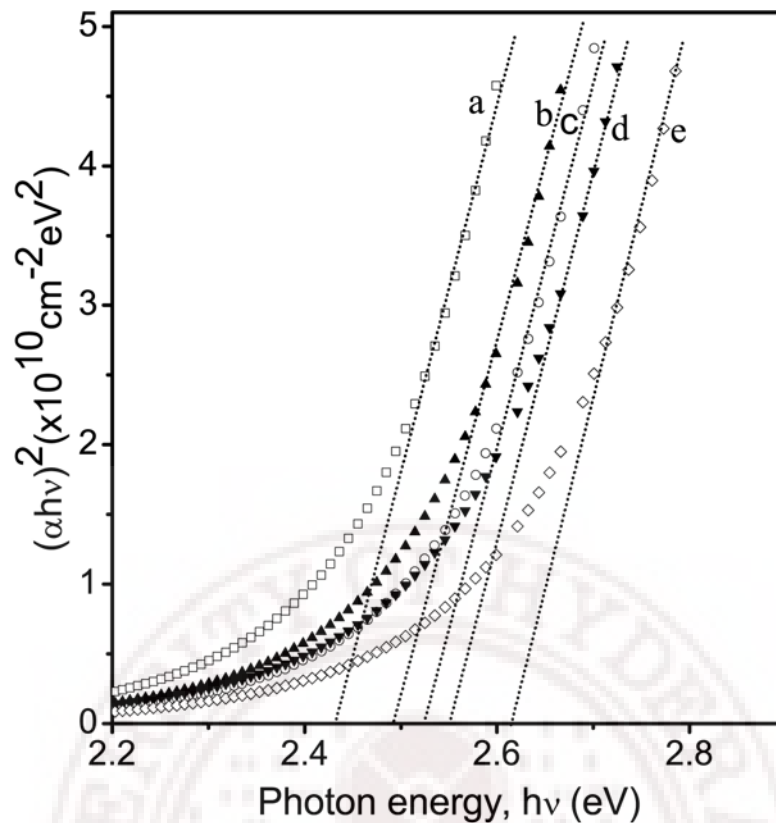


Figure 5.22: Plots of $(\alpha h\nu)^2$ versus photon energy $h\nu$ for Zn-ferrite thin films prepared under (a) 8mTorr Ar, (b) 8mTorr O₂, (c) 18mTorr O₂, (d) 27mTorr O₂ and (e) 31mTorr O₂ gas pressure.

5.2.1.4 Magnetic properties

5.2.1.4.1 M-H curves

Figure 5.23 shows the plots of magnetization versus applied magnetic field curves at RT for the zinc ferrite films deposited at 8 mTorr Ar and 8, 18, 27 and 31mTorr oxygen gas pressure. The as-deposited ZnFe₂O₄ thin films show large magnetization values compared to that of the bulk sample and exhibit ferrimagnetic behavior at room temperature. The magnetization value of the argon-deposited film is lower value compared to that prepared under oxygen atmosphere.

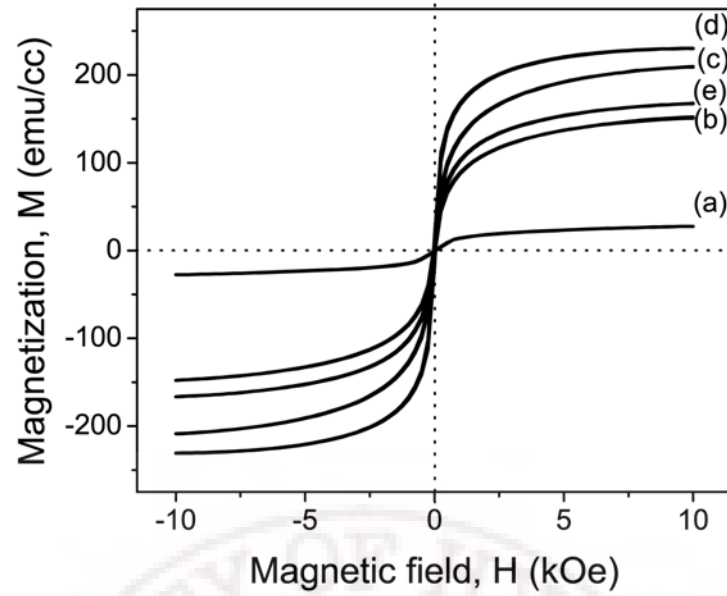


Figure 5.23: Effect of oxygen gas pressure on M-H loops at RT for ZnFe_2O_4 thin films prepared under (a) 8mTorr Ar, (b) 8mTorr O_2 , (c) 18mTorr O_2 , (d) 27mTorr O_2 and (e) 31mTorr O_2 gas pressure.

Significant increase in M with increase in O_2 pressure to reach maximum value of 230 emu/cc (42 emu/g) obtained for the film deposited at 27 mTorr. The value of 42 emu/g for the as-deposited film prepared under normal conditions in the present study is the highest so far reported in the literature. A comparison of magnetization values can be made with the reported values on mechanically processed nanocrystalline samples (12 emu/g) [41], samples prepared by wet-chemical methods (28 emu/g) [42] and (21 emu/g) [43], rf-sputtered crystalline thin films (12 emu/g) [32] and (32 emu/g) [44] and laser ablated thin films in applied magnetic field of 2 kG (56.6 emu/g) [45]. The increase in the magnetization of ZnFe_2O_4 has been attributed to oxygen vacancies and disorder [46], surface effects [47], as well as to cation random distribution of magnetic iron Fe^{3+} ions and diamagnetic Zn^{2+} ions among the interstitial octahedral (B) and tetrahedral (A) sites of the spinel lattice of ZnFe_2O_4 [48]. The occupancy of Fe^{3+} ions on both A - and B -sites leads to strong negative superexchange interaction between Fe^{3+} ions with large magnetization values. During the film deposition, the oxygen vacancy and the disorder on the nanocrystal surface can contribute to cation redistribution on A and B sites leading to high magnetization. The oxygen working pressure of around 27 mTorr appears to be critical as it may provides sufficient time for the nanocrystals to settle down on the substrate in a preferred direction to give maximum magnetization.

Figure 5.24 shows typical magnetization curves of as-sputtered ZnFe_2O_4 thin films at 27 mTorr of oxygen pressure for parallel (H_{\parallel}) and perpendicular (H_{\perp}) orientations of external magnetic field with respect to the film plane. One observes strong dependence of magnetization (M) on the orientation of H . For in-plane magnetization, the saturation takes place at field of about 2 kOe, which is smaller than the saturation field for transverse magnetization. The M_S per unit volume of the as-deposited ZFO films is 230 emu/cc. A well-defined hysteresis is observed with coercivity H_C value of 50 Oe. Such an M_S versus H behavior is an indicative of the expected ferromagnetic ordering at room temperature of ZnFe_2O_4 thin films. Thus the magnetization curves of Figure 5.24 for Zn-ferrite films are totally different from the corresponding magnetization for the bulk ferromagnetic counterparts.

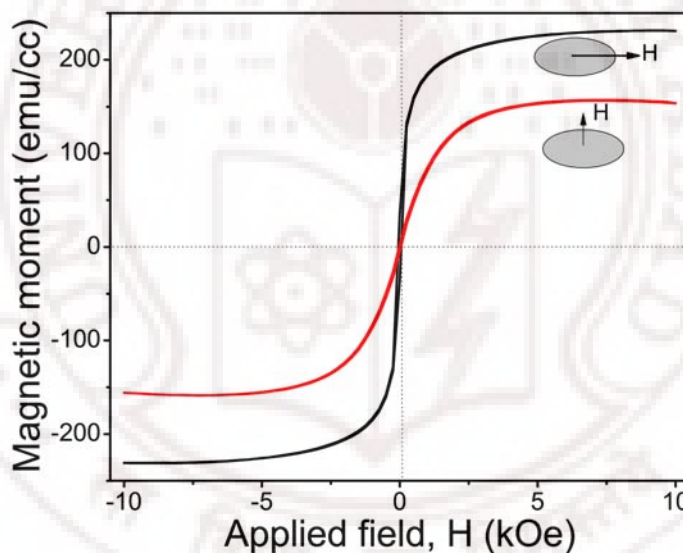


Figure 5.24: Angular dependent M-H curves of as-sputtered ZnFe_2O_4 thin films at 27 mTorr of oxygen pressure.

Magnetizations as a function of the external magnetic field, $M(H)$, are shown at 80 K for ZnFe_2O_4 thin film in figure 5.25. The magnetization at 10 kOe is as high as 230 emu/cc (42 emu g^{-1}) at 300 K and reaches 350 emu/cc (65 emu g^{-1}) at 80 K. The magnetic hysteresis loops are clearly observed in the low-field ranges. The hysteresis loop at 80 K (330 Oe) is much larger than that at 300 K (55 Oe). The higher value of H_C at lower temperature can be assigned to the large disorder in the system.

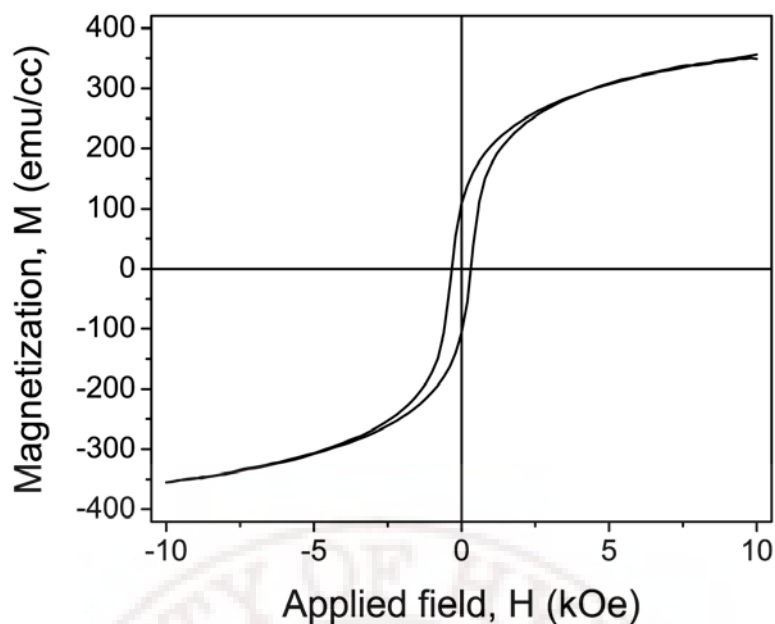


Figure 5.25: Magnetization as a function of the external magnetic field for ZnFe_2O_4 thin film measured at 80 K.

5.2.1.4.2 FMR studies

Figure 5.26 shows comparison of FMR spectra recorded at room temperature of as-sputtered ZnFe_2O_4 films deposited on glass substrates. The films were deposited at ambient temperature in pure Ar gas at 8 mTorr and pure O_2 gas at 8, 18, 27 and 31 mTorr of working pressures. It can be seen that ZnFe_2O_4 films deposited with pure Ar show relatively higher value of FMR peak-to-peak linewidth of around 910 Oe compared to the films deposited in O_2 gas (850 Oe). With increase in O_2 working pressure the linewidth decreases, which can be attributed to the reduction of structural inhomogeneities and magnetic disorder.

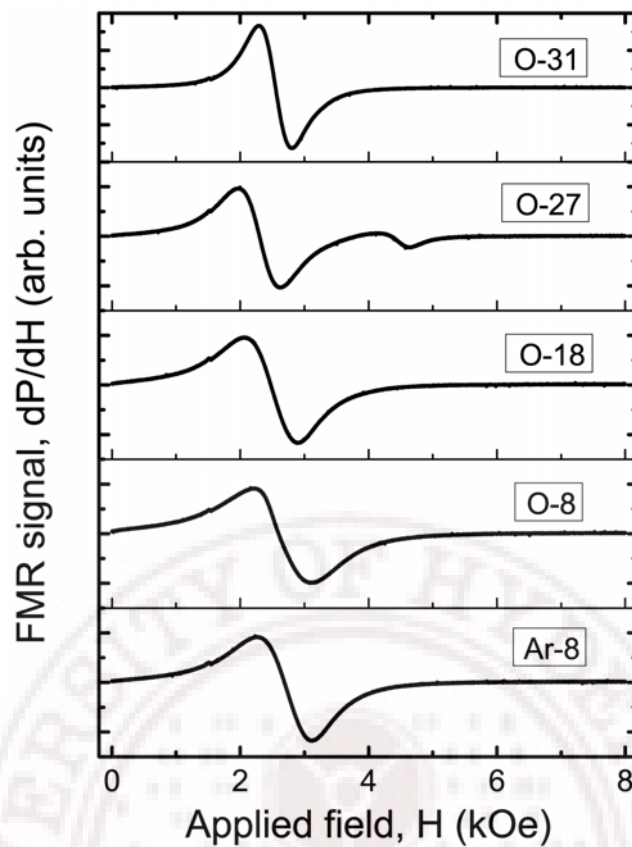


Figure 5.26: FMR spectra of ZnFe_2O_4 thin films deposited in O_2 and Ar environments at various working gas pressures.

Figure 5.27 shows the out-of-plane angular dependent FMR spectra for the as-deposited film in the range $0^\circ - 90^\circ$. The FMR spectra show symmetric Lorentzian line-shape. The signal becomes slightly asymmetric with appearance of another peak which coincides with the in-plane resonance as θ_H approaches zero. The effective saturation magnetization ($4\pi M_{\text{eff}}$) and the effective gyromagnetic ratio (γ_{eff}) are estimated using Kittel relations (5.1) [22,32].

The values of ($4\pi M_{\text{eff}}$) and (γ_{eff}) at RT are 1725 G and 3.08 GHz/kOe respectively. The growth process of the film is affected by internal stresses, preferential alignment of nanocrystalline grains or ions due to inter-atomic forces [49]. This induces additional anisotropy to the geometrical shape anisotropy of the grains.

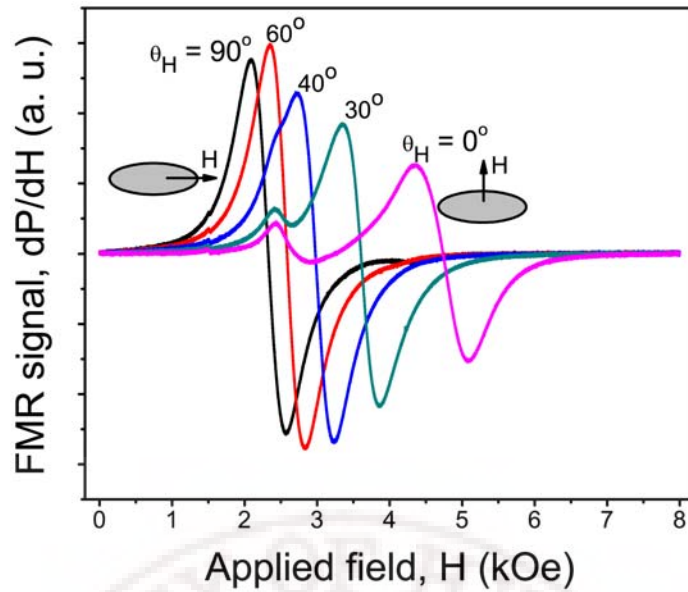


Figure 5.27: Angular dependent FMR signal of as-sputtered ZnFe_2O_4 thin films at 27 mTorr of oxygen pressure.

The temperature dependent FMR spectra for the ZnFe_2O_4 thin films deposited under O_2 pressure of 27 mTorr are presented in figure 5.28 recorded in the temperature range 120 ~ 320 K. The films demonstrate FMR signals in which both position and width of the line strongly dependent on the sample orientation, shifting to lower fields at the parallel orientation (magnetic field in the film plane), and to higher fields at the perpendicular orientation.

Temperature dependent FMR measurements at X-band frequencies were performed to study the effects of spin freezing on high-frequency magnetic parameters of the film. Temperature dependence of FMR line width for a representative sample sputtered in O_2 at 27 mTorr are shown in Figure 5.29, for the static field H parallel (ΔH_{\parallel}) and perpendicular (ΔH_{\perp}) to the film plane. ΔH_{\perp} is relatively larger than ΔH_{\parallel} . An increase in ΔH_{\parallel} and ΔH_{\perp} with decreasing T is evident from the data until 270 K. below 270K their variation is totally different. While ΔH_{\parallel} increases slightly with decreasing temperature, ΔH_{\perp} decreases. This effect can be assigned to the spin freezing at low temperatures as reported by Chen et al. [32] in ferrite. These results are supported by the magnetization vs temperature (M - T) measurements under zero field cooled (ZFC)-field cooled (FC) and shown in figure 5.36.

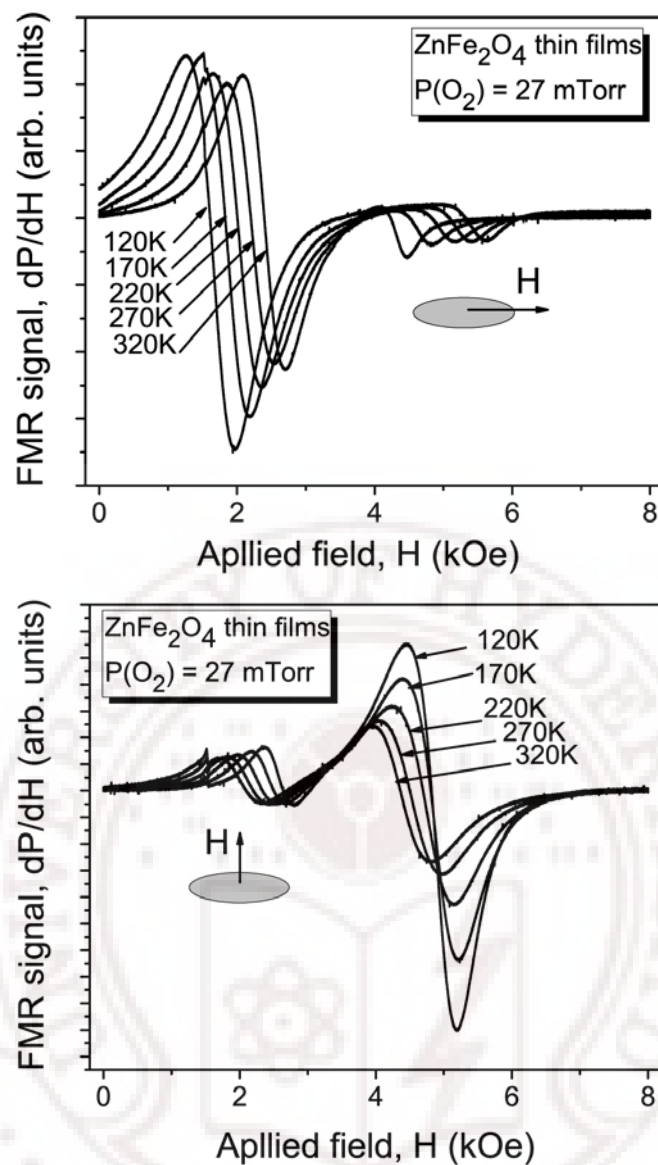


Figure 5.28: Temperature dependence of FMR spectra of as-sputtered ZnFe_2O_4 thin films at 27 mTorr of oxygen working pressure.

Figure 5.29 displays the temperature-dependent resonance field (H_R) of the ZnFe_2O_4 film sputtered under O_2 environment at 27 mTorr on glass substrates for in-plane (H_{\parallel}) and out-of-plane (H_{\perp}) configurations. The resonance field H_{\perp} is larger than H_{\parallel} at all temperatures. An increase in the resonance fields (H_{\parallel}) and decrease in H_{\perp} is observed as the temperature is increased. The temperature dependence of H_{res} manifests that the precession frequency of atomic magnetic moment changes with temperature and the

applied field orientation, and the different values of H_{res} for the out-of-plane and in-plane configurations indicate the presence of magnetic anisotropy in the thin films [50]. The resonance fields H_{\parallel} and H_{\perp} are related to the angular frequency of the microwave radiation, effective magnetization $4\pi M_{\text{eff}}$ of the film and gyromagnetic ratio (γ) by the expressions (5.1). Since the magnetization decreases with increasing T and there is only a small change in the operating frequency one expects a decrease in H_{\perp} and an increase in H_{\parallel} as T is increased. The saturation of H_{\perp} at low temperature can be associated to the spin freezing. One can conclude that the temperature dependence of the resonance parameter is more sensitive in the perpendicular configuration.

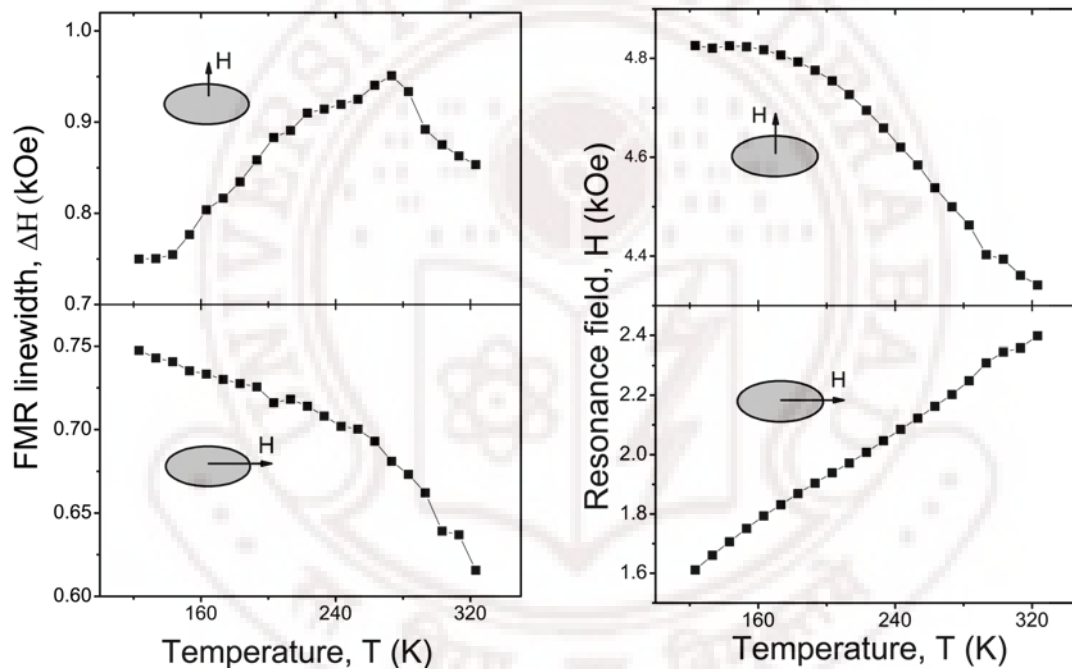


Figure 5.29: Temperature dependence of FMR resonance field and linewidth of ZnFe_2O_4 thin films.

The anisotropic character of the nanocrystalline film is evident from ferromagnetic resonance (FMR) studies at X-band frequencies. The effective saturation induction $4\pi M_{\text{eff}} = 4\pi M_S + H_A$ (where H_A is the anisotropy field parallel to the film plane) and the effective g-factor g_{eff} were estimated from the resonance fields data as done in reference [10].

Figure 5.30 shows the variation in $4\pi M_{\text{eff}}$ and g_{eff} with temperature. A room temperature g_{eff} of 2.2 is estimated for the film. The data indicate an increase in $4\pi M_{\text{eff}}$ and

g_{eff} as T decreases. Such strong temperature dependence for g_{eff} is usually observed around the compensation point in ferrimagnetic crystalline oxides where the sublattice magnetizations cancel each other.

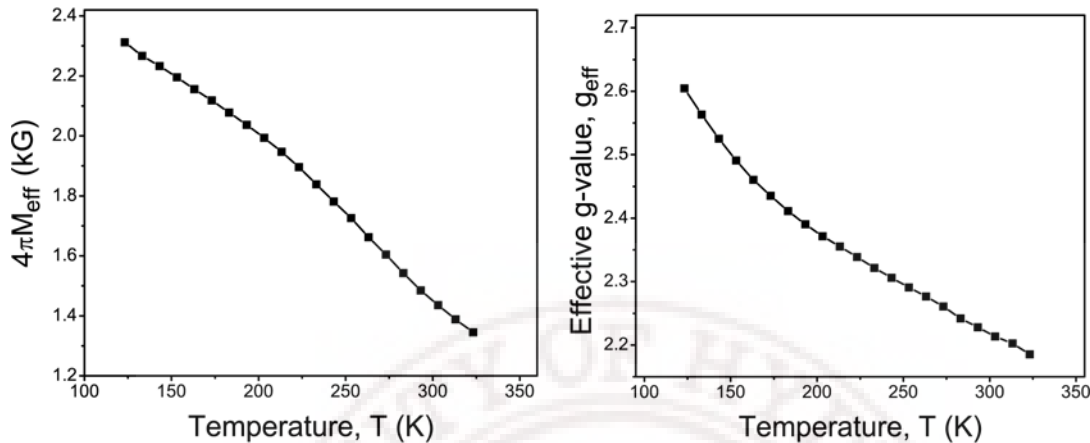


Figure 5.30: The effective saturation magnetization ($4\pi M_{\text{eff}}$) and the effective g-value (g_{eff}) were determined from data on the resonance fields for static fields parallel and perpendicular to the film plane using Kittel relations.

5.2.2 Effect of Heat treatment

The key inference is that the structural, optical and magnetic properties are influenced by the annealing of the Zn-ferrite films. The M_s decreases with increase in annealing temperature which is assigned to the redistribution of the cations among A- and B-sites where they take up their preferable sites as in the bulk sample.

5.2.2.2 Structural analysis (XRD)

The X-ray diffraction spectra for the as-deposited film and the film annealed at 500 °C are displayed in Figure 5.31. The XRD patterns confirm the presence of spinel phase without any impurity phase for both the films. The lines can be indexed to the characteristic interplanar spacing (220), (311), (400), (422), (511) and (440) of the spinel structure with cubic symmetry. The average grain size was estimated from the width of the (311) reflection of the XRD patterns by using the Scherrer's formula. The values of average grain size are 50 and 60 nm for the as-deposited and annealed film respectively. (After subtracting the broadening effects due to strain and experimental broadenings)

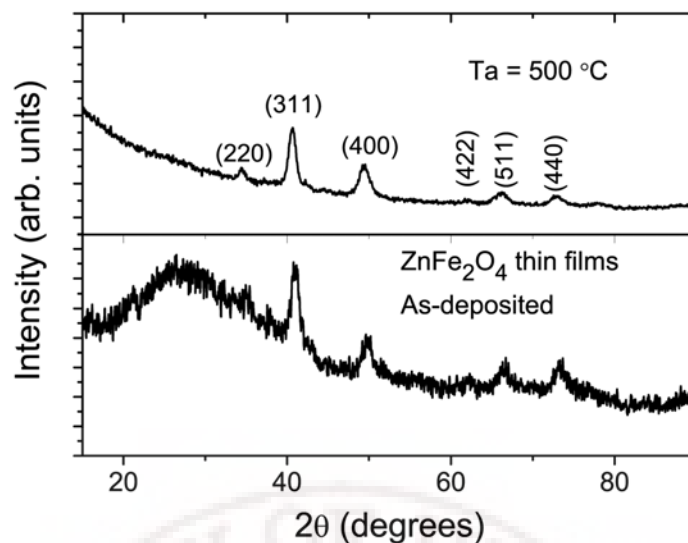


Figure 5.31: X-ray diffraction pattern of the as-deposited and annealed films of ZnFe_2O_4 .

5.2.2.2 Microstructural analysis

Figure 5.32 shows the SEM micrographs of as-deposited and heat treated film at 500 °C for 3 hrs. The SEM micrographs show that the films have nanocrystalline structures with average grain sizes of about 70 and 100 nm for the as deposited and annealed films in accordance with AFM data of the same films. A crack-free, highly uniform and densely packed microstructure is obtained in these films. The grain size and uniformity of the deposited film were enhanced by annealing.

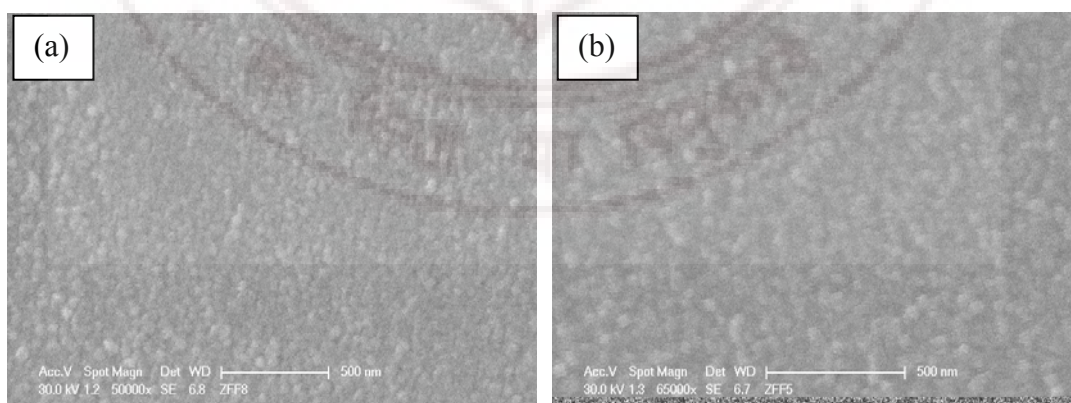


Figure 5.32: SEM images of ZnFe_2O_4 thin films (a) as-deposited at 27 mTorr O_2 (b) annealed at 500 °C for 3 hrs.

To confirm the chemical composition of the as-deposited and the heat treated ZnFe_2O_4 films, EDAX spectra (Figure 5.33) were recorded at a number of positions of the film surface. The chemical signatures obtained are identical within experimental accuracy (5%)

and only Zn, Fe, and O elements are observed with the expected stoichiometric proportions of ZnFe_2O_4 ($\text{Zn/Fe} = \frac{1}{2}$). This further confirms the formation of ferrite crystallites in the as-synthesized sample. XRD and EDAX studies demonstrate that the as-sputtered thin films are nanocrystalline ZnFe_2O_4 ferrites.

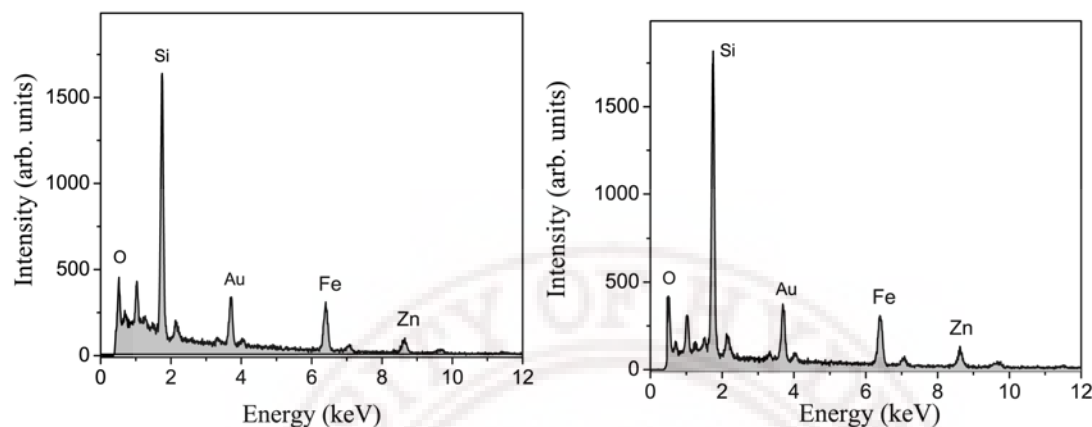


Figure 5.33: EDAX results confirm the formation of ferrite nanocrystallites in the as-deposited and annealed at 500 °C ZnFe_2O_4 films. The chemical signatures obtained are identical. The films deposited on glass substrates and show prominent Si peaks.

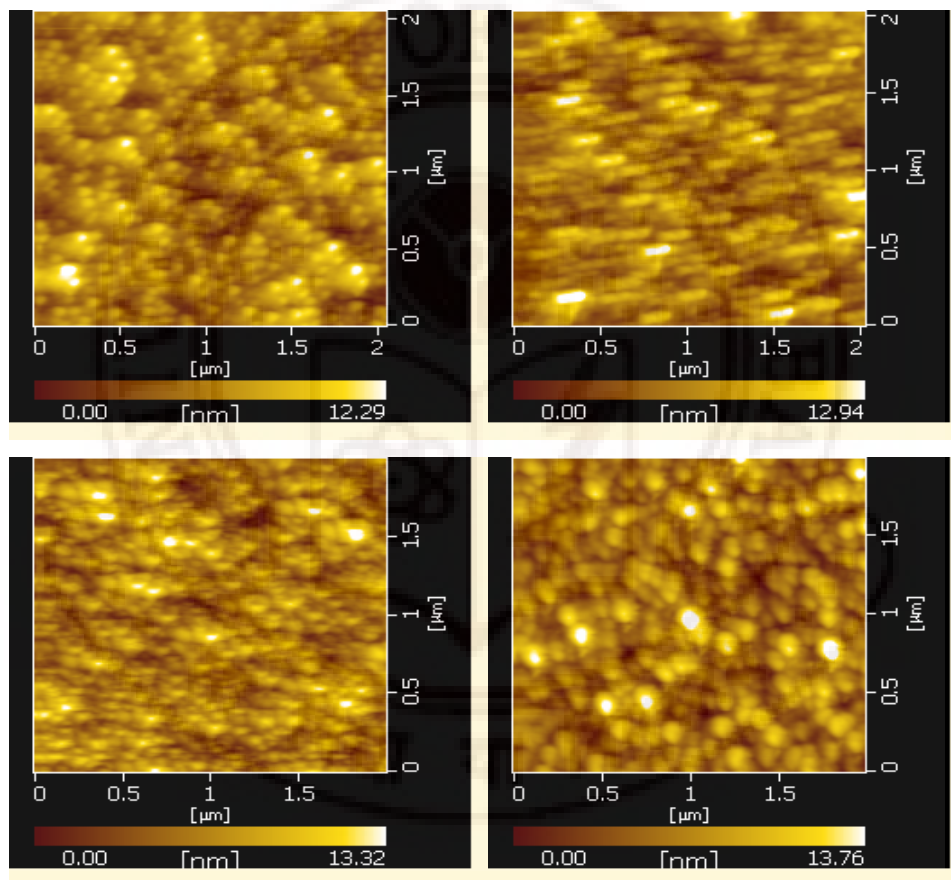
5.2.2.3 Film surface morphology (AFM studies)

The influence of heat treatment on the surface morphology of the film was studied by atomic force microscopy (AFM). The surface morphology of the film is smooth with no cracks and defects, as shown in Figure 5.34. The film exhibited a dense microstructure and the grain size was found to increase from 80 to 120 nm as the annealing temperature is increased from 200 to 500 °C (Table 5.4). The surface morphology of the deposited film is related to the surface kinetic energy and depends on the processing parameters such as annealing temperature, duration and environment [51].

Surface roughness (RMS) was improved with increase in annealing temperature. The average surface roughness is around 2 nm for the film annealed at 500 °C. Higher annealing temperature improved the structural quality of the ZnFe_2O_4 thin films. The kinetic energy of the sputtered atoms increases with increase in annealing temperature resulting in structural improvement of the deposited ZnFe_2O_4 thin films.

Table 5.4: Effect of annealing on the AFM and magnetization parameters.

ZnFe ₂ O ₄ thin film	⟨Grain size⟩ (nm)	⟨RMS⟩ (nm)	M _{S 0} (emu/cc)	H _{C 0} (Oe)	ΔH ₀ (Oe)	H _{R 0} (Oe)
As-deposited	80	2.4	230	55	630	2235
Ta = 200 °C	100	2.2	254	45	551	2221
Ta = 300 °C	110	2.2	220	25	360	2180
Ta = 400 °C	105	2.1	157	14	200	2430
Ta = 500 °C	120	2.0	70	3	210	2587

**Figure 5.34:** AFM images of ZnFe₂O₄ thin films prepared under 31 mTorr Oxygen pressure (a) As deposited and annealed for 3 hrs at (b) 200, (c) 300, and (d) 500 °C

5.2.2.4 M-H plots

Magnetization vs magnetic field plots of ZnFe₂O₄ films deposited in pure O₂ and annealed in air for 3 h at temperatures in the range 200–500 °C are presented in Figure 5.35. It is observed that as annealing temperature increases the saturation magnetization (M_S) of the

films increases and reaches the highest value of 254 emu/cc at $T_a = 200\text{ }^{\circ}\text{C}$ followed by decreasing trend with further increase in annealing temperature (Table 5.4) .

According to XRD observations (see Figure 5.31), the as-deposited film is composed of nanocrystalline particles in amorphous background. AFM images also show the nanocrystalline nature of the films. These nanocrystals align in one direction at $200\text{ }^{\circ}\text{C}$. The nanocrystals merge forming bigger crystals as the annealing temperature is increased to $300\text{ }^{\circ}\text{C}$. The TEM observations on the films prepared by similar method by Nakashima et al. [52] show that the film is composed of crystalline nanoparticles dispersed in an amorphous matrix, and the amorphous phase is converted into the crystalline phase upon annealing at $300\text{ }^{\circ}\text{C}$. The enhancement of magnetization is presumably due to precipitation of a disordered ZnFe_2O_4 crystalline phase from the amorphous phase viz. the volume fraction of the ferrimagnetic ZnFe_2O_4 phase is increased by annealing the film at 200 and $300\text{ }^{\circ}\text{C}$.

The thermal annealing of the film at $T_a > 300\text{ }^{\circ}\text{C}$ decreases M_S and H_C values drastically (figure 5.35 and table 5.4). This reduction can be due to the redistribution of the cations among A- and B-sites where they take up their preferential sites as in the paramagnetic bulk sample and consequently reduce the disorder in the system.

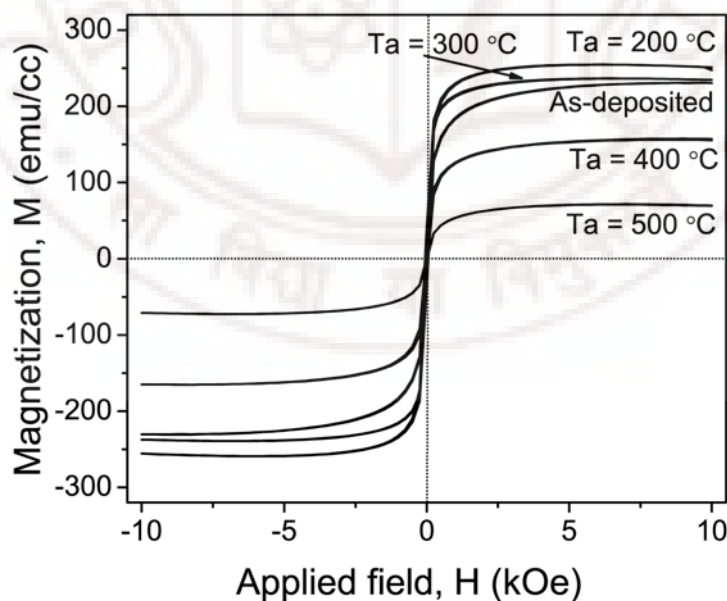


Figure 5.35: Magnetization curves of ZnFe_2O_4 thin films annealed in air for 3 hrs at temperatures in the range 200–500 $^{\circ}\text{C}$.

5.2.2.4 Magnetization studies (ZFC-FC)

Figure 5.36 shows the magnetization versus temperature (M-T) curves of as-sputtered and annealed ZnFe_2O_4 thin films in an applied field of 100 Oe recorded in the zero field cooling – field cooling modes (ZFC–FC) in the temperature range 80–300 K. It can be seen that the ZFC and FC curves for the as-deposited and annealed films show significant irreversibility. The curves coincide initially, separate and follow different trends as the temperature is decreased from 300 to 80 K. In the FC mode, the magnetization continues to increase with decreasing temperature below the peak temperature T_B , without a tendency towards saturation demonstrating Curie-like behavior, whereas the ZFC magnetization shows a maximum followed by a steady decrease to smaller values in the low temperature region. Similar results on ZnFe_2O_4 thin films are reported in the literature [53].

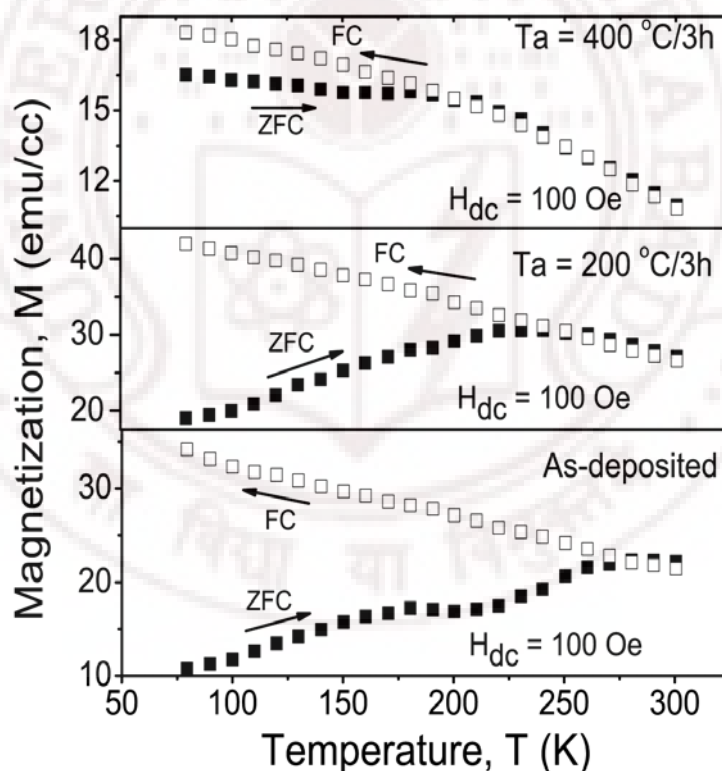


Figure 5.36: Temperature-dependent magnetization under ZFC-FC conditions at applied field of 100 Oe for as-deposited and annealed ZnFe_2O_4 films at 200 and 400 °C.

The ZFC Cusp feature is reported in nanocrystalline materials and thin films of ZnFe_2O_4 . These observations have been attributed to various phenomena such as spin glasses [54], cluster glasses [55], frozen ferrofluids with random anisotropy [56], random

anisotropy ferromagnets [57], polymers containing magnetic components [48], disorder thin films [44,52] and superparamagnets [58-61].

Superparamagnets below the blocking temperature are unable to thermally equilibrate, but no underlying phase transition is present. In contrast, spin glasses and random ferromagnets exhibit a divergent nonlinear or singular susceptibility generally considered indicative of a phase transition. In each of these systems, the FC magnetization departs from the ZFC magnetization at some temperature (which may or may not be equal to the cusp temperature) and either reaches a plateau or monotonically increases below the cusp. In canonical spin glasses, the FC $M(T)$ departs from the ZFC $M(T)$ at or slightly above the cusp temperature and below the cusp temperature. In random anisotropic systems and frozen ferrofluids, the FC curve continues to rise monotonically with decreasing T below the cusp. The saturation or continuous rise of the FC curve below the cusp temperature is likely dependent on the magnitude of interactions and/or size effects [62].

Based on the abovementioned arguments, The M-T behavior in the ZFC-FC modes for present films is caused by the disordered cation distribution of Zn^{2+} and Fe^{3+} ions in the spinel structure and can be explained in terms of superparamagnetism with intercluster interactions [44,52,55], suggesting that a ferrimagnetic order occurs for localized magnetic moments.

The peak temperature shifts toward lower values with increase in annealing temperature. For the as-deposited film, ZFC magnetization exhibits a maximum at around 270 K whereas for the films annealed at 200 and 400 °C it appears at around 230 and 170 K respectively. The variation of T_B with T_a is mainly ascribed to the displacement of Fe^{3+} ions from A- to B-sites, which reduces the strength of strong superexchange interaction between Fe^{3+} ions on A- and B-sites; namely, the redistribution of Zn^{2+} and Fe^{3+} ions toward normal spinel structure that occurs at elevated T_a . Figure 36 also indicates that the room-temperature magnetization at 100 Oe is increased by annealing the film at 200 °C, then decreased at $T_a = 400$ °C. Similar behavior of T_a dependence of magnetization has been reported in reference [52]. As T_a increases, $M(T)$ approaches the value that is observed for normal spinel ZnFe_2O_4 [53].

5.2.2.4 FMR studies

Figure 5.37 shows RT FMR spectra of as-sputtered films in pure O₂ gas at 27 mTorr working pressure and annealed in air at temperatures of 200, 300, 400 and 500 °C. The FMR resonance of the as-deposited film consists of a single line with peak-to-peak linewidth (ΔH) of around 630 Oe. A relatively broad FMR line observed for the as-deposited ZnFe₂O₄ film compared to the bulk ZnFe₂O₄ (480 Oe) is due to the overlapping of FMR line for the grains with randomly oriented magnetic easy axis. The thermal treatment of the film decreases the linewidth significantly and also causes the resonance field to shift towards the higher field which is in conformity with the reduction in magnetization. Linewidth decrease with annealing can be assigned to the reduction of structural inhomogeneities and magnetic disorder (table 5.4).

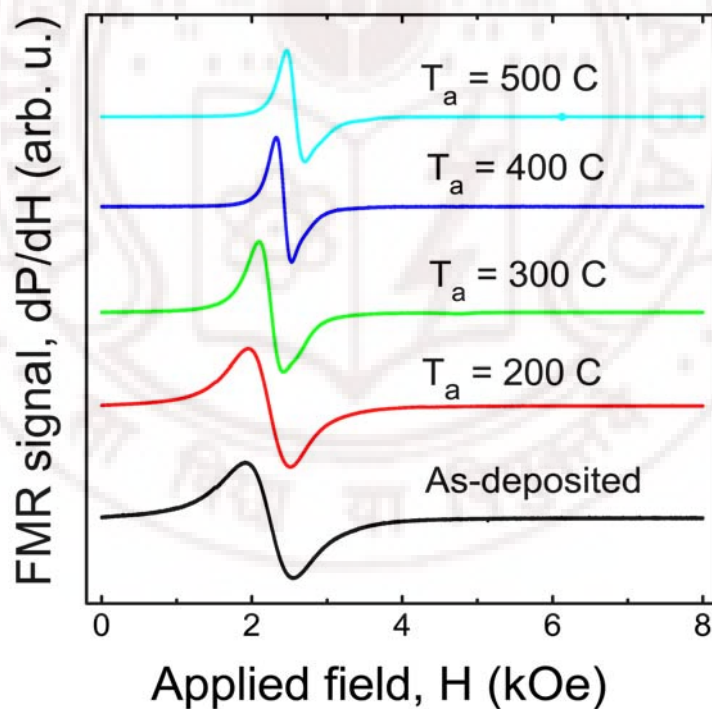


Figure 5.37: FMR spectra of ZnFe₂O₄ thin films deposited at 27 mTorr O₂ gas pressure. The films were annealed for 3 h in air at temperatures of 200, 300, 400 and 500 °C.

Figure 5.38 shows temperature dependence of ΔH of the as-deposited and annealed films. ΔH is large at all temperatures and it increases with decrease in temperature for the as-deposited film, whereas it shows weak temperature dependence for the annealed film. It

is expected that at low temperatures the internal magnetic field originating from magnetic entities is more uniform giving rise to narrow FMR line. The line broadening in the present films indicates the increase in the magnetic disorder in films with decreasing temperature. The strong temperature dependence of disorder indicates the contribution from exchange interactions. The antiferromagnetic contribution to magnetic interactions is also effective and enhances the disorder of the system. The increase in linewidth can be due to distribution of exchange interactions. This effect can also be related to disorderly frozen spin profile as reported in the case of Fe_3O_4 nanoparticles [63].

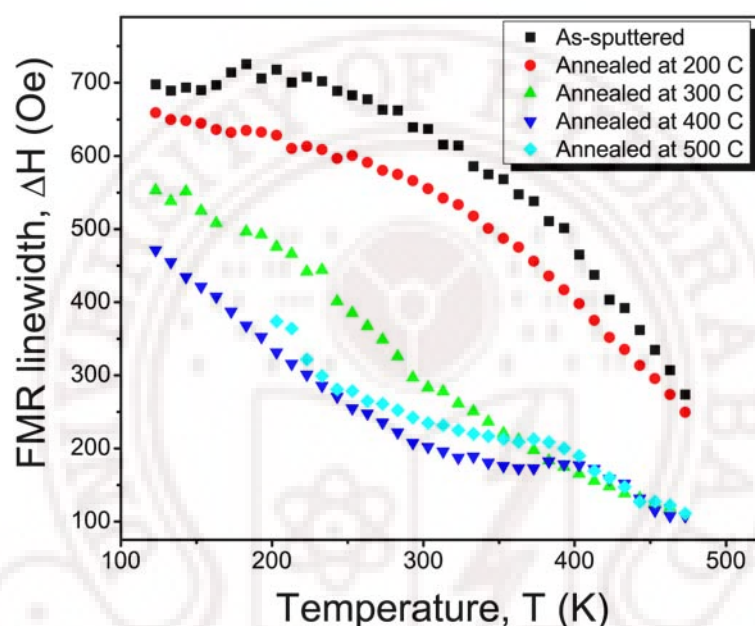


Figure 5.38: Temperature dependence of peak-to-peak linewidth (ΔH) of the as deposited and annealed films of ZnFe_2O_4 .

Figure 5.39 shows the temperature dependence of resonance field (H) of the as-deposited and annealed films. The decrease in H_R value with decrease in temperature shows the increase in internal fields. This result is consistent with ΔH variation with temperature.

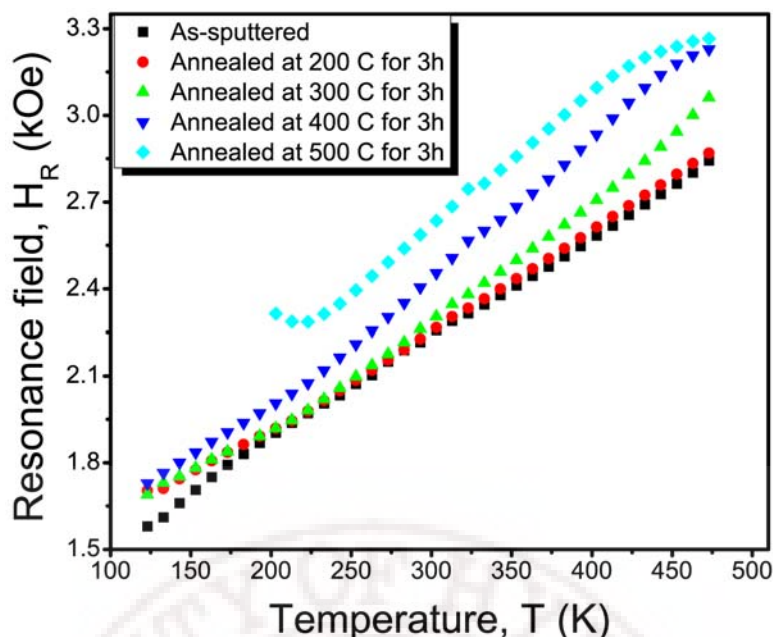


Figure 5.39: Temperature dependence of resonance field (H_R) of the as-deposited and annealed films of ZnFe_2O_4 .

Figure 5.40 shows the RT transmittance spectra for the as-deposited and annealed films. The transmittance spectra show that all the films have sharp absorption edges at ~ 550 nm. The films exhibit high transmittance above the absorption edge. Post-deposition annealing in air influences the optical properties of ZnFe_2O_4 films. The film annealed at 200°C has absorption edge at lower wavelength and enhanced transmittance which could be due to Burstein–Moss band-filling. However, the annealing above 200°C decreases the optical transmittance and shifts the absorption edge towards higher wavelength. This can be due to the increase in grain size in the film and a change in the nature and strength of the interaction potentials between defects and host materials, which increase the tailing of the absorption edge.

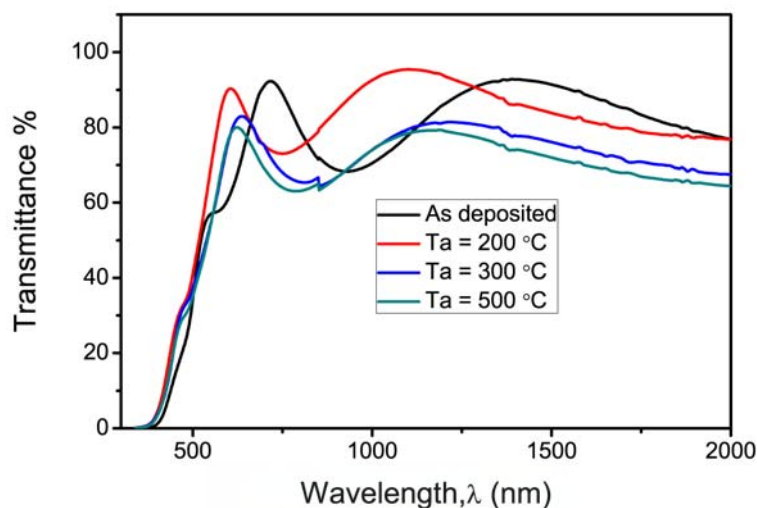


Figure 5.40: Optical transmittance spectra of the as-grown and annealed ZnFe_2O_4 films.

5.3 Copper-zinc ferrite ($\text{Cu}_{0.6}\text{Zn}_{0.4}\text{Fe}_2\text{O}_4$) thin films

This section includes the study of the structure, morphology, magnetic and optical properties of $\text{Cu}_{0.6}\text{Zn}_{0.4}\text{Fe}_2\text{O}_4$ thin films. There is no report on the properties of copper-zinc ferrite thin films and hence this work is an addition to the literature. This composition was chosen because bulk ferrite of this composition has the highest magnetization among all the compositions under study. The films were deposited from a sintered target of $\text{Cu}_{0.6}\text{Zn}_{0.4}\text{Fe}_2\text{O}_4$ composition onto glass substrate using rf-magnetron sputtering system operating at 100 W of rf-power in argon and oxygen environment.

5.3.1 Effect of Ar gas pressure

5.3.1.1 Structural analysis (XRD)

Figure 5.41 shows the XRD patterns of the as-sputtered thin films at various pressure of pure Ar gas. All the peaks belong to spinel structure with cubic symmetry without any secondary or impurity phases. The XRD line width and crystallite size are estimated using Scherrer equation [14] $D = 0.9\lambda / (\beta \cos \theta)$ where, D is particle diameter, λ the wavelength of the X-ray radiation, β a measure of the broadening of diffraction line due to size effect.

It can be seen that the peak broadening decreases with increase in Ar pressure. The average crystallite size increases from 5 to 21 nm with increase in Ar pressure from 5 to 15 mTorr. With increase in Ar content the relative intensity ratios of planes I_{220}/I_{400} , I_{440}/I_{400} and I_{422}/I_{400} increases. It is known that for spinel–ferrite the increase in intensity ratios of these planes is related to the increase in disorder parameter and consequently to the increase in magnetization [7,64]. The diffraction data were fitted with a Lorentzian function to determine the location (2θ) of each peak. Using Bragg's law, the interplanar lattice spacing d_{hkl} and the cell parameter a were calculated. The variation of the average lattice spacing, i.e. the slight shift of the (hkl) peak position, in the direction normal to the plane of the film gives the measure of strain in the film; either compressive or tensile [65]. A characteristic shift towards lower angle compared to that of ideal crystal indicates lattice expansion. The films deposited at lower pressure show higher cell parameter (8.5 Å) compared to the bulk due to the strain introduced in the film during deposition. The origin of the strain in the sputtered films may be related to several factors, including voids, argon inclusions and film substrate mismatch [66]. The strain reduces with increase in Ar pressure and the cell parameter approaches the bulk value of 8.41 Å. With increase in Ar gas pressure the phase collision increases which consequently reduces the kinetic energy of sputtered neutral atoms leading to decrease in strain [30].

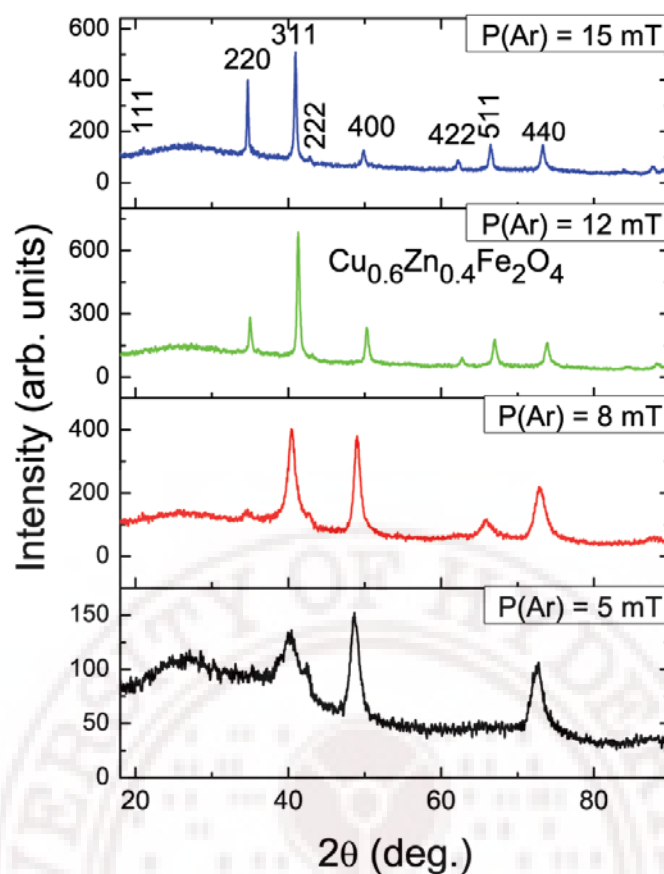


Figure 5.41: The XRD patterns of the as deposited $\text{Cu}_{0.6}\text{Zn}_{0.4}\text{Fe}_2\text{O}_4$ thin films under different Ar gas pressure.

5.3.1.2 Surface morphology (AFM)

Figure 5.42 shows the AFM images of the films deposited at 5 and 12 mTorr of Ar pressure. The average particle size $\langle D \rangle$ and RMS values for various films are listed in table 5.5.

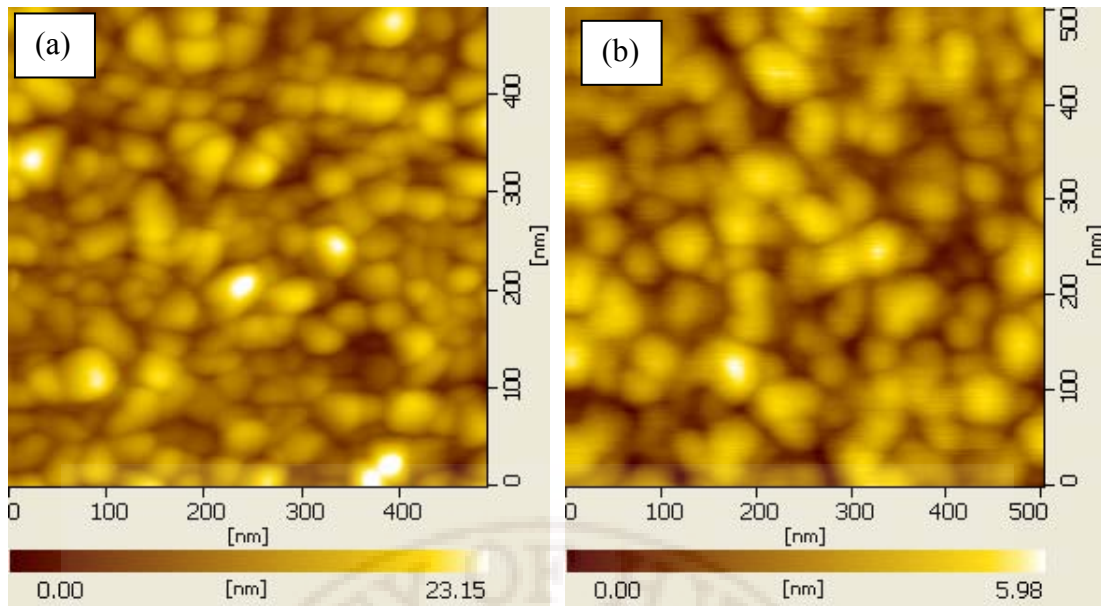


Figure 5.42: AFM images of the as-deposited $\text{Cu}_{0.6}\text{Zn}_{0.4}\text{Fe}_2\text{O}_4$ thin films at (a) 5 mTorr (b) and 12 mT.

The increase in particle size and decrease in (RMS) with increase in Ar gas pressure could be attributed to shadowing effects. There is a variation in the distribution of incident angles and energy of the depositing atoms at low and high deposition pressures [28]. At low deposition pressure few collisions occur within the plasma; therefore incident angles tend to be close to normal and bombarding energy tends to be high. The high bombarding energy leads to a high variation in surface roughness. However, the increase in Ar gas pressure increases the number of collisions occurring in the plasma and consequently to an increase in the incident angles of the particles which leads to smoothening of the films. The results presented here are in good agreement with the model (figure 5.43) proposed in references [28-30].

Table 5.5: AFM and magnetic parameters of $\text{Cu}_{0.6}\text{Zn}_{0.4}\text{Fe}_2\text{O}_4$ thin films deposited under various Ar gas pressure.

Sample Name	$\langle D \rangle$ (nm)	RMS (nm)	M_s (emu/cc)	H_c (Oe)	M_R/M_s %
CZF-Ar5	33	3.8	126	170	25
CZF-Ar8	40	3	132	100	15
CZF-Ar12	43	1.15	283	90	32
CZF-Ar15	55	2.1	295	67	17

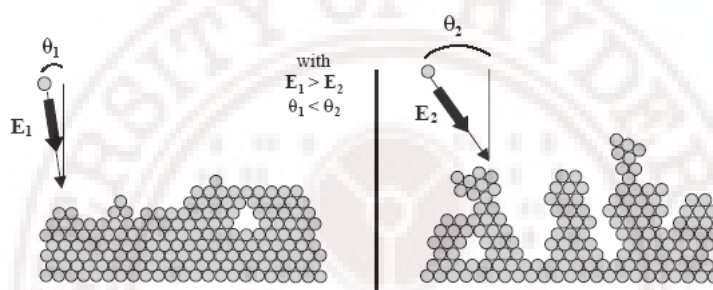


Figure 5.43: Schematic representation of the evolution of the microstructure according to the collision angle (E = bombarding energy, θ = collision angle) [29].

5.3.1.3 Magnetization studies (M - H plots)

Figure 5.44 shows the in-plane M - H plots at RT for the films deposited at various Ar gas pressure. The magnetization (M_s) increases from 126 to 132 emu/cc as the pressure increases from 5 to 8 mTorr followed by sharp increase to 283 emu/cc at 12 mTorr. Further increase in Ar pressure to 15 mTorr leads to an increase in M_s value to 295 emu/cc.

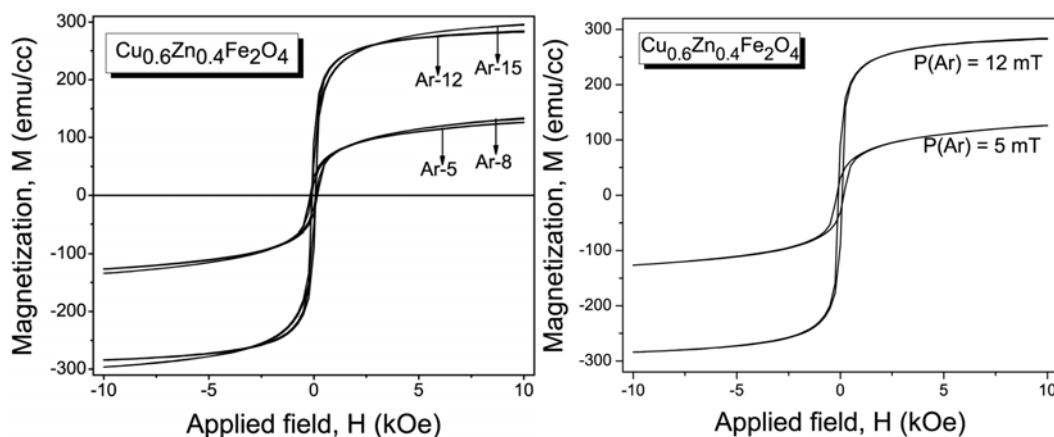


Figure 5.44: Effect of Ar pressure on M-H curves of $\text{Cu}_{0.6}\text{Zn}_{0.4}\text{Fe}_2\text{O}_4$ films

The change in crystal structure and magnetization can be explained in view of preferential occupation of A and B –sites in spinel structure. The high deposition rate in pure Ar environment can lead to freezing of some Cu-ions on tetrahedral A-sites and equivalent number of Fe ions on octahedral B-sites during the deposition process. Furthermore, the deposition in reducing (argon) atmosphere may lead to the formation of Cu^+ ion, having larger ionic radius than the Cu^{2+} ion. The Cu^+ ions prefer occupation of the smaller four-coordinated A-site in the spinel structure and displace Fe^{3+} cations to occupy the B- sites [2,64]. The formation of Fe^{2+} cannot be ruled out in the spinel structure where a fraction of Fe^{3+} will be replaced by Fe^{2+} ions. So the general cation distribution can be represented as



where d is the inversion parameter. The occupancy of the nonmagnetic Cu^+ and Zn^{2+} ions on A-sites dilutes the magnetic moment on A-sites leading to large difference between magnetization on B and A sites causing a strong negative super-exchange interaction between Fe^{3+} ions on both sites which in turn cause ferrimagnetic behavior with large magnetization [44,67]. The value of coercivity, H_C decreases from 170 to 67 Oe with increase in Ar pressure from 5 – 15 mTorr. This can be correlated to the crystallite size and the presence of significant inhomogeneities. The smaller crystallites in the case of thin films deposited under low Ar pressure has larger volume of the boundaries and

consequently more energy is required to rotate the grains by the external field and thus leading to higher coercivity.

Figure 5.45 shows the M-H plots for $\text{Cu}_{0.6}\text{Zn}_{0.4}\text{Fe}_2\text{O}_4$ thin film deposited at 12mT of Ar pressure measured at 300 and 80K. It can be seen that the saturation magnetization and coercivity are slightly higher at 80 K.

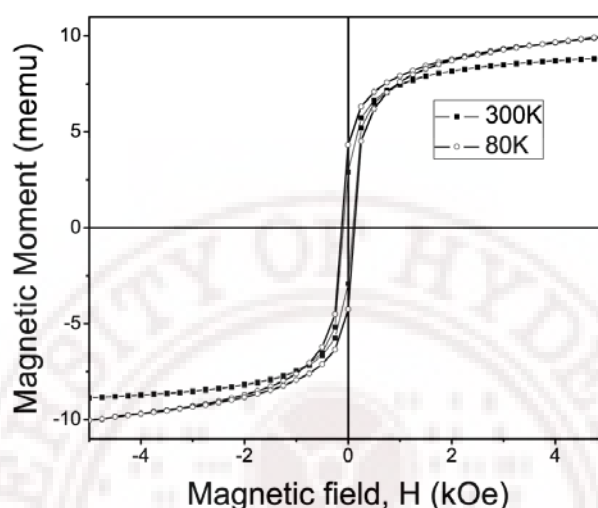


Figure 5.45: M-H plots for $\text{Cu}_{0.6}\text{Zn}_{0.4}\text{Fe}_2\text{O}_4$ thin film deposited at 12 mT measured at 300 and 80K.

5.3.1.4 FMR studies

Figure 5.46 shows the RT FMR spectra of as-sputtered $\text{Cu}_{0.6}\text{Zn}_{0.4}\text{Fe}_2\text{O}_4$ films deposited on glass substrates for both in-plane and out-of-plane configurations. The films were deposited at ambient temperature in pure Ar at 5, 8, 12 and 15 mTorr working pressures.

Table 5.6: FMR parameters of $\text{Cu}_{0.6}\text{Zn}_{0.4}\text{Fe}_2\text{O}_4$ thin films deposited under different Ar pressures.

Sample Name	ΔH_{\parallel} (kOe)	ΔH_{\perp} (kOe)	$H_{R\parallel}$ (kOe)	$H_{R\perp}$ (kOe)
CZF-Ar5	1.18	1.651	1.41	4.4
CZF-Ar8	1.16	1.362	1.66	4.4
CZF-Ar12	0.27	0.196	2.22	5.4
CZF-Ar15	0.26	0.193	2.18	5.5

The FMR parameters of $\text{Cu}_{0.6}\text{Zn}_{0.4}\text{Fe}_2\text{O}_4$ thin films deposited under different Ar pressures are listed in table 5.6. It can be seen that the films deposited at lower Ar pressure show higher ΔH value. With increase in working gas pressure ΔH decreases from 1.18 kOe (5mTorr) to value of 0.26 kOe (15 mTorr). These results are in accordance with the variation in H_C with Ar gas pressure (table 5.5). The line narrowing can be assigned to the reduction of structural inhomogeneities and magnetic disorder. The line widths when field is applied parallel (H_{\parallel}) to the film plane (ΔH_{\parallel}) are larger than those when the field is applied perpendicular (H_{\perp}) to the thin film plane. The narrow lines in the present films clearly support the idea of well aligned clusters, The large ΔH_{pp} values are attributed to anisotropy broadening attendant upon having a random distribution of cluster orientations [68,69].

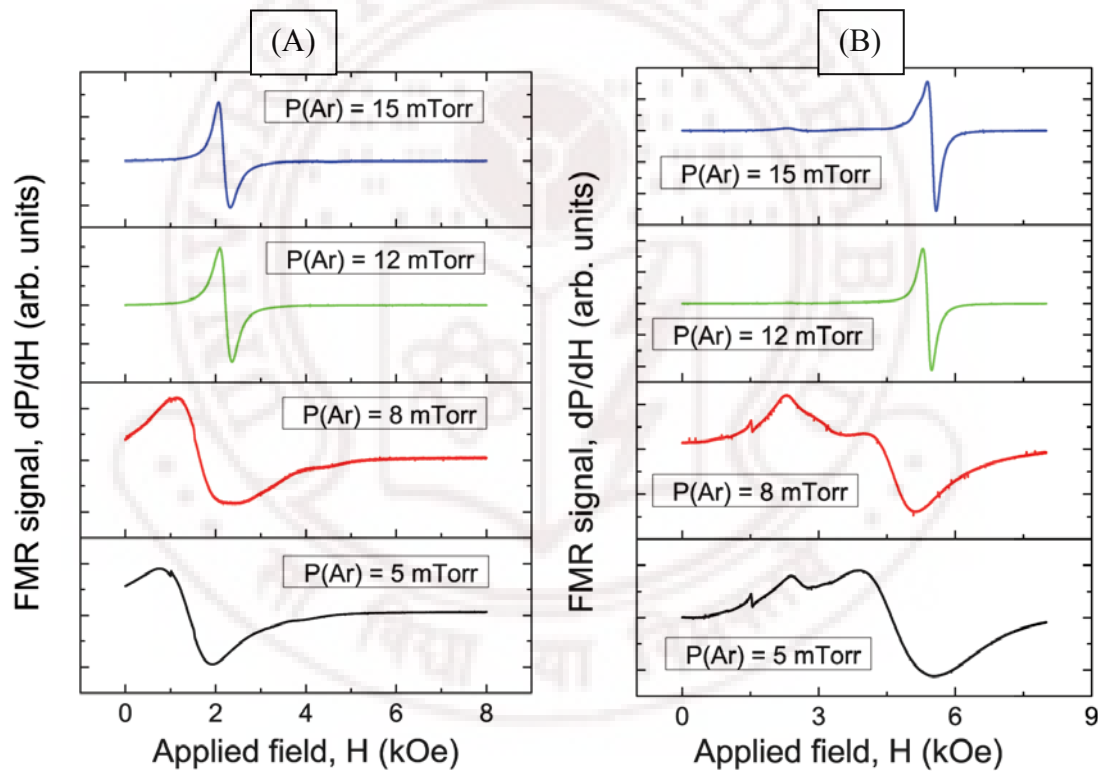


Figure 5.46: Effect of Ar gas pressure on FMR signals of $\text{Cu}_{0.6}\text{Zn}_{0.4}\text{Fe}_2\text{O}_4$ thin films deposited under different Ar pressures with (A) H_{\parallel} and (B) H_{\perp} to film plane.

5.3.2 Effect of O_2 gas pressure

5.3.2.1 Surface morphology

The surface morphology of the $Cu_{0.6}Zn_{0.4}Fe_2O_4$ thin films was analyzed by atomic force microscope (AFM) using non-contact mode with amplitude modulation. The scan area was $1\mu m \times 1\mu m$ (Figure 5.47).

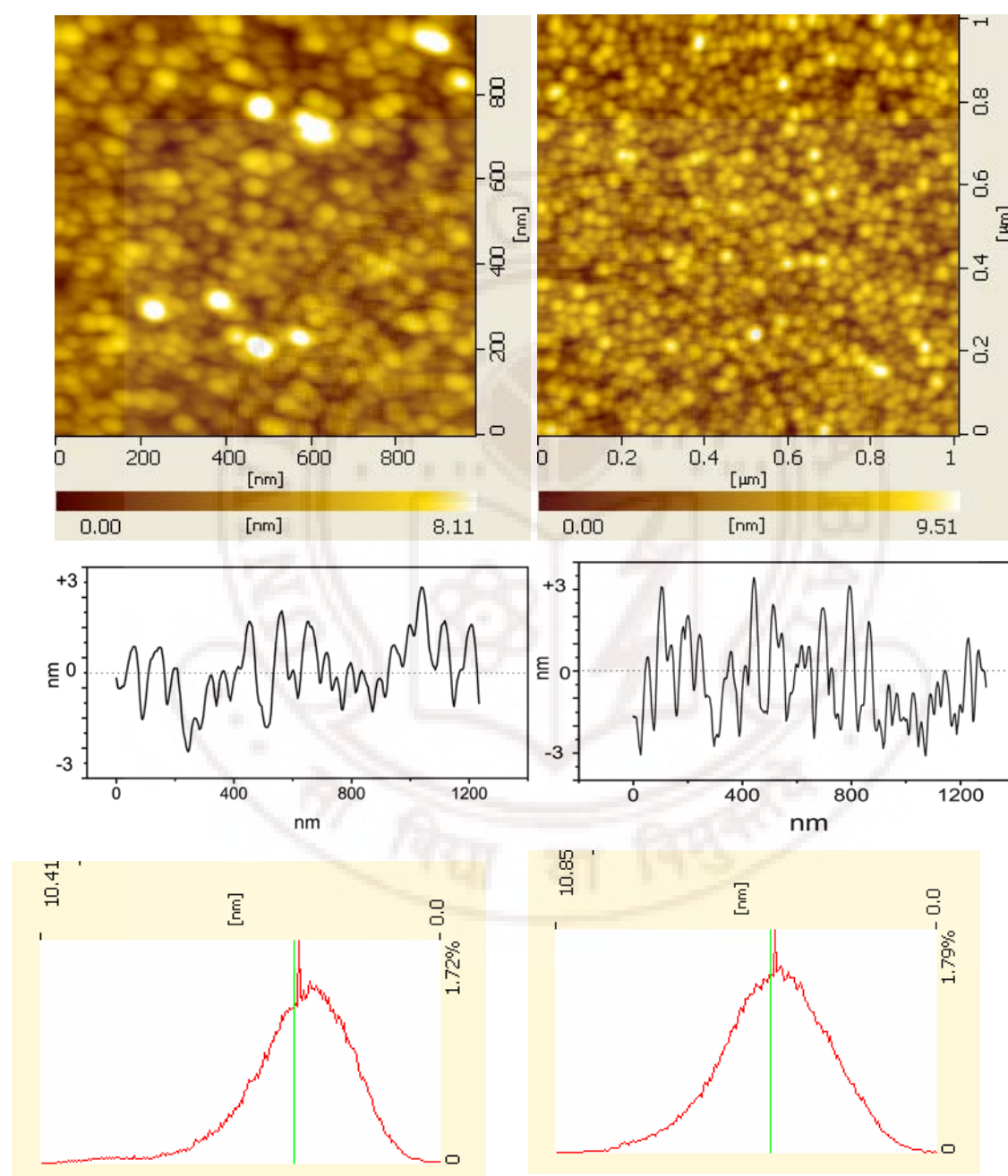


Figure 5.47: AFM images of $Cu_{0.6}Zn_{0.4}Fe_2O_4$ thin films deposited under 5 mTorr (left) and 12 mTorr (right) of Oxygen gas pressure. Surface profiles of the films (medium) and the grain size distribution (below) for the corresponding film images.

The films exhibited a dense microstructure and the grain size was found to decrease with the increase in O_2 pressure. The average grain size for the films deposited at 5 and 12 mTorr of O_2 are 50 and 30 nm respectively. The surface morphology of the films was smooth with no cracks and defects and the average surface roughness was 1.5 nm for films deposited under O_2 environment. There is no significant difference in the surface roughness for the deposited films in O_2 environment as compared to that deposited in Ar atmosphere. Surface analysis is shown in figure 5.47. The narrow distribution of the grains size is observed for these films.

5.3.2.2 Magnetization studies (*M-H plots*)

Figure 5.48 shows in-plane M-H plots at RT for the films deposited at 5, 8, 12 and 15 mTorr of O_2 gas pressure. The magnetization (M_s) values of the films are around 150 emu/cc for various oxygen gas pressures.

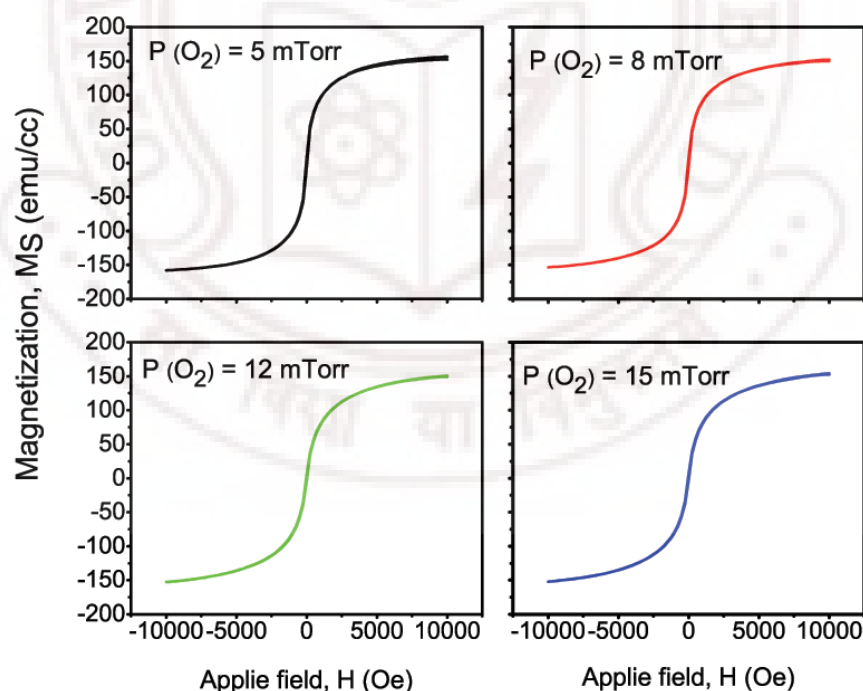


Figure 5.48: M-H curves of $Cu_{0.6}Zn_{0.4}Fe_2O_4$ films: O_2 pressure effect

5.3.2.3 FMR Studies

Figure 5.49 shows room temperature FMR spectra for films deposited at different O_2 pressure for in plane (H_{\parallel}) and perpendicular (H_{\perp}) orientations of the static field with respect to the film plane. The in plane FMR spectra show symmetric Lorentzian line-shape. The signal becomes slightly asymmetric in H_{\perp} configuration. The out-of-plane FMR spectra reveals the presence of a small anisotropy in the films deposited in O_2 gas environment compared to the films deposited in Ar gas. Similar FMR spectra were obtained for films sputtered in (Ar+ O_2) gas mixture.

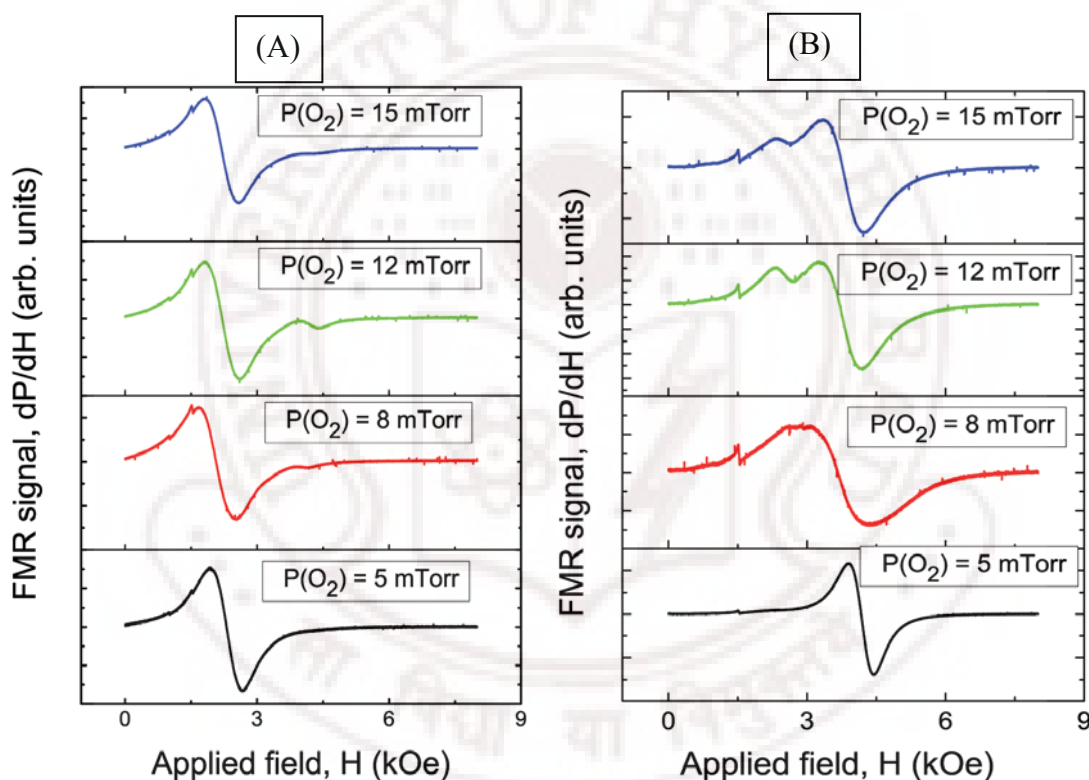


Figure 5.49: FMR signals of $Cu_{0.6}Zn_{0.4}Fe_2O_4$ films: O_2 gas pressure effect with (A) H_{\parallel} and (B) H_{\perp} to film plane.

5.3.3 Effect of (Ar+O₂) gas mixture pressure

5.3.3.1 Structural analysis (XRD)

Figure 5.50 shows the effect of O₂ content in (Ar+O₂) mixture on the XRD patterns of as-deposited Cu_{0.6}Zn_{0.4}Fe₂O₄ thin films at 12 mTorr of gas pressure. The XRD data for the as-deposited films reveal the nanocrystalline nature of the films. The XRD lines can be indexed to the spinel structure with cubic symmetry having the stoichiometry of the ceramic target (metallic cation/oxygen anion ratio equal to $\sim 3/4$). These results have been confirmed by EDAX measurements.

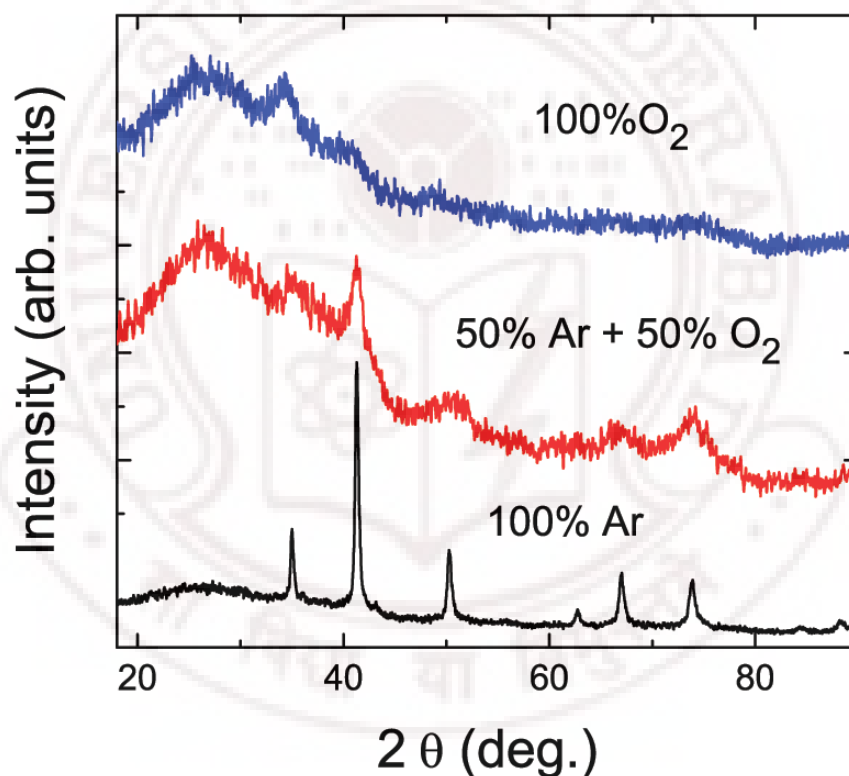


Figure 5.50: Effect of Ar-O₂ content on XRD patterns of Cu_{0.6}Zn_{0.4}Fe₂O₄ thin films deposited at 12 mTorr.

5.3.3.2 Surface morphology (AFM)

Figure 5.51 shows the AFM images of $\text{Cu}_{0.6}\text{Zn}_{0.4}\text{Fe}_2\text{O}_4$ thin films deposited at 12 mTorr of (a) Ar (b) 50% Ar + 50% O_2 (c) O_2 gas pressure. AFM data analysis reveals that the films are made up of grains with a mean diameter centered on 60, 20 and 30 nm for films deposited at 12 mTorr of Ar, Ar+ O_2 and O_2 respectively. The corresponding average RMS values are 1.15, 0.8 and 1.5 nm. The AFM images of the films show a very narrow grain size distribution.

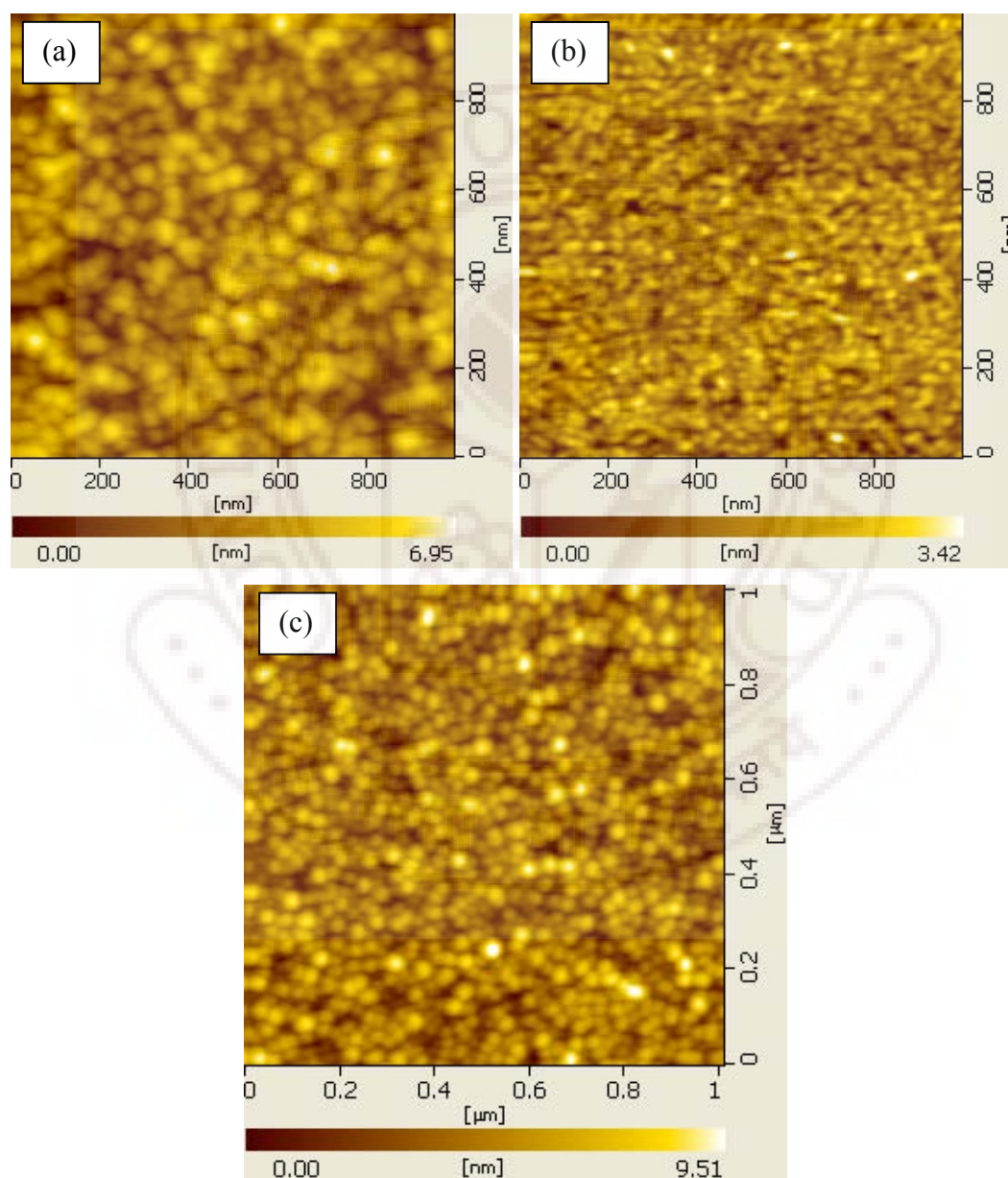


Figure 5.51: AFM images of $\text{Cu}_{0.6}\text{Zn}_{0.4}\text{Fe}_2\text{O}_4$ thin films deposited in 12 mTorr of (a) Ar (b) 50% Ar + 50% O_2 (c) O_2 gas pressure.

5.3.3.3 Magnetization studies (*M-H* plots)

Figure 5.52 shows the plots of magnetization versus applied magnetic field curves at RT for $\text{Cu}_{0.6}\text{Zn}_{0.4}\text{Fe}_2\text{O}_4$ thin films deposited in 12 mTorr of ($\text{Ar} + \text{O}_2$) gas pressure. The magnetization decreases with increasing O_2 content. The high deposition rate in pure Ar environment can lead to freezing of some Cu-ions on tetrahedral A-sites and equivalent number of Fe ions on octahedral B-sites during the deposition process. Furthermore, the deposition in reducing (argon) atmosphere may lead to the formation of Cu^+ ion, having larger ionic radius than the Cu^{2+} ion. The Cu^+ ions prefer occupation of the smaller four-coordinated A-site in the spinel structure and displace Fe^{3+} cations to occupy the B- sites [2,64]. The formation of Fe^{2+} cannot be ruled out in the spinel structure where a fraction of Fe^{3+} will be replaced by Fe^{2+} ions.

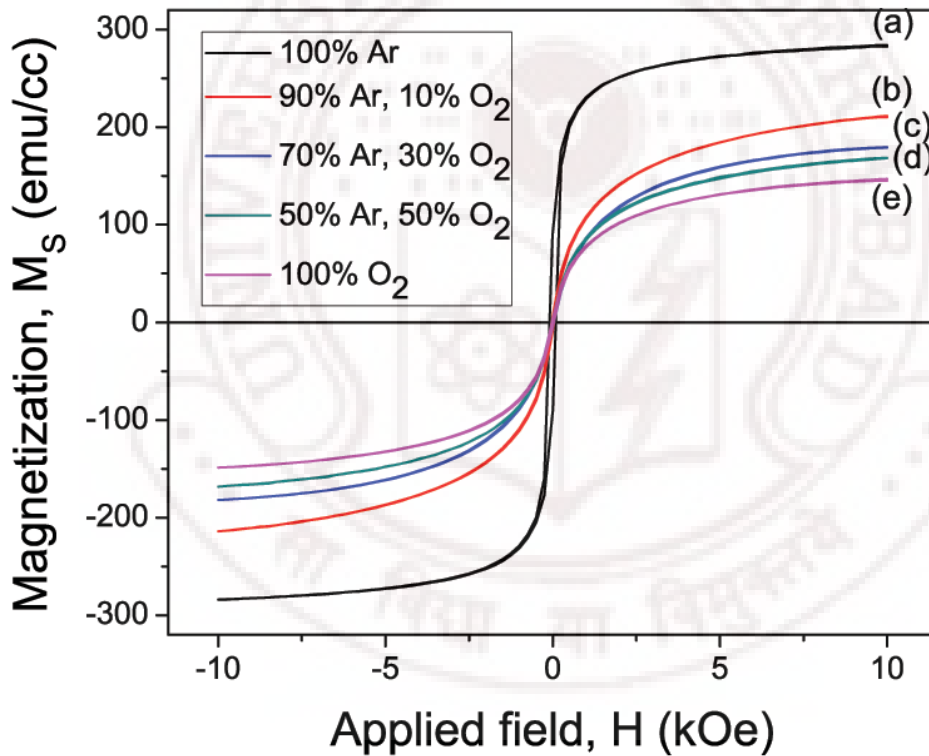


Figure 5.52: M-H curves measured at RT of $\text{Cu}_{0.6}\text{Zn}_{0.4}\text{Fe}_2\text{O}_4$ thin films deposited in 12 mTorr of (a) 100% Ar, (b) 90% Ar + 10% O_2 , (c) 75% Ar + 25% O_2 , (d) 50% Ar + 50% O_2 and (e) 100% O_2 gas pressure.

5.3.3.4 Magnetization studies (*ZFC-FC*)

Figure 5.53 shows temperature dependences of zero-field cooled (ZFC) magnetization $M_{\text{ZFC}}(T)$ and field-cooled (FC) magnetization $M_{\text{FC}}(T)$ for the as-deposited $\text{Cu}_{0.6}\text{Zn}_{0.4}\text{Fe}_2\text{O}_4$ films in Ar and O_2 environments. Both the films show that the $M_{\text{FC}}(T)$ monotonically

increases with decreasing temperature, whereas $M_{ZFC}(T)$ shows a maximum corresponding to spin freezing temperature T_f or what is called blocking temperature T_B . This peak appears at about 275 K for the film deposited under O_2 atmosphere. Such a behavior is caused by the disordered cation distribution of $Cu^{2+}(Cu^+)$, Zn^{2+} and $Fe^{3+}(Fe^{2+})$ ions in the spinel structure and can be explained in terms of superparamagnetism with intercluster interactions [44,52].

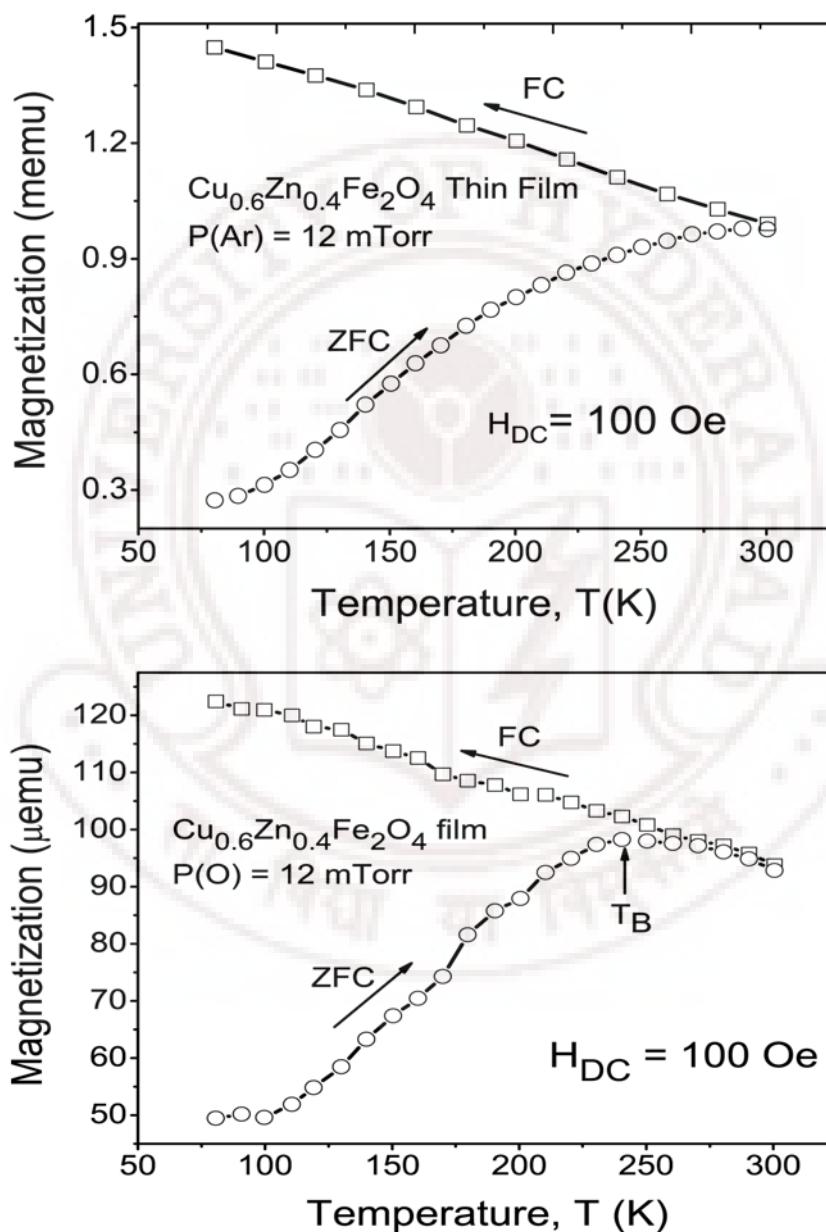


Figure 5.53: Field cooled (FC) and zero field cooled (ZFC) magnetization curves as a function of temperature taken in DC applied field of 100 Oe for the $Cu_{0.6}Zn_{0.4}Fe_2O_4$ thin films deposited at 12 mTorr of (a) Ar (b) O_2 gas pressure.

5.3.3.5 FMR studies

Figure 5.54 shows characteristic FMR spectra recorded at RT for as-sputtered $\text{Cu}_{0.6}\text{Zn}_{0.4}\text{Fe}_2\text{O}_4$ thin films deposited in 12 mTorr of $(\text{Ar} + \text{O}_2)$ gas pressure. The spectras were recorded with the magnetic field applied in plane and out of plane of the thin film. It can be seen that the films deposited with pure Ar show lower ΔH_{pp} value compared to that for films deposited in O_2 environment. With increase in the O_2 working pressure the ΔH_{pp} value increases due to the increase in the structural inhomogeneities and magnetic disorder. For thin films deposited in O_2 environment, it can also be seen that the difference in resonance fields in both configurations (H_{\parallel} and H_{\perp}) is small as expected for the magnetic response of superparamagnetic particles above their blocking temperature. In contrast the thin films deposited in argon show large difference between H_{\parallel} and H_{\perp} values indicating high magnetic anisotropy in these films.

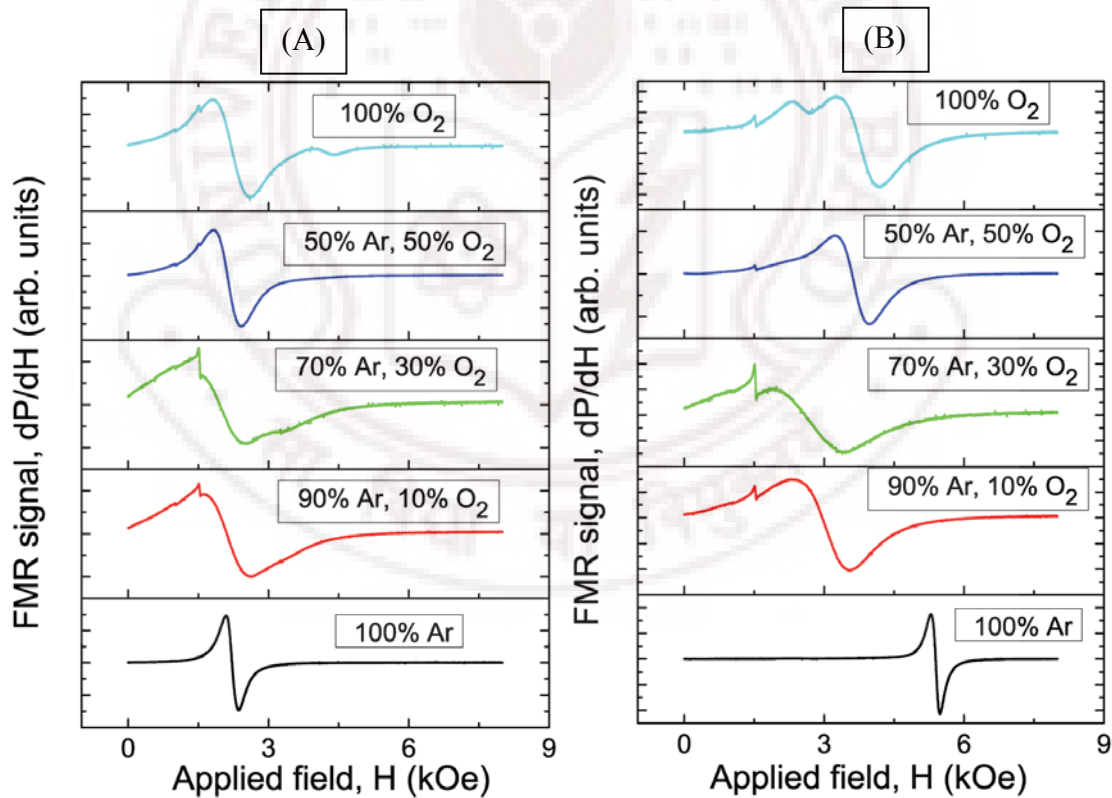


Figure 5.54: FMR spectra recorded at RT of $\text{Cu}_{0.6}\text{Zn}_{0.4}\text{Fe}_2\text{O}_4$ thin films deposited in 12 mTorr of (a) 100% Ar (b) 90% Ar + 10% O_2 , (c) 75% Ar + 25% O_2 , (d) 50% Ar + 50% O_2 (e) 100% O_2 gas pressure with (A) H_{\parallel} and (B) H_{\perp} to film plane.

The temperature dependent FMR spectra for the $\text{Cu}_{0.6}\text{Zn}_{0.4}\text{Fe}_2\text{O}_4$ thin films deposited under Ar gas at pressure of 12 mTorr are presented in figure 5.55. The position and width of the resonance line strongly depend on the sample orientation. It shifts to lower fields in the parallel configuration (magnetic field in the film plane), and to higher fields in the perpendicular configuration. The absence of multiple resonances also suggests that the films are magnetically homogeneous.

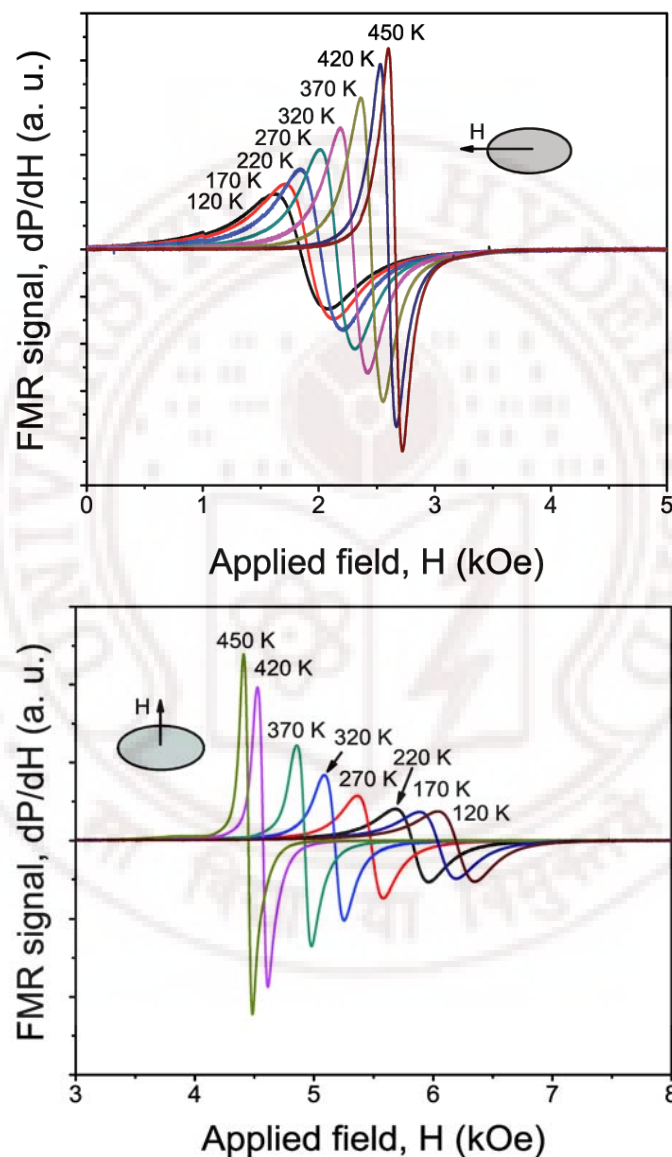


Figure 5.15: Temperature dependence of FMR spectra for $\text{Cu}_{0.6}\text{Zn}_{0.4}\text{Fe}_2\text{O}_4$ thin films deposited under Ar pressure of 12 mTorr. The spectra are for the static magnetic field applied perpendicular and parallel to the film plane.

Ferromagnetic resonance measurements at X-band frequencies were performed to study the effects of spin freezing on high-frequency magnetic parameters for the films. Figure 5.56, which shows the variation of the line width ΔH as a function of temperature for the static field H parallel (ΔH_{\parallel}) and perpendicular (ΔH_{\perp}) to the film plane for the film deposited in Ar gas at 12 mTorr. A gradual increase in ΔH_{\parallel} and ΔH_{\perp} with decreasing T is evident from the data. A relatively large ΔH is measured for H parallel to the film plane. This trend in the CuZn ferrite film is very similar to that reported previously for NiZnCu ferrite films prepared using RF-magnetron sputtering [27]. The ΔH values obtained for Cu-Zn ferrite films are smaller than that of NiZnCu ferrite films. The data in Figure 5.56 show weak temperature dependence of ΔH_{\parallel} and ΔH_{\perp} below 200 K. This could be related to the spin freezing at low temperatures as seen in the magnetization data shown in Figure 5.53

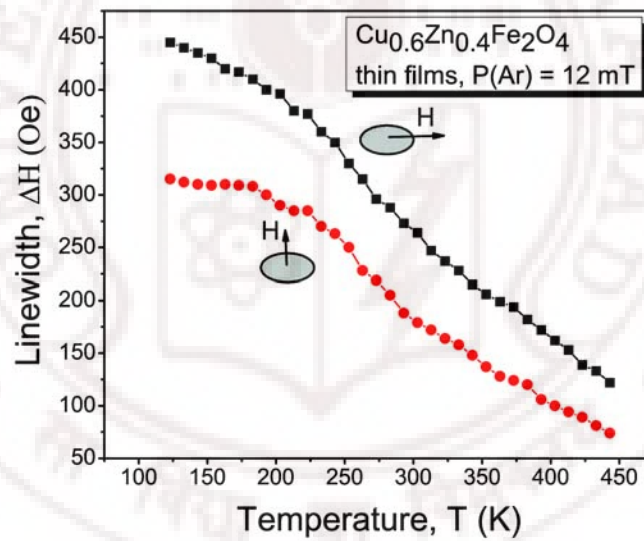


Figure 5.56: Temperature dependence of the FMR linewidth at 9.2 GHz for an argon-sputtered $\text{Cu}_{0.6}\text{Zn}_{0.4}\text{Fe}_2\text{O}_4$ film at 12 mTorr. The data are for the static magnetic field perpendicular and parallel to the film plane.

Figure 5.57 shows temperature dependence of the resonance field for static fields parallel (H_{\parallel}) and perpendicular (H_{\perp}) to the film plane for film sputtered in Ar gas at 12 mTorr. The $H_{R\perp}$ is larger than $H_{R\parallel}$ at all temperatures. An increase in the resonance fields ($H_{R\parallel}$) and decrease in H_{\perp} as the temperature increases is similar to that reported by Han et al. [27] for NiZnCu ferrite system.

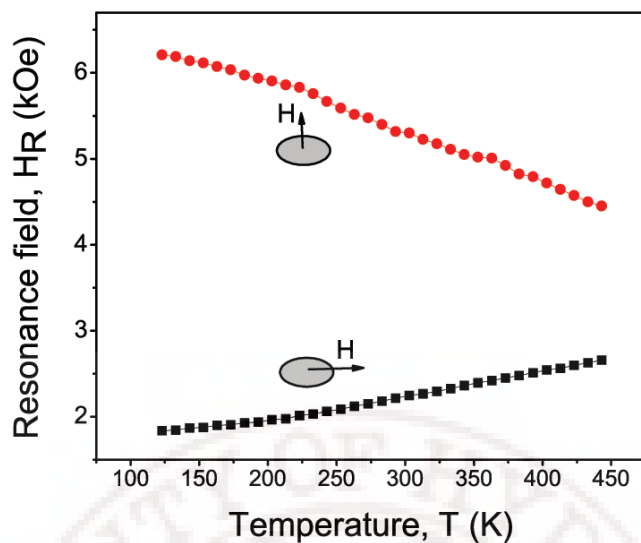


Figure 5.57: Variation of ferromagnetic resonance fields for the static field parallel and perpendicular to the film plane which deposited in Ar-gas at 12 mTorr.

The temperature dependence of the effective saturation induction ($4\pi M_{\text{ef}}$) and effective (g_{eff}) is shown in Figure 5.58. g_{eff} of 2.08 at RT is estimated for the film. As mentioned earlier, the corresponding g-value of 2.1 is in good agreement with the value reported for divalent copper ions in octahedral sites. The data indicate an increase in g_{eff} as T decreases. Such strong temperature dependence for g_{eff} is usually observed around the compensation point in ferrimagnetic crystalline oxides where the sublattice magnetizations cancel each other.

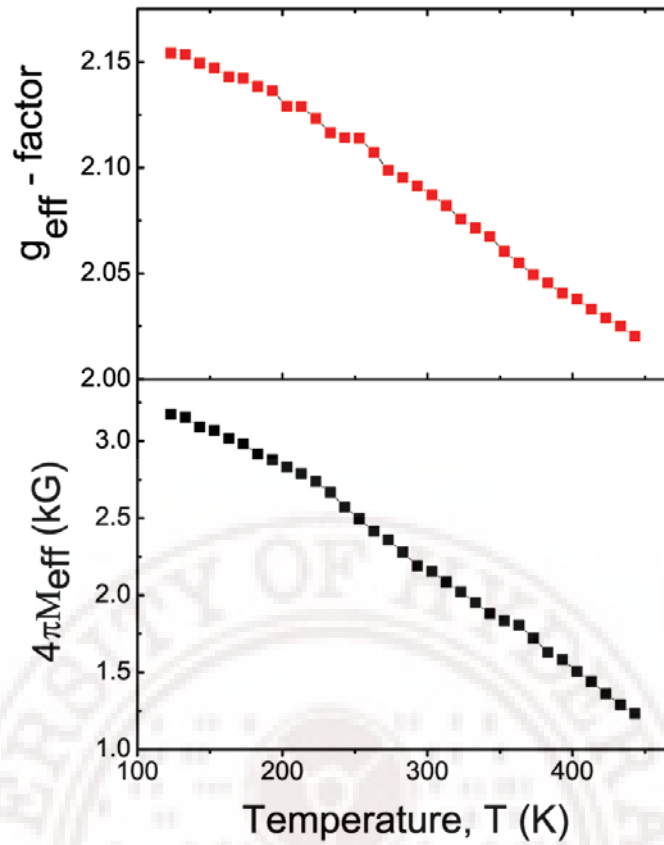


Figure 5.58: Temperature dependence of the effective saturation induction $4\pi M_{\text{eff}}$ and g -factor obtained from FMR studies at 9.2 GHz.

5.3.3.6 Optical properties

Figure 5.59 shows the transmittance spectra measured at RT for the as-grown $\text{Cu}_{0.6}\text{Zn}_{0.4}\text{Fe}_2\text{O}_4$ films deposited in 12 mTorr of $(\text{Ar} + \text{O}_2)$ gas pressure. The transmittance spectra show that all films have sharp absorption edge at about 550 nm. The films exhibit high transmittance above the absorption edge. The variation of Ar- O_2 ratio influences the optical properties of the ferrite films. The Ar-deposited films show less transmittance due to the higher thickness. With increase in the O_2 percentage the film thickness decreases and consequently gives rise to shifting of the absorption edge towards lower wavelengths with enhancement in transmittance. This can also be due to the decrease of grain size and increase in porosity of the film.

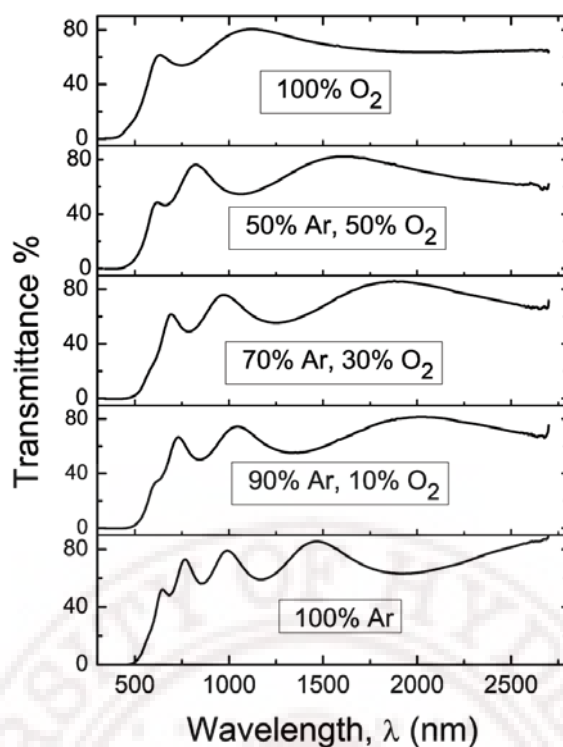


Figure 5.59: Optical transmittance spectra of the as-grown $\text{Cu}_{0.6}\text{Zn}_{0.4}\text{Fe}_2\text{O}_4$ films at 12 mTorr of Ar, O_2 and Ar+ O_2 .

References

- [1] K. Wasa, M. Kitabatake, and H. Adachi, *Thin Films Material Technology: Sputtering of Compound Materials*, William Andrew, USA, (2004).
- [2] K. E. Kuehn, D. Sriram, S. S. Bayya, J. J. Simmins and R. L. Snyder, *J. Mater. Res.* **15** (2000) 1635.
- [3] M. Sultan and R. Singh, *Solid State Physics (India)* **50** (2005) 691.
- [4] I. Nedkov, *Magnetic behavior of polycrystalline magnetite thin films with nano-sized crystallites*. In: I. Nedkov and M. Ausloos, Ed. *Nanocrystalline and Thin films of magnetic oxides*, Kluwer, Netherlands (1999), p. 43-58.
- [5] J. Smit and H. P. J. Wijn, *Ferrites*, Philips Technical Library, Eindhoven (1959).
- [6] C. Baubet, Ph. Tailhades, C. Bonningue, A. Rousset and Z. Simsa, *J. Phys. Chem. Solids* **61** (2000) 863-867.
- [7] H. Ohnishi and T. Teranishi, *J. Phys. Soc. Jpn.* **16** (1961) 35-43.
- [8] Ph. Tailhades, C. Villette, A. Rousset, G. U. Kulkarni, K. R. Kannan, C. N. R. Rao and M. Lenglet, *J. Solid State Chem.* **141** (1998) 56-63.
- [9] M. Kucera, V. Kolinsky, S. Visnovsky, D. Chvostova, N. Venkataramani, S. Prasad, P. D. Kulkarni and R. Krishnan, *J. Magn. Magn. Mater.* **316** (2007) e688- e691.
- [10] G. Srinivasan, B. U. M. Rao, J. Zhao, M. S. Seehra, *Appl. Phys. Lett.* **59** (1991) 372-374.

- [11] M. Desai, S. Prasad, N. Venkataramani, I. Samajdar, A. K. Nigam and R. Krishnan, *J. Magn. Magn. Mater.* **246** (2002) 266-269.
- [12] A. Yang, Z. Chen, X. Zuo, D. Arena, J. Kirkland, C. Vittoria and V. G. Harris, *Appl. Phys. Lett.* **86** (2005) 252510.
- [13] X. Zuo, A. Yang, C. Vittoria and V. G. Harris, *J. Appl. Phys.* **99** (2006) 08M909.
- [14] B. D. Cullity and S. R. Stock, *Elements of X-Ray Diffraction*, Prentice Hall, NJ, (2001), A. L. Patterson, *Phys. Rev.* **56** (1939) 978.
- [15] A. Goldman, *Modern ferrite technology*, 2nd ed., Springer; USA (2006) p. 58.
- [16] F. J. Cadieu, R. Rani, W. Mendoza, B. Peng, S. A. Shaheen, M. J. Hurben and C. E. Patton, *J. Appl. Phys.* **81** (1997) 4801.
- [17] S. Zhou, K. Potzger, Q. Xu, K. Kuepper, G. Talut, D. Markó, A. Mücklich, M. Helm, J. Fassbender, E. Arenholz, and H. Schmidt, *Phys. Rev. B* **80** (2009) 094409.
- [18] M. M. Ibrahim, M. S. Seehra and G. Srinivasan, *J. Appl. Phys.* **75** (1994) 6822-6824.
- [19] S. Roy and J. Ghose, *J. Appl. Phys.* **87** (2000) 6226-6228.
- [20] R. K. Selvan, C. O. Augustin, C. Sanjeeviraja and D. Prabhakaran, *Solid State Comm.* **137** (2006) 512–516.
- [21] Y. Yamamoto, H. Tanaka and T. Kawai, *J. Magn. Magn. Mater.* **261** (2003) 263–268.
- [22] C. Kittel, *Phys Rev* **71** (1948) 155.
- [23] T. Okamura and Y. Kojima, *Phys. Rev.* **86** (1952) 1040.
- [24] B. U. M. Rao and G. Srinivasan, *J. Magn. Magn. Mater.* **111** (1992) 249.
- [25] W. Alayo, E. Baggio-Saitovitch, F. Pelegrini and V. P. Nascimento, *Phys. Rev. B* **78** (2008) 134417.
- [26] R. Valenzuela, G. Alvarez, H. Montiel, M. P. Gutierrez, M. E. Mata-Zamora, F. Barron, A. Y. Sanchez, I. Betancourt and R. Zamorano, *J. Magn. Magn. Mater.* **320** (2008) 1961–1965.
- [27] K. T. Han, B. D. You, D. S. Kang and W. G. Kwon, *J. Korean Phys. Soc.* **28** (1995) 614-619.
- [28] S. Capdeville, P. Alphonse, C. Bonningue, L. Presmanes and P. Tailhades, *J. Appl. Phys.* **96** (2004) 6142.
- [29] I. Sandu, L. Presmanes, P. Alphonse and P. Tailhades, *Thin Solid Films* **495** (2006) 130.
- [30] F. Oudrhiri-Hassani, L. Presmanes, A. Barnabe and P. Tailhades, *Appl. Surf. Sci.* **254** (2008) 5796.
- [31] Y. Zhi-hao, Y. Wei, J. Jun-Hui and Z. Li-de, *Chin. Phys. Lett.* **15** (1998) 535.
- [32] Z. Wu, M. Okuya and S. Kaneko, *Thin Solid Films* **385** (2001) 1090.
- [33] D. Poelman and P. F. Smet, *J. Phys. D: Appl. Phys.* **36** (2003) 1850.
- [34] J. C. Manifacier, J. Gasiot and J. P. Fillard, *J. Phys. E: Sci. Instrum.* **9** (1976) 1002.
- [35] M. Sultan and R. Singh, *J. Phys. D: Appl. Phys.* **42** (2009) 115306, R.J. Swanepoel, *Phys. E: Sci. Instrum.* **16** (1983) 1214.
- [36] S. H. Wemple and M. DiDomenico, *Phys. Rev B.* **3** (1971) 1338.
- [37] L. Meng and M. P. Santos, *Applied Surface Science* **68** (1993) 319.
- [38] E. Marquez, J. R. Malo, P. Villares, R. J. Garay, P. J. S. Ewen and A. E. Owen, *J. Phys. D: Appl. Phys.* **25** (1992) 535.
- [39] J. Tauc, R. Grigorovici and A. Vancu, *Phys. Stat. Sol.* **15** (1966) 627.
- [40] A. F. Qasrawi, *Cryst. Res. Technol.* **40** (2005) 610.

- [41] C. N. Chinnasamy, A. Narayanasamy, N. Ponpandian, K. Chattopadhyay, H. Guerault, and J.-M. Greneche, *J. Phys.: Condens. Matter* **12** (2000) 7795.
- [42] H. H. Hamdeh, J. C. Ho, S. A. Oliver, R. J. Willey, G. Oliveri, and G. Busca, *J. Appl. Phys.* **81** (1997) 1851.
- [43] A. Kundu, C. Upadhyay, and H. C. Verma, *Phys. Lett. A* **311** (2003) 410.
- [44] S. Nakashima, K. Fujita, K. Tanaka, and K. Hirao, *J. Phys.: Condens. Matter* **17** (2005) 137.
- [45] N. Wakiya, K. Muraoka, T. Kadowaki, T. Kiguchi, N. Mizutani, H. Suzuki, and K. Shinozaki, *J. Magn. Magn. Mater.* **310** (2007) 2546.
- [46] G. F. Goya and H. R. Rechenberg, *J. Magn. Magn. Mater.* **196–197** (1999) 191.
- [47] R. H. Kodama, *J. Magn. Magn. Mater.* **200**, (1999) 359.
- [48] S. Ammar, N. Jouini, F. Fievet, Z. Beji, L. Smiri, P. Moline, M. Danot, and J.-M. Greneche, *J. Phys.: Condens. Matter* **18** (2006) 9055.
- [49] [25] R. F. Soohoo, *Magnetic Thin Films*, Harper & Row, New York (1965), p. 119.
- [50] M. D. Huang, N. N. Lee, Y. H. Hyun, J. Dubowik and Y.P. Lee, *J. Magn. Magn. Mater.* **272–276** (2004) 2031–2032.
- [51] C-H. Choi and S-H. Kim, *J. Crystal Growth* **283** (2005) 170–179.
- [52] S. Nakashima, K. Fujita, K. Tanaka, K. Hirao, T. Yamamoto and I. Tanaka, *J. Magn. Magn. Mater.* **310** (2007) 2543–2545.
- [53] S. Nakashima, K. Fujita, K. Tanaka, K. Hirao, T. Yamamoto and I. Tanaka, *Phys. Rev. B* **75** (2007) 174443.
- [54] M. Hofmann, S. J. Campbell, H. Ehrhardt and R. Feyerherm, *J. Mater. Sci.* **39** (2004) 5057–5065.
- [55] Y. F. Chen, D. Spoddig and M. Ziese, *J. Phys. D: Appl. Phys.* **41** (2008) 205004.
- [56] S. Chander, S. Kumar, A. Krishnamurthy, B. K. Srivastava and V. K. Aswal, *Pramana J. Phys.* **61** (2003) 617–624.
- [57] D. J. Sellmyer and S. Nafis, *Phys. Rev. Lett.* **57** (1986) 1173.
- [58] G. Caruntu, G. G. Bush and C. J. O'Connor, *J. Mater. Chem.* **14** (2004) 2753–2759.
- [59] M. Sorescu, L. Diamandescu, R. Swaminathan, M. E. McHenry and M. Feder, *J. Appl. Phys.* **97** (2005) 10G105.
- [60] J-S. Jung, Y-K. Jung, E-M. Kim, S.-H. Min, J.-H. Jun, L. M. Malkinski, Y. Barnakov, L. Spinu, and K. Stokes, *IEEE Trans. magn.* **41** (2005) 3403-3405.
- [61] C. Upadhyay, H. C. Verma, V. Sathe, A. V. Pimpale, *J. Magn. Magn. Mater.* **312** (2007) 271–279.
- [62] D. L. Leslie-Pelecky and R. D. Rieke, *Chem. Mater.* **1996**, *8*, 1770-1783
- [63] Y. Koseoglu, *J. Magn. Magn. Mater.* **300** (2006) e327.
- [64] M. Sultan and R. Singh, *Mater. Lett.* **63** (2009) 1764.
- [65] M. Ahmad and M. Desai, *J. Magn. Magn. Mater.* **320** (2008) L74.
- [66] A. Yang, Z. Chen, X. Zuo, D. Arena et al., *Appl. Phys. Lett.* **86** (2005) 252510.
- [67] M. Sultan and R. Singh, *J. Appl. Phys.* **105** (2009) 07A512.
- [68] K. H. Kim, Y. H. Kim, T. W. Ha, J. S. Lee and M. J. Park, *J. Magnetism (Korean)* **2** (1997) 38-41.
- [69] M. Rubinstein, B. N. Das, N. C. Koon, D. B. Chrisey and J. Horowitz, *Phys. Rev. B* **50** (1994) 184.

Summary and Conclusions

Ferrites refer to the entire family of iron oxides that includes spinels, garnets, hexaferrites, and orthoferrites. Ferrites with spinel structure are cubic and have the form AB_2O_4 (A: divalent cations and B: trivalent cations of Fe). Spinel ferrite is an important class of materials that finds a wide range of applications from microwaves to transformer cores and magnetic recording. The technological importance of ferrites increased continuously as many discoveries required the use of magnetic materials. Nanoscale ferrites have found enormous potential applications in medicine and life sciences. Thin films of spinel ferrites are potential candidates for integrated devices applications.

In this thesis, the system of copper-zinc ferrites with the general formula $Cu_{1-x}Zn_xFe_2O_4$ ($0 \leq x \leq 1$) were synthesized in the form of bulk, nanoparticles, and thin films. The synthesis methods are solid state reaction, coprecipitation and RF-magnetron sputtering for bulk, nanoparticles and thin films of ferrite samples respectively. The latter two methods allow synthesizing nanocrystalline materials with unique characteristics and possible advantages over bulk materials. Coprecipitation method has been used to prepare samples with nanometer sized particles by controlling the pH-value and reaction rate of the precipitates. By adjusting various parameters, RF-magnetron sputtering can offer a way to deposit nanocrystalline ferrite films with highly reproducible properties. Copper and zinc ferrite thin films are interesting for their textural, structural, optical and magnetic properties, which differ substantially from their bulk counterparts. It is shown that the film deposition environments (O_2 -Ar) and gas pressure play a vital role in controlling the morphology and properties of the ferrite films.

Studies on bulk Cu-Zn ferrites

The results obtained on $Cu_{1-x}Zn_xFe_2O_4$ ($0 \leq x \leq 1$) ferrite bulk samples prepared by standard ceramic method are presented as follows

(a) Structural properties

XRD patterns of the samples of the series $Cu_{1-x}Zn_xFe_2O_4$ indicate single-phase cubic spinel structure for all compositions. Fast cooling gives cubic $CuFe_2O_4$ spinel and slow cooling stabilizes tetragonal structure. The lattice parameter increases linearly with increasing x value from 0.0 to 1.0 obeying Vegard's law. The increase in lattice constant with Zinc content can be attributed to the larger ionic size of Zn^{2+} (0.82Å) than that of Cu^{2+} (0.70Å). The homogeneity of the samples was confirmed by EDAX and SEM. The

analysis of EDAX data shows that the samples are in good stoichiometric state. The morphology of the samples investigated by SEM shows that the average grain size is between 5 to 50 μm .

(b) Magnetic properties

The M-H curves for the samples with concentrations ($X = 0.0, 0.2, 0.4, 0.5, 0.6, 0.7, 0.8$ and 1.0) were obtained using vibrating sample magnetometer (VSM) at room temperature. By slow cooling CuFe_2O_4 shows tetragonal structure with higher remanent (M_r) and coercivity (H_C) and lower saturation magnetization (M_s). M_s can be enhanced by quenching from higher temperature with cubic structure. Zn-ferrite is paramagnetic at R.T. M_s reaches maximum at $x = 0.4$ which may be attributed to transition from collinear to non-collinear spin structure arrangement. The coercivity is small and its decreasing trend with increasing zinc content could be due to the decreasing of the magnetic anisotropy as a result of increasing zinc content.

(c) Dielectric properties

The variation of the dielectric constant ϵ' was studied as a function of frequency and composition. All samples show similar behavior (normal behavior) where both ϵ' and $\tan\delta$ decrease with increasing frequency. The values of ϵ' and $\tan\delta$ decrease rapidly in the lower frequency range and marginally in the MHz frequency range. This behavior can be explained on the basis of Koops' model in which the dielectric structure (ferrite) is composed of well conducting grains, which are separated by poorly conducting thin layer grain boundaries, such as an equivalent of a resistor and a capacitor. There are two types of charge carrier exchange in this system i.e. $\text{Fe}^{2+} \rightleftharpoons \text{Fe}^{3+}$ and $\text{Cu}^{1+} \rightleftharpoons \text{Cu}^{2+}$. When an electric field is applied, it could induce a local displacement of charge carriers through hopping to accumulate at the separating boundaries. The build up of charge carriers at the interfaces corresponds to a charge polarization and dielectric constant. At high frequencies, the jumping frequency of electric charge carriers cannot follow the alteration of applied AC-electric field beyond a critical frequency and the probability of charge carriers reaching the grain boundaries decreases resulting in decrease of the polarization and dielectric constant. The dielectric loss ($\tan\delta$) arises due to lag of the polarization behind the applied alternating electric field and is caused by the impurities and imperfections in the crystal lattice.

The AC-resistivity (ρ_{AC}) decreases with increasing frequency. The conduction process in copper ferrites can be explained in terms of the electron-hopping model of Heiks and

Johnson. The charge carriers exchange $\text{Fe}^{2+} \rightleftharpoons \text{Fe}^{3+}$ and $\text{Cu}^{1+} \rightleftharpoons \text{Cu}^{2+}$ occurs by random transfer between adjacent octahedral (B) sites in the spinel lattice. The magnitude of exchange, which controls the conduction in ferrites, depends on the concentration of $\text{Fe}^{2+}/\text{Fe}^{3+}$ and $\text{Cu}^{1+}/\text{Cu}^{2+}$ ion pairs present on B-sites. The dielectric constant and dielectric loss tangent decrease with increasing zinc content up to $x = 0.6$ followed by an increase in x -value. This could be ascribed by the existence of two types of charge carriers created during the sintering process where the $\text{Cu}^{1+}/\text{Cu}^{2+}$ pair decreases and $\text{Fe}^{2+}/\text{Fe}^{3+}$ increases.

Studies on Cu-Zn ferrite nanoparticles

The results on Cu-Zn ferrite nanoparticles synthesized by modified coprecipitation method are presented below

(a) Structural properties

XRD results confirmed the formation of the M-ferrite phase (spinel structure). The XRD-patterns for the as-coprecipitated samples show single broad lines without any impurity or secondary phase. The broadening of XRD peaks may come mainly from the reduced particle size and strain in the crystal. Sharpness of lines increases and (222) peak appears when samples are calcined at 700°C and 850°C. This corresponds to grain growth and improved particle crystallinity. The mean particle size of the as-coprecipitated samples is in the range of 5-10 nm and increases gradually with increase in the calcination temperature for all the compositions. The variation of the lattice parameter as a function of calcination temperature is estimated. This result is in good agreement with the results reported on ferrite fine powders. The thermal treatment of the samples at higher temperatures leads to grain growth and provides sufficient energy to allow reordering of the metal cations into their preferable sites resulting in typical properties of the bulk material. The homogeneity of the samples has been conformed by EDAX and SEM. The EDAX results show that the synthesized samples have stoichiometry close to the starting composition. The morphology of the samples investigated by SEM shows that the average particle size varies in the 50 - 70 nm range.

(b) Magnetic properties

The M-H curves for the samples with concentrations ($X = 0.0, 0.2, 0.4, 0.5, 0.6, 0.7, 0.8$ and 1.0) were obtained using vibrating sample magnetometer (VSM) at room

temperature. The plots were used to estimate magnetic moment for various synthesized samples.

It is found that the magnetic moment of the nanoparticle samples sintered at 850 °C is higher than those of corresponding bulk samples. The magnetic moment also increases with the increase in zinc content up to $x = 0.4$ followed by a decrease with further increase in Zn content similar to the case of bulk samples. The increasing trend in magnetic moment can be explained on the basis of Neel's two sub-lattices model. However, the decreasing trend cannot be explained on the basis of the Neel's two sub-lattices model. It may be due to the non-zero Yafet-Kittel angles for all the samples with $x > 0.4$. The estimated value of Y-K angle increases exponentially with the increase in Zn concentration for $x \geq 0.4$. The non-zero Y-K angle suggests that the magnetization behavior cannot be explained on the basis of Neel two sub-lattices model due to the presence of spin canting on B sites, which increases the B-B interaction and consequently decreases the A-B interaction. These results show that in the present system of ferrites, the randomness increases as Zn is substituted at Cu sites leading to a significant departure from Neel's collinear model. We also found that the magnetic moment of the as-coprecipitated zinc ferrite increases with decrease in particle size. The highest value of magnetic moment for as-prepared zinc ferrite nanoparticle is about 12 emu/g at room temperature. The magnetic moment decreases with increase in calcination temperature.

The variation of the dielectric constant ϵ' of the ferrite nanoparticle samples has been done as a function of frequency and composition. All samples show normal behavior where both ϵ' and $\tan\delta$ decrease with increasing frequency. The values of ϵ' and $\tan\delta$ decrease rapidly in the lower frequency range and marginally in the MHz frequency range. This behavior can be explained on the basis of Koops' model as for the bulk samples. The analysis of the data has been done on the same lines as for the bulk samples.

EPR spectroscopy has provided significant information concerning the homogeneity of the ferrite samples and the dynamics of the ferromagnetic transition. This chapter covers the detailed temperature dependent EPR study on the nanoparticles of zinc ferrite and copper substituted zinc ferrites. For zinc ferrite and copper substituted zinc (10, 20 and 30% Cu) ferrite samples, the temperature dependence of FMR spectra shows substantial changes in the line shape of resonance near the transition temperature due to the existence of multi-magnetic phases (para-, ferro- and antiferromagnetic phases) over a wide range of temperature. For 40 and 60% substituted, the ferro-to-para transition is very sharp. The data is analyzed in view of various theoretical models.

Studies on thin films of Cu-Zn ferrites

The detailed study of the structural, magnetic and optical properties of ferrosipinel $\text{Cu}_{1-x}\text{Zn}_x\text{Fe}_2\text{O}_4$ ($x = 0, 0.4$ and 1) thin films deposited by rf-magnetron sputtering are given bellow.

CuFe_2O_4 thin films

The structure and morphology of the deposited films were investigated using X-ray diffraction (XRD) and atomic force microscopy (AFM). The XRD data indicate that the films crystallize in cubic spinel structure. The AFM images show the nanocrystalline nature of the films. The XRD and AFM studies of the as-deposited films indicate nanocrystalline cubic spinel structure. In case of CuFe_2O_4 films an observed increase in the intensity of (400) line at the expense of (220) line with increase in O_2 content is ascribed to the change in distribution of Cu and Fe-ions among tetrahedral A-site and octahedral B-sites. The grain size depends on the process gas environment and varies between 55 and 75 nm. The smaller value is obtained for the film deposited under the pure argon environment.

The highest saturation magnetization (M_s) of 264 emu /cc (in-plane) and 188 emu /cc (out of-plane) were obtained for the as-deposited CuFe_2O_4 films in pure Ar at 12 mTorr. The high deposition rate in reducing atmosphere leads to the formation of Cu^+ ions which prefer occupation of the A-site in the spinel structure displacing Fe^{3+} cations to occupy the B-sites giving rise to the change in cation distribution among A and B-sites and consequently leading to high value of M_s . The decrease in M_s value with increase in oxygen content is ascribed to decrease in film growth rate and Cu^+ concentration which allow the cations to take up their preferable sites. The observed change in the film properties with environment are due the presence of multivalent copper and iron ions with differing site preferences.

The magnetization-temperature (M-T) curves of as-sputtered CuFe_2O_4 thin films deposited at 12 mTorr of Ar, O_2 and (Ar+ O_2) gas pressure under zero field cooling and field cooling (ZFC-FC) conditions were measured in an external field of 100 Oe in the temperature range 80-300 K. The ZFC/FC measurements for the as-deposited films show significant irreversibility. The discrepancy between the zero-field-cooled (ZFC) and field-cooled (FC) dc magnetizations demonstrate that the magnetism of the present thin film can be attributed to the superparamagnetism with the interaction among magnetic clusters.

ZnFe₂O₄ thin films

The RT-magnetic measurements of ZnFe₂O₄ show ferrimagnetic behavior, and it strongly depends on deposition environment and process gas working pressure. The maximum magnetization of 230 emu/cm³ (42 emu/g) at RT is obtained for the film deposited at 27 mTorr of oxygen pressure. The oxygen vacancy concentration and random distribution of Zn²⁺ and Fe³⁺ on both tetrahedral and octahedral sites are the possible reasons of high magnetization due to rapid cooling of sputtered vapors to form solid state film.

The magnetization versus temperature (M-T) curves of as-sputtered and annealed ZnFe₂O₄ thin films in an applied field of 100 Oe recorded in the zero field cooling – field cooling modes (ZFC–FC) in the temperature range 80–300 K show significant irreversibility. The curves coincide at high temperatures and follow different trends as the temperature is decreased from 300 to 80 K. In the FC mode, the magnetization continues to increase with decreasing temperature below the peak temperature T_B, without a tendency towards saturation demonstrating Curie-like behavior, whereas the ZFC magnetization shows a maximum followed by a steady decrease to smaller values in the low temperature region. The peak temperature shifts toward lower values with increase in annealing temperature. This is due to the disordered cation distribution of Zn²⁺ and Fe³⁺ ions in the spinel structure and can be explained in terms of superparamagnetism with intercluster interactions suggesting that a ferrimagnetic order occurs for localized magnetic moments. The variation of T_B with T_a is mainly ascribed to the redistribution of Zn²⁺ and Fe³⁺ ions toward normal spinel structure.

Ferromagnetic Resonance (FMR) studies were carried out as a function of composition, orientation and temperature on as-deposited RF-sputtered nanocrystalline ferrite thin films. The in-plane FMR linewidth (ΔH) increases and the resonance field (H_R) decreases with decrease in temperature. The annealing of the films in air at 500 °C for 3hrs decreases ΔH confirming disorder as the source of FMR line broadening for the as deposited films. The effective magnetization ($4\pi M_{\text{eff}}$) of 1500 to 2200 G and gyromagnetic ratio (γ_{eff}) of 2.8 to 3.08 GHz/kOe were estimated using Kittel's equations. The uniaxial anisotropic field of 800 to 1164 Oe observed for the films is assigned to preferential orientation of grains.

The optical constants of the films were extracted from the transmission spectra by the envelope method. It is found that the refractive index (n) and the energy band gap (E_g) increase with increase in Zn-content. The films deposited under Ar environment having

lower values of n and E_g . These values are enhanced by depositing the films in higher O_2 gas pressure. The estimated direct energy band gap values for the film deposited at 8 mTorr of gas pressure in pure Ar is 2.43 eV. For the films deposited in pure O_2 , the band gap increases from 2.48 to 2.61 eV as the O_2 pressure is increased from 8 to 31 mTorr. The absorption is attributed to the $3d^5 \rightarrow 3d^4 4s^1$ transition of Fe^{3+} ions, where the $4s$ orbital of Fe^{3+} is thought to contribute to the conduction band. The dispersion of the refractive index (n) is discussed in terms of the single-oscillator Wemple–DiDomenico model. This model is also used to estimate the dispersion parameters and the static refractive index.

Cu_{0.6}Zn_{0.4}Fe₂O₄ thin films

The detailed studies on bulk $Cu_{1-x}Zn_xFe_2O_4$ ferrites show that the highest magnetization of ~ 330 emu/cc is obtained for the composition $Cu_{0.6}Zn_{0.4}Fe_2O_4$. There is no report in the literature on the properties of copper-zinc ferrite thin films. We carried out a detailed study of crystal structure, magnetic and optical properties of $Cu_{0.6}Zn_{0.4}Fe_2O_4$ ferrite thin films. The films were deposited by RF-magnetron sputtering with RF power of 100 W in pure Ar, pure O_2 and (Ar+ O_2) at various working gas pressure. The XRD patterns show that the deposited films are single-phase and belong to spinel $Cu_{0.6}Zn_{0.4}Fe_2O_4$ ferrite with cubic symmetry without any secondary or impurity phases. XRD studies also confirm the change in the crystal structure with gas content and the nanocrystalline nature of the as-deposited films. The average crystallite size increases from 5 to 21 nm with increase in Ar pressure from 5 to 15 mT. With increase in Ar content the relative intensity ratios of planes I_{220}/I_{400} , I_{440}/I_{400} and I_{422}/I_{400} increases. It is known that for spinel–ferrite the increase in intensity ratios of these planes is related to the increase in disorder parameter and consequently to the increase in magnetization. This behavior is an indication of the film orientation which can be assigned to the special conditions of the film preparation and the change in distribution of Cu, Zn and Fe ions among tetrahedral A-site and octahedral B-sites. The films deposited at lower pressure show higher cell parameter (8.5 Å) compared to the bulk due to strain introduced in the film during deposition. The strain reduces with increase in Ar pressure and cell parameter approaches the bulk value.

The saturation magnetization (M_s) increases and coercivity (HC) decreases with increasing Ar pressure. M_s decreases from 283 emu/cc to 150 emu/cc as the O_2 content increases from 0 to 100 % in the (Ar + O_2) mixture. The variation of working pressure does not show any significant effect on the M_s value when the films are deposited in O_2 environment alone. The large magnetization of the films sputtered under Ar environment can be due to the appropriate deposition parameters used in the present study which lead

to preferential orientation of ferrimagnetic clusters. . The high deposition rate in pure Ar environment can lead to freezing of some Cu-ions on tetrahedral A-sites and equivalent number of Fe ions on octahedral B-sites during the deposition process. Furthermore, the deposition in reducing (argon) atmosphere may lead to the formation of Cu^+ ion, having larger ionic radius than the Cu^{2+} ion. The Cu^+ ions prefer occupation of the smaller four-coordinated A- site in the spinel structure and displace Fe^{3+} cations to occupy the B- sites. The formation of Fe^{2+} cannot be ruled out in the spinel structure where a fraction of Fe^{3+} will be replaced by Fe^{2+} ions. So the general cation distribution can be represented as $((\text{Cu}^{2+}\text{Cu}^+)_{\text{d}} \text{Zn}^{2+}\text{Fe}^{3+}_{1-\text{d}})_{\text{tetra}}[\text{Cu}^{2+}_{1-\text{d}}(\text{Fe}^{2+}\text{Fe}^{3+})_{1+\text{d}}]_{\text{octa}}\text{O}_4^{2-}$ where d is the inversion parameter. The occupancy of the nonmagnetic Cu^+ and Zn^{2+} ions on A-sites dilutes the magnetic moment on A-sites leading to large difference between magnetization on B and A sites causing a strong negative super-exchange interaction between Fe^{3+} ions on both sites which in turn cause ferrimagnetic behavior with large magnetization. The value of coercivity, H_C decreases from 170 to 67 Oe with increase in Ar pressure from 5 – 15 mTorr. This can be correlated to the crystallite size and the presence of significant inhomogeneities. The smaller crystallites in the case of thin films deposited under low Ar pressure has larger volume of the boundaries and consequently more energy is required to rotate the grains by the external field and thus leading to higher coercivity.

The M-T studies were carried out in the ZFC/FC modes for the as-deposited $\text{Cu}_{0.6}\text{Zn}_{0.4}\text{Fe}_2\text{O}_4$ films in Ar and O_2 environments. Both the films show that the $M_{\text{FC}}(T)$ monotonically increases with decreasing temperature, whereas $M_{\text{ZFC}}(T)$ shows a maximum, corresponding to spin freezing temperature or what is called blocking temperature T_B . Such a behavior is caused by the disordered cation distribution of $\text{Cu}^{2+}(\text{Cu}^+)$, Zn^{2+} and $\text{Fe}^{3+}(\text{Fe}^{2+})$ ions in the spinel structure and can be explained in terms of superparamagnetism with intercluster interactions

The FMR spectra for the deposited films were recorded at a frequency of 9.2 GHz for parallel (H_{\parallel}) and perpendicular (H_{\perp}) orientations of the applied field with respect to the film plane. The parallel FMR spectra show single symmetric Lorentzian line-shape. The perpendicular FMR spectra show slightly asymmetric with a second minor peak. The strong out-of-plane dependence of the FMR spectra reveals the presence of induced growth anisotropy in the films. This anisotropy decreases with O_2 content. The FMR resonance line width (ΔH) is also strongly influenced by working gas pressure. The decrease in ΔH with Ar pressure correlates with the hysteresis and coercivity in the magnetization data which decrease with increasing Ar pressure. The line shape in perpendicular FMR is more sensitive to microstructural inhomogeneity than the in-plane

case. These qualitative conclusions are also consistent with the highly textured nature of the films. The FMR parameters such as g-value and anisotropy field (H_u) were extracted using Kittel's equations from parallel (H_{\parallel}) and perpendicular (H_{\perp}) orientations of the applied field with respect to the film plane.

The main results presented in the thesis are summarized as follows:

1. The analysis of x-ray diffraction data shows the nanocrystalline nature of the samples indicating the presence of octahedral zinc in ZnFe_2O_4 and tetrahedral Cu in CuFe_2O_4 thin films and nanoparticles.
2. The addition of nonmagnetic zinc to copper ferrite improves the magnetization reaching the highest value of 62 and 67 emu/g at $x = 0.4$ for bulk and nanoparticles respectively followed by a decreasing trend with further increase in zinc content.
3. DC-magnetization studies show superparamagnetic behavior of as-prepared samples of zinc ferrite and copper ferrite nanoparticles. This is attributed to breaking of superexchange bonds due to oxygen vacancies produced during producing stage.
4. DC-magnetization studies show ferrimagnetic behavior of as-deposited zinc ferrite and copper ferrite thin films.
5. An enhanced magnetization compared to bulk zinc ferrite was observed in films prepared by RF-magnetron sputtering. The magnetization reaches value of about 42 emu/g at RT.
6. Temperature dependence of FMR studies show the presence of competing ferro- and antiferromagnetic exchange interactions arising from Fe clustering in Zn and Cu-ferrite nanoparticles and thin films
7. High value of saturation magnetization (M_s) of 264 emu /cc (in-plane) and 188 emu /cc (out of-plane) were obtained for the as-deposited CuFe_2O_4 thin films in pure Ar.

8. The temperature dependent magnetization $M(T)$ measurements in the ZFC-FC mode demonstrate that the magnetism of the films can be attributed to the superparamagnetism with the interaction among magnetic clusters. Spin freezing occurs at a temperature (T_B) close to room temperature in zinc ferrite films. T_B moves towards lower temperature with increase in annealing temperature. The mean blocking temperature for CuFe_2O_4 and $\text{Cu}_{0.6}\text{Zn}_{0.4}\text{Fe}_2\text{O}_4$ films deposited under Ar-atmosphere is well above room temperature which could be due to the larger coercivity field of these films compared to the applied field of 100 Oe. The films deposited in O_2 environment show superparamagnetic behavior at RT and the blocking temperature is $\sim 275\text{K}$.
9. The optical transmission of ZnFe_2O_4 thin films is high in the visible (about 85-80% depending on thickness and gas type and pressure), with excellent UV absorption properties. The transmission and optical band-gap decrease with increase in copper content and thickness of the films.
10. The post-deposition annealing of the films has been found to alter the film's microstructure and properties. Annealing alters the distribution of oxygen defects, reduces the stress of the thin film and causes grain coarsening and recrystallization. Annealing increases the porosity, the transparency and optical band gap for the films deposited in Ar-atmosphere.
11. Annealing at lower temperatures ($< 200^\circ\text{C}$) does not show a significant effect on the crystal structure. But annealing in air at higher temperatures ($> 300^\circ\text{C}$) increases the oxygen content and the porosity of thin films, leading to improvement in the film transparency and grain alignment.
12. The dielectric constant and dielectric loss are smaller in the case of nanoparticle samples than those of bulk counterparts. This could be attributed to improvement in the homogeneity and density of the samples prepared by coprecipitation method.

In conclusion, the thesis presents some new results as well as improvements on the information available in the literature on Cu-Zn ferrites. The thesis presents a systematic study of structural, magnetic and dielectric properties of $\text{Cu}_{1-x}\text{Zn}_x\text{Fe}_2\text{O}_4$ ($0 \leq x \leq 1$) samples in bulk, nanoparticles and thin film form. The thesis provides the preparation method of these ferrites in nanoparticle form by coprecipitation technique at lower sintering temperature of 850 °C with improved dielectric and magnetic properties compared to corresponding bulk ferrites. The systematic studies of structural, magnetic and dielectric properties as a function of nanoparticle size and pH-value are carried out in this work. Such studies are not reported in the literature.

The present work provides extensive study of magnetic, structural and optical properties of Cu, Zn and CuZn ferrite ($\text{Cu}_{0.6}\text{Zn}_{0.4}\text{Fe}_2\text{O}_4$) films. The ferrite films with improved magnetic properties were obtained by RF-sputtering on the unheated substrates using moderate power level without annealing but only by adjusting the process gas environment and target to substrate distance. There is no report on the synthesis and properties of mixed Cu-Zn ferrite thin films. However, there are a number of studies on Cu and Zn-ferrite thin films reported in the literature. In these studies higher magnetization values were achieved either by substrate heating or annealing the films at high temperatures or by using high RF- power level. The magnetic properties of ferrites are determined by site occupancy in the spinel structure. The site occupancy of various cations on A- and B- sites of the spinel structure of the ferrite films has been determined qualitatively using XRD spectra. The observed variation in the relative intensity ratios of I_{220}/I_{400} , I_{440}/I_{400} and I_{422}/I_{400} planes in the XRD spectra of the films is ascribed to the random distribution of the cations (Cu, Zn and Fe) among A- and B-sites. The quantitative analysis using Rietveld fittings of the XRD patterns did not provide accurate values of site occupancy in the spinel structure due to low counts and broad peaks in the XRD spectra. It is known that by using Rietveld refinement of x-ray diffraction data, it is difficult to deduce the degree of cation disordering, due to the similar scattering strength of cations. In the case of nanocrystalline thin films and nanoparticles such as our samples, the problem is more serious because of the broadness of the diffraction peaks. In the recent years the extended x-ray absorption fine structure (EXAFS) analysis has been used

to determine the degree of cation disordering in various spinel ferrites including NiZn ferrite, MnZn ferrite and Cu ferrite. EXAFS offers structural parameters concerning ambient atoms, such as coordination numbers and interatomic distance. On the other hand, x-ray absorption near-edge structure (XANES) analysis provides information about the electronic state and chemical bond of a specific atom. Since EXAFS and XANES give complementary information, the combination of both spectral analyses should be more effective in clarifying the local environment of a specific atom. Recently, these techniques have been used (Ref. 53, Chap. 5) to estimate the cation distribution over A- and B-sites in the spinel structure of ferrite thin films.

There is no report in the literature on FMR and optical properties of Cu-Zn ferrite thin films. The FMR data under zero-field cooled (ZFC) and field cooled (FC) conditions of the sample, confirm the disordered cation distribution of Cu^{2+} , Zn^{2+} and Fe^{3+} ions in the as-deposited spinel lattice. The studies on the thin films annealed in air confirm disorder as the source of FMR line broadening for the as deposited films. The data have been analyzed in view of Kittle's theoretical model.

The optical properties of the present ferrites thin films confirm them to be semi-transparent. The optical experimental data is analyzed in view of single oscillator Wemple-DiDomenico model. The optical studies have provided the estimation of optical constants for these films which will be useful for their application in optoelectronic devices.

The present work on thin films has provided important data which may be useful for their applications in designing micro-transformers, micro-inductors, recording and microwave devices.

PUBLICATIONS

International Journals:

- [1] Magnetic and optical properties of rf-sputtered zinc ferrite thin films
M. Sultan and R. Singh,
J. Appl. Phys. **105** (2009) 07A512
- [2] Structural and optical properties of RF-sputtered ZnFe₂O₄ thin films
M. Sultan and R. Singh,
J. Phys. D. **42** (2009) 115306
- [3] Magnetization and crystal structure of RF-sputtered nanocrystalline CuFe₂O₄ thin films
M. Sultan and R. Singh,
Materials Letter **63** (2009) 1764
- [4] FMR Studies on Nanocrystalline Zinc Ferrite Thin Films
M. Sultan and R. Singh,
J. Phys. Conference Series (accepted)
- [5] Crystal structure and magnetic properties of rf-sputtered Cu-Zn ferrite thin films
M. Sultan and R. Singh,
J. Appl. Phys. (accepted)

Conference papers:

- [1] Structural and Magnetic Properties of Cu-Zn ferrites
M. Sultan and R. Singh,
Solid State Physics, India **50** (2005) 691.
- [2] Dielectric behaviour in Cu-Zn ferrites
M. Sultan and R. Singh,
Solid State Physics, India **51** (2006) 675.
- [3] FMR Synthesis and EPR studies of zinc ferrite nanoparticles
M. Sultan and R. Singh,
Solid State Physics, India **52** (2007) 257.
- [4] Optical properties of RF-sputtered amorphous SnO₂ thin films
S. Saipriya, **M. Sultan** and R. Singh,
Solid State Physics, India **54** (2009) 541.
- [5] Structure and properties of nanocrystalline pure and Mn-Fe doped ZnO thin films
Venkaiah M., **M. Sultan** and R. Singh,
Solid State Physics, India **54** (2009) 563.

Manuscripts in preparation

- [1] Post annealing effect on the structure and magnetic properties of ZnFe₂O₄ thin films
M. Sultan and R. Singh (communicated)
- [2] Ferromagnetic resonance study on Cu-ferrite thin films,
M. Sultan and R. Singh
- [3] The influence of the deposition conditions on the structure and magnetic properties of
Cu_{0.6}Zn_{0.4}Fe₂O₄ thin films
M. Sultan and R. Singh